Immune responses of the Egyptian Rousette Bat

Deciphering the unique immunity of an important reservoir host for zoonotic viruses

Inauguraldissertation

zur

Erlangung des akademischen Grades eines

Doktors der Naturwissenschaften

(Dr. rer. nat.)

der

Mathematisch-Naturwissenschaftlichen Fakultät

der

Universität Greifswald

vorgelegt von

Virginia Friedrichs

Greifswald, Januar 2022

Dekan: Prof. Dr. Gerald Kerth

1. Gutachterin: Prof Dr. Anca Dorhoi

2. Gutachterin: Prof. Dr. Stefanie Scheu

3. Gutachter: PD Dr. Christian Voigt

Tag der Promotion: 06.07.2022

Für meine Familie.

'For as the eyes of bats are to the blaze of day, so is the reason in our soul to the things which are by nature most evident of all.'

Aristotle

Content

Zusammenfassung

Die Ordnung der Fledertiere (*Chiroptera*) macht etwa 20% aller Säugetierarten aus und zieht wegen ihres einzigartigen Viroms weltweit großes Interesse auf sich. Fledertiere können, unter Ausprägung geringer oder keiner Krankheitsanzeichen, eine Vielzahl von hochpathogenen zoonotischen Viren wie Filo-, Lyssa- und Coronaviren beherbergen. Angesichts der Virom-Vielfalt, ihrer Fähigkeit zum autonomen Flug und ihrer globalen Verbreitung ist das Verständnis der Immunität von Fledertieren von entscheidender Bedeutung, um die Einschätzung künftiger Spillover-Ereignisse und Risiken zu optimieren.

Der Mangel an Fledertier-spezifischem oder kreuzreaktivem Material und standardisierten Modellsystemen erschwert dies jedoch bis heute. Darüber hinaus hat die schiere Anzahl der Arten zu isolierten Datensätzen geführt, was Interpretation und Identifizierung allgemeiner und artspezifischer Immunmechanismen erschwert. Um die Immunität der Fledertiere gezielt zu adressieren, benötigt es koordinierte Forschungsansätze zur möglichst umfassenden Untersuchung vieler Arten. In dieser Arbeit wird eine eingehende Untersuchung der angeborenen und adaptiven Immunmechanismen des Nilflughundes (*Rousettus aegyptiacus*, *Egyptian Rousette bat* [ERB]) vorgestellt.

Detaillierte Stabilitätsanalysen identifizierten *EEF1A1* als überlegenes Referenzgen gegenüber *ACTB* und *GAPDH*, deren Expression bei Temperaturerhöhung oder Anwesenheit von Typ-I-Interferon (IFN) instabil ist. Die Expression eines Referenzgens muss auch unter diesen für Fledertiere physiologischen Bedingungen stabil sein. Zur Untersuchung der molekularen angeborenen Immunität, wurden Zelllinien aus dem Nasenepithel, dem Riechsystem und dem Großhirn generiert. Um die Immunreaktionen von primären Epithelzellen einzubeziehen, die für Immunität an Orten der initialen Virusinfektion entscheidend sind, wurden Zellen aus Nasenepithel, Trachea, Lunge und Dünndarm generiert. Die Zellidentitäten wurden mit umfassenden Analysen der von jeder Zelllinie exprimierten Transkripte und Proteine bestimmt. Die Fähigkeit jeder Zelllinie, Typ-I- und III-IFN zu produzieren, wurde bei 37°C und 40°C nach Stimulation mit viralen Mimetika untersucht. Dabei zeigten sich zelltypabhängige Unterschiede in der Fähigkeit, IFN zu exprimieren. Darüber hinaus war die konstitutive Expression von Typ-I- und III-IFN bei 40°C erhöht. Um

die angeborene Immunität von ERB bei Infektionen mit zoonotischen Viren zu charakterisieren, wurden Zellen aus dem Nasenepithel, dem Riechsystem und dem Gehirn mit verschiedenen Lyssaviren infiziert. Darüber hinaus zeigten sich auffällige Unterschiede in der Suszeptibilität, da Zellen aus dem Nasenepithel weniger, Zellen aus dem Riechepithel hingegen vermehrt suszeptibel waren. Ferner konnte gezeigt werden, dass das Lagos bat Lyssavirus (LBV) aufgrund einer fehlenden IFN-Expression in infizierten Zellen vermutlich fortgeschrittene Immunoevasions-Eigenschaften besitzt. Da die aktuelle SARS-CoV-2-Pandemie Fledertiere weiter in den Fokus der Zoonoseforschung gerückt hat, wurden primäre Epithelzellen und Tiere mit diesem Virus infiziert, um ERB-spezifische Immuntranskripte in Zellen und Geweben zu untersuchen. Diese Studien ergaben eine auffallend frühe *IFNG*-Expression im Respirationstrakt infizierter Individuen.

Darüber hinaus wurde das Leukozytenprofil in Peripherie und verschiedenen Geweben bei adulten und juvenilen ERB mittels Durchflusszytometrie und Sequenzierung auf Einzelzellebene (scRNA-seq) analysiert. Die Durchflusszytometrie ergab eine signifikant höhere Anzahl von Granulozyten bei adulten, sowie eine höhere Anzahl von B-Zellen bei juvenilen Tieren. Das scRNA-seq ermöglichte eine detaillierte Identifizierung verschiedener Leukozyten-Untergruppen, unter anderem NKT-ähnlichen Zellen und einer *PLAC8*-exprimierenden B-Zell-Population. Eine funktionelle Charakterisierung von phagozytierenden Zellen und Lymphozyten aus adulten und juvenilen ERB ergab keine signifikanten Unterschiede in zellulärer Funktionalität.

Zusammenfassend lässt sich sagen, dass die vorliegende Arbeit die Eignung aller etablierten ERB-Zelllinien für Untersuchungen der Fledertier-Immunität *in vitro* gezeigt hat. Zu den Kernergebnissen zählt die Analyse der IFN-Expression im Ruhezustand, bei Stimulation oder Virusinfektion. Darüber hinaus konnten mit Hilfe etablierter qRT-PCR-Protokolle die konstitutive und temperaturabhängige Erhöhung der IFN-Expression sowie die Expression immunbezogener Transkripte in mit SARS-CoV-2 infizierten ERB bestimmt werden. Mithilfe von optimierten scRNA-seq Technologien und Durchflusszytometrie konnten Frequenzen und absolute Zellzahlen in ERB unterschiedlichen Alters bestimmt werden, was z. B. altersabhängige Schwankungen in der Zusammensetzung des Leukozytenprofils aufzeigte.

Summary

The order of bats (*Chiroptera*) account for ~20% of all mammalian species and attracted immense global attention due to their identification as important viral reservoir. Bats can harbour a plethora of high-impact zoonotic viruses, such as filoviruses, lyssaviruses, and coronaviruses without displaying clinical signs of disease themselves. Given this striking diversity of the bat virome, their ability of self-powered flight, and global distribution, understanding chiropteran immunity is essential to facilitate assessment of future spillover events and risks.

However, scarcity of bat-specific or cross-reactive tools and standardized model systems impede progress until today. Furthermore, the richness of species led to generation of isolated datasets, hampering data interpretation and identification of general immune mechanisms, applicable for various chiropteran suborders/families. The key to unlocking bat immunity are coordinated research approaches that comprehensively define immunity in several species. In this work, an in-depth study of innate and adaptive immune mechanisms in the fructivorous Egyptian Rousette bat (*Rousettus aegyptiacus*, ERB) is presented.

Detailed stability analyses identified *EEF1A1* as superior reference gene to *ACTB*, and *GAPDH*, which rendered unstable upon temperature increase or presence of type-I-IFN. Since the body core temperatures of pteropid bats reach from 35°C to 41°C and it has been postulated that bats display constitutive expression of IFNs, a suitable reference gene has to be stable under these physiologically relevant conditions. To study cellular innate immunity in detail, cell lines from the nasal epithelium, the olfactory compartment and the cerebrum were generated. To include immune responses of epithelia cells, essential for immunity at sites of primary viral infection, primary epithelia cells from the nasal epithelium, trachea, lung and small intestine were generated. Cellular identities were determined by comprehensive analyses of transcripts and proteins expressed by each cell line. The capacity of each cell line to produce type-I- and III-IFNs was assessed at 37°C and 40°C upon stimulation with viral mimetics. This revealed cell type-dependent differences is the capability to express IFNs upon stimulation. Furthermore, the constitutive expression of

type-I- and III-IFNs was significantly elevated in higher temperatures and quantified at mRNA copy levels. To characterize ERB innate immunity upon infection with high-impact zoonotic viruses, cells from the nasal epithelium, the olfactory system, and the brain were infected with several lyssaviruses. This revealed striking differences in susceptibility: cells from the nasal epithelium rendered least whereas cells from the olfactory epithelium rendered most susceptible to viral infection and replication. Additionally, due to a lack of IFN expression in infected cells, it could be shown that LBV possibly possesses advanced strategies to ensure successful replication in ERB cells. Since the current SARS-CoV-2 pandemic put bats even further in the focus of zoonotic research, primary epithelial cells and animals were infected with this virus to monitor ERB-specific immune transcripts in cells and tissues. These studies revealed a notably early *IFNG* expression in the respiratory tract of infected individuals.

To understand immunomaturation in bats, the immune cell landscape in periphery and various tissue in adult and juvenile ERB was analyzed by flow cytometry and scRNA-seq, revealing intriguing, age-dependent variations in the abundance of granulocytes and lymphocytes. Flow cytometry revealed a significantly higher number of granulocytes in adults, as well as higher numbers of B cells in juveniles. scRNA-seq allowed detailed identification of different leukocyte subsets, uncovering the presence of highly-abundant NKT-like cells and a unique *PLAC8* expressing B cell population. A functional characterization of phagocytic cells and lymphocytes derived from adult and juvenile ERB revealed no significant differences in cellular functionality.

In conclusion, the presented work demonstrated suitability of all established ERB cell lines to study bat immunity *in vitro*, which led to striking findings regarding IFN expression at steady state, or upon stimulation or viral infection. In addition, established qRT-PCR protocols allowed definition of constitutive and temperature-dependent elevation of IFN expression magnitudes, as well as insights into expression of immune-related transcripts in SARS-CoV-2 infected ERB. Finally, based on optimized scRNA-seq technologies and flow cytometry, frequencies and absolute cell counts could be determined in ERB of different ages, revealing e.g. age-dependent variations in leukocyte profile compositions.

List of abbreviations

ABLV	Australian bat lyssavirus
ACE2	angiotensin converting enzyme 2
ACTB	actin beta
ActD	actinomycin D
AIF1	allograft inflammatory factor 1
AIM1/2	absent in melanoma 1/2
AKAP12	a-kinase anchoring protein 12
AmpB	amphotericin B
ANOVA	analysis of variance
APC	antigen-presenting cell
APOB	apolipoprotein B
BCE	before the Common Era
BCR	B cell receptor
BHLHE41	basic helix-loop-helix family member E41
BMDM	bone marrow-derived macrophage
BME	2-mercaptoethanol
BSA	bovine serum albumin
BSL	biosafety level
CALB	calbindin
CCK	cholecystokinin
CCL	CC-chemokine ligand
CD	cluster of differentiation
CDH	cadherin
CDHR	cadherin related family member
cDNA	complementary DNA
CEBPE	CCAAT enhancer binding protein epsilon
CFSE	carboxyfluorescein succinimidyl ester
CFTR	CF transmembrane conductance regulator
cGAS	cyclic GMP-AMP synthase
CHRNA	cholinergic receptor nicotinic alpha 1 subunit
CLDN	claudin
CLSPN	claspin
CNS	central nervous system
CO2	carbon dioxide
COL	collagen
ConA	concanavalin A
CRHR	corticotropin releasing hormone receptor 1
CSF	colony-stimulating factor
Ct	cycle threshold
CTL	cytotoxic T lymphocyte
CUBN	cubilin
CXCL10	C-X-C motif chemokine ligand 10
DC	dendritic cell

ddH2O	double-distilled H_2O
DDX58	DExD/H-box helicase 58
DEG	differentially expressed genes
DEPC	diethyl dicarbonate
DMSO	dimethyl sulfoxide
DNA	deoxyribonucleic acid
dNTP	deoxynucleotide triphosphates
DPF1	double PHD Fingers 1
dpi	days post infection
e.g.	*exempli gratia* (≙ for example)
EBLV	European bat lyssavirus
EBOV	Ebola virus
EDTA	ethylenediaminetetraacetic acid
EEF1A1	eukaryotic translation elongation factor 1 alpha 1
ENO2	enolase 2
EpCAM	epithelial cell adhesion molecule
ERB	Egyptian Rousette Bat
EtOH	ethanol
FACS	fluorescence-activated cell sorting
FAM149A	family with sequence similarity 149 member A
FAP	fibroblast activation protein alpha
FCS	fetal calf serum
FLI	Friedrich-Loeffler-Institut
FLT3L	FMS-like tyrosine kinase 3 ligand
FOXJ1	forkhead box J1
g (xg)	unit of measurement of acceleration force
G0S2	G0/G1 switch 2
GABRB3	gamma-aminobutyric acid type A receptor subunit beta3
GAD	glutamate decarboxylase
GAPDH	glyceraldehyde-3-phosphate dehydrogenase
GAPT	transmembrane GRB2 binding adaptor protein
GATA1	GATA binding protein
GFAP	glial fibrillary acidic protein
GI	gastrointestinal
GM-CSF	granulocyte-macrophage colony-stimulating factor
GNLY	granulysin
GRM2	glutamate metabotropic receptor 2
GZMB	granzyme B
GZMM	granzyme M
HES	hes family bHLH transcription factor
HeV	Henipa virus
HMGN3	high mobility group nucleosomal binding domain 3
hpi	hours post infection
HSP	heat shock protein
HSR	heat shock response
ID4	inhibitor of DNA binding 4
i.e.	*id est* (it is to say)

IAV	Influenza A virus
IFI6	interferon alpha inducible protein 6
IFN	interferon
IFNA	interferon alpha-like
IFNB	interferon beta
IFNE	interferon epsilon
IFNG	interferon gamma
IFNK	interferon kappa
IFNL	interferon lambda-like
IFNW	interferon omega-like
Ig	immunoglobulin
IL	interleukin
ILC	innate lymphoid cell
IRF	interferon regulatory factor
ISD	interferon stimulatory DNA
ISG	interferon-stimulated gene
ITGAM	integrin subunit alpha M
KD	knockdown
KIF15	kinesin family member 15
KIR	killer-cell immunoglobulin-like receptor
KLR (A-D)	killer cell lectin-like receptor
KO	knockout
LAMP2	lysosome-associated membrane protein 2
LBV	Lagos bat lyssavirus
LDH	lactate dehydrogenase
LDR	linear dynamic range
LEF1	lymphoid Enhancer Binding Factor 1
LF	lactoferrin
LOC	identifier for genes with no described orthologs
LPS	lipopolysaccharide
LRR	leucin-rich repeats
LRRFIP1	leucine-rich repeat flightless-interacting protein 1
LTB	lymphotoxin beta
LTC4S	leukotriene C4 synthase
MAFB	musculoaponeurotic fibrosarcoma oncogene homolog B
MARV	Marburg virus
MAVS	mitochondrial antiviral-signaling protein
M-CSF	macrophage colony-stimulating factor
MDA5	melanoma differentiation-associated protein 5
MeOH	methanol
MERS-CoV	Middle East respiratory syndrome
MFI	mean fluorescence intensity
MHC	major histocompatibility complex
mLN	mesenteric lymph node
MMC	mononuclear myeloid cell
MMP	matrix metalloproteinases
MNC	mononuclear cell

MOI	multiplicity of infection
mRNA	messenger-RNA
MTT	3-(4,5-dimethylthiazol-2-yl)-2,5-diphenyltetrazolium bromide
MUC	mucin
Mx1	interferon-induced GTP-binding protein
NCAM	neural cell adhesion molecule
NCF1	neutrophil cytosolic factor 1
NCR1	natural cytotoxicity triggering receptor 1
NEAA	non-essential amino acid
NES	nestin
NGFR	nerve growth factor receptor
NiV	Nipah virus
NK	natural killer cell
NKC	NK-gene complex
NKT	natural killer T cell
NLR	NOD-like receptor
NLRP3	NLR family pyrin domain containing 3
NOD	nucleotide-binding oligomerization domain
NRP	neuropilin 1
OAS1	2'-5'-oligoadenylate synthase 1
OCLN	occludin
OEC	olfactory ensheathing cell
OLIG1	oligodendrocyte transcription factor 1
OMP	olfactory marker protein
PAMP	pathogen-associated molecular pattern
PAX6	paired box 6
PBMC	peripheral blood mononuclear cell
PBS	phosphate-buffered saline
PCLAF	PCNA clamp associated factor
PCR	polymerase chain reaction
pdA:dT	poly(deoxyadenylic-deoxythymidylic) acid sodium salt
PEI	polyethylenimine
Pen/Strep	penicillin/streptomycin
PFA	paraformaldehyde
PGK1	phosphoglycerate kinase 1
pi	post infection
PI3	peptidase inhibitor 3
pI:C	poly I:C
PLAC8	placenta-associated 8
PMN	polymorphonuclear cell
PRF1	perforin 1
PRG3	proteoglycan 3
PRR	pattern recognition receptor
PTGS2	prostaglandin-endoperoxide synthase 2
PTPRC	protein tyrosine phosphatase receptor type C
PYHIN	pyrin and HIN200 domain–containing proteins
qRT-PCR	quantitative real-time PCR

RA	retinoic acid
RABV	rabies virus
RBC	red blood cell
RBFOX3	RNA binding fox-1 homolog 3
rhEGF	recombinant human epithelial growth factor
RIG-I	retinoic acid inducible gene I
RNA	ribonucleic acid
RSAD2	radical S-adenosyl methionine domain containing 2
RSV	respiratory syncytial virus
RT	room temperature (~20°C)
S100B	S100 calcium binding protein B
SARS-CoV-2	severe acute respiratory syndrome coronavirus type 2
scRNA-seq	single-cell RNA sequencing
SD	standard deviation
SEB	*Staphylococcus* Enterotoxin B
SIRPA	signal regulatory protein alpha
SLC1A3	solute carrier family 1 member 3
SST	somatostatin
STING	stimulator of interferon genes
SV40	simian vacuolating virus 40
SYP	synaptophysin
TBR	T-box brain transcription factor
TCEA3	transcription Elongation Factor A3
TCF	transcription factor
TCID50	median tissue culture infectious dose
TCR	T cell receptor
TLR	Toll-like receptor
TMPRSS2	transmembrane serine protease 2
TNFRSF8	tumor necrosis factor receptor superfamily member 8
TPBG	trophoblast glycoprotein
TUBB3	tubulin beta 3 class III
uIFN	universal type-I-IFN
UMAP	uniform manifold approximation and projection
VDAC	voltage-dependent anion channel
VIM	vimentin
VPREB3	pre-B lymphocyte protein 3
VSV	vesicular stomatitis virus
WGS	whole genome sequencing
ZBTB32	zinc finger and BTB domain-containing protein 32
ZNF683	zinc finger protein 683

1 Introduction

1.1 *Chiroptera* – Distinct reservoir hosts for viruses

1.1.1 The unique and diverse physiology of bat species

The order *Chiroptera* is the second largest mammalian order in the animal kingdom with 1428 species[1], subdivided into *Yinpterochiroptera*, the Old World Fruit Bats with 415 species and *Yangochiroptera* with 1013 species[2]. This extraordinary biodiversity is a result of over 58 million years of evolution[2] that subsequently led to exceptional diversity in distribution, size, morphology, specialisations to ecological niches, diets and ways of social interaction[3].

Bats can be found all over the globe except Antarctica, whereas the highest diversity in bat species can be found in equatorial regions[3]. *Rousettus spp.* are the only members from *Yinpterochiroptera* to inhabit areas further away from the equator than other fruit bats, since the distribution area of e.g. ERB, reaches as far as southern Turkey[4]. The range of diets among bats covers insectivorous (majority of *Yangochiroptera*[5]), nectarivorous (mainly New World *Glossophaginae*[6]), fructivorous (mainly *Yinpterochiroptera*[7]) and sanguivorous (*Desmodontinae*[8]) or carnivorous habits (the ghost bat, *Macroderma gigas*[9]). Bat diversity in temperate areas is curtailed and the majority of species is insectivore[3]. On account of their global distribution and dietary variations, bats are essential members of several ecosystems as pollinators, seed distributors as well as ecosystem service providers by consuming herbivorous arthropods[10].

One exceptional feature of bats is their capability of active flight. This way of locomotion requires extraordinary physiological and energetic traits, which other mammals of comparable sizes could not execute according to calculations[11,12]. In bats, the metabolic rates during flight can reach up to 34 times of the roosting stage, with body core temperatures of up to 42°C and heart rates of ~1,000 beats per minute (bpm)[11]. Astoundingly, reaching such elevated physiological stages contradicts the ubiquitous paradigm of longevity and body mass[13]. In general, longevity is linked to body mass and metabolic rates, with an approximate scaling exponent of 0.15-0.3, applicable on all mammalian species[13]. Bats defy this law, which is demonstrated by a bat's lifespan being 3-4 times longer than mammals

with comparable size and body mass, with the oldest bat listed being over 41 years old while weighing only 7 g[14]. Interestingly, this striking longevity developed not only in one specific bat species, but also in several other species, belonging to different families in the two suborders. This indicates a general evolutionary advantage for bats. However, the exact mechanisms behind the longevity of bats remains heavily debated, with only some hints available. For instance, genomic studies on the Brandt's bat (*Myotis brandtii*) revealed a mutation in the growth hormone receptor[15], which correlates with the protection from diabetes and cancers in humans[16]. Other explanations are linked to the positive selection of DNA damage signaling pathway, evidenced by *in vitro* studies with cells from the black flying fox (*Pteropus alecto*)[17] and longitudinal studies of blood samples of the greater mouse-eared bat (*Myotis myotis*)[18]. In support of this assumption, repair of double-strand breaks in the DNA is associated with longevity and low levels of cancer[19].

The impact of temperature oscillations accompanied by flight may significantly shape chiropteran immunity. Bats developed a higher thermotolerance than other animals and it has been shown that this tolerance is sustained by a constitutively activated and more potent heat shock response (HSR)[20]. This feature is unique to bats, since birds, which share the ability to fly and the excessive heat production by wing musculature, do not exhibit such HSR magnitude[20]. This is of particular interest for chiropteran and comparative immunity, as ongoing infections activate HSR pathways, e.g. by fever. Furthermore, although constitutive HSR activity has been verified for bats, they cease to develop degenerative diseases, excessive inflammation or even cytokine storms. This observation is supported by a strong suppression of the activity of inflammasome components, e.g. NLR family pyrin domain containing 3 (NLRP3) in bat immune cells upon toll-like receptor (TLR) activation by either sterile stimuli or viruses like coronaviruses[21]. The impairment in inflammasome function was shown to not affect bat's ability to clear infections, however, it was associated with the striking absence of cytokine storms and degenerative diseases in bats[20]. Additionally, it was recently discovered that higher body core temperatures during flight lead to IFN production in bat cells[22]. Conclusively, bats exhibit considerable immune and metabolic adaptations, possibly linked to flight. In addition, bats occupy a distinct role for transmitting disease agents, since flying allows them to travel notable distances during foraging, up to ~400 km per night (e.g. straw-coloured fruit bat, *Eidolon helvum*[23]).

1.1.2 As bats and time fly by – striking richness of viruses with zoonotic potential

Ages of evolution led to extraordinary diversity of, and impeccable adaptation to many ecological niches by bats. Early human civilizations independently linked bats to disease and death[24,25]. This is demonstrated by the first bat-related rabies case, reported in Babylonia around 2,000 BCE and the Mayan god of sickness and death, displayed as an anthropomorphized leaf-nosed bat, ~100 BCE. This association is probably based on the transmission of disease agents by bats to humans and domestic animals. These primal reports already testify what, 4,021 years later, emerged to be a refined relationship between reservoir hosts and highly pathogenic viruses. Ultimately, bats harbour more zoonotic pathogens than any other mammalian family, even rodents[26-28]. Different habitats, feeding habits, and the need to hibernate in some species lead to disparate reservoir potentials[29,30]. Even social interaction, especially communication, plays a role for viral maintenance within the colony, demonstrated by isolation of diseased animals by healthy individuals (e.g. observed in common vampire bat [*D. rotundus*[31]] and ERB[32] colonies).

Recent phylogenetic analyses revealed that bats harbour significantly more RNA than DNA viruses[28,33]. The majority of viruses discovered in bats belongs to the realm *Riboviria*, predominantly viruses of the order *Mononegavirales* (i.e. distinguished by a linear [-] single-strand RNA [[-]ssRNA] genome[34]) with roughly 3,346 sequences isolated from bats according to DBatVir, the database of bat-associated viruses[35]. Most bat-associated members of the *Mononegavirales*, which are successfully transmitted to other mammals, cause fatal disease in the latter[36]. However, both isolates and reports of infections in other mammals are largely missing, since the majority of viruses could only be found in bats. For instance, viruses of the genus *Lyssavirus* (family *Rhabdoviridae*), accounting for the majority of bat-associated *Mononegavirales* with 1,590 isolated sequences[35], cause mostly lethal rabies. Phylogenetic analyses revealed that nearly all lyssaviruses are of bat origin[37-40] and could be successfully isolated from bats[40-42]. There are only two exceptions to date, namely Mokola virus (MOKV, isolated from shrews[43,44]) and Ikoma lyssavirus (IKOV, isolated from African civets[45]). Spillover events of bat-borne lyssaviruses to carnivorous hosts or humans are well documented[46]. In addition, bat-borne viruses already spilled over to several carnivore hosts and humans around the globe: European Bat Lyssavirus 1 (EBLV-1) originating from *E. serotinus*[47-51], EBLV-2 from Daubenton's bat (*Myotis daubentonii*)[52,53], Australian Bat

Lyssavirus (ABLV) mainly transmitted by *Pteropus spp.*[54-57], possibly MOKV[44,58-61], and Duvenhage lyssavirus (DUVV)[62,63] of unknown bat origin as well as Lagos Bat virus (LBV) originating from Wahlberg's epauletted fruit bat (*Epomophorus wahlbergi*)[59,64,65]. These reports documented fatal disease outcomes in pets, wild carnivores and subsequently infected humans caused by various lyssaviruses. However, bats as the primary reservoir mostly show shallow or delayed severity of symptoms upon infection[46,66], with only ~3% of active infection in a colony. Few individuals among these 3% develop symptoms and succumb to encephalitis[40]. However, experimental infection of *E. serotinus* bats resulted in significant morbidity and mortality, and infections in free-ranging bats might remain partially undetected[67].

Furthermore, Ebola (EBOV) and Marburg (MARV) viruses, both members of the family *Filoviridae,* remain threats by causing epidemics. Although less abundant than lyssaviruses, epidemics caused by filoviruses are associated with devastating mortality rates in infected humans, as shown in West Africa from 2014 to 2016, resulting in over 10,000 deaths and a fatality rate of 71%[68]. While the natural reservoir for Ebola viruses has yet to be identified (putatively African bats like the Angolan free-tailed bat, *Mops condylurus*[69,70], *E. wahlbergi*[71], as well as several fruit bats like *E. helvum* and ERB[71,72]), it has been shown unequivocally that ERB is the natural reservoir for Marburg viruses (MARV and ravn virus, RAVV)[73,74]. Contrasting the high case fatality rates of EBOV/MARV infection in humans, bats do not develop signs of disease upon infection[75].

Furthermore, transmission of Nipah- and Hendraviruses (NiV, HeV), classified in the order *Paramyxoviridae*, from bats (presumably *Pteropus spp.* and *Eidolon spp.*[76-81]) can have severe impacts on local economies as these viruses primarily infect livestock. Mortality rates in both humans and livestock, i.e. horses and swine, range between 40% and 100%[82]. NiV outbreaks in Malaysia (1998) and Bangladesh (2001), along with the HeV outbreak in Australia (1994), resulted in severe economic losses for local communities[83]. The newly isolated paramyxoviruses HeV and Cedar virus (CeV) also originated from bats, specifically *Pteropus spp.*[84]. As already observed for lyssaviruses and filoviruses, NiV and HeV infection in pteropodid bats leads to high viral loads in infected individuals, which only occasionally results in lethal disease progression[85-89]. Strikingly, the entirety of all paramyxoviruses could be identified in bats, suggesting that members of the family *Paramyxoviridae* are

ubiquitous among bats around the globe[90-97]. Furthermore, recent phylogenetic analyses revealed that presumably bats were hosts to the ancestors of all well-defined paramyxovirus species, including measles virus, mumps virus (MeV), parainfluenza virus (PIV), canine distemper virus (CDV), Newcastle disease virus (NDV) and respiratory syncytial virus (RSV)[89]. Finally, newly described members of the order *Bunyavirales* rendered to be of bat origin. For example, the highly pathogenic Rift Valley fever virus (RVFV), isolated from Peters' dwarf epauletted fruit bat (*Micropteropus pusillus*) and the Sundevall's roudleaf bat (*Hipposideros caffer*) in Guinea[98] and the Malsoor virus, recently isolated from Leschenault's rousette bats (*Rousettus leschenaultii*) in India[99]. Infection with bunyaviruses can lead to lethal encephalitis, hemorrhagic fever or multi-organ dysfunction in humans and domestic animals, and should therefore be considered a serious zoonotic threat to global health[100].

Another re-emerging spillover threat of viruses from the realm *Riboviria* is caused by the members of the order *Nidovirales* with about 1,477 sequences derived from bats[35], majorly members of the *Coronaviridae* family. Members of the *Nidovirales* are distinguished by a (+)ssRNA genome, which functionally acts as mRNA[101]. As the result of causing mild or even no apparent clinical symptoms in the majority of infected individuals while being highly infective, Coronaviruses can spread widely before being detected. This caused three historical epi- and pandemics by bat-borne coronaviruses, disrupting global health and economy: SARS-CoV (severe acute respiratory syndrome coronavirus) with the Chinese rufous horseshoe bat (*Rhinolophus sinicus*) as suggested reservoir resulted in 774 deaths worldwide and a case fatality rate of 9.6% by the end of 2004[102]. MERS-CoV (Middle East respiratory syndrome coronavirus), which presumably originated from *Tylonycteris* and *Pipistrellus* bats[103], resulted in 881 deaths and a fatality rate of 34% by the end of 2020[104]. Most recently, the bat-borne coronavirus SARS-CoV-2, presumably originating from *Rhinolophus* bats, causes the current pandemic, paralyzing everyday life around the globe[105]. The most diverse family of bat-borne viruses is in fact the family of *Coronaviridae*, diminishing exact identification of SARS-CoV-2 origin, due to the sheer number of isolated sequences. This is supported by the fact that Rhinolophus CoV sequences only share 96% homology to SARS-CoV-2[106]. Furthermore, SARS-CoV-2 may use a variety of host species as intermediate hosts, hampering the definition of the exact origin[107]. This pandemic already caused ~5.65 million human deaths worldwide as of January 2022[108]. Of note, several

commonalities link coronavirus pandemics to where three facts intertwine and form an everyday threat of viral spillover from bats to humans: First, bats are the order in the animal kingdom richest in coronaviruses[109] and secondly, newly emerged coronaviruses can circulate undetected for some time compared to other zoonotic events, since distinction of CoV-specific clinical signs is challenging due to crossover symptoms to other respiratory infections[110,111] Thirdly, destruction of natural habitats of bats alongside constantly progressing urbanization lead to closer proximity of humans to a vast pool of genetically different coronaviruses[112]. Furthermore, a coronavirus causing diarrhoea in piglets with a case fatality rate of 90%, SADS-CoV (Swine acute diarrhoea syndrome coronavirus), was recently confirmed to have originated from bats[113]. This virus led to the death of 24,000 piglets and considerable economic losses as a result from a spillover event in China in 2017[114]. It is of note that coronaviruses are the only bat-borne viruses with known interspecies transmission between bats of different suborders, as demonstrated for BatCoV HKU10, an alphacoronavirus[115].

Although spillover events of Influenza A viruses (IAV), classified within the family of *Orthomyxoviridae*, mostly originate from aquatic birds, bat-specific IAV variants have been described recently[116]. The hemagglutinin of bat IAV H17N10 and H18N11 do not bind known IAV receptors[117], such as sialic acids or other glycans, but rather human leukocyte antigen DR isotype (HLA-DR), as demonstrated by knockout (KO) experiments[117]. This further demonstrates the diversity and distinctness of bat viruses and highlights the necessity to determine the zoonotic potentials of newly described bat-borne viruses.

While RNA viruses form a substantial majority of viruses found in bats, several bat-associated DNA viruses have also been identified to date, including dsDNA and ssDNA viruses. Especially Eurasian bats were subject of successful isolation of several members of the *Duplodnaviria* realm, including the *Adenoviridae* family (double-stranded DNA [dsDNA] genome)[97,118-124]. Herpesviruses, cumulated in the family *Herpesviridae* (dsDNA genome), including alpha-, beta-, and gammaherpesviruses, were successfully isolated from bat species distributed all over the globe[124-129]. One particularly unique bat-associated herpesvirus is a betaherpesvirus isolated from the common bent-winged bat (*Miniopterus schreibersii*), identified to have major-histocompatibility complex II (MHCII) homologs encoded in the genome[126]. Bat-associated viruses of the *Varidnaviria* realm, characterized by

a ssDNA genome, majorly belong to the families *Anelloviridae*, *Circoviridae* and *Parvoviridae* which also do not result in excessive disease development in bats[120,130,131].

1.2 Molecular innate immunity in bats

One foundation of mammalian success is the development of an effective and refined defense system against pathogens. All living organisms possess defense mechanisms against pathogens. In innate immunity, the entirety of immune reactions, e.g. associated to the recognition of pathogen-associated molecular patterns (PAMPs), recognition is elicited by pattern recognition receptors (PRRs), leading to cellular activation and anti-microbial warfare[132]. Recognition of PAMPs, e.g. viruses[133], bacteria[134], fungi[135] and parasites[134], as well as danger-associated molecular patterns (DAMPs[136]), e.g. extracellular ATP or DNA[137], is mediated by highly conserved PRRs[134]. PRR families include: TLRs, the nucleotide-binding oligomerization domain (NOD)-leucine-rich repeats (LRR)-containing receptors (NLRs), C-type lectin receptors, and retinoic acid-inducible gene 1 (RIG-I)-like receptors and cytosolic DNA sensors, e.g. cyclic GMP-AMP synthase (cGAS[138]), the IFN-inducible protein termed absent in melanoma 2 (AIM2), DEAD-Box Helicase 41 (DDX41[139]), Leucine-rich repeat flightless-interacting protein 1 (LRRFIP1[140]), and Gamma-interferon-inducible protein (Ifi-16[141]). Sensing majorly results in downstream upregulation of a pathogen-specific set of antimicrobial and pro-inflammatory cytokines, mostly IFNs, and other antimicrobial peptides and kinases (AMPs/AMPKs[142]) after upstream activation of interferon regulatory factor 3 and 7 (IRFs)[143,144].

Each individual cell, irrespective of origin and function, is able to mount an antimicrobial state, e.g. by producing IFNs. These IFNs are diverse in structure and function and therefore divided into three groups: type-I-IFNs (*IFNA*, *IFNB*, *IFND*, *IFNE*, *IFNK*, *IFNW*), type-II-IFN (*IFNG*) and type-III-IFNs (*IFNL*s). Type-I- and III-IFN responses hamper viral replication in the infected cell and restrict infection of neighbouring cells[145]. In addition, type-III-IFNs, structurally closer to IL-10 than IFNs[146,147], are known to have tissue-protective properties, by executing antiviral activity with less collateral damage[148]. *IFNG* is predominantly expressed by activated NK cells[149] and natural killer T (NKT) cells[150], as well as activated T helper cells (cluster of differentiation 4 positive [$CD4^+$] Th cells) and $CD8^+$ cytotoxic T cells[151,152], γδ T cells[153], and to a lesser extent mucosal-associated invariant T (MAIT) cells,

innate lymphoid cells (ILCs), and B cells[150]. Secretion of IFNγ promotes inflammation by e.g. enhancement of antimicrobial activities of leukocytes and antigen presentation[151]. Binding of a ligand to specific PRRs triggers the downstream activation of several transcription factors, e.g. IFN regulatory factors (IRFs), nuclear factor kappa-light-chain-enhancer of activated B cells (NF-κB), c-JUN and activating transcription factor 2 (c-JUN/ATF2), and CREB-binding protein and p300 (CBP/p300)[154]. Although IFNs encode a large and diverse family with differing structures, receptor specificities and properties, type-I- and III-IFNs induce similar target genes[155]. Both type-I-, II- and III-IFNs bind to heterodimeric cell surface transmembrane receptors, consisting of IFAR1/IFNAR2[156], IFNGR1/IFNGR2[157], and IFNLR/IL-10R2[146], respectively. Downstream signalling via Janus tyrosine kinase-signal transducer and activator of transcription (JAK-STAT) pathways initiate the expression of IFN-stimulated genes (ISGs)[155]. Aberrant IFN secretion and signalling is associated to both numerous autoimmune diseases, e.g. systemic lupus erythematosus, systemic sclerosis, and rheumatoid arthritis[158], as well as severe immunopathology[159], e.g. in severe SARS-CoV-2 infections[160-162]. The majority of studies on cellular innate immunity on bats were conducted with the following species: *P. alecto*[163-165], *A. jamaicensis*[166], ERB[167,168], *P. vampyrus*[169], *R. sinicus*[170,171], *E. fuscus*[172], and *E. serotinus*[173].

Early comparative studies on functional commonalities and distinctions of bat IFN induction and signalling have been conducted prior to the availability of in-depth genomic or transcriptomic sequencing, mostly relied on cloning and stimulation experiments, like those conducted with *P. alecto* IFNγ[174]. The existence and functionality of bat IFN pathways were first proven in 1969 by demonstrating antiviral activity of the supernatant of stimulated (pI:C, LPS)[175] and later infected (Japanese encephalitis virus) embryo tissue cultures from the Mexican free-tailed bat *Tadarida brasiliensis*[176]. Furthermore, cloning of *E. serotinus IFNE* and *IFNK*[173], *P. alecto IFNG*[174] and *IFNL*[165,177], as well as ERB *IFNW*[167,168] confirmed antiviral activity and capability of inducing ISGs. Yet, whole genome sequences and transcriptomic data of different bat species enabled *in silico* analyses of the molecular fingerprints of chiropteran innate immunity. Pioneer studies sought to determine homologies of immune-related genes and transcripts originating from bats to those of other mammals[166,178,179]. Around 3.5% of all transcripts in tissue samples of three *P. alecto* bats

were immune-related[179]. In seemingly closely related species, such as the Jamaican fruit bat (*Artibeus jamaicensis*) and ERB, 2.32%[166] and 2.75%[178] of all identified transcripts derived from pooled RNA of various tissue were immune-related, respectively. Interestingly, bats not only seem to have less immune-related genes than other mammals e.g. humans with up to 7% of genes being linked to immunity[180], but also show unique transcripts, as defined in the *P. alecto* transcriptome. These transcripts could not be annotated successfully, indicating the existence of bat-specific transcripts, putatively essential for their immune systems.[179].

Taking cloning and sequencing results together, commonalities in PRR subtypes, ligand specificities, and activation kinetics, JAK/STAT signalling, IFN presence, receptor interaction, and antiviral activity, as well as ISG expression were defined in different bats. This includes both *Yinptero-* and *Yangochiroptera*: e.g. *A. jamaicensis*[166], the big brown bat (*Eptesicus fuscus)*[181], the serotine bat (*Eptesicus serotinus)*[173,181], David's myotis (*Myotis davidii)*[182], the little brown bat (*Myotis lucifugus)*[183], P. *alecto*[165,177,179,182,184-186], the Malayan flying fox (*Pteropus vampyrus)*[187], ERB[167,168,188], *R. leschenaultii*[184], *and R. sinicus*[170]. Most strikingly, such studies also revealed a plethora of bat-specific distinctions in innate immunity. These distinctions were defined in different bat species and include: more isoforms of TLR7 and RIG-I, dampened NLRP3 and caspase-1 activity, contractions or expansions in IFN loci, IFN expression magnitude and kinetics, broad distribution and constitutive expression of IRF7 and IFNs, as well as a lack of PYHIN and classical NK cell receptor sequences in the genome (the Greenish naked-backed fruit bat *Dobsonia viridis*[189], *M. davidii*[190,191], *M. lucifugus*[183,187], *P. alecto*[21,190], *P. vampyrus*[177,187], ERB[168]).

1.2.1 Structure and function of PRRs in bats

Pioneer studies revealed significant genomic[168,170,182] and transcriptomic[169,179,192] differences regarding sensing of danger signals between bats and other mammals, e.g. contractions or expansions in various IFN loci[168,191,193]. However, since the bat virome mainly consists of RNA viruses[33], progressive endeavours in studying bat-specific innate immune responses, especially to RNA viruses, have been made. Considering that recognition of PAMPs by PRRs is prerequisite to mounting a well-tailored IFN response, identifying similarities and variations between PRRs of bats and other mammals was and still is essential. *In silico* analyses allowed detection of *RIG-I*, melanoma differentiation-associated protein 5 (*MDA5*)[179,194] and TLR transcripts[195] and relation to similar expression patterns in humans and mice. Whole transcripts of bat *TLR1-TLR10* could be identified, as well as a *TLR13* pseudogene, yet their exact function and contribution to bat immunity remains unknown[185]. Bioinformatical calculations on *TLR8* structures originating from 21 bat species revealed striking differences between bat and other mammalian *TLR8* sequences[195]. However, *TLR8* also already varies between different bat species[195]. The ligand for TLR8, an endosomal TLR, is GU-rich ssRNA[196], originating from viruses such as Influenza and Sendai virus (SeV). However, the function of TLR8 differs between mammalian species: murine TLR8 seemingly counteracts TLR7 functions[197], and recognition of GU-rich sequences is not sufficient for TLR8 activation in humans[198]. It could be shown that the majority of bat *TLR8* variants differ to up to 7% compared to other mammals in regard of the ligand-binding domain[195]. This possibly indicates unique properties of bat TLR8 in regard of PAMP recognition. General functionality of PRRs and corresponding pathways in bats (e.g. *P. alecto* and *E. fuscus*) could be demonstrated by IFN induction upon stimulation with polyinosinic:polycytidylic acid (pI:C), a widely used dsRNA mimic[186,194].

Validation of functionality of cytosolic RNA sensors in various bat cells has already yielded an overview of analogies and distinctions in PRR structure, while analysis on IFN signalling in different bats and bat cells leads to even more striking findings. IRF sequences, especially *IRF3*, in numerous bat species vary from their orthologs in other mammals like cattle and humans[199]. Yet, *IRF3* still mediates antiviral signalling, as observed pI:C treated or MERS-CoV-infected *E. fuscus* cells[172]. The relevance of *IRF3* in IFN signalling in *E. fuscus* and *P. alecto* has been demonstrated by deficient *IFNB* expression in *IRF3* knock-down (KD) cells[172].

It has been shown that MERS-CoV suppresses *IFNB* expression in human, but not bat cells, implying that bat cells can counteract viral immune evasion strategies[172]. Furthermore, conservation of this effect among distantly related bat species implies a general feature of chiropteran immune systems. In addition, importance and functionality of *IRF7* in bats was demonstrated by KD of *IRF7* in *P. alecto* cells, which failed to express *IFNB* upon SeV infection and reached higher viral titers compared to wild type cells[200]. Furthermore, functionality of mitochondrial-antiviral signalling protein (MAVS) seems to be conserved between bats and other mammals, as orthologs identified in *R. sinicus* and *E. helvum* are similar to those in mice and men. Moreover, introduction of bat MAVS in human MAVS KO cells resulted in *IFNB* and ISG expression upon SeV infection, indicating similar functional properties[201].

1.2.2 Functionality of IFN and inflammasome pathways in bats

The type-I-IFN locus experienced both contractions (*IFNA* in *P. alecto*[193]) and expansions (*IFNW* in ERB[168]) in bats. This indicates specialized roles of certain IFNs in different bats, probably linked to the virome specific for each species. In *P. alecto*, only ten type-I-IFNs could be found in the locus, which is significantly reduced compared to other mammals like swine with 57 genes encoding for functional type-I-IFNs[202]. However, this locus has three functional *IFNA* loci, which are constitutively expressed in cells and tissues at steady state[193]. Notably, findings of constitutive *IFNA* expression in ERB are disputed, as confirming and disapproving evidence exists[168,203]. In ERB, the *IFNW* locus is remarkably expanded[168]. In addition, several studies on type-I-IFNs in bats confirmed their functionality, as demonstrated by inhibition of vesicular stomatitis virus (VSV) growth in ERB cells and inhibition of lyssavirus growth in *E. serotinus* cells. These effects on inhibiting viral replication could be directly linked to *IFNW*[167,204] and *IFNK/IFNW*[173], respectively.

Since type-III-IFNs also play a crucial, yet distinct role in innate immunity, studies on bat IFNs aimed to analyse *IFNL*s as well. Induction of *IFNL* expression leads to the expression of ISGs and therefore the mounting of an antiviral state[205]. Furthermore, *IFNL* expression is essential for polarization processes in antigen-presenting cells (APCs), e.g. macrophages and DCs[206,207], which promotes activation and proliferation of helper T cells[208,209]. *IFNL* functionality could be validated in bats, e.g. by expression in *P. alecto* splenocytes upon

infection with bat paramyxovirus (Tioman virus)[177]. Conclusively, bats have evolved to constitutively express certain IFNs and still mount a robust IFN response upon infection with various RNA viruses. However, an excessive pro-inflammatory response is inhibited, protecting cells and tissue from virus-induced immunopathology[210]. This contrasts the kinetics of antiviral responses in other species, e.g. humans, in which dysregulated IFN responses are associated with severe disease progression[211,212].

In human and other mammalian cells, IFN signalling is dependent on the interaction of IFNAR1 and IFNAR2, forming the type-I-IFN receptor, subsequently leading to the expression of several ISGs[213]. IFNAR2 KD in *P. alecto* cells resulted in increased H1N1 replication, suggesting the involvement of IFNAR2 in antiviral signalling in bats[164]. Since a multispecies comparison based on RNA sequencing revealed that each mammalian species possesses a unique fingerprint of ISGs[214], it can be assumed that the ISG repertoire varies significantly between bat species. Inducibility of downstream ISGs was validated by pI:C treatment which ultimately resulted in expression of *RIG-I*, *MDA5*, radical S-adenosyl methionine domain containing 2 (*RSAD2*), 2'-5'-oligoadenylate synthase 1 (*OAS1*), myxovirus resistance 1 (*Mx1*), IRF7 and IFN-inducible protein 6 (*IFI6*) in kidney cells from *E. fuscus*[194] as well as *Mx1* and *OAS1* in *P. alecto* cells[215]. Furthermore, bat ISGs were proven to mount effective antiviral stages and reduce viral growth This was demonstrated by impaired replication of Influenza A virus (IAV)[216] or NDV[169] in 293T cells expressing cloned bat ISGs, e.g. Mx1 from *Yinptero-* and *Yangochiroptera*.

Although sensing of DNA viruses in bats is less studied than immune responses to RNA viruses, an overall dampening of DNA sensing pathways in bats has been uncovered[21,191,217]. Interestingly, evidence indicated an impairment in activation and signalling of an important sensor of cytosolic DNA: the stimulator of interferon genes (STING) protein, ultimately affecting the whole cGAS/STING pathway[217]. This impairment is caused by the bat-specific loss of a serine residue at position 358, which results in the inability to activate downstream signalling[218]. Taken together, STING deficiency could alter detection of DNA viruses in bats, e.g. of herpes simplex virus (HSV)[218].

In addition to the absence of PYHIN protein family members (e.g. AIM2-like receptors essential for inflammasome activation)[191], another sensor of danger signals, NLRP3, is

impaired in both transcription and subsequent signalling in bats (*M. davidii*, *P. alecto*[190]), which restricts the inflammasome assembly[21]. Lower NLRP3 induction, compared to murine and human orthologs, results in both diminished induction of ASC speck formation (apoptosis-associated speck-like protein containing a caspase activation and recruitment domain [CARD]) and impaired secretion of IL-1β[190,219]. This observation was made after stimulation with viral mimetics, as well as upon infection with IAV, MERS-CoV, or Melaka virus (MELV)[190]. Dampened secretion of IL-1β in bats was shown to be the result of inhibitory residues within the bat caspase-1, as well as unique residues lateral to cleavage sites[219]. Both observations support generalization of chiropteran immunity, since the inflammasome pathway was dampened in members of both the *Yinptero-* and *Yangochiroptera* (*P. alecto* and *M. myotis*)[219].

Conclusively, several commonalities and distinctions regarding innate immunity of bats compared to other mammalian species have been successfully defined. While bats seemingly refined sensing of RNA-based PAMPs, DNA sensing and subsequent inflammasome assembly evolved to be heavily impaired. IFN pathways were shown to be fully functional in bats and similar to human IFN-signalling. However, data suggests that IFN signalling, especially IFNα, is constitutively present in various cell types and tissues of different bat species. Recent hypotheses seek to explain these findings with bat-specific adaptations to self-powered flight. Bats putatively evolved to coexist with a plethora of viruses by constantly producing IFNs[182,220], yet heat shock-associated DNA damage and constitutive HSR activity would lead to unwanted permanent inflammasome activation.

1.3 Cellular immunity in bats

Phenotypic and functional characterization of bat leukocytes remain challenging mainly due to the lack of species-specific reagents and limited accessibility to fresh samples, since most and especially *Yangochiroptera* bat species are protected by law[221]. Furthermore, the vast variety of bat species convolutes the ability of research to define universal bat-specific traits in antiviral immunity. Nevertheless, regular identification of cross-reactive antibodies and tools enables immunophenotyping, and establishment of captive breeding colonies significantly facilitates access to specimens. Studies on phenotype and function of bat leukocytes are mostly based on data derived from *Yinpterochiroptera*: ERB[222,223], *P. alecto*[224-226], *E. spelaea*[227,228] and the Malayan flying fox (former *Pteropus giganteus*, now *P. vampyrus*[229-232]), the greater horseshoe bat (*Rhinolophus ferrumequinum*[233]), the lesser horseshoe bat (*Rhinolophus hipposideros*[233]). This is due to eased accessibility to specimens and the possibility to conduct comprehensive studies due to their size. However, leukocyte profiles in members of the *Yangochiroptera*, although mostly being too small to study leukocyte frequencies and function in detail with the tools at hand, were analysed in, e.g. in *D. rotundus*[234], *M. myotis*[233], the long-fingered bat (*Myotis capaccinii*[233]), the northern bat (*Eptesicus nilssonii*[235]). This chapter will introduce the current knowledge about phenotype and function of chiropteran leukocytes, derived from both *Yango-* and *Yinpterochiroptera*, with focus on the latter.

1.3.1 Phenotype and function of innate immune cells in bats

Cells of the innate immune system, namely granulocytes, DCs, monocytes, and macrophages, are often defined as the first responders to pathogen invasion and crucial for initiating a pathogen-specific immune response. Granulocytes readily engulf microbes and possess antimicrobial mediators exhibiting biocidal function[236]. Monocytes exhibit phagocytosis, cytotoxicity, and secretion of biocides[237]. Macrophages act upon recognition of PAMPs, e.g. LPS, with enhanced function after priming with lymphocyte-specific IFNγ[238]. All phagocytes share the ability to process and present microbial antigens to naïve T cells and lead to clonal expansion and activation in presence of cytokines[239].

Early studies on bat immune cells date back to the late 1980's, where first morphological descriptions of immune cells and ratios from *P. giganteus* were carried out[230,231]. These studies revealed, along with later studies of other species (e.g. *T. brasiliensis*[240]) that bat leukocytes are seemingly smaller (infiltrating macrophages 4-5 µm, T cells 6-7 µm, and B cells 7-9 µm) compared to counterparts in other mammals. Furthermore, the ratio of immune cells was comparable to mice with 1:2:9 for macrophages/B cells/T cells. Notably, the leukocyte profile within a bat species is highly dependent on geographical distribution and inhabited ecological niches, as demonstrated for *D. rotundus*[234]. In general, bats putatively share population frequencies and ratios with mice, rather than humans[230,231].

In-depth studies on phenotype and function of immune cells in bats remain scarce, but recent advancements defined bat-specific properties, especially in antigen presentation. Using *P. alecto* kidney cells (PaKi), presentation of self and HeV peptides in the context of MHCI molecules was characterized. This revealed that bat MHCI molecules can present overall larger molecules compared to humans and rodents, due to three additional amino acids (methionine, aspartic acid and leucine) forming a supplementary salt bridge for high affinity peptides[241-243]. Bone marrow-derived macrophages (BMDM) and DCs from *P. alecto* and the common dawn bat (*Eonycteris spelaea*) were shown to respond similarly to human and murine counterparts to PAMP stimulations (pI:C, lipopolysaccharide [LPS]), i.e. by expressing *TNFA*, *IL-8*, and nitric oxide synthase 2 (*NOS2*)[190,226,228]. Establishment of the bat-specific stimulating factors granulocyte-macrophage colony-stimulating factor (GM-CSF, CSF2), macrophage colony-stimulating factor (M-CSF, CSF1), tyrosine kinase 3 ligand (FLT3L), and interleukin 4 (IL-4) enabled *in vitro* differentiation, phenotyping and verification of phagocytic activity of macrophages as well as putative monocytes and DCs[190,226,228]. Based on these observations, bat bone marrow-derived myeloid cells are possibly similar to human and rodent orthologs regarding morphology and function. Additionally, bone marrow-derived DCs (BMDCs) from ERB were successfully generated utilizing recombinant GM-CSF and IL-4. Fully differentiated BMDCs, characterized by CD11b and CD14 expression, cleared MARV infection *in vitro* by upregulation IFN-related genes while downregulating pro-inflammatory mediators, such as *ISG15*, *OAS3*, and Interferon Induced proteins with Tetratricopeptide repeats 1 and 2 (*IFIT1, IFIT2*)[223]. Furthermore, an

upregulation of PRR expression, NF-κB signalling and maturation mediators have been observed in ERB BMDCs upon stimulation with LPS or infection with SeV[223].

More recent studies defined immune-related genes in ERB that significantly differ from the orthologs in other mammals. Namely diversified and expanded NKG2-C type II integral membrane protein C/D (KLRC/KLRD) gene families of NK cell receptors, type-I-IFN genes and MHCI genes[168]. Receptors of NK cells, namely killer cell lectin like receptors (KLRs) and killer immunoglobulin like receptors (KIRs), recognizing MHCI are encoded by two gene families: the leukocyte receptor complex (LRC) and the natural killer complex (NKC). NK cells detect absence of MHCI on the cell surface, which is often induced by viruses, and eliminate cells by apoptosis or lysis[244]. The KLRC/KLRD heterodimer (CD94/NKG2 [KLRC1]) serves as an additional receptor on NK cells to detect self-MHCI and initiate cytotoxicity upon absence[245]. The striking difference between NK cell receptor repertoires in bats and other mammals could possibly indicate a distinct role of NK cells in bats. It is of particular interest that among ten putatively functional *NKG2A/B* genes, six encode both activating and inhibitory motifs. Among the remaining four genes, three encode for inhibitory motifs, one for activating motifs[168]. Furthermore, *CD94* and *NKG2* genes were found to be equally expressed in tissues from bats as in tissues from humans[168]. However, the expression of inhibitory genes like *NKG2-13* and *NKG2-14* is also elevated in bats as shown for ERB[168], implying rather inhibitory functions of NK cells in this bat species. Additionally, one particular lymphocyte subset shares properties with both NK cells and T cells: NKT cells. They can exhibit NK cell-associated properties, e.g. FcγRIII (CD16), neuronal cell adhesion molecule (NCAM) and granzyme B production[246,247]. Other than classical T cells, NKT cells primarily recognise the non-polymorphic CD1d molecule, presenting lipids and glycolipids of host or microbial origin[246,248]. Given the difficulties in annotating and defining bat NK cell receptors as well as CD16 (sequence remains as unannotated LOC), this cell subset is of particular interest for chiropteran immunity, but remains to be identified.

1.3.2 Adaptive immunity in bats: inflammation and regulation

Adaptive immunity, inherent to vertebrates, is directly dependent on and downstream of a functional innate immunity. Its major advantage is an antigen-specific army of T cells[249] and the ability to establish immunological memory[250], enabling more rapid secondary

responses[250]. T cells can roughly be divided into $CD4^+$ T_H cells, orchestrating inflammation and humoral immunity[251], and $CD8^+$ cytotoxic T lymphocyte (CTLs), executing a targeted attack on virus-infected cells by inducing apoptosis or lysis[252]. Comprehensive studies on major T and B cell populations[224,225], as well as MR1-restricted T cells with MAIT-characteristics[253] and differentially activated T cell subsets in lymphatic tissues could successfully be conducted for *P. alecto*[224]. It could be shown that bat lymphocyte frequencies are comparable to observations in humans.

B cells restrict reinfection by producing circulating antigen-specific antibodies, which bind to and directly neutralize the pathogen or may initiate inflammation[254]. Robust evidence of B cells executing APC function by activating naïve T cells through peptide presentation emerged, especially in the last decade[255]. Identification of a set of cross-reactive antibodies enabled phenotyping of lymphocytes in several bats. Abundances of lymphocytes derived from wild-caught *P. alecto* and temporarily housed *E. spelaea* bats overall match the ones described for humans, although these bat species had more T cells in the periphery than B cells[224,225]. *P. alecto* bats showed a prevalence of $CD4^+$ T cells in periphery, various lymph nodes and bone marrow (~70% $CD4^+$, ~30% $CD8^+$), whereas $CD8^+$ T cells were dominant in the spleen (~15% $CD4^+$, ~45% $CD8^+$)[224]. This suggests the presence of T cells of various activation stati in bat tissue (lymph node, bone marrow, spleen, and periphery), which was supported by the differential representation of various T cell-associated transcription factors, such as T-box transcription factor (T-bet), GATA-binding protein 3 (GATA3), and eomesodermin (EOMES)[224]. It was further defined that T cells proliferate and increasingly express *IL10*, tumor necrosis factor α (*TNFA*), granzyme B (*GRZB*), perforin (*PERF*) and *IFNG* upon mitogenic stimulation with phorbol 12, 13-dibutyrate (PDBu) and ionomycin[224]. Furthermore, MR1-restricted T cells were recently defined in circulation and tissues of *P. alecto* bats, employing human MR1 tetramers, loaded with the corresponding ligands 5-(2-oxopropylideneamino)-6-D-ribitylaminouracil(5-OP-RU) or 6-formyl pterin (6-FP)[253]. These cells share functional similarity to human counterparts, as demonstrated by PLZF, RORγt (Th17 master transcription factor), T-bet, and EOMES expression[253]. Characterization of B cells was successfully carried out employing cross-reactive antibodies targeting a receptor of the complement system (CD21), a cysteinprotease (CD27) as well as one bat-specific antibody recognizing surface-bound immunoglobulin (Ig)[225]. *P. alecto* B cells share

functionality with rodent and human B cells, since they proliferate upon mitogenic stimulation with LPS, hinting towards conserved TLR4 function. Additionally, the percentage of B cells in *P. alecto* spleen and peripheral blood mononuclear cells (PBMCs) increased significantly upon injection of the individuals with LPS[225]. Furthermore, B-cell receptor (BCR) crosslinking on B cells has been observed after LPS stimulation, which ultimately resulted in calcium influx. This further indicates a conserved function of bat cells compared to human cells[225].

1.4 The unique reservoir function of bats

1.4.1 Hypotheses regarding fundamentals behind a bat's reservoir function

Although the unique role of bats in zoonotic events has been confirmed, the underlying mechanisms remain unknown. One putative explanation for viral richness in bats is the long co-evolution of bats and their viruses, in regard to their phylogenetic age[256]. Another possible explanation on how bats do not display clinical signs of disease despite harbouring deadly viruses is stated in hypothesis related to body core temperature. Since bats experience significant temperature oscillations with up to 41°C during flight and down to 4°C in hibernation or 35°C during roosting, these situations putatively induce immune variations during hibernation[257] and restrict viral replication during flight[220]. This is supported by evidence regarding adaptation of expression of genes associated to mitochondrial and nuclear oxidative phosphorylation[258,259] as well as considerably high amounts of heat shock proteins in bat cells[260]. However, this hypothesis experienced a recent shift since reports indicate that viral titers in bat cells infected *in vitro* are both high and unchanged by high temperature[261]. Furthermore, the entirety of studies related to chiropteran immunity indicates a balanced relation between host resistance mechanisms and host fitness to infection, i.e. tolerance to disease or immune resilience, as mutual defence mechanisms.

1.4.2 *Disce pati* - Bats display immune resilience rather than elevated immune responses

The effectivity of the complex mammalian immune system is founded on a delicately calibrated balance between mounting an appropriate immune response and limiting excessive inflammation to minimize tissue damage. An imbalance towards excessive or dysregulated responses can lead to diseases linked to immunopathology, which is associated to immense severity in many diseases, e.g. Coronavirus disease 2019 (COVID-19)[262]. Interestingly, several bat-borne viruses, like EBOV and SARS-CoV-2, are both highly pathogenic in humans and associated to abnormal activation of innate immunity, resulting in extended and/or more excessive immune responses[160-162]. Main evidence supporting the

newly emerged hypothesis of a delicate balance between resistance and immune resilience mechanisms in bats is summarized in **Figure 1.1**.

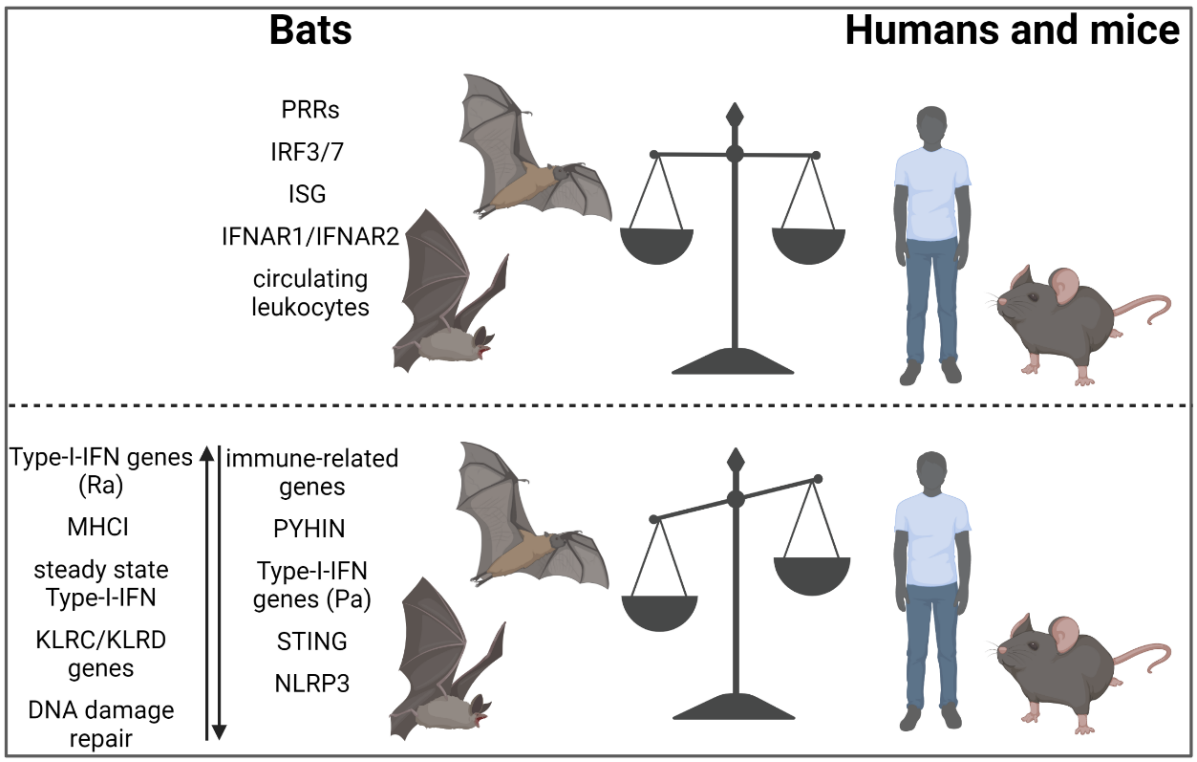

Figure 1.1 | Evidence points toward balance of resistance and immune resilience mechanisms in bats. Bats seemingly evolved towards a well-refined balance between host defence and immune resilience. This balance is unique and includes several bat-specific adaptations in multiple immune-related pathways. Bats share function of PRRs, IRFs, ISGs and IFNAR1/IFNAR2 signalling as well as abundance of circulating leukocytes with other mammals like humans and mice. However, their distinctions lie within expansions (Ra = ERB) or contractions (Pa = *P. alecto*) in type-I-IFN gene families, constitutive IFN expression, diversified and expanded KLRC/KLRD gene families and specific mutations to enhance DNA damage repair processes. In addition, many components involved in DNA sensing and inflammasome activity (STING, NLRP3, caspase-1) are impaired and PYHIN gene families are largely missing. Based on Irving et.al.[30], modified. Figure generated with BioRender.

This newly emerged hypothesis is based on numerous findings related to bat-specific patterns in IFN baseline expression, induction and kinetics of IFN signalling, as well as shallow immune responses upon natural or experimental infection. Studies on bat IFNs revealed an already striking difference between bats and other mammals, since bats express type-I-IFNs, especially *IFNA* at steady state, as demonstrated for *P alecto*[193] or ERB PBMCs[203]. In humans, baseline IFN levels are low and highly inducible upon stimulation and infection[263]. It is of note, due to species diversity within the bat family, that bat IFN signalling not only differs compared to other mammals[264], but already varies between bat species. This is demonstrated by e.g. contraction/expansion of different IFN genes across bat species, like an expanded *IFNW* locus in ERB[168]. Furthermore, IFN signalling kinetic differ between bats

and e.g. humans and mice, as demonstrated by lower induction capacities of *IFNA* and *IFNB* in bats[169,214,265]. However, several bat species constitutively express not only IFNs[193,203], but also ISGs at steady state[169,214,265]. Particularly noteworthy are bat-specific expression dynamics of *IRF3*[199] and *IRF7*[200], as well as ribonuclease L (*RNASEL*), which rendered to be IFN-induced in bats[163,265] compared to other mammals[169]. Intriguingly, upon infection with EBOV[266] and MERS-CoV[267], bats do not exhibit clinical disease despite high viral titers in tissue and sera in infected individuals[266], respectively. Similar observations could be found in bats inoculated with bat coronaviruses[268] and NiV[269]. These findings highlight a possible resilience mechanism of bats towards infection with RNA viruses, supporting the fact that bats harbour significantly more RNA viruses than DNA viruses[33].

The previously mentioned impairment in STING activation was initially believed to be caused by bat evolution prioritizing management of DNA virus infection[218]. However, it was recently linked to evolution towards resilience, since free host DNA accumulates during flight[218] (temperature stress) and would ultimately lead to an overactivation of STING[270]. This is supported by the thorough loss of members of the PYHIN gene family[191], resulting in the absence of inflammasome sensors for intracellular DNA AIM2 and IFI16[271] in bats. Conclusively, dampening of inflammasome signalling impacts the cleavage of pro-IL-1β and pro-IL-18 by caspase-1[219]. Furthermore, it can be postulated that during flight, once the bat body core temperature is elevated, cellular danger signals like free host DNA, ATP or reactive oxygen species would accumulate and therefore trigger inflammasomes on a daily basis[30].

This bias towards immune resilience is also mirrored by constitutive expression of immunomodulatory transforming growth factor beta 1 (*TGFB1*), *IL17A* and *IL22* in $CD3^+$ T cells, which highlights a predominance of Th17 and Tregs and therefore immune tolerance in some bat species[224]. In addition, NK cell receptors defined were found to have more inhibitory motifs than NK cell receptors of other species[168], indicating regulatory features in NK cell function as well. Conclusively, these findings suggest that bat-borne viruses, are impaired in their ability to modulate innate immune pathways in bats.

1.5 Aim of this thesis

The unique reservoir function of bats is uncontested. Especially in the wake of the current pandemic, bats and their seemingly extraordinary immunity have become a focus of antiviral research. However, although the probably best-studied bat is *P. alecto*, thorough studies including several approaches are missing for other species. This results in numerous isolated datasets, hampering correlations between the unique immunity of bats, zoonotic risks and events as well as their role for One Health. With this work, in-depth data regarding innate and adaptive immunity of ERB is provided.

The first part of this work focuses on the assessment of molecular immunity in ERB. In this section, hypotheses on constitutive, and temperature-dependent elevation of IFN expression was addressed. Included are the establishment of ERB-specific tools to study specifically IFN-responses on transcript level, upon stimulation with viral mimetics and infection with several lyssaviruses (model for neurotropic viruses) in immortalized cell lines and SARS-CoV-2 (model for respiratory viruses) in primary epithelial cells *in vitro*. A prerequisite for IFN-related studies in ERB was the selection of a thoroughly stable reference gene. Additionally, the unique physiology of bats was considered by monitoring IFN kinetics upon temperature oscillations, mimicking daily ERB roosting and flying phases. Furthermore, cytokine distribution in tissue after SARS-CoV-2 infection was monitored in adult ERB.

In the second part, the immune cell landscape in periphery and lymphoid as well as non-lymphoid tissue of adult and juvenile ERB was analysed using flow cytometry and single-cell-RNA sequencing (scRNA-seq). This section aimed to elucidate the effects of age on leukocyte profiles in ERB and therefore distinct roles of both age groups in the reservoir function of this species, as suggested for MARV[272]. Abundances of myeloid and lymphoid cells were determined, considering immunomaturation-related differences described for other mammals. To gain a detailed insight into leukocyte abundance and function in ERB, functionality of myeloid as well as lymphoid cells was assessed to define similarities and distinctions to human and rodent immunity.

2 Material

2.1 Laboratory equipment

2.1.1 Laboratory devices

Table 2.1 | Laboratory devices used.

Denomination	Origin / Vendor
Accu-jet® pro pipette controller	Brand
Axio Scope.A1 microscope (+ AxioCam ICc3)	Carl Zeiss
BD FACSAria™ III	BD Biosciences
BD FACSCanto™ II	BD Biosciences
BD LSRFortessa™	BD Biosciences
BioAnalyzer 2100	Agilent
Biometra Trio PCR thermal cycler	Analytik Jena
BioRad Cycler C1000 (+CFX96)	Bio Rad
Centrifuge 5427 R	Eppendorf
Centrifuge 5810 R	Eppendorf
ChemiDoc™ Imaging Systems	Bio Rad
CO_2 Incubator (MCO-19AIC)	Sanyo
Cryo-freezing unit (Quick-Freeze)	Hartenstein
Finnpipette® F2 multichannel pipettes	ThermoFisher Scientific
Finnpipette® F2 pipettes	ThermoFisher Scientific
Freezer, -20°C/-80°C	Liebherr
HeraSafe 2020, Laminar Flow	Thermo Fisher Scientific
Infinite® M200PRO ELISA reader	Tecan
Liquid Nitrogen Preservation System, -190°C	Messer
MACSmix™ Tube Rotator	Miltenyi Biotec
Magnetic stirrer, Combimag	IKA
Milli-Q water purification (A10)	Millipore
NanoDropo™ 2000	ThermoFisher Scientific
NanoDrop™ One	ThermoFisher Scientific
neoFuge® 8-6K micro centrifuge	neoLab
Nikon Eclipse TS2 microscope	Nikon

Denomination	Origin / Vendor
Orion 3 STAR pH meter	ThermoFisher Scientific
PowerPac™ Basic Power Supply	Bio Rad
Precision scale	Mettler Toledo
QuantStudio 6 Flex qRT-PCR thermal cycler	Applied Biosystems, ThermoFisher Scientific
REAX 2000 vortex	Heidolph
Refrigerator, 4°C	Liebherr
Scale (EMB 100-3)	KERN
Sub-Cell® GT, large horizontal gel chamber	Bio Rad
Sub-Gel Mini, small horizontal gel chamber	ThermoFisher Scientific,
TableTop shaker	Edmund Bühler, 7400 Tübingen
Thermomixer 5436	Eppendorf
Thunder Imager	Leica Microsystems
Vaportec Isoflurane Vaporiser	Burtons Medical Equipment Ltd.
VWR Thermal cycler XT96	VWR

2.1.2 Glassware and Tools

Table 2.2 | Glassware and tools used.

Denomination	Origin / Vendor
Dissection tools (scissors, forceps)	Hartenstein
Glass bottles	Schott-DURAN
Glass pipettes	Scherf-Präzision
Glass tumblers	Schott-DURAN
Neubauer counting chamber	Carl Roth
Slides for microscopy	R. Langenbrinck

2.1.3 Plastics and Consumables

Table 2.3 | Plastics and other consumables used.

Denomination	Origin / Vendor
6-, 24-, 96-well plate, flat bottom	Corning
Cell culture flask, T25, T75, T175	Corning
Centrifuge tubes 15ml, 50ml	Sarstedt
Cryo.s freezing tubes	Greiner Bio-One
EASY strainer™ cell sieve	Greiner Bio-One
FACS tubes	BD Falcon
Filter tips	Nerbe Plus
Filtration system, 0.22 µm, 500 ml	Corning
Flowmi® cell strainers	Sigma Aldrich
K3E tubes, 1.3 ml	Sarstedt
LoBind reaction tubes 1.5 ml	Eppendorf
Low Multiplate for PCR, white, 96-well	Bio Rad
MicroAmp® Optical 96-well reaction plate	Applied Biosystems, ThermoFisher Scientific
MicroAmp® Optical adhesive film	Applied Biosystems, ThermoFisher Scientific
Microseal 'B' film	Bio Rad
Millex-GP, 0.22 µm filters	Millipore
PCR soft tubes 0.2 ml	BioZym
PCR tube strips, 8×0.2 ml	Eppendorf
Pipette tips	Greiner Bio-One
Polystyrene centrifugation tube, 12 ml	Greiner Bio-One
Reaction tubes	Eppendorf
Scalpel blades	Aesculap, Braun
Scalpel handle	Aesculap, Braun
S-Monovette® Lithium-Heparin, 5 ml	Sarstedt
Sterican® cannula, 26G	Braun
Stripette pipettes	Costar
Tuberculin (TBC) syringe	MediWare Servoprax, GmbH

2.2 Biological material and chemicals

2.2.1 Chemicals and reagents

Table 2.4 | Chemicals and other reagents used.

Denomination	Origin / Vendor
AccuCheck Counting Beads	ThermoFisher Scientific
Acetic acid (CH_3COOH)	Sigma Aldrich
Actinomycin D (ActD) from *Streptomyces spp.*	Sigma Aldrich
Ambion™ nuclease-free water	Invitrogen
Ammonium chloride (NH_4Cl)	Carl Roth
Ammonium chloride (NH_4Cl)	Carl Roth
Bromophenol Blue	Sigma Aldrich
Calcium chloride ($CaCl_2$)	Carl Roth
Chloroform	Sigma-Aldrich
Collagen Type I	Corning
Collagenase Type IV 160 U/mg	Worthington Biochemical
Concanavalin A (ConA)	Sigma-Aldrich
D(+)-Saccharose (RNAse/DNAse free)	Carl Roth
Deoxy-nucleoside triphosphate mix (dNTPs), 10 mM	Jena Bioscience
Diethyl pyrocarbonate (DEPC)	Carl Roth
Disodium EDTA (Na_2EDTA)	Carl Roth
Disodium phosphate (Na_2HPO_4)	Carl Roth
Dimethyl sulfoxide (DMSO) for molecular biology	Sigma-Aldrich
DNase I grade II from bovine pancreas	Merck
Dulbecco's Phosphate Buffered Saline (DPBS)	Gibco® by Life Technologies
EB buffer	Qiagen
***Escherichia coli* BioParticles™**	Invitrogen
Ethanol (EtOH)	Carl Roth
Ethidium bromide (EtBr) solution, 1%	Carl Roth
Ethylenediaminetetraacetic acid (EDTA)	Carl Roth
Ficoll-Paque™ PLUS (1.077 g/ml)	Cytiva, GE Healthcare
Glycerin, 50% aqueous solution	Ricca Chemical
Glyoxal solution, 40% in water	Sigma-Aldrich
Hybri-Max™ DMSO	Sigma-Aldrich

Denomination	Origin / Vendor
Hydrogen peroxide, 30% in water	ThermoFisher Scientific
Imiquimod (TLR7 ligand)	Enzo Life Sciences
ISD (cGAS activator)	InvivoGen
Isoflurane CP®	CP-Pharma
Isopropanol	Carl Roth
LE Agarose	Lonza Bioscience
Lipopolysaccharide (LPS)	Sigma Aldrich
Marker for agarose gels 50 bp, 100 bp, 1 kb+	ThermoFisher Scientific
Methanol (MeOH)	Carl Roth
Paraformaldehyde (PFA), 32% EM grade	EM Sciences
Poly I:C (TLR3 ligand)	InvivoGen
Poly(dA:dT) (CDS, RIG-I l ligand)	InvivoGen
Potassium bicarbonate ($KHCO_3$)	Carl Roth
Potassium chloride (KCl)	Carl Roth
Potassium dihydrogenphosphate (KH_2PO_4)	Carl Roth
R848 (TLR7/8 ligand)	Enzo Life Sciences
Recombinant RNasin Ribonuclease	Promega
Roti-Gel stain, red	Carl Roth
Saponin	Carl Roth
Skim milk powder	Hobbybäcker-Versand
Sodium chloride [NaCl]	Carl Roth
Sodium Pyruvate solution, 100 mM	Gibco® by Life Technologies
SPRI select size selection beads	Beckman Coulter
***Staphylococcus* Enterotoxin B (SEB)**	Sigma Aldrich
TE buffer	Invitrogen
Tetrasodium EDTA (Na_4EDTA)	Carl Roth
Thiazolyl Blue Tetrazolium Bromide (MTT) powder	Sigma-Aldrich
Tris-base	Carl Roth
Triton X-100	Sigma Aldrich
TRIzol® Reagent	ThermoFisher Scientific
Tween 20, 10% solution	Bio Rad
UltraPure™ bovine serum albumin (BSA)	ThermoFisher Scientific
Universal Interferon (uIFN)	PBL Assay Science

2.2.2 Antibodies, dyes and fluorophores

The following table includes all primary (*) and secondary (#) antibodies used for FACS analysis (FACS) and immunofluorescence (IF), as well as intercalating dyes used in qRT-PCR (qPCR). For clarity, all applications were assigned abbreviations, subsequently used in the table.

Table 2.5 | Primary* and secondary# antibodies, dyes, and fluorophores used.

Denomination target	Linked Fluorophore	Clone	Application	Origin / Vendor
Annexin V*	APC	-	FACS, 5 µl per 10^6 cells	BioLegend
α-bovine CD172a*	-	DH59B	FACS, 1:100	Bio Rad
α-human CD206*	APC/PE-Cy7	15-2	FACS, 1:20	BioLegend
α-human CD3*	Pacific Blue	CD3-12	FACS, 1:100	Bio Rad
α-human CD79a*	PerCP-Cy5.5	HM47	FACS, 1:50	BioLegend
α-human Ki-67*	BV786	B56	FACS, 1:50	BD Biosciences
α-mouse IgG1#	BV421	RMG1-1	FACS, 1:400	BioLegend
α-mouse/human CD11b*	BV711	M1/70	FACS, 1:100	BioLegend
α-rabbit IgG (H+L)#	Alexa Fluor 488	Donkey polyclonal	IF, 1:1,000	Invitrogen
α-rabies virus N protein (RVN161-5)*	-	Rabbit polyclonal	IF, 1:5,000	Lab. Prof. Dr. Finke, FLI[273]
α-rat IgG /H+L)#	APC	Goat polyclonal	FACS, 1:1,000	ThermoFisher Scientific
α-rat/mouse I-A/I-E (MHCII)*	PE	2G9	FACS, 1:100	BD Biosciences
EVAGreen® Fluorescent DNA stain, 100 µM	-	-	qPCR, 1:100	Jena Bioscience
Hoechst33342	-	-	IF, 1:20,000	ThermoFisher Scientific
Propidium Iodide (PI)			FACS, 2 µl/sample	BioLegend
ROX Reference Dye, 25 µM	-	-	qPCR, 1:500	Jena Bioscience
α-mouse CD326*	-	G8.8	FACS, 1:100	BioLegend
α-pan Cytokeratin#	FITC	PCK-26	FACS, 1:100	GeneTex

2.2.3 Media, cell lines and supplements

The following table contains all media and supplements used for culturing immortalized bat cell lines, human and bat fibroblasts, and bat epithelial cells. For clarity, abbreviations were assigned to each medium/supplement in accordance to their use in immortalized cell line (I), fibroblast (F) and epithelial cell (E) culture.

Table 2.6 | Media and supplements used in cell culture.

Denomination	Application	Origin / Vendor
2-Mercaptoethanol (BME)	White blood cell cultivation	Gibco® by Life Technologies
Amphotericin B (AmpB)	E, 1:10,000	Sigma Aldrich
Cholera toxin (*Vibrio cholerae*)	E, 50-100 ng/ml	Enzo Life Sciences
Cytiva HyClone™ HEPES solution	E	ThermoFisher Scientific
Dulbecco's Modified Eagle Medium (DMEM, E, high glucose, 4.5 g/l)	F	FLI Riems, cell culture service
Fetal calf serum (FCS)	I, F, and E, 10%	FLI Riems, cell culture service
Ham's F-12 and Dulbecco's Modified Eagle Medium (DMEM, E, high glucose, 4.5 g/l)	E	FLI Riems, cell culture service
Ham's F-12 and Iscove's Modified Dulbecco's Medium (IMDM), mixed 1:1	I	FLI Riems, cell culture service
Insulin-Transferrin-Selenium (ITS-G), 100X	E, 1:100	Gibco® by Life Technologies
L-Glutamine solution, 200 mM	E, 2 mM	Gibco® by Life Technologies
Minimum Essential Medium (MEM) nonessential amino acids (NEAA) solution, 100X	F and E	Gibco® by Life Technologies
Mouse neuroblastoma cells (Na42/13)	titration of supernatants (lyssavirus studies)	FLI, collection of cell lines in veterinary medicine (CCLV)
Neonatal human dermal fibroblasts (HDFn)	-	ThermoFisher Scientific
Opti-MEM	I, F, and E for transfection	Gibco® by Life Technologies
Penicillin-Streptomycin (10,000 U/ml)	I, F, and E, 100 U/ml	Gibco® by Life Technologies
Recombinant human epidermal growth factor (rhEGF)	E, 25-50 ng/ml	BioLegend
Retinoic acid (RA)≥98%	E,	Avantor™ (by VWR™)

Denomination	Application	Origin / Vendor
Roswell Park Memorial Institute (RPMI) 1640	Phagocytosis assay (blood and lung)	Gibco® by Life Technologies
Sodium Pyruvate (S-Pyruvate)	E, F	Gibco® by Life Technologies

2.2.4 Composition of media and buffers

All components and their distributors are listed separately in Table 2.4 and 2.6; therefore, short denominations are used in this table.

Table 2.7 | List of all components and amounts used for media and buffers.

Denomination	Contents	Application
'BatEpi' Medium for bat epithelia cells (1:1 Ham's F-12 and Dulbecco's Modified Eagle Medium)	FCS [10%] HEPES [10 mM]] ITS-G [1:100] L-Glutamine [2 mM] Pen/Strep [100 U/ml] rhEGF [25-50 ng/ml] Cholera toxin [50-100 ng/ml] AmpB [1:10,000] NEAA [1:100] S-Pyruvate [1 mM]	Cultivation of primary bat epithelia from nose, trachea, lung and gut
'BatFib' Medium for bat fibroblasts (DMEM)	FCS [10%] L-Glutamine [2 mM] Pen/Strep [100 U/ml] S-Pyruvate [1 mM] NEAA [1:100]	Cultivation of primary bat fibroblasts
'BatIm' Medium for immortalized bat cells (1:1 Ham's F-12 and IMDM)	FCS [10%] Pen/Strep [100 U/ml]	Cultivation of immortalized bat cell lines from nose, olfactory system and cerebrum
'BatLeuko' medium for PBMCs and splenocytes (BatIm medium)	BME [0.1%] HEPES [10 mM]	Proliferation assay with primary bat leukocytes
'BatPhago' Medium for phagocytosis assays (RPMI 1640)	FCS [2%] pH 7.4 HEPES [10 mM] BME [0.1%] L-Glutamine [2 mM]	Phagocytosis assay with whole blood and enzymatically digested lung tissue
'MTT-Fix' fixation buffer (1x PBS)	Formaldehyde [3.7%] Triton X-100 [1%]	Fixation and permeabilisation of cells
10x Phosphate buffered saline (PBS)	NaCl [1.37 M] KCl [27 mM]	Used for washing steps in several applications

Denomination	Contents	Application
	Na_2HPO_4 [100 mM] KH_2PO_4 [18 mM]	
50x Tris-acetate-EDTA (TAE) buffer	Na_2EDTA [50 mM] Tris-base [2 M] Acetic acid [1 M]	Base for agarose gels and running buffer (working solution: 1x TAE, diluted in ddH_2O)
Annexin binding buffer (1x PBS)	HEPES [10 mM] NaCl [150 mM] $CaCl_2$ [2.5 mM]	For apoptosis assay
Collagen coating solution (1x PBS)	Collagen [1:80]	Used to enhance adherence of epithelial cells
DEPC-treated water (ddH_2O)	DEPC [0.1%] Incubated 12h at 37°C Autoclaved 2x prior to use	For PCR and qRT-PCR, RNAses efficiently inactivated
Erythrocyte lysis buffer[274] (ddH_2O)	NH_4Cl [1.55 mM] Na_4EDTA [12.7 mM] $KHCO_3$ [100 mM] pH 7.4	High-salt buffer used to lyse erythrocytes (FACS)
FACS buffer[274] (1x PBS)	FCS [0.1%] NaN_3 [1:25,000 of 1 M] EDTA [1 mM]	Buffer used for antibody working dilutions and washing steps (FACS)
Glyoxal fixing solution	Nuclease-free H_2O [2.8 ml] 100% EtOH [790 ml] 40% glyoxal [310 ml] Acetic acid [30 µl] RNasin [1:25]	Alternative fixation of lymphocytes prior to intracellular staining
Loading dye (10 ml ddH_2O)	Saccharose [4 g] Bromophenol Blue [0.04g] EDTA [1 mM]	High-sugar buffer mixed with PCR products prior to loading the gel (tracking dye)
PBS-BSA (DPBS)	UltraPure™ BSA 20 µg/ml	For all washing steps during cell preparation for scRNA-seq
PBS-EDTA (1x PBS)	EDTA [1 mM]	Washing during tissue preparation and PBMC isolation steps
Trizol	Phenol [38%] Guanidinethiocyanate [0.8M] Ammoniumthiocyanate [0.4M] Sodium Acetate [0.1M] Glycerol [5%]	Used to lyse cells for subsequent RNA extraction

2.2.5 Viruses

The following table provides details on all lyssaviruses and coronaviruses used in this work. All lyssavirus infections were performed by Jeannette Kliemt, technical assistance (Lab Prof. Dr. Finke, Dr. Müller, Dr. Freuling, FLI). The SARS-CoV-2 infections was performed by Dan Balkema, technical assistance and PD Dr. Anne Balkema-Buschmann (FLI).

Table 2.8 | Neurotropic and respiratory viruses used.

Denomination	Isolate	Origin / Vendor
European bat 1 lyssavirus (EBLV-1)	RV9, ref: 20174 (23.09.2015)	FLI, lab Finke/Müller/Freuling
Lagos bat lyssavirus	ref: 37515 (01.06.2017)	FLI, lab Finke/Müller/Freuling
Rabies lyssavirus (RABV)	dog Azerbaijan	FLI, lab Finke/Müller/Freuling
RABV vaccine strain (SAD)	B19, ref: 47991-48011 (08.04.2020)	FLI, lab Finke/Müller/Freuling
SARS-CoV-2	2019_nCoV Muc-IMB-1 isolate	FLI, Institute for virus diagnostics

2.2.6 Primers

The following table contains all primers used in this work. Primers were either used in PCR or qRT-PCR assays. Indicated are sequences of both forward and reverse primers [5'-3'], as well as amplicon sizes. Primer performance was improved by heating primer stocks once to 95°C for 2min prior to use and by adding 1% molecular grade DMSO to each reaction. All primers were designed using the PrimerQuest™ Tool. Secondary structures, which would impair primer performance, were excluded by quality control using the OligoAnalyzer™ Tool.

Table 2.9 | Gene symbols and names, primer sequences, and amplicon sizes of all primers used.

Gene symbol	Gene name	Gene ID	Primer sequences [5'3']	Amplicon size [bp]
ACE2	angiotensin converting enzyme 2	107497263	F-TATTGAGCCAACACTGGGAAC R-CGACAAAGATGAGCAGGACAA	113
ACTB	actin beta	107515934	F-GCCTTGGTCGTGGATAATG R-GGGATACTTCAGGGTCAGGATA	193
AIF1	allograft inflammatory factor 1	107498495	F-CAGAAGGCCGTGAGAAAGGA R-TTCCTCCCTGTAGATCCCGG	111
APOB	apolipoprotein	107510821	F-CTTAGTGTTTCGTCGGCCCT R-AAGTCTGTAGTCTTGCGGGC	447
CALB1	calbindin 1	107507481	F-GAGAACTTCGTGCTGCTCTT R-TGGTGTCCAGATCCTGTTTATTC	430
CALB2	calbindin 2	107520554	F-TCCTGTCTGACCTGCTGAA R-CCACTTCCATCCTTGTCGTAAA	235
CCK	cholecystokinin	107519989	F-GAGAGCAGTGCACAGGATG R-TGTAGTCCCGGTCGCTTAT	161
CD14	CD14 molecule	107521575	F-CTGCGAAGTGGACGACAA R-CGACAGCACTAATACAATTCAAGG	95

Gene symbol	Gene name	Gene ID	Primer sequences [5'3']	Amplicon size [bp]
CD16 (LOC107502476)	low affinity immunoglobulin gamma Fc region receptor III-B	107502476	F-GAAGCAGCCTCTCCAATCAG R-CCTGGAAATACTGGACCTTCAC	240
CD163	CD163 molecule	107519759	F-GTGCCTGTTTGATTACCAGTTC R-TAGACATCGGTTTCCTCCATTC	398
CD34	CD34 molecule, immature HSC	107513503	F-CACAATATCACCAGCCCCGT R-GTCAGTTCCTCTCCCTTGGC	191
CD3E (for part 4.1.1)	CD3e molecule (TCR accessory protein)	107516045	F-TTCTGCTGTTCACCACCACC R-AGGGTTGCCAAAGAGAGAGC	151
CD3E (for part 4.3.2.1)	CD3e molecule (TCR accessory protein)	107516045	F-ATGTATTCGGGAAATCTCTGG R-GGGTGTTGCCTTCAAAGTATAG	208
CD44	CD44 molecule (Indian blood group)	107499244	F-CAACTCTAACTCCAGCAACTCC R-CACTGATGCCACTTCTGTCTAC	326
CD5	CD5 molecule, lymphocytes	107504736	F-GTCTGCTACGGATCACTGGG R-GGAGTCGTCTTCTGTGGCTC	104
CD68	CD68 molecule	107506400	F-CTACCACAGGCACCATCAG R-CAGGGCTGGGAACCATTAG	229
CD79A	CD79a molecule	107502589	F-CACCCTGGCAACAATACCT R-GCGTCTATTCCAAACTTCACATTC	368
CDH1	cadherin 1	107520648	F-GTCAAACGGCCTCTACAGCT R-ACGTGAGCACTTCTGTCTGG	184
CDHR1	cadherin related family member 1	107498492	F-CCACAGTCCCAGTCACCATC R-CTCCCTGGTCCGAGTCATTG	168
CFTR	CF transmembrane conductance regulator	107519971	F-GAGACCATCCTGCCTCGAAG R-ATGCTGCTGTCTTTCGGTGA	133
CHRNA1	cholinergic receptor nicotinic alpha 1 subunit	107505010	F-AAGATGGGGTGTCTGCTTGG R-CCAATCAAGGGTACGGCACT	162

Gene symbol	Gene name	Gene ID	Primer sequences [5'3']	Amplicon size [bp]
CLDN1	claudin 1	107505909	F-CGCAATAACTTCCTCCACGC R-GTTCCGATCCAGCCCAAGAA	176
CLDN4	claudin 4	107511819	F-GAAACACCTCCCTCTGCTCC R-CTCTCCCGACGATCAGAAGC	142
COL1A1	collagen type I alpha 1 chain	107517613	F-TGGTGCCAGAGGACTTGTTG R-CCACGAGAACCAGGACTTCC	179
COL1A2	collagen type I alpha 2 chain	107518820	F-CCTGCCGCAAAGAGTCTACA R-CTTCTTGGCCCTCCTCTTGG	121
CRHR1	corticotropin releasing hormone receptor 1	107508175	F-GAACCTCATCTCAGCCTTCATC R-CAGCACTTCTCATTGTCGTAGTA	309
CUBN	cubilin	107513675	F-GTTCACCTCGGACTTCAGCA R-TGGACAGCAATGACCAGACC	183
CXCL10	C-X-C motif chemokine ligand 10	107516366	F-CTTTAGAAGTACACGCTGTGTCTGC R-CTTTAGAACTACACGCTGTGTCTGC	209
DDX58 (RIGI)	DExD/H-box helicase 58	107502800	F-AACAACAGGGGTGCAATGGA R-CACGGAACCAGCCTTCTTCT	79
EEF1A1	eukaryotic translation elongation factor 1 alpha 1	107509282	F-GTATGCCTGGGTCTTGGATAAA R-GCCTGTGATGTGCCTGTAA	162
ENO2	enolase 2	107519838	F-TGTCTCTCCCCTGCTCTCTC R-ACACACACAGAACCAGCACA	217
FAP (LOC107511737)	fibroblast activation protein alpha	107511737	F-TCAGTTGGCTTACGTGGGTT R-CAGCCCATCCAGTTCTGCTT	165
FOXJ1	forkhead box J1	107501379	F-CTATTCCTACGCTACGCTCATC R-GGCGGAAGTAGCAGAAGTT	110
GABRB3	gamma-aminobutyric acid type A receptor subunit beta3	107515750	F-CGGTGAATCCAGCCATCTT R-GAACACTTTCGCTGCCATATTC	251

Gene symbol	Gene name	Gene ID	Primer sequences [5'3']	Amplicon size [bp]
GAD1	glutamate decarboxylase 1	107521061	F-ACACAGGGTGGCTCCAAAAA R-TCTTGGATTGGGGGACATGC	481
GAD2	glutamate decarboxylase 2	107500115	F-GTGCTGGCGATGGGATATT R-GCTCAGTTTCCACTTGTGTTTC	449
GAPDH	glyceraldehyde-3-phosphate dehydrogenase	107519804	F-CAAGTTCAAAGGCACAGTCAAG R-TATTCAGCACCAGCATCACC	120
GFAP (LOC107508155)	glial fibrillary acidic protein	107508155	F-TCTCCATCTCTCTGCCAGCT R-CTCTACCTTCCCCTCAGCCT	699
GRM2	glutamate metabotropic receptor 2	107504180	F-CTACAGCGACGTCTCCATCC R-CGGGACTTGTCACTCAGCTT	102
HES1	hes family bHLH transcription factor 1	107505922	F-TCTGAGCACAGAAAGTCATCAA R-AAGGCGACACTGCGTTAG	689
HES2	hes family bHLH transcription factor 2	107521016	F-AGATGCGGCAGAACTTCGTA R-GTCAGTCGCTCCACGCA	270
IFIH1 (MDA5)	interferon induced with helicase C domain 1	107511736	F-AGAAGCCTGTCCCGTCTACT R-GCCGTCCTCTGTATCTGCTC	196
IFNA1	interferon alpha-1-like (multiple LOCs)	-	F-CTTCCAGAGACTCTTCCTCTATCT R-TCCTTACTCCTTGATCTTTCCTTC	129
IFNA4 (LOC107518587)	interferon alpha-4-like	107518587	F-TGGTGGCTGTGGTGGTG R-GAGGAAGGTCTGTTGGGTCA	245
IFNB1	interferon beta 1	107518589	F-CAGAAGGAGGACGCAGTATT R-GGCTGTATCCAGAAGGTCTATC	153
IFNE	interferon epsilon	107506704	F-TCCCCATTGTGTTGCTGTT R-TTTGCTCCTGAGTGCCATGT	245
IFNG	interferon gamma	107512682	F-ATAACCCGACCATTCAAAGCAGTG R-AAACGGACTCTGACTCCTTTTCCT	176

Gene symbol	Gene name	Gene ID	Primer sequences [5'3']	Amplicon size [bp]
IFNK	interferon kappa	107516486	F-CCAGCTGACCAACCTAGAGC R-AACCACCACCAATCTAGCCG	264
IFNL	interferon lambda-1/3-like (multiple LOCs)	-	F-GGCTTTGGAGGCTGAACT R-AGGCGGAAGAGGTTGAATG	261
IFNW1	interferon omega-1-like (multiple LOCs)	-	F-TGCCTGAATGACAGAACCGA R-AGATGGTGGAAACAGGTGCG	92
IFNW2 (LOC107518583)	interferon omega-2-like	107518583	F-ACACACAAACACATTGGCCTG R-ACTGCGTAAAAATCGGTCTTCTC	123
IL10	interleukin 10	107502233	F-TATTGCTGAACGGGTCCTTG R-TTCACAGGGTAGAAAGCGATG	209
IL1B	interleukin 1 beta	107514900	F-AGACGGTGTACCTCGAAGAT R-CAGGAAGACGGGCATCTG	149
ITGAM	integrin subunit alpha M	107506837	F-GGGTTATGCTGCCGAAGTTA R-GCTCTGTGTCTGTCTGTATGTG	904
MUC1	mucin 1	107505454	F-TCCCTCACAGACCCCATCAA R-ATGTTCCGGTTCCCACTGTC	134
MUC5B	mucin 5B	107511644	F-CGCTCTGCCACAACTATGA R-CACTCCGTCCACCAACATT	231
NCAM1	neural cell adhesion molecule 1	107512956	F-TTGCCCAGCTCCAACTACAG R-AAGATGGGGTGTCTGCTTGG	172
NCF1	neutrophil cytosolic factor 1	107514979	F-AAAGCGAGAGTGGTTGGT R-AGCAGTGTAGGCTCTGATG	255
NES	nestin	107521451	F-GTAGAGGTGGCGAGATGTTTAG R-GCGTGACCCTTGATTCTCTT	325
NGFR	nerve growth factor receptor	107517615	F-CCTGGACAGTGTGACGTTCT R-TCGGTGTTCTGCTTGTCCTG	234

Gene symbol	Gene name	Gene ID	Primer sequences [5'3']	Amplicon size [bp]
NRP1	neuropilin 1	107499293	F-TCCTGCTCCACAAGTCTCT R-GGTGCTCCCTGTTTCATCTATT	188
OCLN	occludin	107498712	F-GGAGACCAGAGCAAGACCAC R-CCTGATCCAGTCCTCCTCCA	83
OMP (LOC107519195)	olfactory marker protein	107519195	F-AGGTCTGCTCTCCCTACAGG R-ACACGCACACAGAAGAGAGG	798
PAX6	paired box 6	107512006	F-ACCTCCTCGTACTCCTGCAT R-TCTTTCCTTCCTGAACGCCC	307
PGK1	phosphoglycerate kinase 1	107503843	F-GATTACCTTGCCTGTTGACTTTG R-GACAGCCTCAGCATACTTCTT	148
PTPRC (CD45)	protein tyrosine phosphatase receptor type C	107513637	F-TTGCCCTTCTCATTGTTCTCTAT R-TTGTTCCTGTTACCCTCTTCAC	508
RBFOX3	RNA binding fox-1 homolog 3	107510075	F-CAACATCCCCTTCCGGTTCA R-AGGGGTTCGCAGTCTTCTTG	248
S100B	S100 calcium binding protein B	107510232	F-GAACCCTAACCCCCAAGAGC R-CGTGATCATCTCCCCTTCGG	238
SIRPA	signal regulatory protein alpha	107499673	F-CATCACTTGTCAGGCGAAGA R-GCTGGCATACTCTGTGTAGTT	559
SLC1A3	solute carrier family 1 member 3	107509715	F-ATGAAGGAGCAGGGACAAGC R-AGAAGTAGAGGAGGGGCAGG	238
SST	somatostatin	107505869	F-TGGCTTTGGGCGGTGTC R-GCCTCATTTCATCCTGCTCAGT	201
SYP (LOC107515005)	synaptophysin	107515005	F-CCACAGACCCAGAAACCGTT R-GCCTGTCTCCTTGAACACGA	173
TBR1	T-box brain transcription factor 1	107508547	F-CCAGTGCCATGTTCCCGTAT R-CTGTTGTAGGCTCCGTTGGT	118

Gene symbol	Gene name	Gene ID	Primer sequences [5'3']	Amplicon size [bp]
TBR2	eomesodermin	107513186	F-CAGTTCATTGCCGTGACTGC R-AGAAGGACTGAACGCCGTAC	202
TLR3	toll like receptor 3	107510436	F-ACAACTTAGCTCGCCTCTGG R-CCTTGAAGACCTCTGCTGGG	132
TLR7	toll like receptor 7	107497585	F-ACAGCAAGCCACCTCTATTT R-CTCTGTCACTGCTAGGTCTTTAG	147
TLR8	toll like receptor 8	107497537	F-ACCAGACATCTCTCCAGCCT R-GGCCCCAGTCGAATAGGTAC	90
TMPRSS2	transmembrane serine protease 2	107504925	F-GTCCTCTGGTCACTTTGAAGAA R-TTGCCCTCATTTGTCGGTAG	144
TPBG	trophoblast glycoprotein	107513198	F-GCACCTGGACCTTCGTAACA R-ACCTCTGTCTCCTTGAGCCA	231
TUBB3 (LOC107502098)	tubulin beta 3 class III	107502098	F-CGGACGAGACCTACTGCATC R-CTTCGTACATCTCGCCCTCC	729
VIM	vimentin	107513674	F-CCTGGAGCAGCAGAACAAGA R-GAGCCTCATGATGTCCTCGG	187

2.3 Kits

Table 2.10 | List of kits used.

Denomination	Application	Origin / Vendor
Agilent High Sensitivity DNA Kit	Quality control of scRNA-seq cDNA and libraries	Agilent
CellTrace™ Cell Proliferation Kit	Labelling of lymphocytes with CFSE to monitor proliferation	Invitrogen
Chromium Single Cell 3' GEM, Library & Gel Bead Kit v3	Generation of single cell sequencing libraries	10x Genomics
Cytotoxicity Detection Kit (LDH)	Quantitative lactate dehydrogenase activity	Sigma Aldrich
GoTaq® DNA Polymerase	DNA Polymerase with buffers	Promega
iScript™ cDNA Synthesis Kit	Generation of first strand cDNA using RT-qPCR	Bio Rad
Kwik-Diff™ Staining Kit	Commercial Romanowsky stain variant (Wright-Giemsa staining)	ThermoFisher Scientific
Lipofectamine™ 2000 Transfection Reagent	Optimized transfection with low toxicity	ThermoFisher Scientific
Lipofectamine™ 3000 Transfection Reagent	Optimized transfection with low toxicity	ThermoFisher Scientific
LunaScript® RT SuperMix Kit	cDNA synthesis in a two-step RT-qPCR	New England BioLabs
NucleoMag® VET RNA extraction kit	Extraction of RNA from SARS-CoV-2 infected cells	Macherey-Nagel
QIAquick Gel Extraction Kit (50)	Recovery of amplicons from an agarose gel	Qiagen
RNeasy™ Mini Kit	RNA purification	Qiagen
***Taq* DNA Polymerase with ThermoPol® Buffer**	Improved PCR performance with demanding templates (high GC)	New England BioLabs
True-Nuclear™ Transcription Factor Buffer Set	Optimized fixation and staining of intracellular molecules	BioLegend
Zombie Aqua™ Fixable Viability Kit	Amine-reactive fluorescent dye staining dead cells	BioLegend

2.4 Databases, Services and Software

Table 2.11 | Databases, Services and Software used.

Denomination	Application	Origin / Vendor
Avian, amphibian, reptile and fish genome assemblies and annotations	Generation of primers	bGalGal1.mat.broiler.GRCg7b, Xenopus_laevis_v10.1, GRCz11, USDA_OmykA_1.1, CrpPor_comp1
Bat genome assemblies and annotations	1. Generation of primers 2. Consensus analysis	NCBI Genomes: ASM32557v1, Pvam_2.0, Myoluc2.0
BioRender	Figure making	BioRender
EndNote™ 20	Literature management	Alfasoft GmbH
FlowJo™	Analysis of flow cytometry data	BD Life Sciences
Geneious vR11 and Prime 2019-2021	Consensus analysis, primer generation	Biomatters
GraphPad Prism v7-9	Statistical analysis and data visualization	GraphPad Software
ImageJ	Analysis of IF data	National Institute of Health (NIH)
Mammalian genome assemblies and annotation	1. Generation of primers 2. Consensus analysis of protein sequences	NCBI Genomes: GRCm39, GRCh38.p13, Sscrofa11.1, mRatBN7.2, ARS-UCD1.2, ROS_Cfam_1.0, EquCab3.0
Oligo Analyzer™ Tool	Primer quality control	IDT
Office 2016-2021 (Word, PowerPoint, Excel)	Manuscript writing, preparation of presentations, data analysis	Microsoft
PrimerQuest™ Tool	Primer generation	Integrated DNA Technologies (IDT)
***Rousettus aegyptiacus* Genome Assembly and Annotation (Reference Genomes)**	1. Generation of ERB-specific primers 2. Consensus analysis of protein sequences 3. Annotation of scRNA-seq data	National Center for Biotechnology Information (NCBI) Genomes: Raegyp2.0, mRouAeg1
TubeSeq Service	Amplicon sequencing	Eurofins Genomics
ZEN lite v3.1	leukocyte imaging	Carl Zeiss

3 Methods

3.1 Animal experimental methods

3.1.1 Animals and animal housing

Male and female ERB were housed in captive breeding colonies at the Friedrich-Loeffler-Institut (FLI) of 20 m^2 per aviary under quarantine conditions according to current German Animal Welfare Regulations. Bats were kept in colonies of approx. 20 animals per room in a Biosafety Level (BSL) 1 facility, at 24-26°C and 60-70% humidity. Light was provided between 6 am and 6 pm inclusive of a dimming phase. Dietary requirements were met by providing varying fruits and vegetables. Only limited number of staff have access to the rooms in order to reduce stress levels of the bats. All samples were derived from animals of the FLI ERB breeding colony. Sampling was conducted in agreement with European and National Animal Welfare regulations. Ethical review and approval by the authority of the Federal State of Mecklenburg-Western Pomerania, Germany (file number 7221.3-2-042/17) was confirmed. All experiments were carried out according to ARRIVE guidelines (https://arriveguidelines.org).

3.1.2 Collection of blood and tissue samples

Peripheral blood from both male and female ERB was obtained in the course of short time sedation with Isoflurane, carried out using an Isoflurane vaporizer with simultaneous O_2 supply and a mask, fitted for the head size of the animals. Sampling was carried out when animals were fully sedated. Blood was drawn from the uropatagial vein with a 26G cannula and collected in EDTA-containing (K3E) tubes for subsequent FACS analysis or RNAseq.

Prior to necropsies, bats were sedated with Isoflurane and euthanized via exsanguination. The blood was drained in the course of cardiac puncture and collected in either K3E or Lithium/Heparin tubes. For phagocytosis assays (section 3.2.9), blood was collected in Lithium/Heparin tubes, since the EDTA in K3E tubes would impair Ca^{2+} influx processes during the assay. Afterwards, the body cavity was opened using sterile instruments and

multiple lymphatic (mesenteric lymph node, spleen) and non-lymphatic (lung) organs were collected and stored in serum-free BatIm medium (Table 2.7) until further preparation.

3.1.3 Experimental SARS-CoV-2 infection of ERB

This animal experiment was carried out in the context of another scientific approach [76]. All animal experimental work, including infection with SARS-CoV-2 (2019 nCoV Muc-IMB-1 isolate), was executed by the authors of the published study.

Bat samples were kindly prepared and provided by PD Dr. Anne Balkema-Buschmann (FLI) and Dr. Melanie Rissmann (FLI) under BSL3 conditions (file number 7221.3-2-010/18). Tissue was homogenized in Trizol after necropsies in BSL3 conditions and used for RNA isolation purposes under BSL 2 conditions.

The same set of tissue samples (nose, trachea, lung, lung lymph node [luLN], spleen, blood, duodenum, and mesenteric lymph node [mLN]) was derived from uninfected contact animals from another animal trial and served as negative control for normalization. This animal trial consisted of experimental infection of ERB with IAV strain H9N2 (file number LVL MV TSD/7221.3-1-021/18 and LVL MV TSD/7221.3-2-010/18, Dr. Donata Hoffmann, FLI). The used contact animals remained IAV-negative throughout the trial. Tissue samples originating from uninfected contact animals of the IAV-trial were also utilized to determine tissue distribution of ERB reference gene candidates. Specimens were kindly provided by Dr. Donata Hoffmann (FLI).

3.2 Cell biological methods

3.2.1 Tissue preparation

The following chapter describes methods employed to isolate various cells from different lymphatic and non-lymphatic tissues from ERB. Since the isolated cells were subjected to a broad variety of assays, different cell isolation protocols were used.

3.2.1.1 Isolation of epithelial cells

Establishment of all epithelial cell cultures was done in cooperation with Dr. Gang Pei (FLI). To extract epithelial cells from mucosal surfaces, nasal epithelium, trachea and small intestine of one juvenile female bat were collected, briefly minced and subsequently digested in 5 ml trypsin overnight at 4°C. After digestion, remaining organ bits were collected and stored in BatEpi medium (Table 2.7) while the cell suspension was centrifuged at 350 × g for 10 min. Afterwards, organ bits and resuspended cells were plated in a collagen-coated petri dish in 15 ml BatEpi medium. Collagen coating of tissue culture plates was carried out by using 5 ml of 1:80 collagen in 1x PBS and an incubation overnight at room temperature (RT). The next day, collagen-containing PBS was removed, and the dish was washed twice with 1x PBS. Petri dishes and low-serum medium were used to hamper fibroblast attachment and ultimately minimize contamination of bat epithelial cell cultures by bat fibroblasts. Cells were cultivated at 37°C in the presence of 5% CO_2.

Lung tissue was digested with Collagenase IV (800 µg/ml) and DNaseI (125 µg/ml) in 1.5 ml serum-free BatIm medium for 1 h at 37°C under rocking. Afterwards, the enzymatic digestion was terminated by adding 12 ml PBS-EDTA (Table 2.7). The cell solution was filtered through a 100 µm cell strainer to remove indigestible tissue. After centrifugation at 350 × g for 10 min, the cell pellet was resuspended in 5 ml BatIm medium. Subsequently, 100 µl of the cell suspension was subjected to each flow cytometry panel (myeloid and lymphoid, Table 3.3) and each condition within the phagocytosis assay.

3.2.1.2 Isolation of epithelial fibroblasts

Lung fibroblasts were derived from the lung of a juvenile female bat by briefly mincing the tissue and subsequent digestion with 5 ml trypsin overnight at 4°C. After digestion, trypsin was inactivated by adding 10 ml BatFib medium (Table 2.7). Cells were centrifuged at 350 × g for 10 min, the pellet was resuspended and plated into a 6-well plate in BatFib medium.

3.2.1.3 Isolation of leukocytes from lymphatic tissue

Single cell suspensions from spleen and mLNs were obtained by carefully grinding the tissue through a 100 µm cell strainer with ice-cold 1x PBS-EDTA. Single cell suspensions were centrifuged at 350 × g for 15 min at 4°C and pellets were resuspended in FACS buffer (Table 2.7).

3.2.1.4 Isolation of cells from olfactory and neuronal tissue

Olfactory epithelium, *Nervus olfactorius*, *Bulbus olfactorius* and the cerebrum were collected from an adult male ERB (**Figure 3.1**), briefly minced with sterile scissors and digested in 5 ml trypsin for 12 h at 37°C. After digestion, trypsin was inactivated by adding 15 ml BatIm medium. Afterwards, cells and tissue bits were seeded in a 6-well plate. Cells were cultivated at 37°C with 5% CO_2 until cellular growth could be observed.

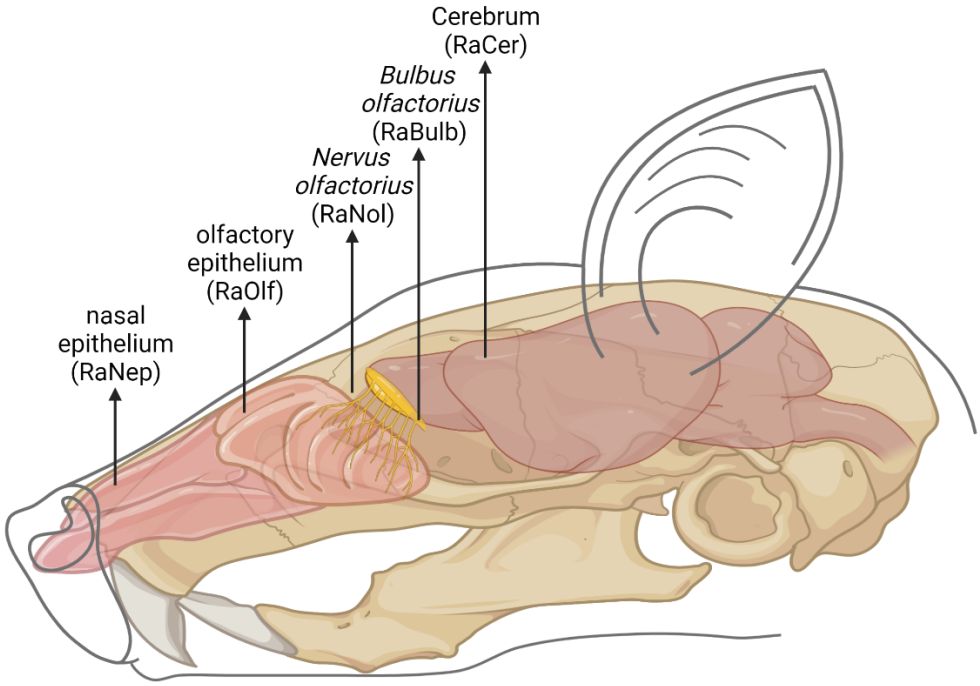

Figure 3.1 | Sites of collection to generate immortalized cell lines from ERB.
To study cell type-specific innate immunity *in vitro*, various cells were isolated from adjoining tissue. Five different cell lines from the nose-to-brain route were to be generated. Therefore, the nasal epithelium, the olfactory epithelium, the *Nervus* and *Bulbus olfactorius*, and the cerebrum of an adult male ERB were collected and cells were isolated. Figure generated with BioRender.

3.2.1.5 Isolation of PBMCs and splenocytes

PBMCs and splenocytes were isolated by adding 3 ml of FicollPaque Plus (density 1,077 g/ml) into a 12 ml polystyrene centrifugation tube (black-cap tube) and slowly layering the sample on top by pipetting. To avoid contamination of the samples by endotoxins and thus subsequent impairment of functional assays, all pipetting steps during blood/organ preparation were carried out with plastic pipettes (stripettes). Various volumes of blood were mixed 1:1 with PBS-EDTA and directly administered onto the Ficoll, whereas the spleen was first homogenized and filtered, then RBCs were lysed once by resuspending the splenocytes in 3-5 ml red blood cell (RBC) lysis buffer (Table 2.7) after centrifugation. The cells were incubated in RBC lysis buffer for 5-10 min, washed with cold PBS-EDTA and resuspended in 5 ml PBS-EDTA. The RBC lysis step did not lyse the entirety of RBCs in the sample, but considerably improved yield of mononuclear cells (MNCs) after gradient centrifugation if included. The mixture was then added to the Ficoll. Density centrifugation was carried out at 760 × g for 30 min, with acceleration and brakes switched off. The cell containing opaque ring was carefully collected into a new 12 ml centrifugation tube, PBS-

EDTA was added to a total volume of 15 ml and cells were centrifuged at 350 × g for 10 min. Afterwards, PBMCs and splenocytes were seeded in BatLeuko medium (Table 2.7) into a 96-well plate at a density of 2×10^5 cells/well.

3.2.1.6 Sample collection and preparation for scRNA-seq

A total of 300 µl of whole blood from three adult (older than three years) and three juvenile (around one year of age) ERB was collected and immediately subjected to RBC lysis using 10X RBC lysis buffer (BioLegend), diluted 1:10 in endotoxin-free water. All washing steps were carried out with PBS-BSA buffer (Table 2.7). After resuspension in 500 µl PBS-BSA, the cells were filtered through 70 µm Flowmi® cell strainers and sorted with a cell sorter FACSAria Fusion (section 3.2.10). A small aliquot was stained with Zombie fixable viability dye to assess cell death induced by RBC lysis. Upon completion of sorting, cells were centrifuged at 400 × g and 4°C for 15 min. Following centrifugation, the cell count was set to 1,000 cells/µl in PBS-BSA. A small aliquot of each sorted sample was collected and directly mixed with 1 µl Propidium Iodide (PI) solution to determine cell viability after sorting/centrifugation.

3.2.2 Immortalization and cultivation of bat cells

Proliferation of cells derived from the nasal epithelium (RaNep) olfactory epithelium (RaOlf), the *N. olfactorius* (RaNol), the *B. olfactorius* (RaBulb) and the cerebrum (RaCer) could be observed 7-14 days after seeding. The tissue bits were removed and medium was filtered through a 0.22 µm filter and mixed 1:1 with fresh BatIm medium to ensure both nutrition and presence of important factors for growth of primary cells. The cells were kept until reaching ~70% confluency, then seeded into a 24-well plate at a density of 1.5×10^5 cells/well. Further on, only adherent cells were propagated. Following attachment overnight at 37°C and 5% CO_2, cells were transfected with 1µg/well Simian Vacuolating Virus 40 large T (SV40T) antigen expressing pRSVAg1 plasmid to induce immortalization by stable transfection. The transfection reagents were prepared according to instructions of the manufacturer given in Table 3.1. After incubating overnight, 1 ml of BatIm medium was added to each well. After five days, cells were detached with trypsin and transferred into a T25 cell culture flask each. The cells were cultivated until they reached confluency and then

detached with trypsin to enable seeding for limited dilution cloning. Limited dilution cloning was carried out to obtain a monoclonal cell line from a polyclonal mix of cells. Therefore, the cells were seeded and diluted in a 96-well plate to reach a cell density of 0.8 cells in each well in row H (8 cells/ml in row H). To increase the probability of obtaining a monoclonal cell line, another dilution approach was applied. The suspension containing the parenteral cells was set to 2×10^4 cells/ ml and 100 µl were added to well A1 to a 96-well plate with 100 µl BatIm medium in each well. Afterwards, a 1:2 dilution series was carried out from A1 to H1. After adding 100 µl BatIm medium to wells A1-H1, a second 1:2 dilution series was carried out from column 1-12. Two 96-well plates per method and cell line were prepared and incubated at 37°C in the presence of 5% CO_2 for up to 4 weeks until a few wells could be selected for screening. Growth curves were carried out by seeding 10^5 cells in each well of a 6-well plate. Viable and dead cells were counted every 12 h for 10 days. Doubling times were calculated: (duration ×[ln[2]÷ln [final concentration/initial concentration]). Brightfield microscopy was carried out utilizing a Nikon microscope with 10X objective.

Table 3.1 | Reagents for 1 stable transfection reaction with Lipofectamine 2000 or 3000.

Content tube A		Content tube B
Option 1	50 µl Opti-MEM +2 µl Lipofectamine 2000	50 µl Opti-MEM + 1µg total DNA
Option 2	50 µl Opti-MEM +2 µl Lipofectamine 3000	50 µl Opti-MEM + 1µg total DNA+ P3000 reagent
For both options, the mixed contents of tube B were added to the mixed contents of tube A and incubated for 10-15 min to ensure formation of DNA-lipid complexes. After incubation, mixture was added to the cells.		

3.2.3 Cultivation of primary bat epithelia and fibroblasts

Bat fibroblasts were generated and kindly provided by Dr. Gang Pei (FLI). Only adherent cells were propagated and bat primary bat fibroblasts were cultivated in BatFib medium at 37°C in the presence of 5% CO_2 until experiments were carried out. Following trypsin digestion and centrifugation described in chapter 3.2.1, primary epithelial cells were propagated on collagen-coated flasks only. For a T25 flask 3 ml of 1:80 collagen in PBS was used, for a T75 flask 5 ml, for a T175 flask 10 ml and for a 24-well plate 1 ml. All primary epithelia cells were kept in BatEpi medium and cultivated in 37°C and 5% CO_2.

3.2.4 Cryopreservation

All successfully established bat cell lines were cryostocked for further use. For that, cells were detached with trypsin, enzymatic reaction was stopped using corresponding media for each cell line and suspensions were centrifuged at 350 × g for 5 min. Pellets were resuspended in FCS + 10% Hybri-Max DMSO at a cell density of max. 5×10^6 cells/ml. After transferring the suspension at 1ml/tube into cryopreservation tubes, the cells were transferred to a pre-cooled Quick-freeze unit and stored at -80°C for at least 24 h before being transferred to liquid nitrogen storage. To thaw the cells, the vials were recovered from storage, thawed at 37°C and transferred to a 15 ml centrifugation tube. To allow gentle diffusion of DMSO out of the cells, FCS-containing medium was added slowly. The suspension was then centrifuged at 300 × g for 5 min, cells were resuspended and plated in T25 flasks.

3.2.5 Stimulation experiments

3.2.5.1 Stimulation with viral mimetics

For all IFN-related studies, cells were either stimulated with pI:C, Poly(dA:dT) (poly[deoxyadenylic-deoxythymidylic] acid sodium salt, pdA:dT), ISD (interferon stimulatory DNA) or Imiquimod (Imi) and R848. All chemicals were all reconstituted according to manufacturer's protocols. Cells were transfected with 10 µg/ml pI:C, 10 µg/ml pdA:dT, 10 µg/ml ISD or 5 µg/ml Imi + 5 µg/ml R848, respectively. For transient transfection, a polyethylenimine-based (PEI) approach was used and reaction setups are listed in Table 3.2. The stimulations were kept for either 4 h and 8 h (pI:C, pdA:dT, ISD) or 2 h, 4 h and 8 h (Imi/R848, pI:C).

Table 3.2 | Reagents for 1 transient transfection (1µg/ml) reaction with PEI.

Content tube A	Content tube B
50 µl Opti-MEM +2 µl PEI	50 µl Opti-MEM + 1µg total DNA
The mixed contents of tube **B** were added to the mixed contents of tube **A** and incubated for 10-15 min to ensure formation of DNA-lipid complexes. After incubation, the mixture was added to the cells.	

3.2.5.2 ActD treatment for analysis of primer efficiencies

To support standard curves, primer efficiencies were further determined by treating RaNep cells (representative, proof of principle) with ActD. This agent intercalates into DNA at the transcription initiation complex, resulting in a shutdown of all transcription processes and therefore a biological dilution of mRNA. RaNep cells were seeded into a 24-well plate at a density of 10^5 cells/well and left to attach overnight at 37°C with 5% CO_2. On the next day, cells were transfected with 10 µg pI:C per well to initiate IFN production. ActD at a concentration of 10µg/ml was added 4 h prior to sample collection to each well at a final concentration of 10 µg/ml. Cells were lysed in Trizol directly (0 h), 1 h, 2 h, 4 h, 6 h, 8 h and 10 h, respectively. Afterwards, RNA extraction and cDNA synthesis were performed (section 3.4.2.1).

3.2.5.3 Stimulation of bat primary ERB cells with universal Interferon

Stimulation of bat primary fibroblasts with uIFN was carried out by adding 1,000 U/ml uIFN in BatFib medium to each respective well in a 24-well plate, since uIFN has been described to induce ISG production in bat cells[163]. Stimulation with uIFN was incubated for 4 h at 37°C in the presence of 5% CO_2. Cells were homogenized in Trizol to measure stability of different reference gene candidates by qRT-PCR.

Stimulation of EpiTrachea was carried out by adding 1,000 U/ml of uIFN to BatEpi medium. The cells were seeded into a 24-well plate, previously coated with collagen to ensure adherence overnight. After adding uIFN to the cells, the plate was incubated at 37°C and 5% CO_2 for 4 h and 8 h, respectively. Upon completion of stimulation, the cells were harvested and lysed in Trizol to determine type-I-IFN-related variations in expression of SARS-CoV-2 receptors.

3.2.5.4 Bat lymphocyte proliferation assay

Purified and washed PBMCs and splenocytes from three adult and three juvenile female ERB were resuspended in 1 ml of 1x PBS. To track proliferation, cells were labeled with carboxyfluorescein succinimidyl ester (CFSE) by adding a final concentration of 5 µM CFSE to the cell suspension and incubating for 15 min at RT in the dark. The PBMCs and splenocytes were then incubated with 14 ml BatLeuko medium and centrifuged at 350 × g and 4°C for 10 min. After washing, ~2-3×10^5 cells were seeded into each well of a 96-well plate. The wells in which the cells were seeded into already contained either 10 µg/ml Concanavalin A (ConA), 10 µg/ml LPS, 200 ng/ml Staphylococcal Enterotoxin B (SEB) or PBS in BatLeuko medium as negative control. The stimuli were diluted so that the final concentration for ConA was 5 µg/ml, 5 µg/ml for LPS, and 100 ng/ml for SEB. The cells were exposed to mitogenic stimulation for 5 days at 37°C. Since CFSE labels amino groups, $CFSE^{low}$ cells were defined as proliferating cells (diluted CFSE signal corresponds to proliferating cells).

3.2.6 Infection experiments *in vitro*

3.2.6.1 Infection of immortalized cell lines with lyssaviruses

All ERB cell lines were seeded under BSL2 conditions, allowed to attach overnight at 37°C and 5% CO_2 and then transferred to a BSL3 laboratory. All infection experiments under BSL3 conditions were carried out by Jeannette Kliemt, technical assistance in the laboratory of Prof. Dr. Stefan Finke, Dr. Thomas Müller and Dr. Conrad Freuling (FLI).

For infection studies with different lyssaviruses, the cells were seeded at a density of 4×10^4 cells/well into a 96-well plate. To determine the specific $TCID_{50}$ for each lyssavirus listed in Table 2.8, the cells were infected with RABV, LBV, EBLV-1 and SAD B19 in quadruplets. Each virus was titrated on each cell line, starting with a dilution of the stock of 1:10^{-1} and further dilutions up to 1:10^{-8} (virus in 100 µl). The cells were incubated with the viruses for 24h, then the supernatants were removed and the cells were fixed using 4% PFA in 1x PBS for 30 min prior to transfer into BSL2 conditions. To permeabilize, the fixation solution was removed and 1x PBS containing 0.5% Triton X-100 was added and incubated for 20 min. After permeabilization, the cells were washed with dH_2O and 100 µl 1x PBS/well was added

prior to storage at 4°C to avoid impairment of subsequent staining. The subsequent infection experiments were carried out using respective $TCID_{50}$ values as points of reference. Values of RaOlf were taken as points of reference for RaNep infection with SAD B19 and EBLV-1, since infection of RaNep did not allow $TCID_{50}$ calculations.

Furthermore, a growth kinetic was performed with SAD B19, EBLV-1 and LBV on RaNep and RaOlf cells, to compare the least and most susceptible cell line. For the kinetic, RaNep and RaOlf were seeded in T25 flasks at a density of 10^6 cells per flask. Infection was carried out using 10^4 infectious units in 300 µl for each flask. 1 ml of supernatant was collected at 16 h, 24 h, 48 h, and 72 h post infection (pi). The infectious virus titers were determined by titrating the supernatant on Na42/13 cells, which were previously seeded into 96 well plates at a density of 4×10^4 cells/well. After 48 h incubation at 37°C and 5% CO_2, the plates were fixed as described above and immunofluorescence staining (section 3.2.7) to visualize nuclei and lyssaviral N protein was performed.

To evaluate transcriptional changes upon infection, RaNep and RaOlf cells were infected with SAD B19, LBV and EBLV-1. The cells were seeded into 24 well plates at a density of 1.5×10^5 cells/well and infected with a multiplicity of infection (MOI) of 0.1 (2×10^4 virions in 200 µl). The plates were incubated with the viruses for 24 h at 37°C and 5% CO_2 and 10 µg pI:C/well was added 4 h prior to cell lysis with Trizol. After lysis, the Trizol samples were transferred to the BSL2 laboratory for RNA extraction (section 3.4.2).

3.2.6.2 Infection of primary epithelial cells with SARS-CoV-2

Infection of epithelia with SARS-CoV-2 (2019_nCoV Muc-IMB-1 isolate) was carried out under BSL3 conditions by PD Dr. Anne Balkema-Buschmann and Dan Balkema (technical assistance, FLI). Briefly, cells were seeded at a density of 5×10^5 cells/well in a 6-well plate under BSL2 conditions and transferred to a BSL3 laboratory. The cells were infected at an MOI of ~2, whereas a control well for each cell type remained uninfected. The virus was diluted in BatEpi medium and after removal of the medium, 500 µl of diluted virus was added to the cells. The infection was incubated at 37°C and 5% CO_2 for 1 h. Subsequently, the virus suspension was removed and 1.5 ml BatEpi medium was added to each well. Cells were harvested after 8, 24, and 48 hpi by scraping the cells and subjecting 100 µl cell

suspension to RNA extraction using the NucleoMag® VET kit. Upon completion, extracted RNA was transferred to BSL2 conditions for subsequent qRT-PCR analysis.

3.2.7 Immunofluorescence

After fixation of the cells infected with lyssaviruses, the cells were covered with 100 µl PBS/Well and the plates were transferred to a BSL2 laboratory. Afterwards, the PBS was discarded and 50 µl/well of 50 mM ammonium chloride in PBS solution was added and incubated for 10 min at RT. After incubation, the solution was discarded and the plates were washed with 100 µl of 1x PBS/well. Then, 50 µl of a 0.5% skim milk in PBS solution was added for blocking and incubated for 5 min at RT. The primary antibody targeting lyssavirus N protein (RVN161-5) was diluted 1:6,000 in PBS and 50 µl were added to each well. After incubation for 1 h at RT, the supernatant was removed and the plates were washed with 100 µl PBS/well. The secondary antibody (donkey anti-rabbit, Alexa Fluor 488, 1:1,000) and Hoechst 33342 (1:20,000) were diluted in PBS. Then, 50 µl per well of the antibody/Hoechst solution was added and incubated for 1h at RT in the dark. After incubation, the supernatant was removed, the cells covered with 100 µl PBS/well and stored at 4°C wrapped in tinfoil until further use. To acquire the plates, they were equilibrated at RT for at least 1h prior to measurements to prevent condensation and impairment of microscopy. The signals were acquired using a wide field fluorescence microscope (Leica Thunder) and the automatic acquisition function to analyze Alexa 488 and Hoechst 33342 signals. After acquisition, the overlay was created using ImageJ.

3.2.8 Flow cytometry

Staining protocols were established and validated using blood samples from 23 adult and 21 juvenile ERB. 50 µl whole blood was used for each the myeloid and lymphoid panel.

Antibodies targeting surface molecules were diluted in FACS buffer (Table 2.7), antibodies targeting intracellular components were diluted in permeabilization buffer provided with the True-Nuclear transcription factor buffer set. The workflow of both the myeloid and lymphoid panel can be seen in Table 3.3. Cells were incubated with 100 µl of pre-mixed antibodies in FACS / permeabilization buffer for 15 min (surface molecules) or 25 min

(intracellular molecules) at 4°C in the dark. Each washing step was carried out with either FACS or permeabilization buffer and a centrifugation step at 350 × g and 4°C for 5 min.

First, the surface molecules were stained and the fixable viability dye Zombie Aqua was included in the mix. Whenever Zombie Aqua was present in the mix, the incubation time was increased to 20 min at 4°C instead of 15 min at 4°C for staining of surface molecules only. After staining of surface molecules, RBCs were lysed using 2 ml erythrocyte lysis buffer per sample. The sample was briefly vortexed and left at RT until the solution turned transparent. Due to the high RBC count in bat blood, this step had to be executed twice in order to achieve sufficient RBC lysis. Then, 3 ml FACS buffer were added to stop the reaction and cells were pelleted. For the myeloid panel, the pelleted cells were resuspended in remaining buffer and measured in the BD LSRFortessa cytometer. For the lymphoid staining, the remaining buffer was removed and the cells were resuspended adding 100 µl fixation solution (True-Nuclear transcription factor buffer set). The cells were vortexed and incubated for 35 min at RT in the dark. After fixation, fixation solution was removed by washing each sample with 4 ml permeabilization buffer. The cells were pelleted and intracellular targets were stained by corresponding antibodies diluted in 100 µl permeabilization buffer. After 25 min, the cells were washed, resuspended in remaining buffer and samples were acquired using the BD LSRFortessa cytometer. Acquired samples were analyzed using the FlowJo v10.5.3 software.

Furthermore, cells from mLN, spleen and lung of three adult and three juvenile female ERB were isolated according to protocols described in section 3.2.1 and 50 µl of each cell suspension was subjected to both the myeloid and lymphoid panel. A negative control for each organ/staining protocol was always included.

Table 3.3 | Workflow for staining myeloid and lymphoid cells in ERB. Antibody origin, working dilutions, and target specificities are given in Table 2.5.

	Myeloid panel			Lymphoid panel	
	Diluted antibodies	**Incubation**		**Diluted antibodies**	**Incubation**
1	**α-CD172a** **Zombie Aqua**	4°C, 20 min	1	**α-CD11b** **Zombie Aqua**	4°C, 20 min
2	**α-mouse IgG1**	4°C, 15 min	2	**RBC lysis**	RT, ~10 min
4	**α-CD11b** **α-MHCII** **α-CD206**	4°C, 15 min	4	**α-CD79a** **α-CD3** **(α-Ki-67 for proliferation assay)**	4°C, 25 min
5	**RBC lysis**	RT, ~10 min	5	**Sample acquisition**	
6	**Sample acquisition**				

To assess integrity of immortalized (RaNep) and primary (EpiNose, EpiTrachea, EpiLung, and EpiGut) epithelial cells, pan cytokeratin (clone PCK-26, FITC-labelled) and epithelial cell adhesion molecule (EpCAM, clone G8.8) staining was employed. Since the epitope for EpCAM recognition is located on the cell surface, this antibody was diluted 1:100 with Zombie Aqua at 1:500 in FACS buffer. The cells were stained with 100 µl of the antibody solution for 20 min at 4°C. After washing, the cells were incubated with α-mouse IgG1 (BV421) as a secondary antibody to EpCAM primary staining. After incubation and washing, the cells were fixed using the True-Nuclear transcription factor buffer set for 45 min. After fixation and subsequent washing, 100 µl of a αpan cytokeratin antibody diluted 1:100 in permeabilization buffer, was added to the cells and incubated for 25 min at 4°C. Upon completion, the cells were washed, supernatant was discarded and the cells were resuspended in the remaining buffer. Sample acquisition was carried out using a BD LSRFortessa.

3.2.9 Phagocytosis assay

To assess the phagocytic activity of alveolar phagocytes, 100 µl of the lung cell suspension was diluted in 900 µl BatPhago medium (Table 2.7). For blood, 500 µl of whole blood was diluted 1:1 with BatPhago medium. Each reaction had a total volume of 1 ml. After preparing the dilutions, 8×10^5 *E. coli* bioparticles/ml were added to each tube, leaving untreated tubes as controls. The tubes were placed in a MACSmix tube rotator and placed in an incubator

with 37°C and 5% CO_2. The cells were given 10 min, 30 min, and 1 h to phagocytose particles, respectively. Upon completion of the incubation, the tubes were removed from the incubator and 200 µl of each sample was collected and subjected to staining the myeloid panel for flow cytometry.

3.2.10 Cell sorting with BD FACSAria Fusion

Debris, non-viable cells, and doublets were excluded from the sorting process. To validate the specificity of cross-reactive antibodies used to detect ERB leukocytes, the following populations were sorted with a BD FACSAria Fusion: $CD11b^+$, $CD11b^-$, $CD11b^+CD172a^+$, $FSC^{high}SSC^{high}$, $CD3^+$, and $CD79a^+$. Sorting of the cells was carried out with a 100 µm nozzle, the lowest flow rate and the 'purity' setting of the sorter. Sorted cells were collected in Trizol or prepared for microscopy.

Sorting of total leukocytes for scRNA-seq was carried out using a 100 µm nozzle, the lowest flow rate and the 'single cell' setting of the sorter. The cells were sorted into Protein LoBind tubes pre-coated with FCS. Coating with FCS was carried out for 1 h prior to sorting. The FCS was removed, the tubes were flushed with PBS-BSA and 300 µl of PBS-BSA was transferred to each tube as buffer for sorted cells. The sorter was pre-cooled to 4°C prior to sorting. Sorted cells were kept on ice until sample collection was complete.

3.3 Protein biochemistry methods

3.3.1 Viability assays

3.3.1.1 Assessment of metabolic activity and cell death

To confirm that all newly established cell lines are viable in different temperatures, two approaches were used. First, viability was assessed using a MTT (3-[4,5-dimethylthiazole-2-yl]-2,5-diphentyltetrazolium bromide) test. In brief, 100 µl of a cell suspension with 5×10^5 cells/ml were seeded into each well of a 96-well plate and left to attach overnight at 37°C and 5% CO_2. The MTT labeling reagent was prepared by dissolving 5 mg MTT powder in 1 ml 1x PBS and mixing with BatIm medium to obtain a 5% MTT solution. To mimic the daily body core temperature oscillations of an adult ERB, a temperature profile (**Figure 3.2**) was generated according to data derived from the FLI breeding colony, kindly provided by PD Dr. Anne Balkema-Buschmann. This temperature profile was used to incubate the cell lines according to daily temperature oscillations in ERB. Ultimately, 35°C was chosen as the lowest temperature observed during roosting, 40°C was selected as the highest recorded temperature during flight and 39°C was included as intermediate temperature. The cells were incubated for 4.5 h at 35°C, 8.5 h at 40°C or 2.5 h at 39°C in presence of 5% CO_2, respectively. 90 min prior to completion of the incubation time for each temperature, 100 µl of the 5% MTT solution was added and the cells were further incubated until completion. Afterwards, the supernatant was removed and the cells were fixed with the MTT-Fix solution (Table 2.7) for 30 min. After fixation, 50 µl 99% Isopropanol per well were added directly before acquiring the signal using an ELISA-Reader. Secondly, viability of the cells at different temperatures was evaluated using a lactate dehydrogenase (LDH) assay according to manufacturer's instructions. Briefly, the cells were incubated as described above, and the level of free LDH in supernatants was evaluated by mixing 50 µl of supernatant with 50 µl reaction solution and the absorbance at 490nm was measured with an ELISA-Reader. As positive control, assigned control wells, were treated with saponin, 20 min prior to sample collection to induce the release of all intracellular LDH.

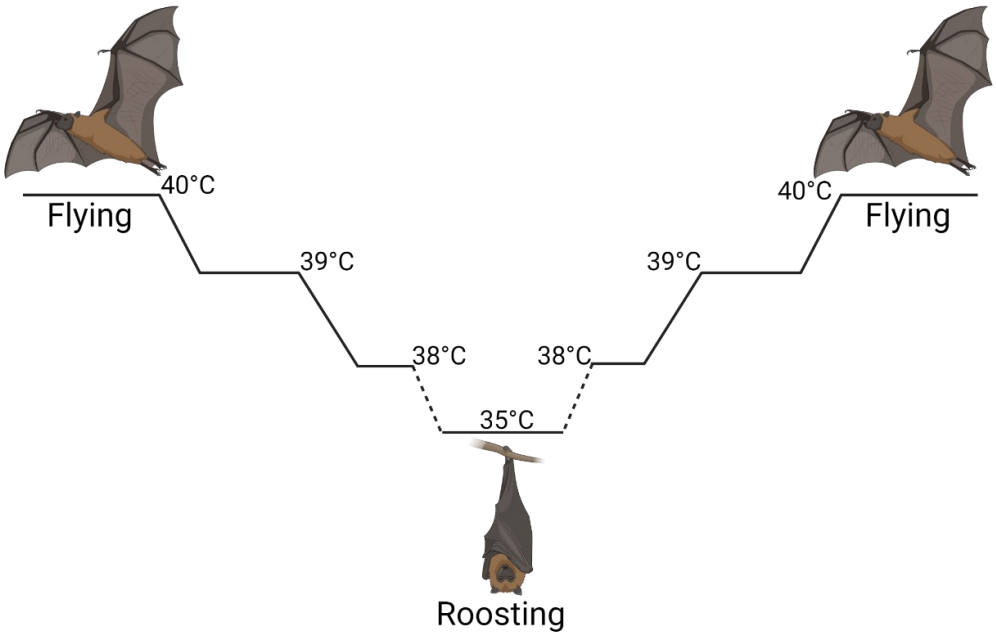

Figure 3.2 | Body core temperature profile of ERB.
The mean duration of the flying (active) phase of adult ERB with body core temperatures reaching up to 40°C was 10 h, encompassing the night (6 pm-6 am). Duration of the roosting phase with body core temperatures of down to 35°C during the day was equally 10 h. Two hours each before and after flight served as periods to elevate/lower the body core temperature, respectively. Figure generated with BioRender.

3.3.1.2 Apoptosis assay

Furthermore, viability was assessed by apoptosis analysis. The cells were seeded into a 24-well plate at a density of 2×10^5 cells/well and left to attach overnight at 37°C with 5% CO_2. As the positive control, assigned control wells, were treated with 150 µM H_2O_2 in 1x PBS to initiate apoptosis. After incubation, the cells were detached using 200 µl of trypsin per well and collected in FACS tubes. The cells were centrifuged at 350 × g and 4°C for 5 min and resuspended in 1 ml Annexin binding buffer. To avoid the loss of non-adherent apoptotic cells, the supernatant was collected, centrifuged at 750 × g and 4°C for 5 min and added to the cell pellets. The pellets were resuspended in 1 ml Annexin binding buffer. For Annexin staining, 100 µl (~10^6 cells) were transferred to a new FACS tube and subsequently incubated with 5 µl Annexin-APC, for 15 min at RT in the dark. After incubation, 400 µl of Annexin binding buffer were added to each sample. Directly before sample acquisition in the FACSCanto II, 1 µl of PI was added to each sample. Amounts of apoptotic, necrotic and live cells was carried out by Annexin V/ PI staining as established elsewhere[275].

3.3.2 Wright-Giemsa staining

In brief, after sorting, myeloid cells were centrifuged for 15 min at 400 × g and 4°C and resuspended in remaining buffer. The suspension (~50-100 µl) was then pipetted as droplet onto a glass microscopy slide and air dried for about 15 min. After almost all liquid was evaporated, the sorted leukocytes were stained using the Kwik-Diff™ Kit. First, the slides were dipped 6 times into a fixing agent (MeOH, blue color). The excessive liquid was removed by a paper towel at the edge of the glass slide. The slides were then dipped 6 times into an eosinophilic solution (red) and finally dipped 6 times into a basophilic solution (blue). The slides were rinsed with H_2O, air dried and stored in the dark until further use. Microscopy pictures were taken with a Axio Scope.A1 microscope, equipped with an AxioCam ICc3 and 100x N-Achroplan objective, used with emulsion oil. Since $CD3^+$ and $CD79a^+$ cells had to be fixed in order to stain intracellular targets, a morphological analysis was not carried out due to known alterations in cell morphology following fixation (e.g. shrinking cytoplasm due to water loss[276]).

3.4 Molecular biological methods

3.4.1 Design and quality control of ERB-specific primers

All primers specific for ERB-transcripts were designed using the PrimerQuest™ Tool and sequences are listed in Table 2.9. The primers had to meet certain criteria in order to be selected: primer lengths had to be around 17-30 bp, GC content between 40-55%, optimal melting temperature at 61°C-62°C. The amplicon length of primers suited for qRT-PCR had to be within the range of 100-250 bp. Selected primer pairs were evaluated using the OligoAnalyzer™ Tool to exclude primers with possible hairpin structures and high probability of homo- and/or heterodimer formation. Additionally, sequences were blasted using the NCBI BLAST tool and alignment to NCBI sequences in Geneious Prime v2021 to verify their specificity to ERB transcripts. Primer pairs which met all criteria were accepted as suitable for PCR and qRT-PCR. Pictures were processed and exported using the ZEN lite Software.

3.4.2 RNA extraction and cDNA synthesis

3.4.2.1 Standard RNA extraction from single cells and cDNA synthesis

To extract mammalian RNA, cells were lysed in Trizol (Table 2.7) and RNA was extracted as published before[77]. Briefly, 250 µl of Chloroform were added per 1 ml Trizol used and vigorously shaken for 15 s. After a 5 min incubation period at RT, samples were centrifuged at 13,000 rpm and 4°C for 5 min at 8,000 × g to allow phase separation. After centrifugation, the aqueous phase was transferred into another tube and immediately mixed with 500 µl Isopropanol. The samples were mixed and left at RT for 5 min, then centrifuged for 20 min at 13,000 rpm and 4°C. The supernatant was discarded and the pellets were resuspended in DNaseI solution to ensure removal of DNA contaminants. A total of 0.5 Kunitz units per sample was used and the digestion was incubated for 10 min at RT. Afterwards, RNA was washed with 1 ml pure Ethanol each. After another centrifugation at 13,000 rpm, 4°C for 5 min, the supernatants were discarded and pellets air-dried for 10-15 min. Dried RNA was reconstituted in DEPC-treated H_2O. The purified RNA was quantified utilizing a NanoDrop 2000c spectrophotometer.

For cDNA synthesis, the LunaScript RT SuperMix Kit was used. In brief, 800 ng RNA were mixed with 2 µl LunaScript RT SuperMix and nuclease-free H_2O was added to obtain a total volume of 10 µl. The cDNA was synthetized in a thermal cycler, running the following program: 25°C for 2 min – 55°C for 10 min – 95°C for 1 min. Afterwards, 90 µl nuclease-free H_2O were added for a total volume of 100 µl. The cDNA was quantified using a NanoDrop and stored at -20°C until further use.

3.4.2.2 RNA extraction and cDNA synthesis from tissue samples and fixed single cells

Since whole organs were homogenized in Trizol and contamination with polysaccharides can result in low RNA yields due to encapsulation of nucleic acids[277], a Trizol/RNeasy hybrid-protocol was used for samples derived from the SARS-CoV-2 trial. First, tissue samples were homogenized in Trizol at a ratio of 1 ml Trizol per 0.1 g tissue used. After homogenization, the samples were stored for 5 min at RT and subsequently frozen until transfer to a BSL2 laboratory. The samples were then thawed, left at RT for 5 min and centrifuged at 12,000 × g for 10 min at 4°C, to remove polysaccharides and debris. After centrifugation, 250 µl

Chloroform per 1 ml Trizol was used, the samples were mixed vigorously for 20 s and incubated at RT for 3 min. After incubation, the samples were centrifuged at 10,000 × g for 18 min at 4°C. The aqueous phase was collected into a new tube and slowly mixed with an equal volume of 70% EtOH. The mixture was transferred to a RNeasy column, placed in a collection tube prior to sample application and centrifuged at 8,000 × g for 2 min. The flow-through was discarded and the samples centrifuged in same conditions after applying 700 µl buffer RW1. The column with bound RNA was transferred to a new collection tube and 500 µl buffer RPE was added before centrifugation (1 step 30s, second step 2 min). To elute RNA, the column was placed in a 1.5 ml collection tube, 35 µl DEPC-treated H_2O was applied to the membrane containing the RNA. RNA was eluted by centrifuging the samples at 8,000 × g for 1 min. Eluted RNA was quantified using a NanoDrop and stored at -80°C until further use.

Identity of sorted $CD3^+$ and $CD79a^+$ lymphocytes (section 3.2.10) was characterized via PCR. Since the cells had to be fixed prior to staining and PFA-based fixation rendered RNA extraction highly inefficient, a different fixation protocol was used. Instead of fixation with PFA-based solutions, the cells were fixed with glyoxal[278]. Briefly, extracellular staining and RBC lysis was performed according to instructions provided in section 3.2.8, but the cells were resuspended in 100 µl 3% Glyoxal fixation solution (Table 2.7) and incubated for 15 min on ice. After incubation, 1 ml of 1x PBS with 1:100 RNasin was used for washing. Washing was carried out at 2,000 × g and 4°C for 3 min. The supernatant was discarded and the cells were resuspended in 100 µl pure MeOH supplemented with 1:25 RNasin each. This solution was applied to the samples by slowly adding droplets while vortexing the cells on the lowest setting. Afterwards, the cells were incubated with MeOH for 30 min on ice. Upon completion of incubation, the cells were washed with 1 ml 1x PBS with 1% BSA and 1:100 RNasin at 2,000 × g and 4°C for 3 min. After centrifugation, the supernatant was discarded and the cells were resuspended in 100 µl diluted antibody. Unlike other FACS procedures described in this work, the antibodies were diluted in 1x PBS supplemented with 1% BSA and 1:25 RNasin (for dilution, see Table 2.5). The cells were incubated with the antibodies for 1h on ice and washed with 1 ml 1x PBS with 1% BSA and 1:100 RNasin at 2,000 × g and 4°C for 3 min. The supernatant was discarded and the cells were resuspended in 300 µl 1x PBS supplemented with 1% BSA and 1:100 RNasin and kept on ice until sorting,

which was carried out according to instructions in section 3.2.10. After sorting, the cells were centrifuged and lysed in 1 ml Trizol for each sorted population.

3.4.3 Analysis of ERB-specific transcripts using PCR and qRT-PCR

3.4.3.1 Species-specific *APOB* PCR

To confirm identity and origin of the newly established ERB cell lines, the expression patterns of different markers specific for various cell types as well as an ERB-specific apolipoprotein B (*APOB*) PCR was used. To confirm species-specificity of the immortalized cell lines, primers specific for ERB *APOB* were derived and recognition of *APOB* from several other species (mammals, amphibians, fish and reptile, reference genomes are listed in Table 2.11) was ruled out. PCR was carried out by extracting genomic DNA from *Sus scrofa* lung, *Oncorhynchus mykiss* spleen, *Mus musculus* spleen, A549 cells (*H. sapiens*) and ERB PBMCs (kindly provided by Sabine Weber, Lab Dr. Bernd Köllner). All primer sequences and amplicon sizes for actin beta (*ACTB*) and *APOB* detection in other species than ERB are listed in Table 2.9. A total of 50 ng of genomic DNA was used for *APOB* and *ACTB* detection. The PCR reaction was carried out following the reaction setup and program provided in Table 3.4, with an annealing temperature of 58°C and extension time of 1 min. All PCR reactions had a final volume of 25 µl and were performed with a Biometra thermal cycler.

Table 3.4 | Reagents for one reaction and program used for PCR and qRT-PCR. Reagents were either part of the GoTaq Kit or listed in Table 2.4.

Reagent	Amount	Temp. [°C]	Time [min]
5x reaction buffer	5 µl	**95°C**	2
$MgCl_2$	1.5 mM	**95°C**	0.5
DEPC-H_2O	ad 25 µl total	**58-62°C**	0.5
dNTPs (10 mM)	5 mM	**72°C**	1/kb
Taq Polymerase	1.25 U	***rep. step 2-4***	*37-40x*
Primer F (100 pmol/µl)	0.1 µM	**72°C**	10
Primer R (100 pmol/µl)	0.1 µM	**4°C**	indefinite
DMSO	1-3%, template dependent		
DNA	25-100ng		
(qPCR only) EVA Green	1:100		
(qPCR only) ROX dye	1:500		

3.4.3.2 Characterization of immortalized cell lines by PCR

Characterization of RaNep was carried out by determining the expression levels of markers specific for epithelial cells (e-cadherin [*CDH1*], claudin 1 and 4 [*CLDN1*, *CLDN4*], collagen 1 and 2 [*COL1A1*, *COL1A2*], cubilin [*CUBN*], forkhead-box protein 1 [*FOXJ1*], mucin 1 and 5B [*MUC1*, *MUC5B*], and occludin [*OCLN*], Table 2.9). RaOlf, RaNol and RaBulb, as cell lines derived from the olfactory system, were characterized by analysing the expression of markers specific for granule cells, mitral/tufted cells, periglomerular cells, olfactory sensory neurons and olfactory ensheathing cells (Calbindin 1 and 2 [*CALB1, CALB2*], cholecystokinin [*CCK*], Cadherin Related Family Member 1 [*CDHR1*], Corticotropin Releasing Hormone Receptor 1 [*CRHR1*], enolase 2 [*ENO2*], gamma-aminobutyric acid type A receptor subunit beta3 [*GABRB3*], glutamate decarboxylase 1 [*GAD1*], glutamate decarboxylase 2 [*GAD2* or *GAD65*], glial fibrillary acidic protein [*GFAP*], p75 neurotrophin receptor [*NGFR*], olfactory marker protein [*OMP*], paired box protein [*PAX6*], RNA Binding Fox-1 Homolog 3 [*RBFOX3*], calcium-binding protein B [*S100B*], somatostatin [*SST*], T-Box Brain Transcription Factor 1 [*TBR1*], T-Box Brain protein 2 [*TBR2* or *EOMES*], Trophoblast Glycoprotein [*TPBG*], and tubulin beta 3 class III [*TUBB3*], Table 2.9). Cells originating from the brain were identified by determining the expression of markers found in mature and

immature neurons, radial glia cells, astrocytes and microglia (ionized calcium-binding adapter molecule 1 [*AIF1*], *CDH1*, *ENO2*, glial fibrillary acidic protein [*GFAP*], Glutamate Aspartate Transporter [*SLC1A3*], hes family bHLH transcription factor 1 and 5 [*HES1*, *HES5*], integrin α-M [*ITGAM*], nestin [*NES*], *PAX6*, *RBFOX3*, synaptophysin [*SYN*], *TUBB3*, vimentin [*VIM*], Table 2.9). To rule out a possible contamination with either fibroblasts or cells of the hematopoietic lineage, all cell lines were tested for *CD3E*, *CD5*, *CD34* and fibroblast activation protein alpha (*FAP*) expression.

Each PCR reaction was performed using 25-50 ng of cDNA in 5 µl to minimize pipetting errors. The PCR was performed according to the instructions given in Table 3.4, with an annealing temperature of 60°C and 37 cycles.

3.4.3.3 Agarose gel electrophoresis

All amplicons were visualized by size separation in an agarose gel. Depending on expected amplicon sizes, a 0.5% - 1.5% agarose in 1x TAE solution was prepared. The solution was heated in a microwave until boiling, supplemented with 1:15,000 EtBr or 1:20,000 GelRed. The mixture was then poured into a gel casting device with a comb and left until dry. Once dried, the gel was transferred to a horizontal electrophoresis chamber containing 1x TAE buffer and the samples were loaded after mixing with loading dye at a ratio of 1:5. According to expected sizes, a marker (50 bp, 100 bp or 1 kb PLUS) was added and the gel was run at 100 V for 1 h. Upon completion of the run, all gels were visualized using a ChemiDoc. To validate specificity of newly established primer pairs, amplicons were cut and sent out for sequencing, using the TubeSeq service by Eurofins.

3.4.3.4 qRT-PCR

To accurately quantify ERB-specific templates, qRT-PCR reactions were performed with EvaGreen Fluorescent DNA stain and ROX as an internal reference dye, as well as GoTaq Polymerase, according to Table 3.4. To minimize pipetting errors, cDNA templates were diluted and 5 µl of diluted cDNAs were used for each reaction in qRT-PCR. Each well contained one primer pair, reactions were not multiplexed. Measurements were performed

using a Cycler C1000 (+CFX96 real time system) or a QuantStudio 6 Flex Real-Time PCR System. All melting curves ranged between 60.16°C to 94.885°C in steps of 0.193°C.

3.4.3.5 Establishment of standard curves to evaluate amplification efficiencies of selected primer pairs

Standard curves were generated for reference gene candidates (*ACTB*, *EEF1A1*, *GAPDH*, *PGK1*) and selected IFNs (*IFNA1*, *IFNB1*, *IFNL*), when exact determination of copy numbers was necessary. All standard curves ranged from 3 to 300,000 copies in 10-fold dilution steps. To achieve these accurate dilution steps, the specific mass for one amplicon was calculated using the amplicon sizes of each gene (specific weights are listed in Table 3.5). Based on these values, the specific weight of 3 – 300,000 amplicons were determined and the dilutions were prepared accordingly[279]. Afterwards, 5 µl of each dilution was used per qRT-PCR reaction (Table 3.4). The resulting Ct values were used to determine exact copy numbers for specific qRT-PCR reactions. The amplification efficiency of primers for reference gene candidates and selected IFNs was determined by calculations based on the slope of each curve ($10^{-1/slope}$-1). The linear dynamic range (LDR), defined as range between highest and lowest quantifiable copy numbers, was assessed for each of the genes.

To evaluate the efficiency of primer pairs for the genes *IFNA4*, *IFNE*, *IFNK*, *IFNW1*, and *IFNW2*, the template was diluted in 8 1:2 dilution steps to generate a standard curve. To validate the accuracy of this approach, RaNep cells were exemplarily treated with ActD to 'naturally' dilute the mRNA (section 3.2.5.2). The slope of these curves was used to determine the amplification efficiency of each primer pair. The efficiency values of accurate primer pairs range between 90% and 110%.

Table 3.5 | Specific weight of amplicons used for standard curve generation.

Amplicon	Weight [g]
ACTB	2.12×10^{-19}
EEF1A1	1.78×10^{-19}
GAPDH	1.32×10^{-19}
IFNA1	1.42×10^{-19}
IFNB1	1.68×10^{-19}
IFNL	2.87×10^{-19}
PGK1	1.62×10^{-19}

3.4.4 scRNA-seq and library generation

Chromium Next GEM (nanoliter-scale Gel Beads-in-emulsion) Single Cell 3' Reagents Kits v3.1 were used for library generation. All material needed for scRNA-seq procedures, but omitted from the kits, was obtained in accordance to recommendations from the manufacturer (10X Genomics). The samples of three adult ERB and three juvenile ERB were pooled prior to loading the chip. Partitioning oil, GEM gel beads, and glycerol was added to the cavities, following the scheme given in Table 3.6. In the last step, a total of 13,000 cells (13.2 µl) for each age group was mixed with 31.8 µl master mix and 30 µl nuclease-free H_2O and added to one cavity on a Chromium chip each. Upon completion, 100 µl of generated GEMs were aspirated and transferred to a 0.2 ml tube and cDNA was generated using a XT96 thermal cycler. After cDNA synthesis, the partitioning oil was removed with 125 µl/sample recovery agent and the cDNA-containing aqueous phase was further purified with 200 µl Dynabeads Clean-up Mix per sample. After purification, the cDNA was amplified according to the protocol provided in the Chromium Next GEM Single Cell 3' Reagent v3.1 protocol. The amplified cDNA was quantified and quality was verified using a High Sensitivity Chip and a BioAnalyzer. The obtained cDNA concentrations (pg/µl) were then used to determine the input mass for library construction. Using the Gene Expression and library construction kit, the libraries were generated according to the manufacturer's instructions. To be able to sequence both libraries (samples from adult and juvenile ERB) in one sequencing run, a sample index PCR was performed in order to attach an individual index to each library. After sequencing, the libraries can be demultiplexed according to their

individual index. After library generation and index PCR, a quality control step using the BioAnalyzer was included before shipping the libraries to collaboration partners.

Table 3.6 | Reagents pipetted into each cavity on a Chromium chip for GEM generation in scRNA-seq.

A	B	C	D	E	F	G	H
PO 45	PO 45	G 45	G 45	G 45	G 45	G 45	G 45
GB 50	GB 50	G 50	G 50	G 50	G 50	G 50	G 50
CMM 70	CMM 70	G 70	G 70	G 70	G 70	G 70	G 70
empty	empty	empty	empty	empty	empty	empty	empty
Partitioning oil (PO), Gel Beads (GB), Cells + H_2O + master mix (CMM), Glycerol (G): various amounts. All volumes in µl.							

3.4.5 Sequencing and annotation of scRNA-seq libraries

The collaboration partners performing library sequencing and annotation were Dr. Antoine-Emmanuel Saliba and Christophe Toussaint, Helmholtz HIRI (Helmholtz-Institut für RNA-basierte Infektionsforschung), Würzburg, Deutschland. This section gives a brief introduction into the sequencing and annotation of ERB libraires generated at the FLI.

Briefly, both libraries were sequenced together in a multiplexing approach using an Illumina NovaSeq 6000 platform and the paired-end setting. The sequencing data was pre-processed using the Cell Ranger Software by 10x Genomics and mapped to the latest ERB reference genome[170]. Since the cells of different individuals were experimentally combined, a demultiplexing step had to be included to define the origin of each cell based on the genotype. Therefore, after sequencing, the samples were demultiplexed with the Souporcell method, which clusters cells based on their specific genetic variant[280]. Demultiplexed data was visualized by scaling the log-normalized counts of the top 3,000 variable genes and subsequent dimensionality reduction with Uniform Manifold Approximation and Projection (UMAP[281]) and Principal Component Analysis (PCA). Afterwards, the cell clusters were defined by the Leiden algorithm[282], which detects highly inter-connected cell groups. Application of Wilcoxon Rank-Sum testing allowed definition of differentially expressed genes (DEGs) among the clusters. Results from DEG identification were used to identify and label all cell clusters in UMAP. To define low-abundance subsets, cell clusters belonging to myeloid and lymphoid compartments were separated and dimensional reduction was

performed again. After identifying additional subsets, another dimensional reduction was performed on the entirety of T cells in order to define more populations.

3.5 Algorithmic and statistical analyses

3.5.1 Algorithmic stability analyses

In order to determine the expression stability of *ACTB*, *EEF1A1*, *GAPDH* and *PGK1*, two algorithms performing statistical analyses were used: BestKeeper[33] and NormFinder[35]. Highest expression stabilities corresponded to the lowest variation of expression in various tissues, uIFN treatment and temperature oscillations[33,35]. Briefly, BestKeeper performs stability calculations with raw Ct values as input. The parameters needed for stability assessment provided by the algorithm are SD (std dev [± CP]) and the Pearson coefficient of correlation (*r*). An efficient reference gene should have SD values of <1, <2 for SD (std dev [± CP]) and 1 for *r*. The other algorithm used, NormFinder, determines stability based on normalized values ($2^{-\Delta ct}$). The advantage of utilizing NormFinder was to be able to assess the stability for each experimental condition separately (uIFN treatment and temperature oscillations) and the total stability, using the normalized Ct values from all experimental setups. NormFinder values of a suitable reference gene are close to 0.

3.5.2 Statistical analysis of qPCR data

To determine whether differences among all investigated groups reach statistical significance, two-way analysis of variance (ANOVA) and one-way ANOVA were performed, with a Holm-Šidák's post-hoc test to correct for multiple testing. The statistical analysis was performed with GraphPad Prism 9. Statistically significant differences were defined as $P < 0.05$ (*), $P < 0.01$(**), $P < 0.001$(***), and $P < 0.0001$ (****).

3.5.3 Statistical analysis of flow cytometry data

Analysis was performed using GraphPad Prism 8. Shapiro-Wilk normality test was used to determine data distribution. Paired and unpaired *t*-tests were performed on data consisting of two groups. Datasets consisting of three or more groups were subjected to One-Way ANOVA. Two-Way-ANOVA was applied to conduct statistical analysis of leukocyte frequencies and absolute numbers in ERB circulation and tissue. Multiple comparisons were carried out with the Holm-Šidák's post-hoc test for correction. Statistically significant differences were defined as $P < 0.05$ (*), $P < 0.01$(**), $P < 0.001$(***), and $P < 0.0001$ (****).

4 Results

Bats can harbour a plethora of highly pathogenic viruses mostly without exhibiting clinical signs of disease themselves[27], with only few exceptions, e.g. rabies[283,284]. However, the paucity of tools still restricts in-depth analyses of bat-specific antiviral immune responses. To gain deeper understanding about primarily innate immune characteristics of ERB, several immortalized and primary cells were analyzed in this work, e.g. by monitoring the induction of IFNs upon stimulation (viral mimetics), and viral infection. Since the immortalized ERB cells cover the olfactory route to the brain, these cells were experimentally infected with neurotropic lyssaviruses, while primary ERB epithelia were infected with the respiratory virus SARS-CoV-2. Furthermore, effects of temperature oscillations (relevant for ERB physiology) on the induction of IFNs were investigated. Finally, phenotypic and functional characterization of ERB leukocytes at steady state allowed conclusions on age-dependent variations as well as on commonalities and distinctions to other mammalian species.

4.1 Generation and characterization of ERB cell lines and primary cells to study tissue-specific innate antiviral immunity *in vitro*

The first aim was to establish an *in vitro* platform to analyse cell type-specific type-I- and III-IFN kinetics in ERB. For a comprehensive overview of IFN expression in bats, five cell lines originating from different bat tissues were generated. Cells were derived from nasal epithelium, olfactory epithelium, *N. olfactorius*, *B. olfactorius* and the cerebrum. The cells were characterized by monitoring their growth and viability, as well as detecting cell type-specific transcripts and proteins. These cells were employed to study innate immune responses to lyssaviruses. Furthermore, ERB primary epithelia originating from nasal epithelium, trachea, lung and small intestine were established to study ERB- and tissue-specific innate immunity as well as susceptibility to the respiratory virus SARS-CoV-2. The cells were characterized by detecting epithelia-specific transcripts with qRT-PCR and epithelia-associated proteins like cytokeratins (1, 4, 5, 6, and 8) and Epithelial Cell Adhesion Molecule (EpCAM) with flow cytometry.

4.1.1 Morphology and identity of newly established immortalized ERB cell lines

Five ERB cell lines were successfully immortalized. All cell lines vary in size and morphology. Cells from the nasal epithelium (RaNep) showed a cuboid cell shape with contact-dependent growth inhibition (**Figure 4.1**), which is characteristic of epithelial cells[285]. Cells from the olfactory epithelium (RaOlf) were spindle-shaped with long outgrowths, cells from the *N. olfactorius* (RaNol) were spherical with long protrusions. Cells from the *B. olfactorius* (RaBulb) were about the same size as RaNep cells with a elliptical shape, but showed granule-like formations in the cytoplasm. Cells from the cerebrum (RaCer) were heterogeneous in morphology, depending on confluency. RaCer at confluency of 30-70% were spindle-shaped, with small outgrowths at each pointy end (**Figure 4.1**).

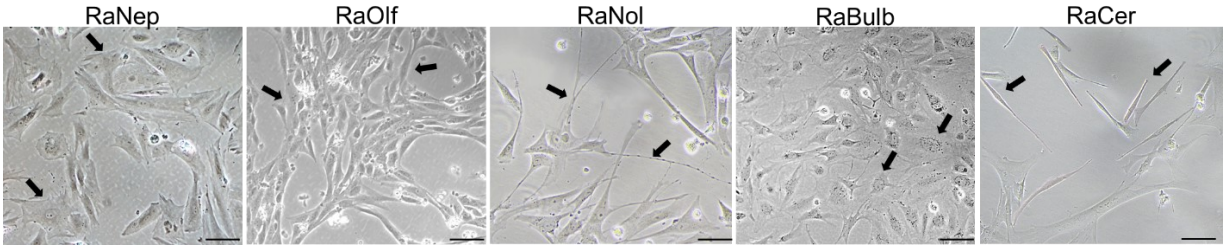

Figure 4.1 | Newly established cell lines vary in size and morphology.
The cells were grown in identical conditions and displayed cell-specific features, as indicated by arrows. In all cultures, few dead and apoptotic cells were present, identified by spherical shape and formation of apoptotic blebs (indicated in RaOlf culture). The cells were imaged using a 10x objective and Nikon imaging system. Scale bar = 10 µm.

To evaluate cellular growth, all cell lines were incubated for 5 days at 37°C. Live and dead cells were subsequently counted every 12 h. All cell lines proliferated under given cultivation conditions, although several differences could be observed (**Figure 4.2, A-E**). RaNep cells reached confluency at around 72 h after seeding and stopped proliferation while maintaining a monolayer without dead cells accumulating (dead cells defined as floating cells). RaNol also reached confluency at around 72 h after seeding, but the cells started dying even after growth inhibition was already initiated. RaOlf reached confluency at around 96 h, although the cells appeared apoptotic as early as 48 h after seeding and many dead cells were observed. RaBulb cells grew slower compared to all other cell lines and ultimately reached confluency 108 h after seeding. RaCer cells grew similarly to RaNol with dead cells starting to accumulate at 96 h after seeding and reaching confluency at 108 h. Interestingly, RaCer cells were the only cell line to display a contracting monolayer after reaching full

confluency (**Figure 4.2, E**). The doubling times were 53.75 h for RaNep, 49.88 h for RaNol, 48.79 h for RaOlf, 60 h for RaBulb, and 50.88 h for RaCer (**Figure 4.2, F**).

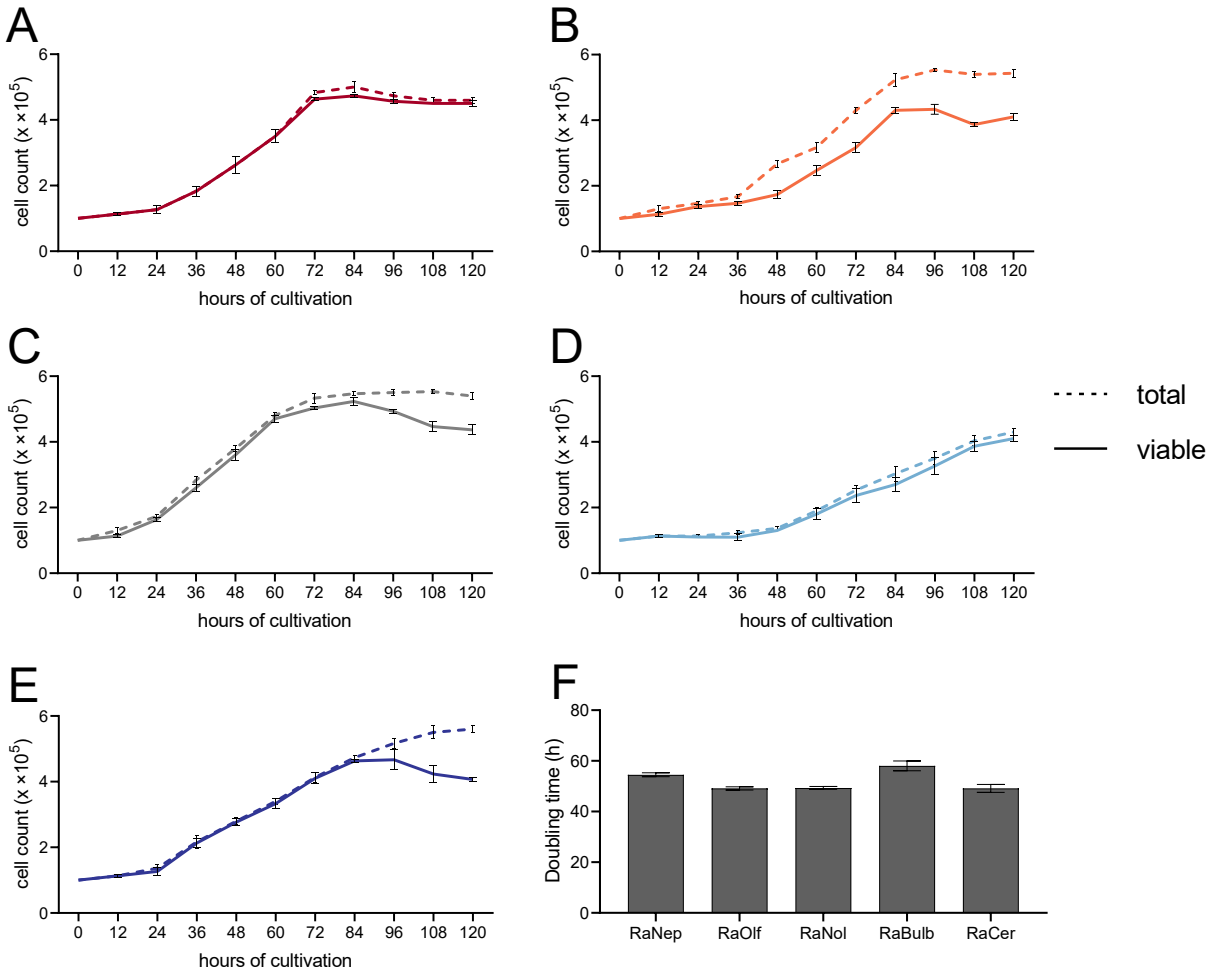

Figure 4.2 | Growth patterns of newly established ERB cell lines at 37°C vary according to origin. All cell lines were incubated at 37°C for up to 5 days. Growth curves depict total cell growth and viable fraction (total cell count – dead cell count, determined by Trypan Blue staining) of RaNep (**A**), RaOlf (**B**), RaNol (**C**), RaBulb (**D**), and RaCer (**E**). Bar plot represents the cell doubling time, calculated with the mean values of three experiments (**F**). Curves show mean ±SD of three independent experiments, bars represent mean doubling time ± SD.

To demonstrate distinct identity of all ERB cell lines, exclusion PCRs were carried out. First, a possible contamination with fibroblasts was excluded by examining the expression of *FAP* transcripts in all cell lines (**Appendix 10.4, B**). Absence of cells of hematopoietic origin was verified by unsuccessful detection of *CD3*, *CD5,* and *CD34* expression by PCR (**Appendix 10.4, B**). Additionally, an ERB-specific PCR to confirm species identity by bat *APOB* expression was established (**Appendix 10.4, A**)[171]. To obtain specific primers, the ERB *APOB* sequence was aligned to various mammalian (*Bos taurus, Canis lupus familiaris, Equus caballus, Homo sapiens, Mus musculus, Myotis lucifugus, P. alecto, P. vampyrus, Rattus norvegicus, Sus scrofa*), avian (*Gallus gallus*), amphibian (*Xenopus laevis*), fish

(*Danio rerio, Oncorhynchus mykiss*) and reptile species (*Crocodylus porosus*). PCR was carried out with genomic DNA of ERB*, S. scrofa, H. sapiens, M. musculus,* and *O. mykiss*, where only ERB DNA rendered positive results, confirming integrity of the cell lines (**Appendix 10.5, A**).

To determine the identities of all new ERB cell lines, the expression of several lineage markers of cell populations typically obtained from these organs was determined via PCR (**Figure 4.3**). Given their cuboid morphology and large size resembling epithelia cells, the expression of epithelia-specific markers was analyzed[286] (**Figure 4.3**): *CDH1*, *CLDN1*, *CLDN4*, *COL1A1*, *COL1A2*, *CUBN*, *FOXJ1*, *MUC1*, *MUC5B*, and *OCLN*. For RaOlf, RaNol and RaBulb, derived from the olfactory complex, typical markers for cells present in the olfactory system were used for identification[227,287-290] (**Figure 4.3**): *CALB1, CALB2*, *CCK*, *CDHR1*, *CRHR1*, *ENO2*, *GABRB3*, *GAD1*, *GAD2* (or *GAD65*), *GFAP*, *NGFR*, *OMP*, *PAX6*, *RBFOX3*, *S100B*, *SST*, *TBR1*, *TBR2* (or *EOMES*), *TPBG*, and *TUBB3*. Expression patterns of the above-mentioned markers determine cellular identity, e.g. simultaneous expression of *PAX6*, *GAD1*, *TPBG*, and *CRHR1* would indicate granule cell identity, while expression of *TBR1*, *GAD1*, *OMP*, and *CDHR1* suggests mitral/tufted cell identity. For RaCer which were derived from the ERB cerebrum, analysis of markers specific for cells of the brain[291], i.e. *AIF1*, *CDH1*, *ENO2*, *GFAP*, *SLC1A3*, *HES1*, *HES5*, *ITGAM*, *NES*, *PAX6*, *RBFOX3*, *SYN*, *TUBB3*, and *VIM* was carried out (**Figure 4.3**). Cell types found in the brain express distinct patterns of these markers, e.g. expression of *GFAP*, *SLC1A3,* and *GFAP* would indicate astrocytes, while additional expression of *AIF1* and *ITGAM* identifies microglia.

RaNep cells expressed structuring components that are essential for tight junctions like *OCLN* and *CLDN1* and *4*, cell-cell adhesion and stability of epithelial cells[292,293], namely *CDH1*[294], *COL1A1* and *2*[295] and other genes which are typically highly expressed in epithelia like *CUBN*[296]. Interestingly, of mucin and cilia formation-encoding genes that are only expressed in fully differentiated epithelia[297], only *MUC1* could be detected. Expression of *FOXJ1* and *MUC5B* could only be detected in RA-differentiated RaNep cells (**Appendix 10.1**). Furthermore, utilizing a mouse-specific antibody which cross-reacted with the ERB ortholog, flow cytometry confirmed the presence of epithelial-specific cytokeratins and EpCAM in RaNep cells (**Appendix 10.2**). The mean percentage of cells which stained positive for cytokeratin was 96.6% and 91.8% for EpCAM, indicating homogeneity and epithelial

identity (**Appendix 10.3**). The mean fluorescence intensity (MFI) of FITC (cytokeratin) in RaNep cells was 3,362 and 5,893 for APC (EpCAM, **Appendix 10.3**).

Cells from the olfactory complex, namely RaOlf, RaNol and RaBulb, showed varying expression patterns of genes characteristic for cells found along the olfactory route. RaOlf exhibited expression of genes which are typical for olfactory ensheathing cells (OECs)[298], namely *S100B*, *NGFR*, *GFAP* and *CDHR1* (**Figure 4.3**). In RaNol cells, expression of *PAX6*, *GAD1*, *TPBG* and *CRHR1* could be detected, while *S100B*, *GFAP* and *CDHR1* were absent, which indicated granule cell-like identity (**Figure 4.3**). This further suggests that these cells are indeed different from RaOlf, despite derived from adjoining tissue. On the other hand, RaBulb cells expressed *GAD1*, *CALB1*, *CALB2*, *GAD2*, *NGFR*, *GABRB3*, *TBR1* and *CDHR1* (**Figure 4.3**), hinting towards periglomerular cell-like identity. As cells derived from the brain, precisely the cerebrum, the cellular identity of RaCer was determined with a completely different set of markers and revealed expression of *VIM*, *PAX6*, *GFAP*, *SLC1A3*, *CDH1*, *HES1* and *HES5*, specific for radial glia-like cells (**Figure 4.3**).

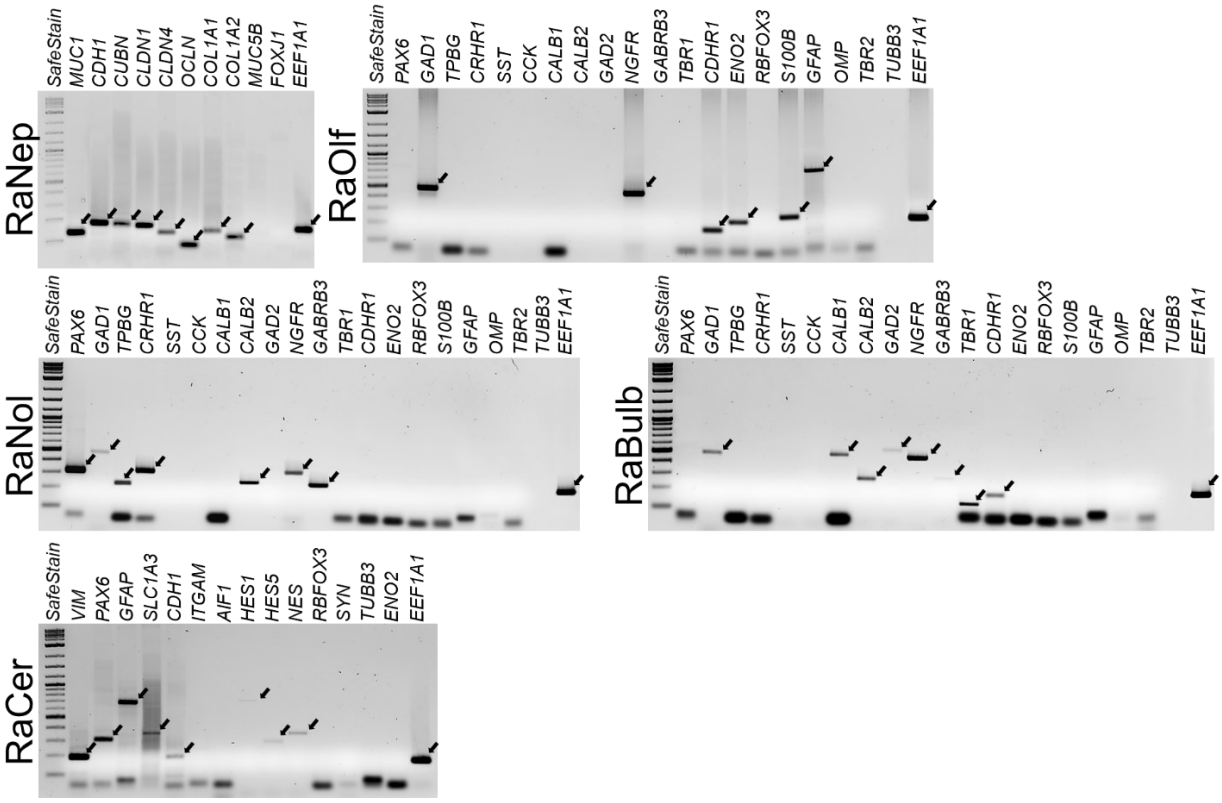

Figure 4.3 | Expression patterns of lineage markers enables definition of cellular identity.
Newly established cell lines were analysed in regard of expression of markers, specific for epithelial cells, cells from the olfactory system and the brain. PCR was carried out and amplicons were visualized on an 1.5% agarose gel. Correct bands are indicated with bold arrows, unlabelled bands originate from primer dimers.

4.1.2 Viability of novel ERB cell lines at temperatures relevant in chiropteran physiology

To take the unique physiological traits of bats into account, the newly established cell lines were incubated at temperatures matching the body core temperatures an adult ERB exhibits within 24h (**Figure 3.2**). These daily temperature oscillations range from up to 40°C during flight down to 35°C during roosting phases. The lowest (35°C, 5 h), as well as the highest (40°C, 9 h) and intermediate (39°C, 3 h) temperature recorded in the FLI captive breeding colony were selected. First, the viability of the cells at different temperatures was evaluated by determining metabolic activity (MTT test), LDH release, and apoptosis upon temperature oscillations (**Figure 4.4, Figure 4.5**). Since cellular oxidoreductases are able to reduce the tetrazolium dye MTT upon enzymatic activity[299], the intensity of reduced dye serves as readout for the amount of viable cells in a monolayer (**Figure 4.4, A**). Whether cells experienced disruption of the cell membrane in different temperatures was evaluated by the amount of free LDH in the medium (**Figure 4.4, B**). Necrosis results in the release of LDH into the surrounding environment[300]. It was evident, that viability of all newly established cell lines was not affected by both low or high temperatures, as metabolic activity remained intact and free LDH at a minimum (**Figure 4.4, B**). RaOlf was the only exception with significantly higher free LDH in the medium at 35°C compared to 40°C.

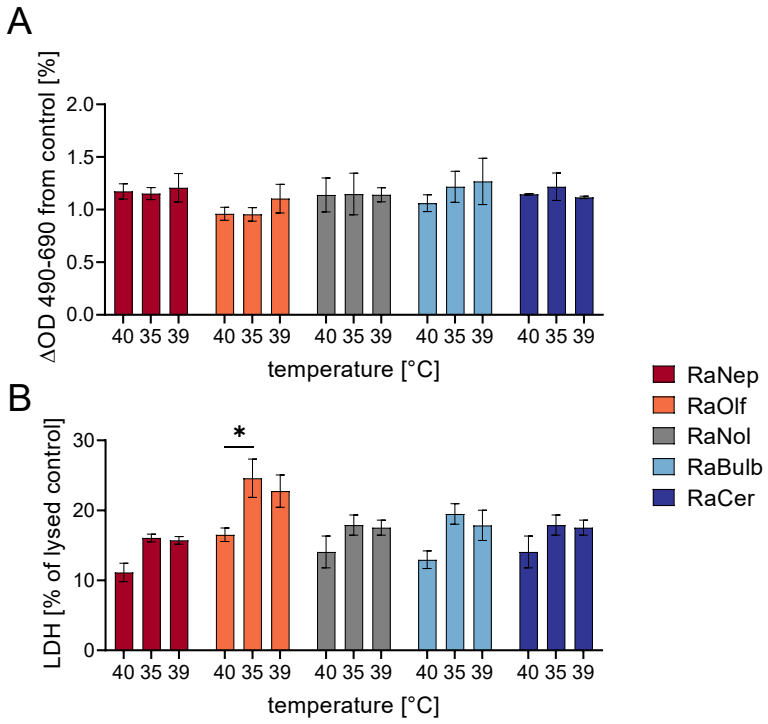

Figure 4.4 | Temperature oscillations minorly affect metabolic activity and membrane integrity of ERB cell lines.
To determine whether temperature oscillations, relevant for ERB physiology, impair cellular integrity, all cell lines were incubated at 40°C, 35°C, and 39°C. Metabolic activity was assessed by MTT test (**A**) and membrane integrity was determined via analysis of free LDH in supernatants, given as percent of lysed control cells (**B**). Statistical significance was determined by Two-Way-ANOVA with Holm- Šidák's post-hoc test, $P \leq 0.05$ (*), mean±SD of three independent experiments.

Apoptosis on the other hand is characterized by a well-coordinated chain of events, resulting in a complete shutdown of the cell, e.g. cleavage of DNA and shrinking of the cytoplasm[301]. Both early and later stages of apoptosis can be defined and separated from necrotic cells using an Annexin V/PI staining, since phosphatidylserine, a component located at the inner plasma membrane, is exposed on the outside surface, leading to the binding of Annexin V[302]. Annexin$^-$/PI$^-$ cells were defined as viable, Annexin+/PI- cells as early apoptotic, Annexin+/PI+ cells as late apoptotic, and Annexin-/PI+ cells as necrotic[303].

Apoptosis was evaluated upon incubation of cells at 35°C, 39°C and 40°C, compared to a control at 37°C (**Figure 4.5**). Early and late apoptotic cells stayed at negligible percentages, with the majority of cells remaining viable. An exception, RaOlf, turned out to exhibit apoptotic characteristics according to Annexin/PI staining, which supports findings from LDH assays (**Figure 4.4, B**), and growth curves at 37°C (**Figure 4.2, B**) and 40°C (**Appendix 10.6**). The growth pattern at 40°C revealed a slight curve shift, indicating slower growth of all cell lines at this temperature, which was supported by the doubling times:

56.14 h for RaNep, 60 h for RaOlf, 51.68 h for RaNol, 61.12 h for RaBulb and 53.75 h for RaCer (**Appendix 10.6, F**). Overall, RaNep, RaNol, RaBulb and RaCer were viable at 35°C, 39°C and 40°C with negligible apoptosis and necrosis rates. However, RaOlf showed slight apoptotic activity in all conditions tested.

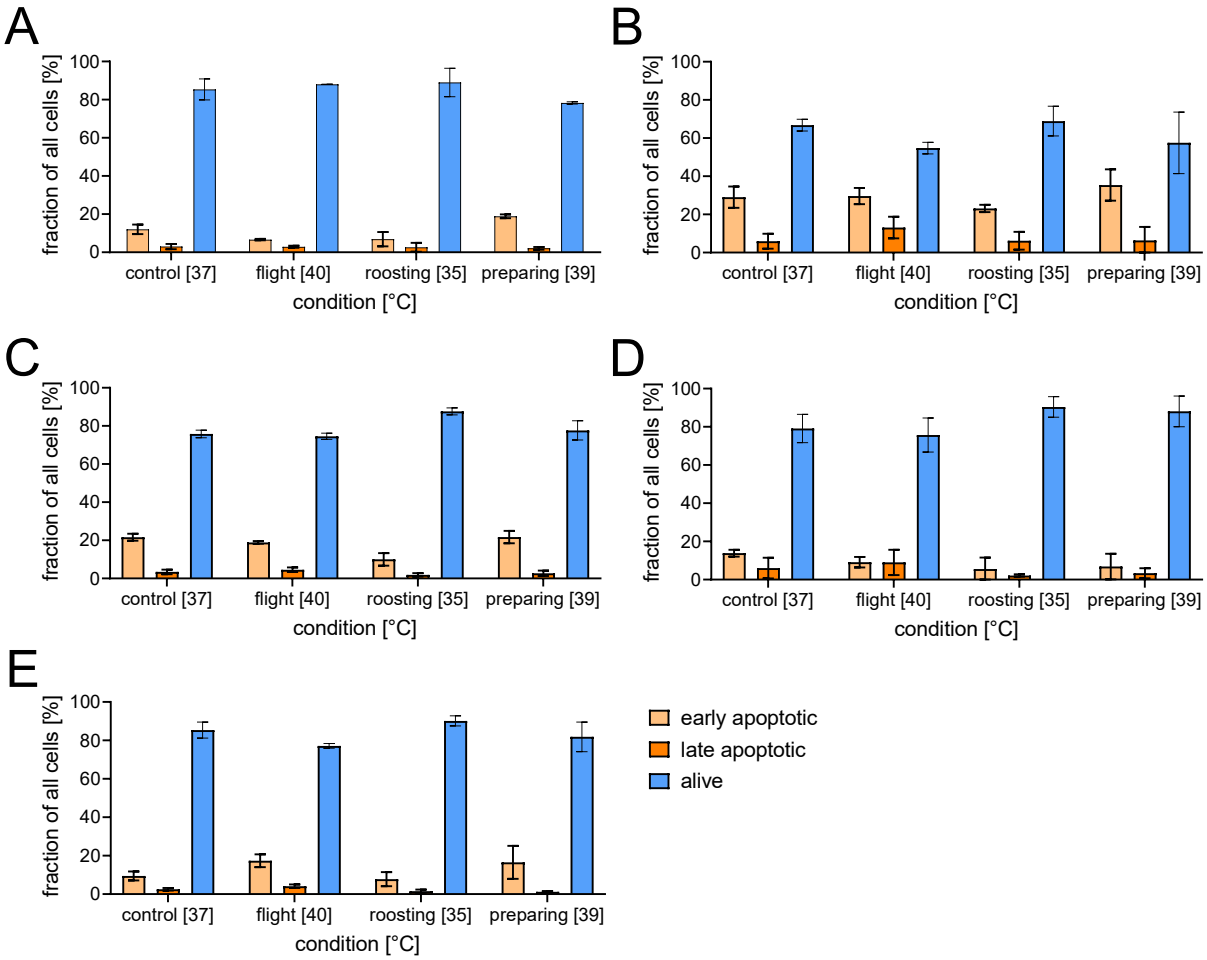

Figure 4.5 | Temperature oscillations do not induce apoptosis in ERB cell lines.
Apoptosis was monitored upon incubation at 40°C, 35°C and 39°C via Annexin V / PI staining in RaNep (**A**), RaOlf (**B**), RaNol (**C**), RaBulb (**D**), and RaCer (**E**). A control, incubated at standard conditions (37°C), was included as reference. Graph shows mean±SD of three independent experiments.

Considering the heterogenous morphology, growth patterns and expression of various markers, five unique cell types were successfully established to study bat innate immune responses *in vitro*. Cells from the nasal epithelium showed expression of tight junction markers and mucin, indicating epithelial identity. Despite being derived from adjoining tissue, three different cell types from the olfactory system could be successfully isolated and cultivated: olfactory ensheathing-like cells (RaOlf), granule-like cells (RaNol) and periglomerular-like cells (RaBulb). Radial glia-like cells were isolated from the ERB cerebrum (RaCer). All markers used to determine cellular identity are listed in Table 4.1. All

cell lines are viable upon incubation at ERB-specific temperatures, as determined by viability assays.

Table 4.1 | All markers examined to specify cellular identity. Successful detection is indicated in bold.

RaNep	RaOlf	RaNol	RaBulb	RaCer
MUC1	*PAX6*	***PAX6***	*PAX6*	***VIM***
CDH1	***GAD1/2***	***GAD1/2***	***GAD1/2***	***PAX6***
CUBN	*TPBG*	***TPBG***	*TPBG*	***GFAP***
CLDN1/4	*CRHR1*	***CRHR1***	*CRHR1*	***SLC1A3***
OCLN	*SST*	*SST*	*SST*	***CDH1***
COL1A1	*CCK*	*CCK*	*CCK*	*ITGAM*
COL1A2	*CALB1/2*	***CALB1/2***	***CALB1/2***	*AIF1*
MUC5B	***NGFR***	***NGFR***	***NGFR***	***HES1/5***
FOXJ1	*GABRB3*	*GABRB3*	*GABRB3*	***NES***
	TBR1	***TBR1***	***TBR1***	*RBFOX3*
	CDHR1	***CDHR1***	***CDHR1***	*SYN*
	ENO2	*ENO2*	*ENO2*	*TUBB3*
	RBFOX3	*RBFOX3*	*RBFOX3*	*ENO2*
	S100B	*S100B*	*S100B*	
	GFAP	*GFAP*	*GFAP*	
	OMP	*OMP*	*OMP*	
	TBR2	*TBR2*	*TBR2*	
	TUBB3	*TUBB3*	*TUBB3*	
epithelial cells	olfactory ensheathing cells	granule-like cells	periglomerular-like cells	radial glia-like cells

4.1.3 Generation and morphology of ERB primary epithelial cells of different origin

Four cell lines originating from the upper and lower respiratory as well as gastrointestinal tract of a juvenile ERB could be successfully established by Dr. Gang Pei, FLI. Epithelial cells were isolated from nasal epithelium (EpiNose), trachea (EpiTrachea), lung (EpiLung) and small intestine (EpiGut) and after adaptation to cell culture conditions, cells exhibited a robust proliferation. Having a cuboid and polygonal shape in a monolayer, all cells exhibited epithelial-like morphology and contact-dependent growth inhibition, except EpiGut (**Figure 4.6**). EpiNose and EpiGut were rather homogenous cells with cuboid structure, whit visible vacuoles in EpiNose cells. EpiTrachea and EpiLung were heterogenous with cuboid and spindle-shaped cells, but also visible vacuoles in EpiTrachea, especially (**Figure 4.6**). Since the cells were not separated by limited dilution, choleratoxin B was added to the culture medium to minimize growth of contaminating fibroblasts. All cultures were examined for expression of *FAP* to confirm absence of fibroblasts (**Appendix 10.14**). However, due to heterogeneity of the primary cell culture, *FAP* mRNA could be detected, but in considerably lower amounts than in bat fibroblasts, which were included as positive control.

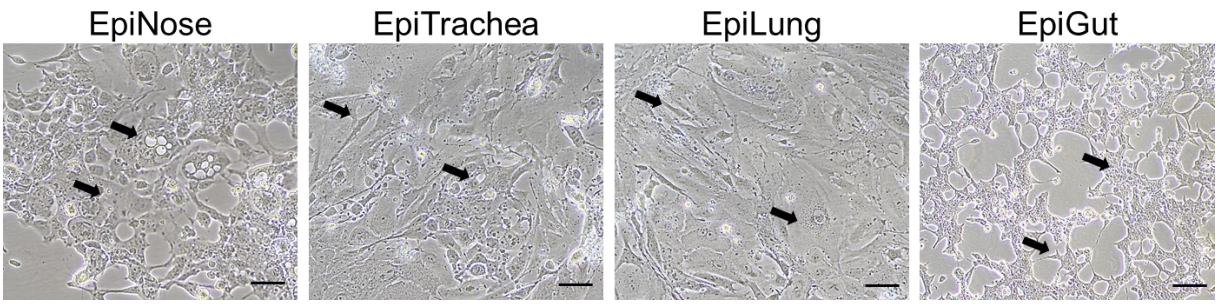

Figure 4.6 | Epithelial cells from various mucosal surfaces vary in morphology.
EpiNose and EpiGut displayed cuboid shapes while EpiNose exhibited vacuoles and EpiGut showed granules. EpiTrachea and EpiLung consist of a mixture of cuboid and spindle-shaped cells with visible vacuoles. Scale bar = 10 µm.

4.1.4 Expression of epithelia-related transcripts with and without differentiation

To confirm epithelial identity of all cell lines, expression of epithelia-associated transcripts was assessed by qRT-PCR. Since epithelial cells are known to change their properties upon cultivation in liquid-layered cultures[285,304], differentiation with RA was employed. Relative expression levels of *CDH1*, *CFTR*, *COL1*, *COL2*, *CUBN*, *OCLN*, *CLDN1*, *CLDN4*, *MUC1*, *MUC5B*, and *FOXJ1* were assessed in presence or absence of RA (**Figure 4.7**). All markers selected for verifying epithelial identity were expressed in all cells. Differentiation markers *MUC5B* and *FOXJ1* (mucin- and cilia-associated) were highly expressed after 2 weeks of RA treatment, further confirming the epithelial identity of the cells. As expression levels of specific markers did not allow concluding on homogeneity of cultures, EpCAM and cytokeratin expression was further evaluated by flow cytometry. Staining for both EpCAM and cytokeratin on live single epithelia cells demonstrated homogeneity of all epithelial cell cultures (**Appendix 10.2**). The mean percentage of cytokeratin expressing cells was lowest in EpiNose (85.2%) and highest in EpiTrachea (92.4%) (**Appendix 10.3, B**), which could be supported by MFI values (2,645 for EpiNose and 8,529 for EpiTrachea, **Appendix 10.3, A**). Additionally, the percentage of cells expressing EpCAM on the cell surface was lowest in EpiNose (88.9%) and again highest in EpiTrachea (95.9%). Interestingly, MFI values demonstrated that EpiNose exhibited the lowest signal intensity with a value of 4,202, while EpiGut had the highest with 6,289 (91.3% APC^+ cells).

Conclusively, four different primary epithelia cell lines were successfully generated. The cells originate from different mucosal surfaces and epithelial cell identity was confirmed by evaluation of lineage marker expression as well as staining of surface molecules.

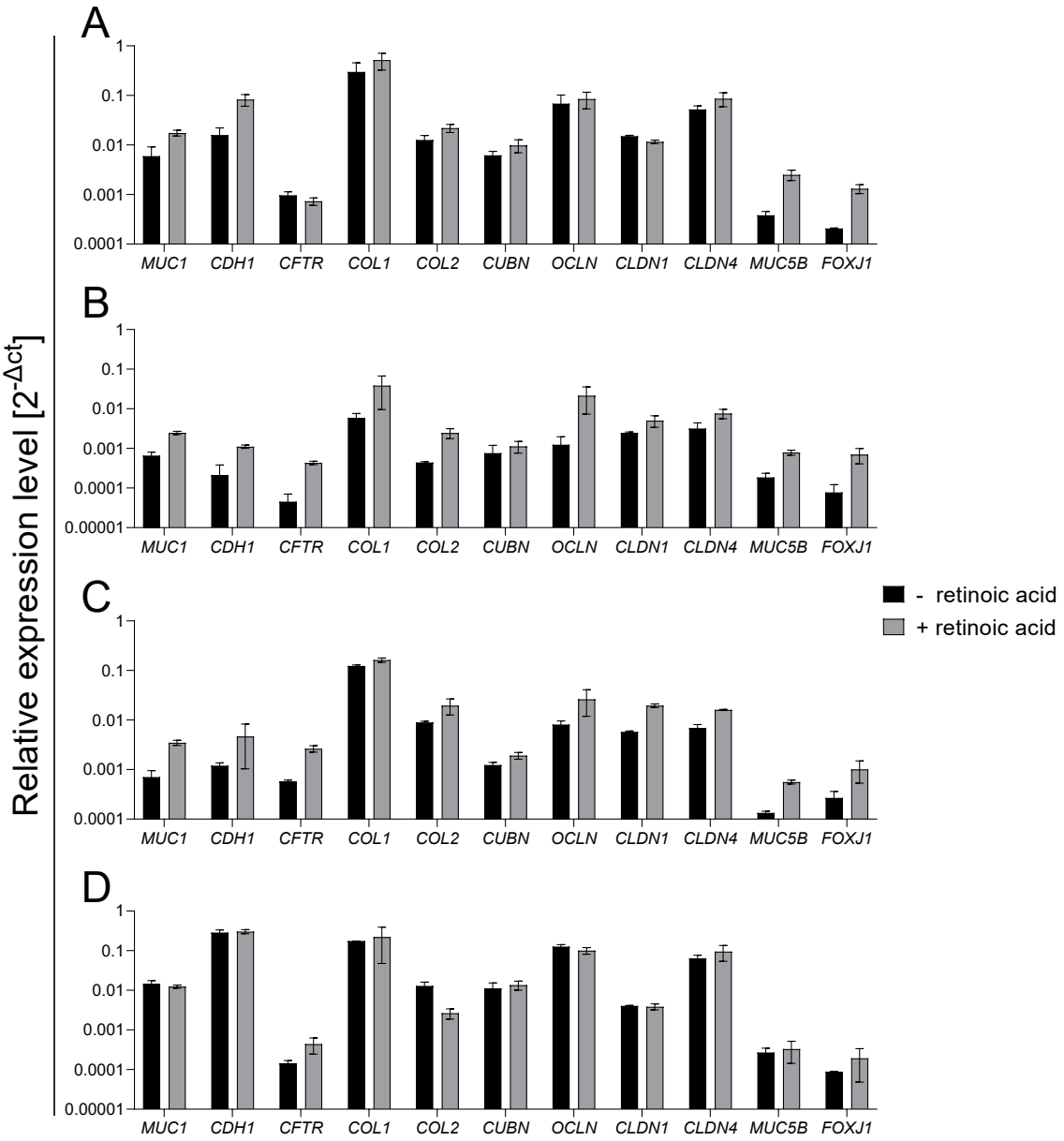

Figure 4.7 | Expression of epithelia-associated markers is enhanced by retinoic acid-dependent differentiation.

To verify epithelial identity of the established cells, the basal expression of epithelial lineage markers was quantified by qRT-PCR and normalized to *EEF1A1* expression. Expression levels were assessed in EpiNose (**A**), EpiTrachea (**B**), EpiLung (**C**), and EpiGut (**D**). Furthermore, integrity of epithelial cells was further determined by RA-induced differentiation. Graph shows mean of two independent experiments ± SD.

4.2 Innate immune responses of novel ERB cell lines to stimulation with PAMPs and viral infection

4.2.1 Selection of a stable reference gene to quantify immune-related transcripts in ERB cells and tissue

Selection of reference gene candidates was based on previous utilization in other bat species (*ACTB*[190,305], *GAPDH*[190,194]) as well as novel descriptions for superior candidates in mice and humans (*EEF1A1*, *PGK1*)[306,307]. Stability was assessed upon temperature change and in presence of universal IFN (uIFN) via qRT-PCR and algorithmic calculations. Data regarding tissue distribution of selected reference gene candidates was generated using samples derived from the IAV animal trial (Dr. Donata Hoffmann, PD Dr. Anne Balkema-Buschmann, FLI[308]).

4.2.1.1 Performance of primers to quantify reference gene candidate expression

Prior to stability analysis, verification of primer specificity in qRT-PCR assays was necessary. Therefore, amplicons were evaluated using melting curves, agarose gel electrophoresis and sequencing verification. Melting curve analysis resulted in one single peak for each reference gene candidate primer pair (**Appendix 10.7, A**). Agarose gel electrophoresis revealed a single band for each candidate, supporting melting curve results (**Appendix 10.7, B**). Sequencing of amplicons allowed verification of species-specificity by BLAST analysis and full-length homology to the corresponding sequence.

To confirm suitability in qRT-PCR assays, amplification efficiencies were evaluated by a standard curve, following 10-fold dilution steps. The linear dynamic range (LDR) as well as precision for each pair were assessed according to MIQE guidelines[30] (**Figure 4.8**). All included primer pairs were evaluated according to MIQE amplification efficiency criteria. Primer pair efficiency was 100.51% for *ACTB*, 99.53% for *EEF1A1*, 106.52% for *GAPDH* and 106.44% for *PGK1* (**Appendix 10.8**). Standard curves ranged from 3 to 300,000 copies and LDR values of all primer pairs tested varied from 0.31 for *EEF1A1* (lowest) to 1.27 for *ACTB* (highest, **Appendix 10.8**). Excellent linearity of each standard curve was demonstrated by the correlation coefficient (R^2), which was above 0.99 for all primer pairs tested. Hence, all selected primer pairs exhibited excellent specificity and efficiency in qRT-PCR assays.

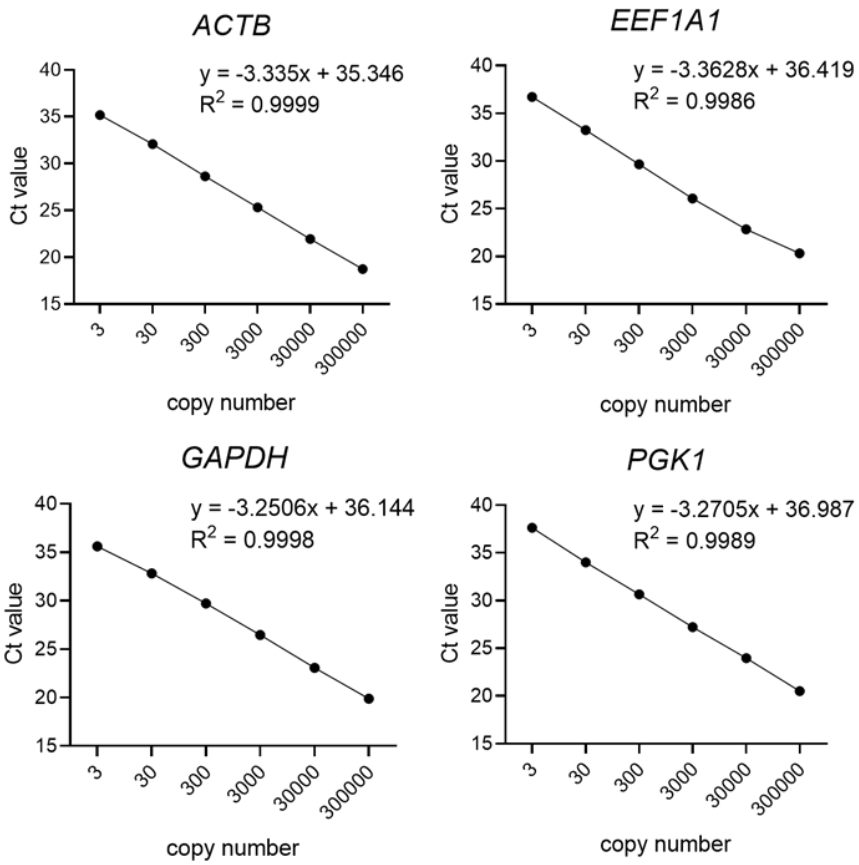

Figure 4.8 | Standard curves of selected ERB reference genes reveal optimal efficiency in qRT-PCR. Standard curves were generated ranging from 3 to 300,000 copies total. To determine efficiency (%), slopes and correlation coefficients (R2) were used.

4.2.1.2 Basal expression of reference gene candidates in various ERB tissues

To investigate the basal expression profile of selected reference gene candidates in tissues of ERB, cDNA of tissue lysates originating from 12 adult ERB were pooled. Basal gene expression was assessed in nose (nasal epithelium), trachea, lung, blood, spleen and duodenum via qRT-PCR. Expression levels of all candidates varied as shown by threshold cycles (Ct) values, whereas *EEF1A1* had the highest basal expression in all tissues tested. Overall Ct values were 33±3 for *ACTB*, 23±1.5 for *EEF1A1*, 27±2 for *GAPDH* and 27±1.5 for *PGK1*, respectively (**Figure 4.9**). Taken together, *EEF1A1* and *PGK1* had the lowest variation of Ct values, indicating a more homogenous expression in various tissues than *ACTB* and *GAPDH*.

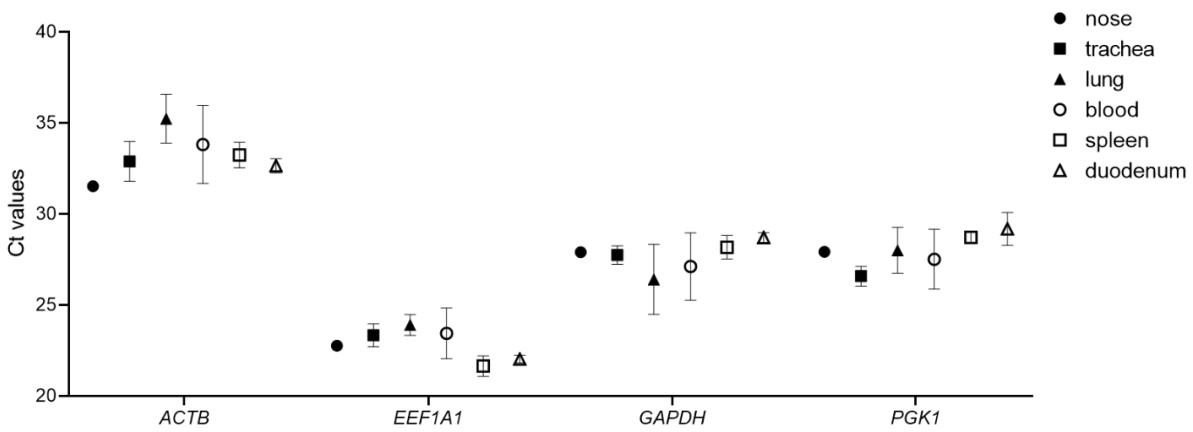

Figure 4.9 | Expression levels of selected reference genes are comparable in various ERB tissues. RNA was isolated from nasal epithelium, trachea, lung, blood, spleen and duodenum of 12 adult ERB. Prior to qRT-PCR, cDNA from individual ERB was pooled. Data represents three independent experiments as mean±SD.

4.2.1.3 Expression stability of reference gene candidates and IFN-dependent *GAPDH* expression in ERB fibroblasts upon IFN-I stimulation and temperature oscillations

After determining specificity and efficiency of primer pairs as well as tissue distribution of reference gene candidates, expression stability in conditions relevant for ERB physiology was determined. Thus, ERB primary fibroblasts were incubated at 35°C, 37°C or 40°C, with or without uIFN stimulation for 4 h. Furthermore, temperatures were selected based on ERB temperature profiles while roosting (35°C) and flying (40°C). Expression patterns of all reference gene candidates under these conditions were monitored by qRT-PCR (**Figure 4.10**). Ultimately, Ct values of *ACTB* and *GAPDH* showed broad variety. Expression of *ACTB* varied greatly in high temperatures, precisely from 29.7 to 39.01 at 40°C. Contrastingly, Ct values of *ACTB* at 35°C were marginally lower with 31.5±0.7 compared to 33.5±1 at 37°C, implying unstable expression upon temperature oscillation (**Figure 4.10**). Opposingly, expression levels of *EEF1A1*, *GAPDH* and *PGK1* were stable at 35°C, 37°C and 40°C, indicating stability upon temperature change of these reference gene candidates.

Since uIFN can successfully activate type-I-IFN signalling in bats[31], it was employed to monitor expression levels of reference gene candidates upon type-I-IFN stimulation. Interestingly, mean Ct values of *GAPDH* decreased significantly after stimulation, independent of temperature change (**Figure 4.10**), suggesting an expression increase of *GAPDH* mediated by IFN. Expression of *ACTB*, *EEF1A1* and *PGK1* was unaffected by uIFN

stimulation. However, only *EEF1A1* and *PGK1* expression was unaffected by both temperature oscillation and uIFN treatment (**Figure 4.10**). This highlights a stable expression of *EEF1A1* and *PGK1* in conditions which need to be considered in studies of chiropteran systems, while *ACTB* and *GAPDH* expression was unstable.

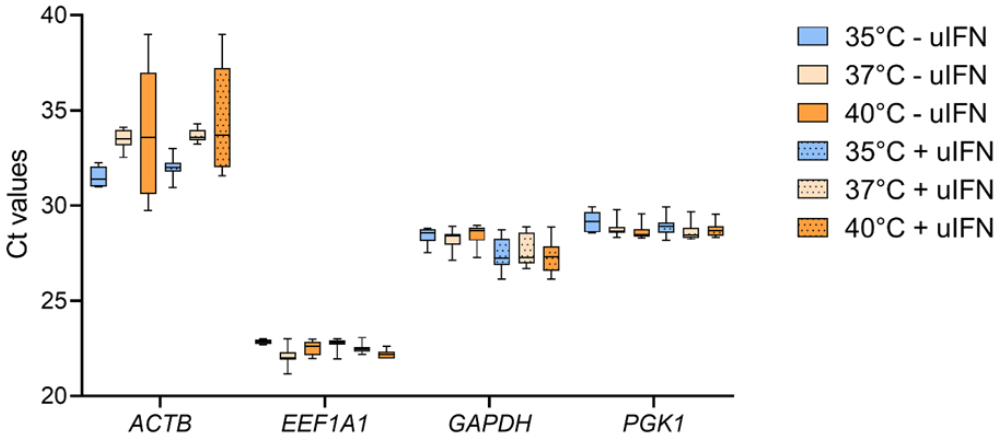

Figure 4.10 | Common reference genes are unstable in conditions relevant for ERB physiology.
ERB fibroblasts were incubated at 35°C, 37°C, and 40°C to mimic ERB body core temperature profiles. Expression levels of *ACTB*, *EEF1A1*, *GAPDH*, and *PGK1* in ERB fibroblasts. Furthermore, the cells were treated with 1,000 U/ml uIFN or PBS to assess IFN-dependent reference gene stability. Box plot depicts mean±SD of three independent experiments.

To further evaluate the stability of expression of *ACTB*, *EEF1A1*, *GAPDH* and *PGK1*, Ct values were subjected to statistical analysis with the algorithms BestKeeper and NormFinder. BestKeeper executes pairwise correlation, regression analysis[32,33] as well as calculation of standard deviations (SD) based on all Ct values [SD (± Ct)]. These factors in addition to the standard deviation of absolute regulation coefficients are used to precisely define expression variability [SD (± x-fold)]. According to BestKeeper, optimal reference gene display SD (± Ct) values of <1, SD (± x-fold) of <2 and correlation coefficients (*r*) of 1[34]. BestKeeper calculations resulted in [SD (± Ct)] values of 1.40 for *ACTB,* 0.34 for *EEF1A1*, 0.76 for *GAPDH* and 0.36 for *PGK1*. Corresponding *r*-values were 0.52, 0.96, 0.78 and 0.88, respectively (**Appendix 10.9**). A second algorithm, NormFinder was utilized as another readout for evaluating gene expression stability. NormFinder enables precise evaluation of overall stability (all conditions merged) as well as stability for each condition separately[35]. According to the NormFinder definition of stability, a reference gene is more stable the closer the corresponding stability value is to 0. Using this algorithm, the overall stability of *ACTB* was 0.097, 0.013 for *EEF1A1*, 0.05 for *GAPDH* and 0.015 for *PGK1* (**Appendix 10.9**). Furthermore, expression instability of *ACTB* upon temperature change as well as type-I-IFN-

associated instability of *GAPDH* expression has also been verified. Taken together, employment of these algorithms further demonstrated that *EEF1A1* displays highest expression stability in various conditions, followed by *PGK1*, while the expression of *ACTB* and *GAPDH* was affected by either temperature change or uIFN treatment.

To further analyse the previously observed effects of uIFN-dependent changes in *GAPDH* expression and temperature-dependent instability of *ACTB* expression, ERB primary fibroblasts were incubated in presence or absence of uIFN and varying temperatures for 1 h, 2 h and 4 h (**Appendix 10.10**). Expression of *ACTB*, *GAPDH* and *PGK1* was normalized to the most stable candidate, *EEF1A1*. Irrespective of temperature change or uIFN treatment, the expression of *PGK1* remained stable at all timepoints (**Appendix 10.10**). Relative expression of *ACTB* was overall stable upon uIFN treatment, but varied significantly between 35°C, 37°C, and 40°C upon 2h uIFN treatment in 40°C (**Appendix 10.10, C**). Intriguingly, relative expression levels of *GAPDH* were significantly increased upon uIFN treatment in all temperatures evaluated (**Appendix 10.10**).

To validate a bat-specific induction of *GAPDH*, human fibroblasts were stimulated with uIFN and incubated in ERB-related temperatures (**Appendix 10.11**). Since *GAPDH* and *ACTB* are frequently used as reference genes in human research[36,37], these genes were selected to compare reference gene stabilities between bats and humans. While both genes were stable at 37°C independent of uIFN treatment, high variations at 40°C have been observed, contrasting to ERB fibroblasts, indicating unstable expression of *GAPDH* upon 40°C stimulation. Unlike in ERB fibroblasts, *GAPDH* expression in human fibroblasts remained unchanged upon stimulation with uIFN in all selected temperatures (**Appendix 10.11, B**).

Stability analysis of *ACTB*, *EEF1A1*, *GAPDH* and *PGK1* revealed homogenous expression of all candidates in various ERB tissue, excellent specificity of primer pairs, and optimal efficiency in qRT-PCR assays. However, *ACTB* expression rendered unstable upon temperature oscillations, and *GAPDH* expression was significantly induced by uIFN. Since ERB putatively exhibits constitutive IFN expression and experiences daily temperature oscillations associated to flight and roosting[22,203], reference genes have to be stable at these physiologically relevant conditions. Both *EEF1A1* and *PGK1* showed exceptional homogeneity in tissue distribution, specificity of primer pairs as well as stability in all conditions tested.

4.2.2 Quantification of type-I- and III-IFN responses upon stimulation, infection, and temperature changes relevant for ERB physiology

After successful establishment of cell lines, expression kinetics and magnitudes of type-I- and III-IFNs was monitored using agonists for TLR3, RIG-I/MDA5, and cGAS to determine IFN capacity in these ERB cells. To ensure detection, basal expression of corresponding PRRs was analyzed. IFN expression upon stimulation and temperature oscillations was assessed at 4 h and 8 h after treatment. In a subsequent step, the susceptibility of the cell lines to different lyssaviruses, for which almost all known variants originate from bats[37-40] was determined. The analysis included two well-characterized lyssaviruses, the vaccine-strain SAD and the highly pathogenic RABV isolate Dog-Azerbaijan, which leads to high mortality in mice and other mammals[309]. EBLV-1 and LBV were of particular interest, as these viruses could solely be isolated from bats until now, but still pose the risk of spillover events in the future.

4.2.2.1 Expression levels of selected PRRs in immortalized ERB cell lines

Basal expression levels of PRRs, namely *MDA5*, *TLR3* and *RIG-I, TLR7,* and *TLR8* were assessed to confirm the expression of these PRRs which detect all viral mimetics used in this study: pI:C, pdA:dT, ISD, and Imiquimod/R848, activating TLR3, RIG-I/MDA5, and cGAS, respectively (**Figure 4.11**). While basal expression levels of *MDA5* were comparable amongst the cell lines, basal expression of *TLR3*, *RIG-I*, *TLR7* and *TLR8* differed. For *TLR3*, the relative expression level was highest in RaOlf and RaCer, while lowest in RaNol. The relative expression level of *RIG-I* was comparable amongst the cell lines with the exception of RaOlf, which displayed only minor basal expression (**Figure 4.11**). Regarding *TLR7* and *TLR8* expression levels both RaNol and RaBulb had the highest basal expression level, while RaNep and RaOlf had the lowest level of *TLR7*, expression levels of *TLR8* were low in all cell lines.

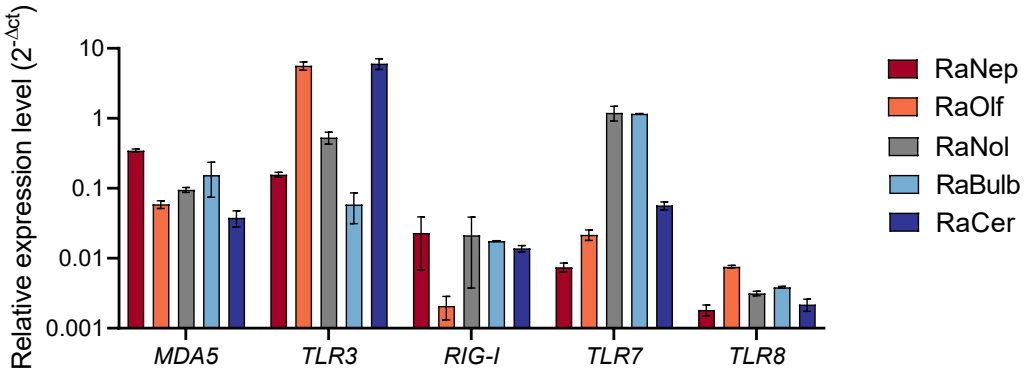

Figure 4.11 | Expression profile of selected PRRs in immortalized ERB cell lines.
Relative expression levels of *MDA5*, *TLR3*, *RIG-I*, *TLR7* and *TLR8* were assessed with qRT-PCR and subsequent normalization to *EEF1A1*. Results of three independent experiments are displayed as mean±SD.

To investigate the expression levels of PRRs in differentiated epithelial cells, RaNep cells were incubated in the presence or absence of 50 nM RA. This agent was included to further differentiate RaNep towards epithelial identity, since it is essential for differentiation and maintenance of the mucous phenotype of epithelial cells[310]. It has been reported that the properties of epithelial cells are altered upon cultivation in a 2-dimensional manner[304]. To circumvent possible changes in PRR expression due to the lack of further differentiation, relative expression levels of selected PRRs were monitored upon differentiation (**Figure 4.12**). This comparison revealed that differentiation with RA does not affect the basal expression level of PRRs in RaNep, which were therefore cultured under same conditions like all other ERB cell lines to minimize cultivation-driven deviations.

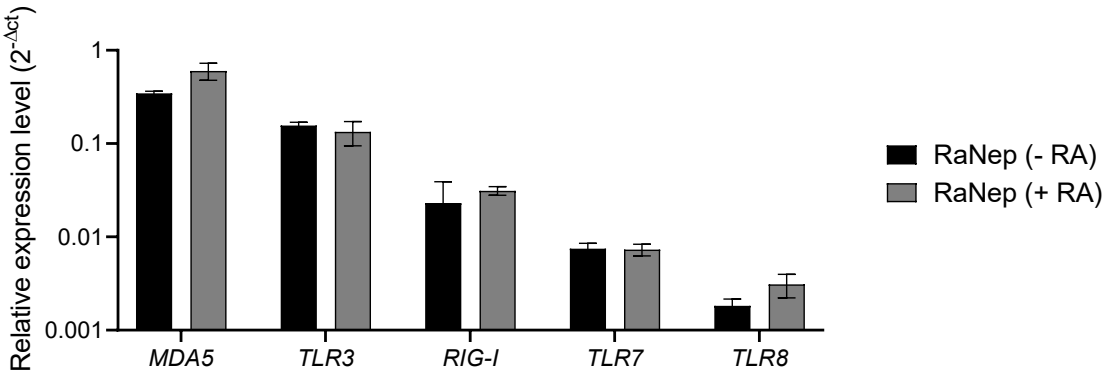

Figure 4.12 | Basal expression levels of selected PRRs upon differentiation in RaNep.
RaNep cells were differentiated with 50 nm RA for 7 days and basal expression of selected PRRs was monitored by qRT-PCR. Bars represent mean±SD of two independent experiments.

4.2.2.2 Verification of dampening effect of excessive passaging on IFN capacities

Properties of immortalized cell lines can change over passaging and IFN responses could be affected[311,312]. To evaluate such modifications, *IFNA1*, *IFNB1* and *IFNL* expression was assessed in all cell lines upon different stages of passaging. As expected, all cell lines were impaired in their ability to express type-I- and III-IFNs after sequential passaging 15-40x, compared to passages 1-10 (**Figure 4.13**). Expression of *IFNA1* was significantly decreased upon passaging in all cell lines (**Figure 4.13, A**), *IFNB1* expression capacity was significantly impaired in RaNep, RaOlf, and RaCer (**Figure 4.13, B**). Since *IFNL* expression was only detected in RaNep, RaOlf, and RaCer, statistical significance was solely evaluated in these cells, which rendered positive results for RaNep and RaOlf (**Figure 4.13, C**). These findings demonstrated the necessity to solely use low-passage cells for IFN-related studies *in vitro* and supported continuation of all further experiments with cells under passage 11.

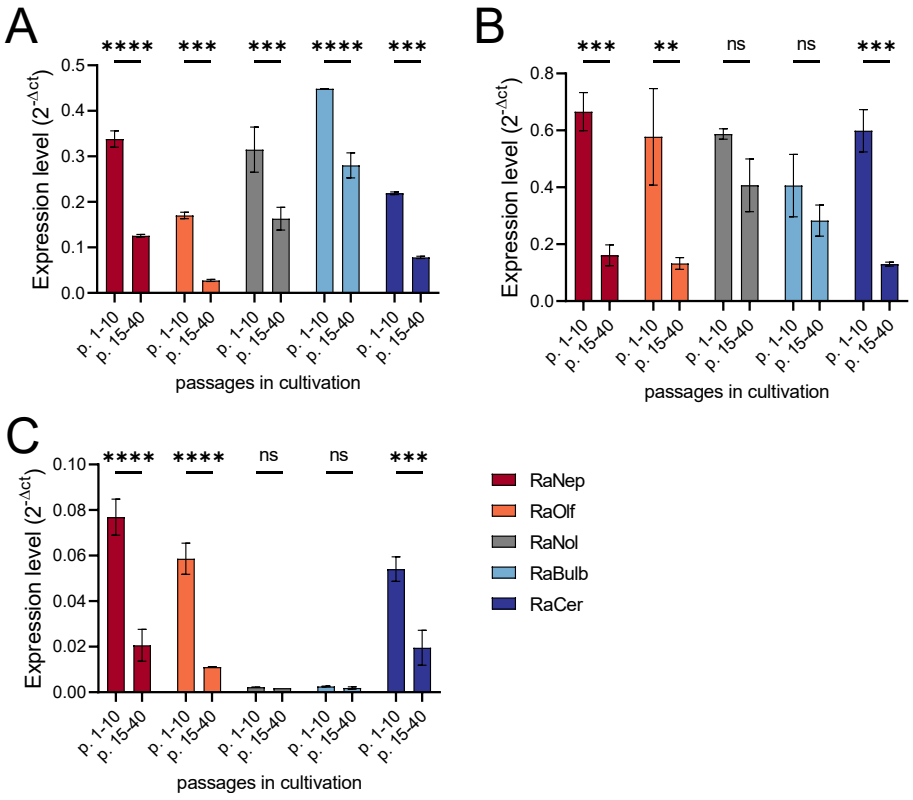

Figure 4.13 | Dampening effects of continuous passaging on IFN expression in ERB cells.
Expression levels of *IFNA1* (**A**), *IFNB1* (**B**), and *IFNL* (**C**) were assessed after stimulation with pI:C for 4 h by qRT-PCR and normalized to *EEF1A1* expression. All cells were passaged 1x, 5x, 10x and data was summarized. Further passaging for 15, 20, 25, 35, and 40 passages was summarized and compared to early passaging stages. Results of three technical replicates are displayed as mean±SD. Statistical significance was calculated with Two-Way ANOVA and Holm-Šidák's post-hoc test. (**) $P \leq 0.01$, (***) $P \leq 0.001$, (****) $P \leq 0.0001$.

4.2.2.3 Temperature-dependent expression of type-I- and III-IFNs

Since genes of type-I- and III-IFNs in bats tend to have a higher GC content than orthologs of other species and newly established primer pairs used in RT-qPCR needed to follow MIQE guidelines[313], validation of efficiency of all primer pairs subsequently used for IFN detection was critical (**Appendix 10.12, A**). Efficiencies were calculated according to the standard curve slope and the efficiency of all primer pairs were 88% to 121% in detecting their respective target. ActD treatment validated the general efficiency of the qRT-PCR setup, as demonstrated by *IFNA1* expression in pI:C treated RaNep cells (**Appendix 10.12, B**).

Stimulation of the cells with pI:C and pdA:dT resulted in upregulation of *IFNA1* and *IFNB1* in all cell lines as early as 4 h post stimulation (**Figure 4.14, A, B**). Strikingly, the expression level of *IFNA1* was significantly higher upon incubation at 40°C compared to 37°C in RaNep, RaOlf and RaCer (**Figure 4.14, A**). For *IFNB1*, only pI:C stimulation resulted in a significant difference of expression between 40°C and 37°C in RaNep and RaCer (**Figure 4.14, B**). Unlike *IFNA1* and *IFNB1*, *IFNL* expression is strictly tissue-specific[314] and was only induced in RaNep, RaOlf and RaCer upon stimulation with pI:C and pdA:dT (**Figure 4.14, C**). Interestingly, although derived from neuronal tissue, RaCer also highly upregulated *IFNL* expression after stimulation and even showed the highest significance in temperature-related differences. For all cell lines and temperatures, stimulation with ISD did not induce *IFNA1*, *IFNB1* nor *IFNL* expression. This is consistent with previous reports about dampened inflammasome activation in bats, where impaired sensing could be linked to hampered STING functionality, resulting of an amino acid exchange[217].

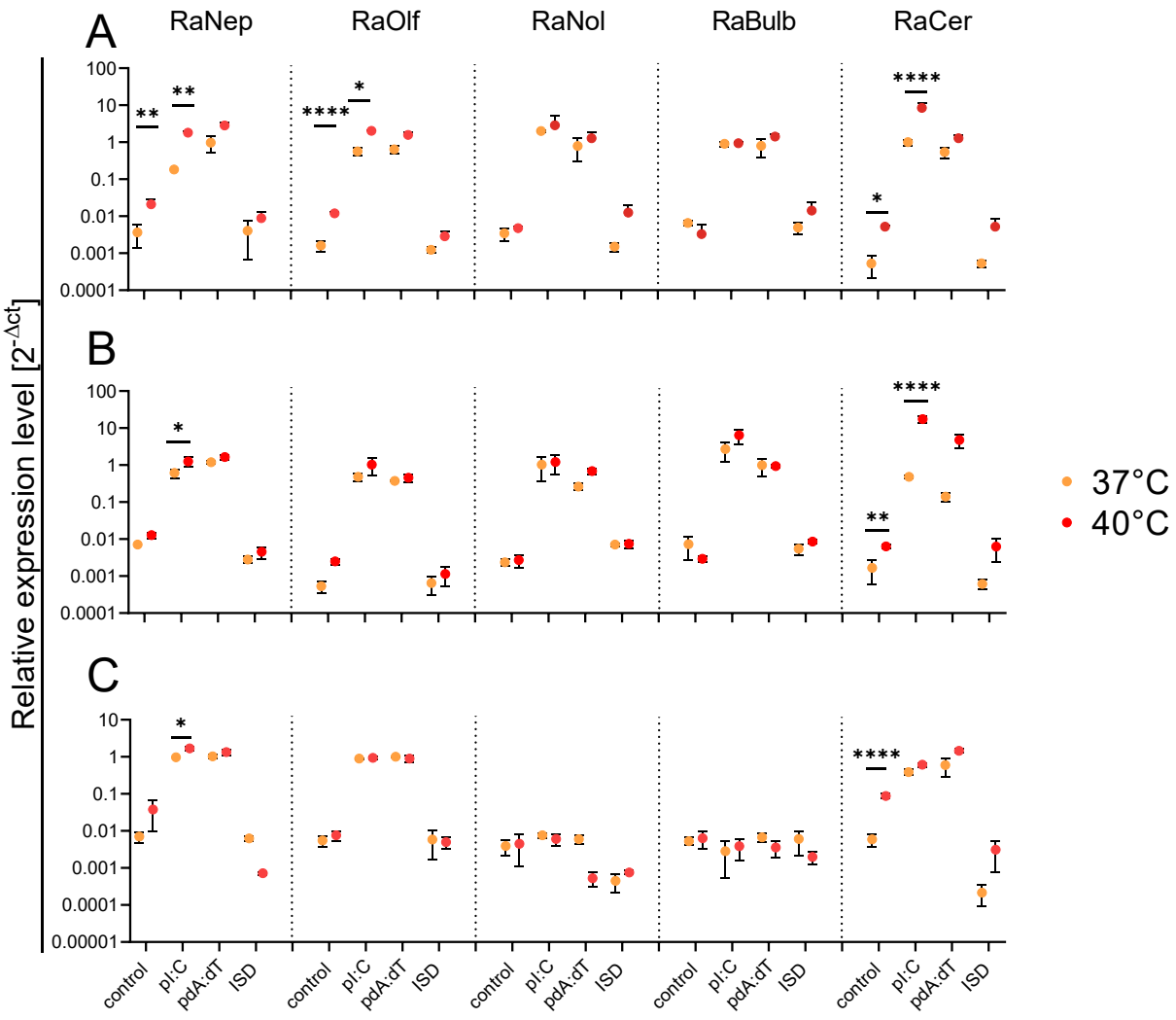

Figure 4.14 | Expression of type-I- and III-IFNs is elevated upon temperature increase in ERB cell lines.
Relative expression of *IFNA1* (**A**), *IFNB1* (**B**), and *IFNL* (**C**) normalized to *EEF1A1* upon stimulation with indicated viral mimetics for 4 h. Expression data was generated with qRT-PCR. All cells lines were stimulated with either pI:C, pdA:dT, or ISD and incubated at 37°C and 40°C, respectively. Graph shows mean±SD of three independent experiments. Statistical significance was calculated with Two-Way ANOVA and Holm-Šidák's post-hoc test. (*) P≤0.05, (**) P≤0.01, (****) P≤0.0001.

The temperature-dependent effect was diminished upon increasing stimulation duration to 8 h and differences failed to reach statistical significance (**Figure 4.15**). While stimulation with viral mimetics resulted in upregulation of type-I- and III-IFN expression even after 8 h post stimulation, there was no significant difference between cells incubated at 37°C or 40°C. Similar to the expression levels detected at 4 h post stimulation, ISD treatment did not induce *IFNA1*, *IFNB1*, or *IFNL* upregulation even 8 h post stimulation (**Figure 4.15**). Interestingly, the significant increase of basal expression of *IFNA1*, *IFNB1* and *IFNL* observed at 40°C and 4 h was also diminished upon increasing the incubation time.

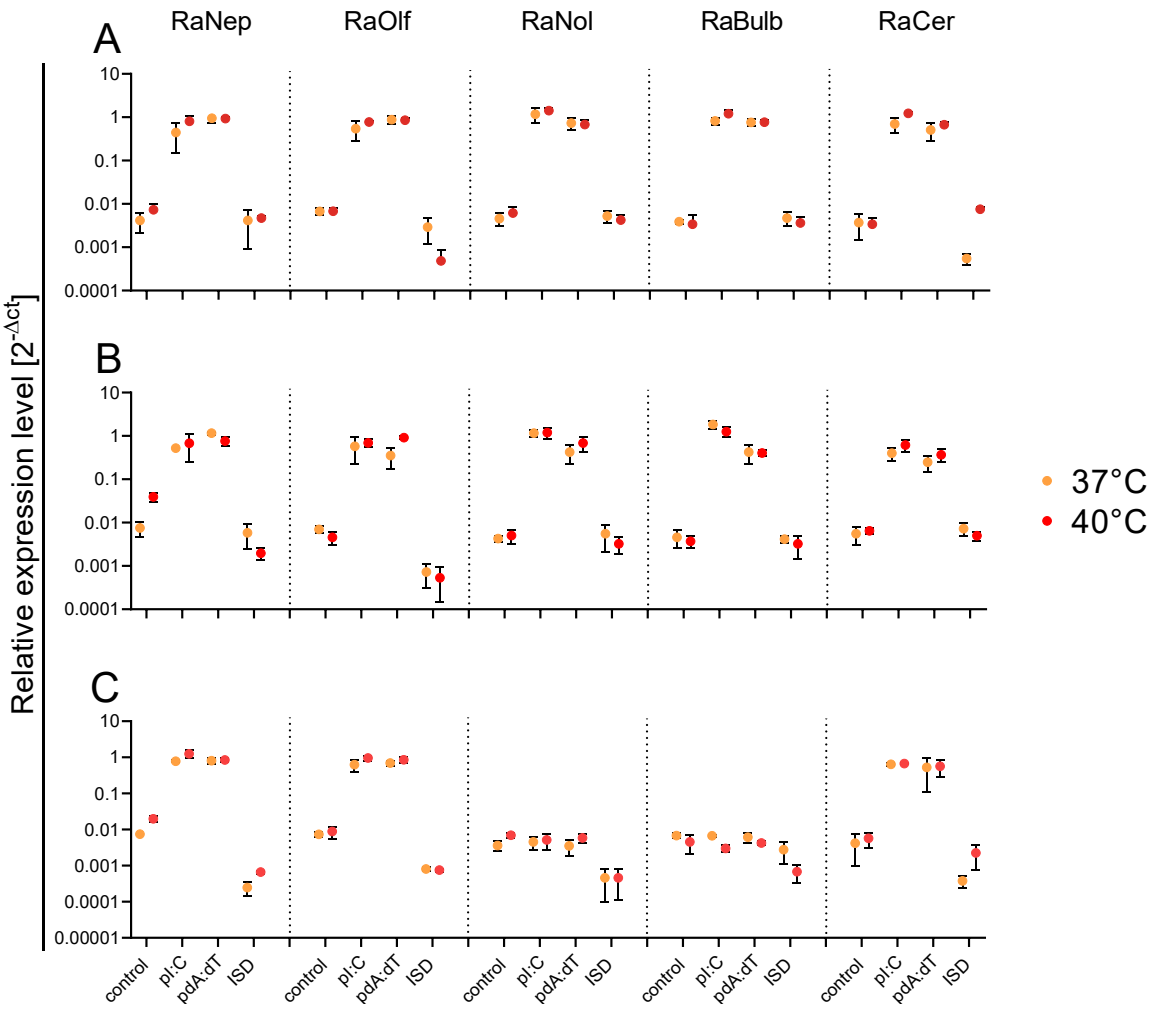

Figure 4.15 | Temperature-dependent elevation of type-I- and III-IFN expression is diminished over time.

Relative expression of *IFNA1* (**A**), *IFNB1* (**B**), and *IFNL* (**C**) normalized to *EEF1A1* upon stimulation with indicated viral mimetics for 8 h. Expression data was generated with qRT-PCR. All cell lines were stimulated with either pI:C, pdA:dT, or ISD and incubated at 37°C and 40°C, respectively. Graph shows mean±SD of three independent experiments.

4.2.2.4 Analysis of expression of various type-I- and III-IFNs in novel ERB cell lines

To assess kinetics of other type-I- and III-IFN genes found in the ERB genome, all cells were treated with pI:C or Imi/R848 (I/R) for 2 h, 4 h and 8 h, respectively (**Figure 4.16**). Ultimately, expression kinetics of *IFNA4*, *IFNE*, *IFNK*, *IFNW1* and *IFNW2* were monitored. It has been shown that the different members of the type-I-IFN family exhibit unique tissue and cell type specificities[315-317], as well as pathogen-dependent kinetics in multiple species[318]. Additionally, the *IFNW* locus is expanded in ERB[168], and therefore monitoring expression kinetics of other type-I-IFNs in the newly established cell lines was of particular interest.

Expression levels of *IFNA4*, *IFNE* and *IFNK* differed amongst cell lines derived from respiratory tissue (RaNep, RaOlf) and cell lines derived from neuronal tissue (RaNol, RaBulb, RaCer). Furthermore, *IFNA4* was primarily induced by pI:C rather than I/R in all cell lines, with the highest relative expression levels detected in RaNep, RaOlf and RaCer (**Figure 4.16, A**). For RaNep, RaNol, RaBulb and RaCer, *IFNA4* expression appeared as early as 2 h post treatment, peaked at 4 h, and declined at 8 h. However, the expression in RaOlf peaked at 8 h post treatment and could be first detected after 4 h rather than 2 h. The expression of *IFNE* was induced by both pI:C and I/R in a cell-specific manner (**Figure 4.16, B**). Only RaNol showed early induction at 2 h. In RaNep and RaBulb, the expression of *IFNE* occurred at 4 h and remained stable up to 8 h, while RaOlf and RaCer showed a delayed expression, peaking at 8 h. Only marginal *IFNK* expression could be observed in RaNol and RaCer, while RaBulb showed the highest time-dependent increase amongst cells derived from neuronal tissue (**Figure 4.16, C**). Induction of *IFNK* expression in RaNep occurred as early as 2h after treatment and peaked at 4 h, while I/R-dependent expression was highest at 8 h. For RaOlf, both pI:C and Imiquimod/R848 treatment resulted in the highest induction of *IFNK* expression at 4 h.

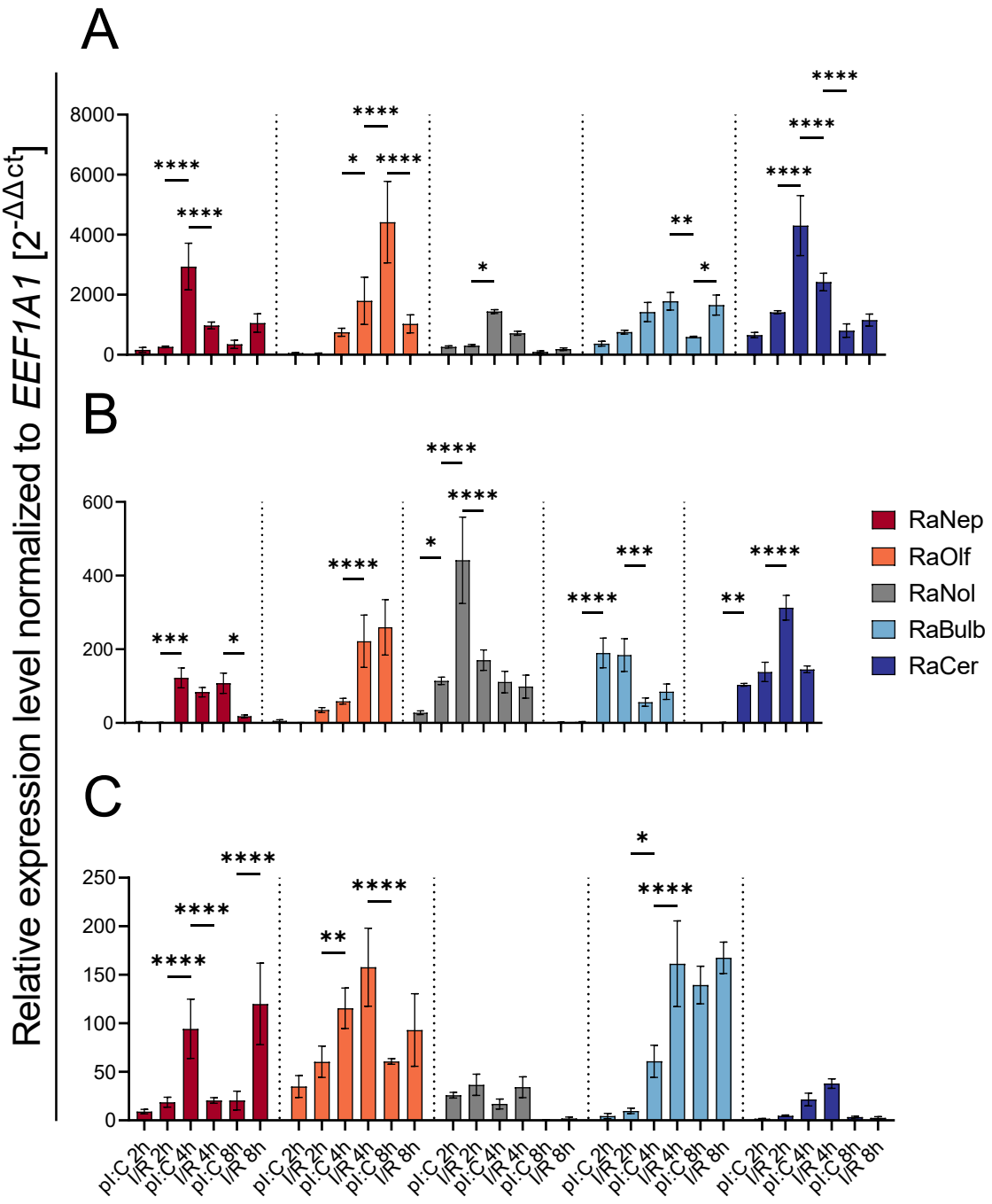

Figure 4.16 | Expression of distinct type-I-IFNs found in the ERB genome is cell type- and time-dependent.
Expression levels of *IFNA4* (**A**), *IFNE* (**B**) and *IFNK* (**C**) were determined by qRT-PCR and subsequent normalization to *EEF1A1* expression and a PBS-treated control. All cell lines were stimulated with either pI:C or Imiquimod/R848 and incubated at 37°C for 2 h, 4h, and 8 h, respectively. Graph shows mean±SD of three independent experiments. Statistical significance was calculated with One-Way ANOVA and Holm-Šidák's post-hoc test. (*) P≤0.05, (**) P≤0.01, (***) P≤0.001, (****) P≤0.0001.

Since the *IFNW*, especially *IFNW1,* locus is considerably expanded in the ERB genome[168] and different *IFNW* subtypes elicit diverse antiviral properties[167], *IFNW1* and *IFNW2* expression upon treatment with viral mimetics was examined (**Figure 4.17**). For all cell lines, relative *IFNW1* expression peaked at 4 h post treatment. RaNol and RaBulb showed early induction

at 2h (**Figure 4.17, A**). In contrast to *IFNW1* and all other type-I-IFNs evaluated, relative *IFNW2* expression peaked the earliest, at 2 h post treatment for both pI:C and I/R treatment (**Figure 4.17, B**).

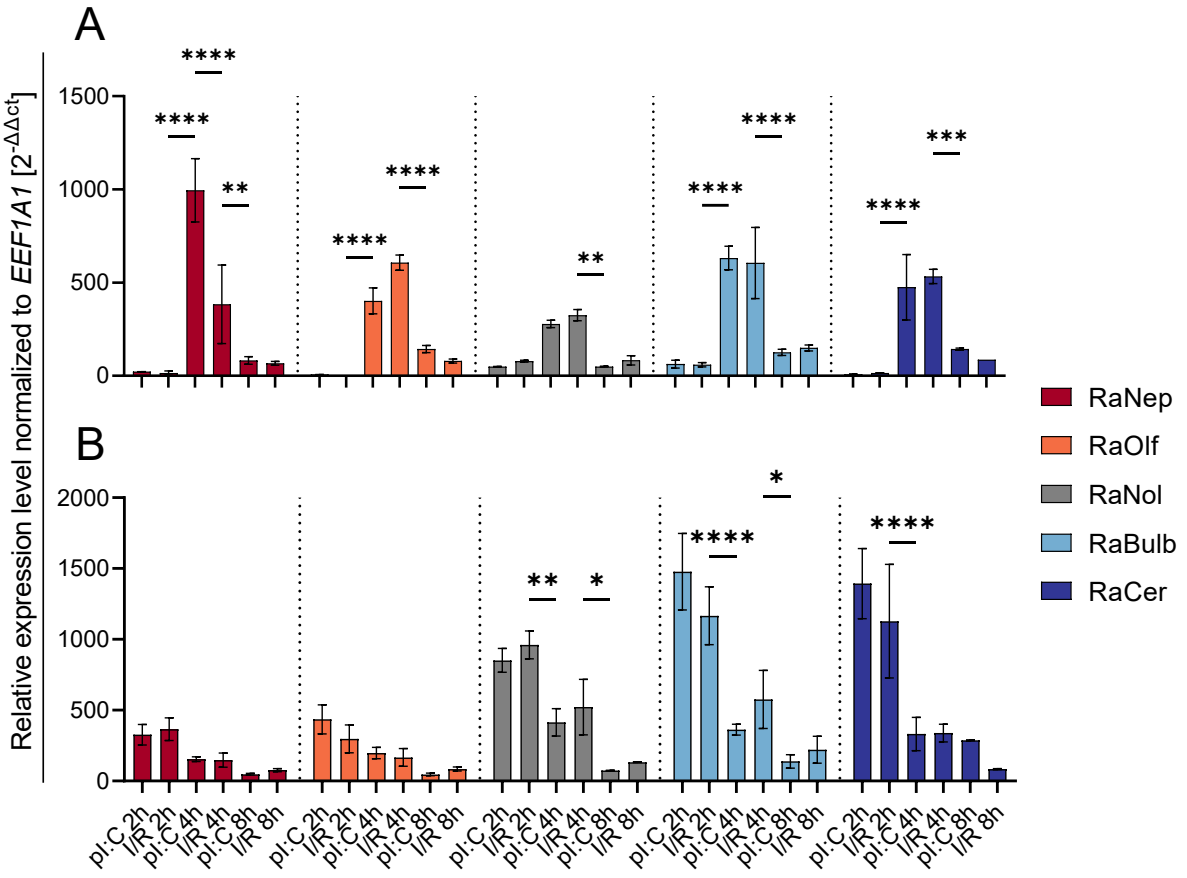

Figure 4.17 | Expression kinetics of *IFNW1* and *IFNW2* in ERB cell lines are cell type-dependent.
Expression levels of *IFNW1* (**A**) and *IFNW2* (**B**) were determined by qRT-PCR and subsequent normalization to *EEF1A1* expression and a PBS-treated control. All cell lines were stimulated with either pI:C or Imiquimod/R848 and incubated at 37°C for 2 h, 4 h, and 8 h, respectively. Graph shows mean±SD of three independent experiments. Statistical significance was calculated with One-Way ANOVA and Holm-Šidák's post-hoc test. (*) P≤0.05, (**) P≤0.01, (***) P≤0.001, (****) P≤0.0001.

4.2.2.5 Type-I- and III-IFNs are constitutively expressed in specific ERB cells

Basal *IFNA1*, *IFNB1* and *IFNL* expression could be observed in unstimulated controls at 37°C and 40°C (**Figure 4.14**). In addition, a temperature-dependent increase could be observed in RaNep, RaOlf and RaCer (**Figure 4.14**). To further validate constitutive IFN expression in unstimulated cells, absolute *IFNA1*, *IFNB1* and *IFNL* gene copy numbers were calculated by using a standard curve. Thus, qRT-PCR standard curves ranging from 3 to 300,000 copies in 10-fold dilution steps for these genes were generated (**Figure 4.18**).

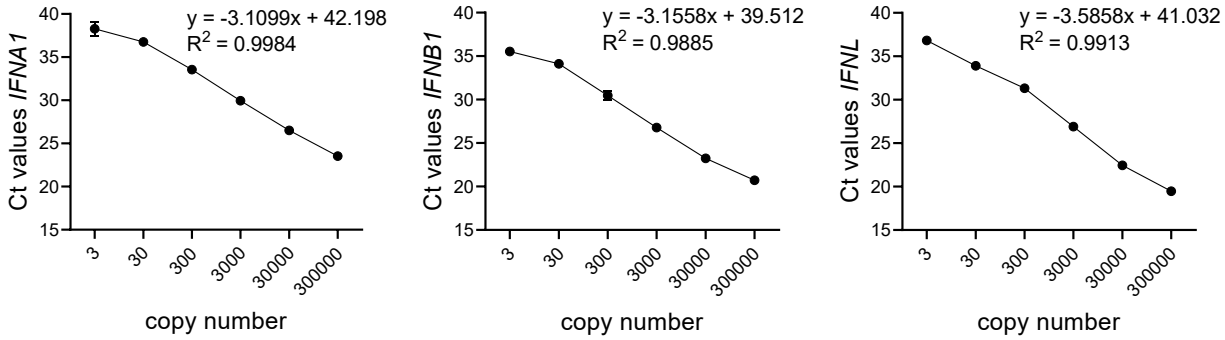

Figure 4.18 | Standard curves of *IFNA1*, *IFNB1* and *IFNL* allow calculation of exact copy numbers. Standard curves were generated ranging from 3 to 300,000 copies total. To determine efficiency (%), slopes and correlation coefficients (R2) were used.

Using the standard curves and the Ct-values of *IFNA1*, *IFNB1* and *IFNL* from unstimulated cells incubated at 37°C and 40°C, observations of relative expression levels overall matched absolute copy numbers (**Figure 4.19**). It could be confirmed that *IFNA1* copies increased in RaNep and RaOlf at 40°C, however, only data for RaOlf reached statistical significance. Copies of *IFNB1* significantly increased in RaNep, RaOlf, and RaCer, whereas differences in *IFNL* copy numbers failed to reach statistical significance for all cell lines (**Figure 4.19, A**). Furthermore, correlation of Ct values and exact copy numbers of *IFNA1*, *IFNB1*, and *IFNL* with high significance was verified (**Figure 4.19, B**).

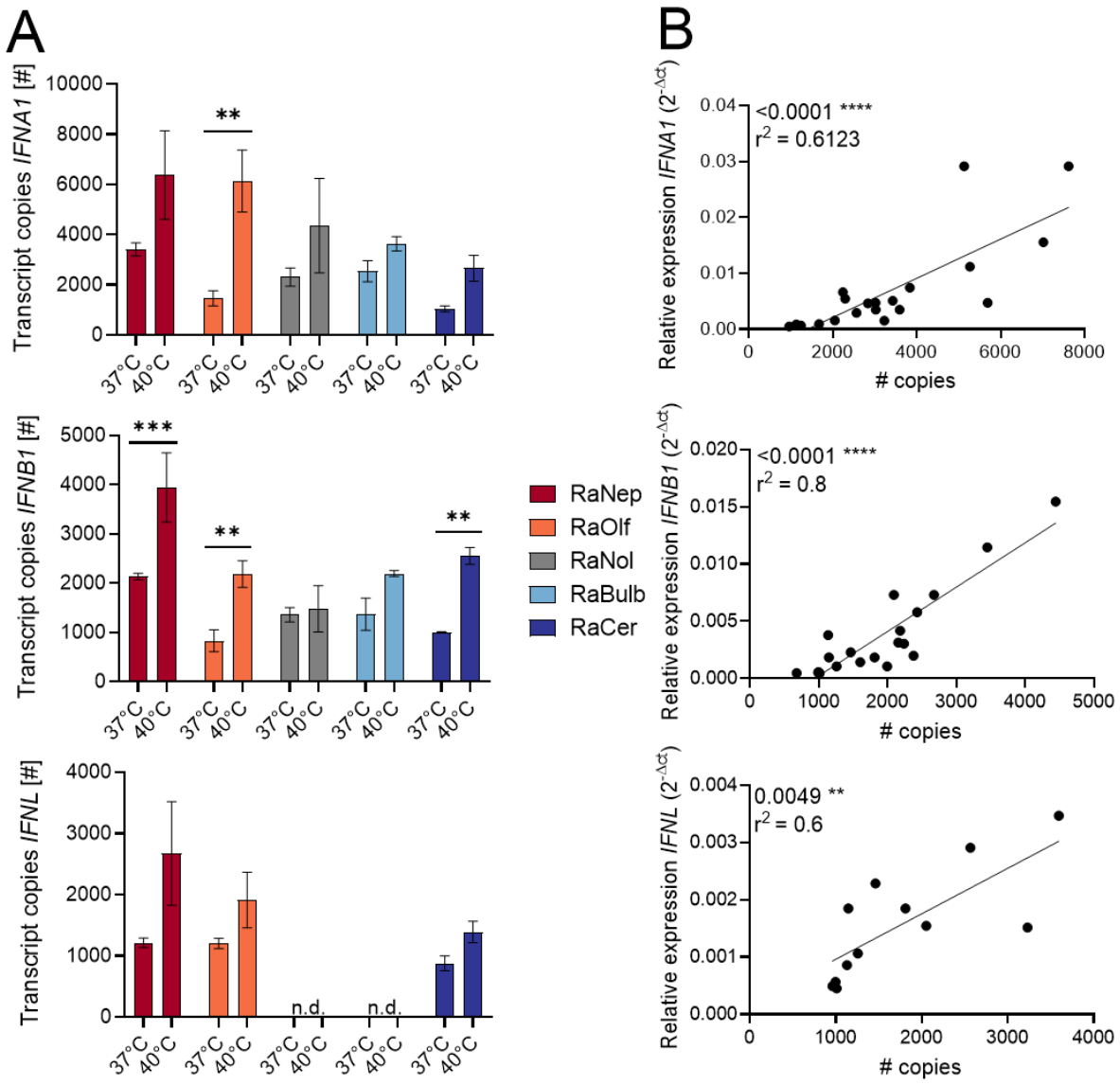

Figure 4.19 | Constitutive expression of type-I- and III-IFNs is elevated at higher temperatures in ERB cell lines.
Absolute mRNA copies (**A**) of *IFNA1*, *IFNB1* and *IFNL* were calculated upon incubation at 37°C and 40°C, respectively. Standard curves ranging from 3 to 300,000 copies were generated and enabled determination of exact IFN copy number. Calculation of correlation (**B**) between relative expression level (normalization to *EEF1A1*) and absolute mRNA amounts was carried out. Each qRT-PCR reaction was carried out using 100 ng cDNA. Results of three independent experiments are displayed as mean±SD. Statistical significance was calculated with Two-Way ANOVA and Holm-Šidák's post-hoc test. (**) P≤0.01, (***) P≤0.001.

In conclusion, the responsiveness of all five ERB cell lines to the viral mimetics pI:C, pdA:dT and I/R could be confirmed. The expression of both type-I-IFNs (*IFNA1*, *IFNA4*, *IFNE*, *IFNK*, *IFNW1*, *IFNW2*) and type-III-IFNs (*IFNL*) was upregulated in ERB cell lines. However, magnitude and kinetic of IFN expression varied between the different cell lines and *IFNL* expression was restricted to RaNep, RaOlf, and RaCer. Besides, kinetics of type-I-IFNs especially varied between the cell lines. Furthermore, constitutive expression of type-I- and III-IFNs in ERB cell lines could be confirmed, as well as elevated basal expression in higher

temperatures. Cells from the respiratory region (RaNep, RaOlf) and RaCer of neuronal origin exhibited elevated basal expression and induction at 40°C. Lastly, impairing effects of excessive passaging on the IFN capacity in all cell lines demonstrated the necessity of using cells of low passage for IFN-related studies *in vitro*.

4.2.2.6 Basal expression level of lyssavirus receptors in ERB cell lines

To ensure that the newly established cell lines could be infected with lyssaviruses, the basal expression level of known receptors for lyssavirus entry was assessed: neuronal cell adhesion molecule (*NCAM*), neuronal acetylcholine receptor subunit alpha-1 (*CHRNA1*), nerve growth factor receptor (*NGFR*) and glutamate metabotropic receptor 2 (*GRM2*), although the latter remains a matter of discussion[319]. Detection of *NGFR* was already carried out in section 4.1.2. to characterize cells originating from the ERB olfactory system, but not quantified. To determine whether the newly established cell lines express the receptors essential for lyssavirus entry, basal expression levels of all described lyssavirus receptors was assessed. Cells of olfactory and neuronal origin expressed *NGFR*, with comparable levels in RaBulb and RaCer, as well as RaNol and RaCer. Expression was lowest in RaNep, indicating tissue-specific distribution of *NGFR* in ERB. Interestingly, *NCAM* was highly expressed in RaNep. The basal expression of *CHRNA1* and *GRM2* was comparable for all cells derived from olfactory and neuronal tissue. Cells from the nasal epithelium expressed *GRM2* in similar amounts as all other cells, *CHRNA1* expression was lowest in RaNep. In conclusion, the ERB cell lines express lyssavirus receptors with different magnitude and therefore enable infection studies *in vitro*.

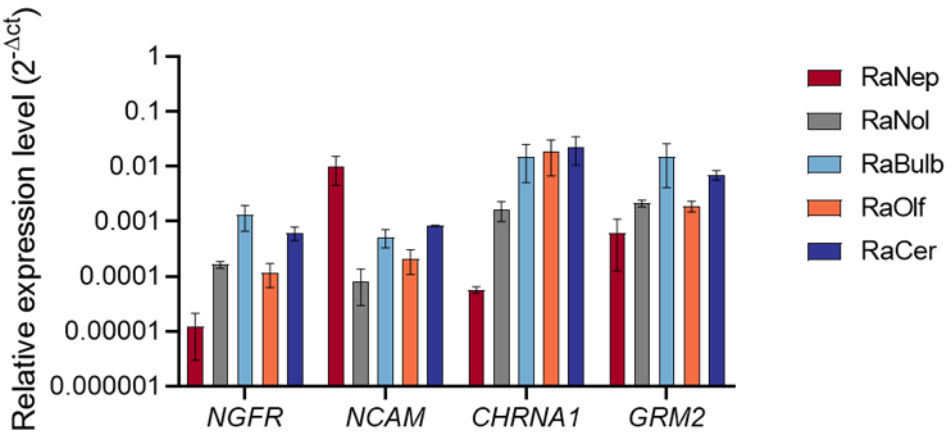

Figure 4.20 | Lyssavirus receptors are expressed in immortalized ERB cell lines.
The basal expression level of all described receptors was evaluated by qRT-PCR. Expression of receptors was normalized to *EEF1A1* expression to obtain relative expression levels. Results of three independent experiments are displayed as mean±SD.

4.2.2.7 Cell type-dependent susceptibility of immortalized ERB cell lines to various lyssaviruses

To determine the susceptibility of all ERB cell lines to different lyssaviruses, they infected with either RABV, SAD B19, EBLV-1, or LBV. Cell-dependent susceptibility of ERB cell lines to various lyssaviruses was observed. The highly pathogenic RABV field strain (Dog-Azerbaijan) could not successfully infect or replicate in the ERB cell lines (**Appendix 10.13**). To gain insight into the specific infectivity of different lyssaviruses in ERB cell lines, all viruses were titrated on each cell in 10-fold dilution steps to calculate the $TCID_{50}$ value (values in Table 4.2). For RABV, no $TCID_{50}$ value could be determined, due to abortive infection. The $TCID_{50}$ values for SAD B19 were 10^4 for RaOlf, 10^3 for RaNol, and $10^{2.75}$ for RaCer, with no detectable signal in RaNep and RaBulb cells. EBLV-1 was more successful in infecting the ERB cell lines, since $TCID_{50}$ values ranged from $10^{4.5}$ for RaOlf, 10^4 in RaNol, and 10^3 in RaBulb to 10^4 in RaCer. Strikingly, LBV turned out to be the only lyssavirus which could successfully infect and replicate in RaNep cells. Although of immediate bat origin, only LBV was able to mount active infection in RaNep, while EBLV-1 resulted in infected single cells only (**Appendix 10.13**). The $TCID_{50}$ values were high in all cell lines with $10^{6.25}$ in RaNep, $10^{7.75}$ in RaOlf, 10^8 in RaNol, 10^7 in RaBulb, and $10^{6.25}$ in RaCer. To conclude, the lyssavirus specific to African bats was most successful in infecting and replicating in ERB cell lines. In addition to calculating the $TCID_{50}$ as a value of specific infectivity, the amount

of infectious particles produced by infected ERB cells was determined after 16 h, 24 h, 48 h, and 72 h, respectively. Since RaNep cells showed the least and RaOlf the highest susceptibility to various lyssaviruses, these two cells were selected for the kinetic. Furthermore, RABV was excluded from further experiments due to poor infectivity *in vitro*. Supernatants were collected at indicated timepoints and titrated on a murine neuroblastoma cell line (N2a/13). The titration experiments were performed using previously calculated $TCID_{50}$ values as reference: LBV $10^{6.25}$ for RaNep and $10^{7.75}$ for RaOlf, EBLV-1 $10^{4.5}$ for RaOlf and SAD B19 10^{4} for RaOlf. Values of RaOlf were taken as reference for RaNep infection with SAD B19 and EBLV-1. Interestingly, although infection of RaNep with EBLV-1 and SAD B19 did not allow calculation of a $TCID_{50}$ value, titration of respective supernatants resulted in comparable titers of LBV, EBLV-1, and SAD B19 on N2a/13 cells (Table 4.2). Similar results could be observed after titration of RaOlf culture supernatants (Table 4.2). However, supernatants of both LBV infected RaNep and RaOlf cells contained the highest titers of infectious particles, although titers were generally higher in RaOlf culture supernatants. In addition, titers of infectious particles decreased in RaNep culture supernatants over time, whereas titers kept increasing in RaOlf supernatants (Table 4.2).

Table 4.2 | TCID50 values and titration results after lyssavirus infection in ERB cell lines. * = only infected single cells at lowest dilution, no $TCID_{50}$ calculated. Data derived from two independent experiments.

$TCID_{50}$ calculation	**RaNep**	**RaOlf**	**RaNol**	**RaBulb**	**RaCer**
RABV	*	*	*	*	*
EBLV-1	*	$10^{4.5}$	10^{4}	10^{3}	10^{4}
LBV	$10^{6.25}$	$10^{7.75}$	10^{8}	10^{7}	$10^{6.25}$
SAD B19	*	10^{4}	10^{3}	*	$10^{2.75}$

Titration	**RaNep**				**RaOlf**			
	16 h	24 h	48 h	72 h	16 h	24 h	48 h	72 h
EBLV-1	$10^{4.25}$	$10^{4.25}$	$10^{3.75}$	$10^{3.25}$	$10^{4.25}$	$10^{3.5}$	$10^{5.5}$	$10^{6.25}$
LBV	$10^{5.5}$	10^{6}	10^{5}	10^{5}	$10^{5.75}$	10^{6}	$10^{6.25}$	$10^{6.5}$
SAD B19	$10^{3.75}$	$10^{3.75}$	10^{3}	$10^{2.75}$	$10^{2.5}$	10^{3}	$10^{5.25}$	$10^{6.25}$

4.2.2.8 Type-I- and III-IFN expression patterns upon lyssavirus infection

To monitor type-I- and III-IFN responses in the least (RaNep) and most lyssavirus-susceptible (RaOlf) ERB cell line, the cells were infected with SAD B19, EBLV-1 and LBV. Cells treated with PBS served as negative control, while the positive control was transfected with 10 µg/ml pI:C for 4 h. Expression of *IFNA1* was significantly higher in RaNep (**Figure 4.21**, **A**) cells compared to RaOlf (**Figure 4.21, B**) after stimulation or infection with EBLV-1 or SAD B19. The pattern of *IFNB1* expression was similar to *IFNA1*, but only infection with EBLV-1 resulted in significant differences between RaNep and RaOlf. Expression of *IFNL* after stimulation with pI:C was higher in RaNep, whereas the expression levels were higher in RaOlf after infection with EBLV-1 or SAD B19. However, differences in *IFNL* expression failed to reach statistical significance. Strikingly, no expression of type-I- and III-IFNs could be detected in both RaNep and RaOlf after LBV infection.

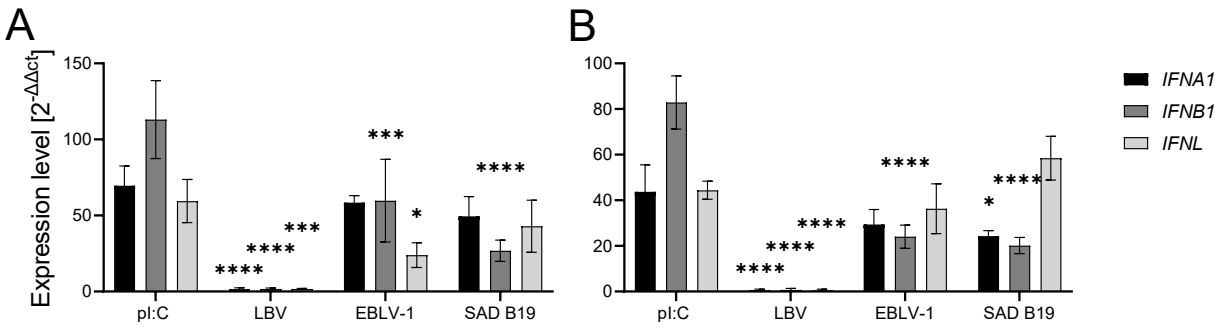

Figure 4.21 | Expression of type-I- and III-IFNs is impaired upon LBV infection in ERB cell lines. Expression of *IFNA1*, *IFNB1*, and *IFNL* was monitored in RaNep (**A**) and RaOlf (**B**) after infection with LBV, EBLV-1, and SAD B19. Stimulation with pI:C (4 h) was included as positive control, samples were collected 24 hpi. Expression levels were analysed by qRT-PCR and normalized to *EEF1A1* as well as an uninfected control. Graph shows mean±SD of three biological replicates. Statistical significance of expression to positive control (pI:C) was calculated with One-Way ANOVA and Holm-Šidák's post-hoc test. (*) $P \leq 0.05$, (***) $P \leq 0.001$, (****) $P \leq 0.0001$.

To conclude, it could be demonstrated that the newly established ERB cell lines show cell type-dependent differences in susceptibility to lyssaviruses. RABV infection did not result in satisfactory infection and no replication could be observed. Titration experiments to determine the specific infectivity of each virus rendered RaNep least susceptible, and RaOlf as the most susceptible. However, although both EBLV-1 and LBV are bat-specific lyssaviruses with zoonotic potential, differences in infectivity and replication rates could be observed. Isolated from European bats (*E. serotinus*)[320], EBLV-1 was more successful in infecting and replicating in ERB cell lines than RABV or SAD B16. However, as a lyssavirus

specific to African bats (*E. wahlbergi*[321], *E. helvum*[322]), LBV infection resulted in high amounts of infectious virions being released from infected RaNep and RaOlf cells. Differences in the infectivity of lyssaviruses and susceptibility of ERB cell lines is seemingly associated with IFN expression and bat-origin of the viruses.

4.2.3 Innate immune responses of ERB primary epithelia to SARS-CoV-2 and viral mimetics

ERB primary epithelia originating from nasal epithelium, trachea, lung and small intestine were established as an *in vitro* platform to study ERB-specific innate immunity and susceptibility to respiratory viruses, e.g. SARS-CoV-2. Early and late type-I- and III-IFN profiles were assessed upon stimulation with various PAMPs. Furthermore, expression of SARS-CoV-2 receptors angiotensin-converting enzyme 2 (*ACE2*)[323], transmembrane protease serine subtype 2 (*TMPRSS2*)[324], and neuropilin 1 (*NRP1*)[325] was quantified in all cells prior to subsequent infection with SARS-CoV-2 *in vitro*.

4.2.3.1 Temperature-dependent type-I- and III-IFN expression upon stimulation with viral mimetics

To gain insight into the IFN capacity of ERB primary epithelia and to confirm data gained using immortalized cell lines, cells derived from different mucosal sites were stimulated with pI:C, pdA:dT, and ISD for 4 h and 8 h, respectively. The unique physiology of ERB was taken into account by incubating stimulated and PBS-treated cells in 37°C and 40°C. The basal expression of *IFNA1*, *IFNB1,* and *IFNL* (as representatives of type-I- and III-IFNs) as well as expression upon stimulation in the context of temperature oscillations was monitored (**Figure 4.22**). Similar to what was observed for immortalized ERB cells from various tissues, basal expression of type-I- and III-IFNs differed in a cell type-dependent manner. Cells originating from the upper respiratory tract (EpiNose, EpiTrachea) displayed the most pronounced increase of basal and induced levels of *IFNA1* upon temperature rise (**Figure 4.22, A**). Interestingly, *IFNA1* expression in EpiGut was not affected by temperature increase. For *IFNB1*, basal expression in EpiNose, EpiTrachea, and EpiLung was elevated in higher temperatures, while levels of induced *IFNB1* remained mostly stable in different temperatures (**Figure 4.22, B**). The basal expression levels of *IFNB1* were, similar to *IFNA1* expression, most pronounced in cells from the upper respiratory tract. Expression of *IFNB1* in epithelial cells from the gastrointestinal (GI) tract was not affected by incubation at different temperatures. Basal expression of *IFNL* was slightly elevated in cells from the upper respiratory tract, whereas the difference failed to reach statistical significance (**Figure 4.22, C**). Levels of stimulation-induced *IFNL* was not affected by temperature oscillations in any of the epithelia cells. In conclusion, the temperature-dependent elevation

of basal and induced expression of type-I- and III-IFNs was most conspicuous in cells from the upper respiratory tract (EpiNose, EpiTrachea). In EpiLung, the effect was rather moderate, but not detectable in EpiGut.

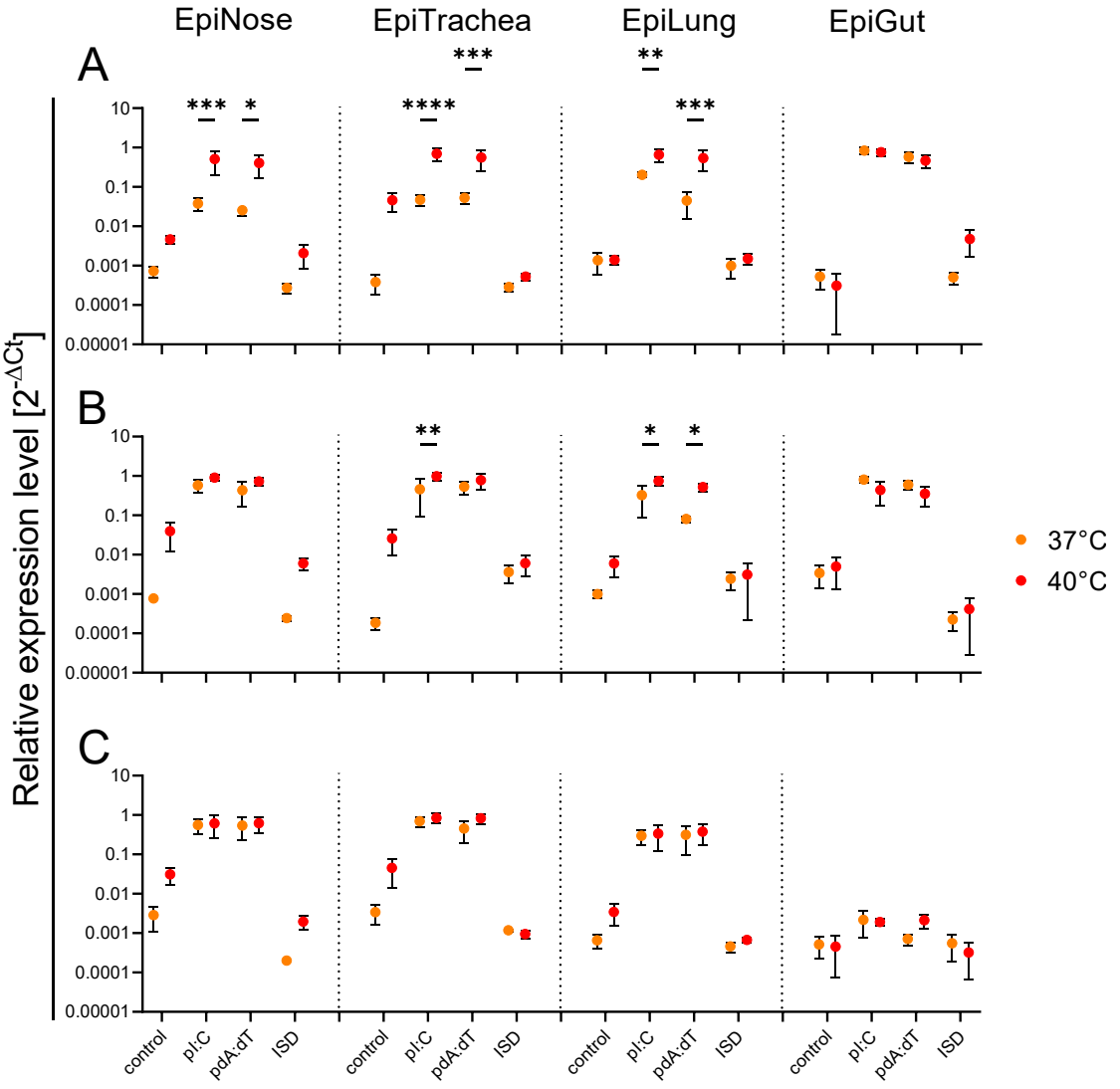

Figure 4.22 | Kinetics of basal and stimulus-induced type-I- and III-IFNs differ in primary ERB epithelia.
Relative expression of *IFNA1* (**A**), *IFNB1* (**B**) and *IFNL* (**C**) normalized to *EEF1A1* in primary ERB epithelia upon stimulation with indicated viral mimetics for 4 h. Expression data was generated with qRT-PCR. All cells were stimulated with either pI:C, pdA:dT, or ISD and incubated at 37°C and 40°C, respectively. Graph shows mean±SD of three independent experiments. Statistical significance was calculated with Two-Way ANOVA and Holm-Šidák's post-hoc test. (*) $P \leq 0.05$, (**) $P \leq 0.01$, (***) $P \leq 0.001$, (****) $P \leq 0.0001$.

To monitor both early and late type-I- and III-IFN kinetics, all cells were stimulated with pI:C, pdA:dT, and ISD and incubated at 37°C and 40°C. Overall, in accordance with data generated from immortalized ERB cell lines, the temperature-dependent effect was diminished upon longer incubation periods (**Figure 4.23**). While early (4 h) expression of type-I- and III-IFNs was elevated in higher temperatures, especially in cells from the upper

respiratory tract, only minor differences could be detected after 8h stimulation. Expression of *IFNA1* was significantly increased in EpiNose and EpiTrachea upon stimulation with pdA:dT and incubation at 40°C. Expression of *IFNB1* was overall elevated in higher temperatures after stimulation in EpiNose cells. Basal expression did not differ significantly between both temperatures in all cell lines, with exception of *IFNL* in EpiNose cells (**Figure 4.23**).

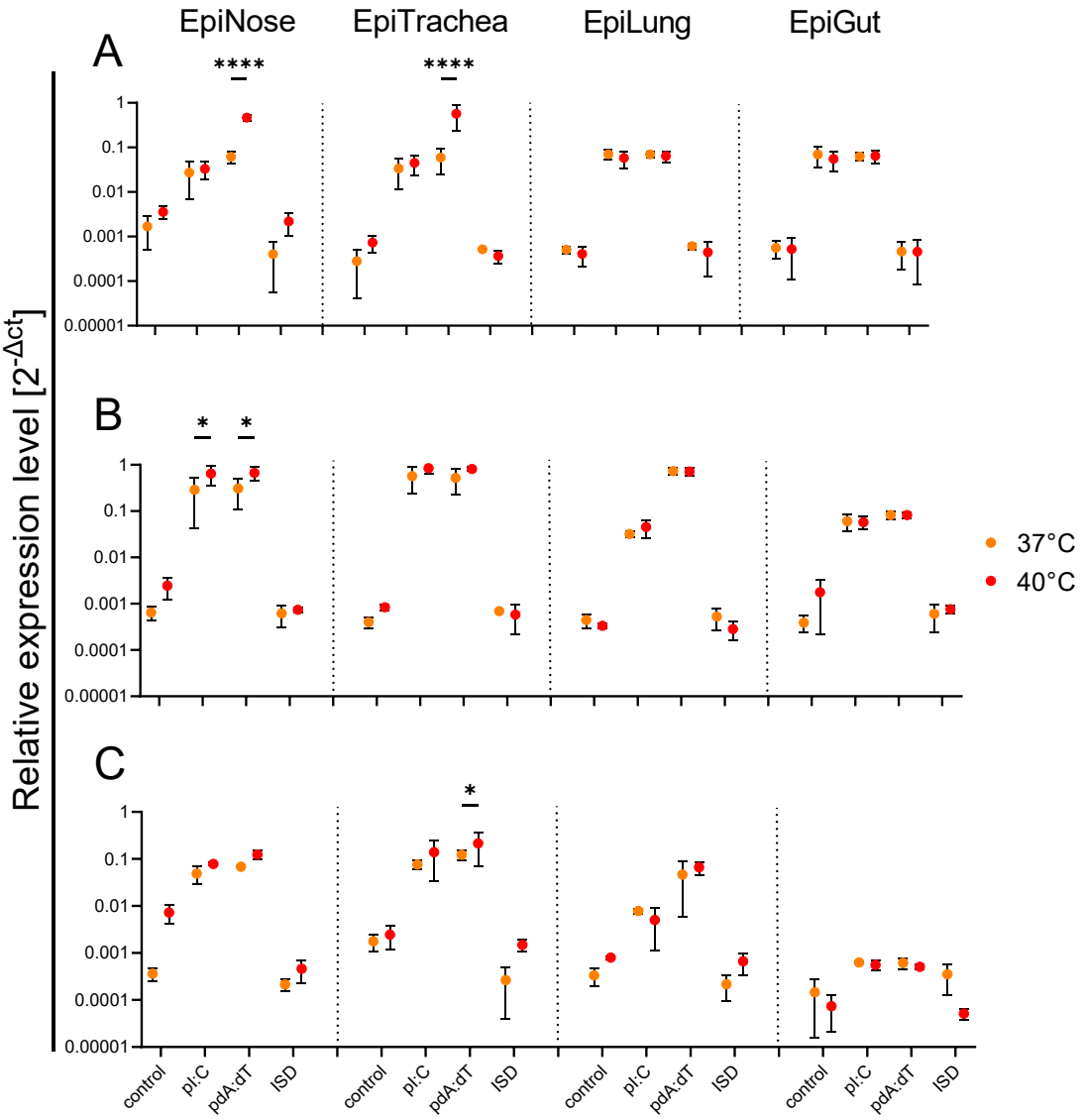

Figure 4.23 | Temperature-dependent increase in basal and induced type-I- and III-IFNs is diminished over time.

Relative expression of basal and induced *IFNA1* (**A**), *IFNB1* (**B**) and *IFNL* (**C**) normalized to *EEF1A1* upon stimulation with indicated viral mimetics for 8 h. Expression data was generated with qRT-PCR. All cells were stimulated with either pI:C, pdA:dT, or ISD and incubated at 37°C and 40°C, respectively. Graph shows mean±SD of three independent experiments. Statistical significance was calculated with Two-Way ANOVA and Holm-Šidák's post-hoc test. (*) $P \leq 0.05$, (****) $P \leq 0.0001$.

4.2.3.2 IFN-dependent variations in basal expression of CoV receptors

Three essential components for SARS-CoV-2 entry have been described to date: *ACE2*[323], *TMPRSS2*[324] and *NRP1*[325]. To ensure that all newly established ERB epithelial cells have the prerequisites for SARS-CoV-2 entry, the basal level of all three receptors was determined by qRT-PCR. While basal expression of *NRP1* did not differ amongst the cell lines, *ACE2* expression was comparable between EpiNose, EpiTrachea, and EpiGut, but low in EpiLung. Relative expression of *TMPRSS2* was similar in EpiTrachea and EpiLung, lowest in EpiGut.

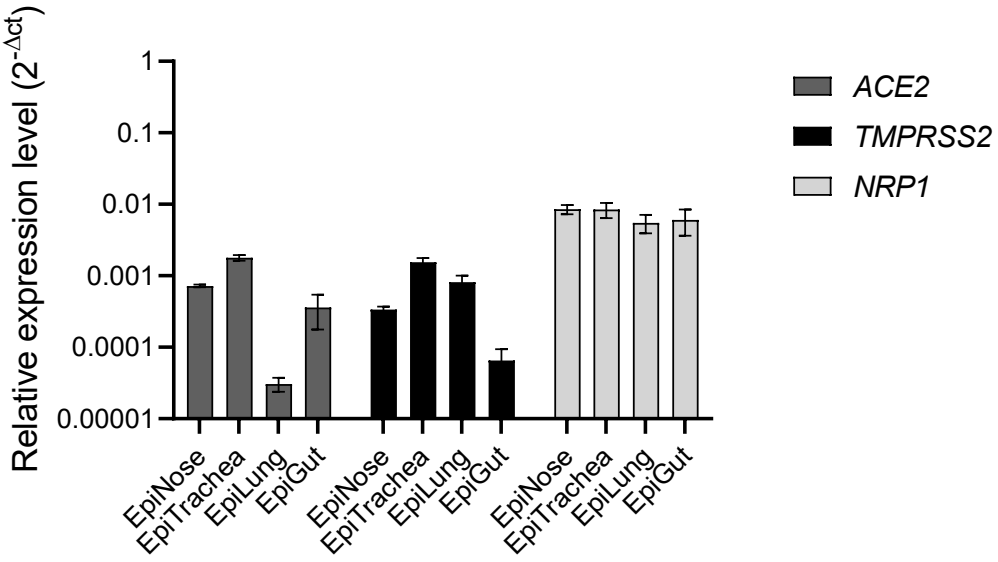

Figure 4.24 | SARS-CoV-2 receptors are expressed in ERB primary epithelia.
Basal expression of SARS-CoV-2 receptors *ACE2*, *TMPRSS2*, and *NRP1* was calculated by normalizing to *EEF1A1* and values were generated with qRT-PCR. Graph shows mean±SD of three independent experiments.

It has been shown that *ACE2* expression is inducible by type-I-IFN[326]. To determine whether similar expression patterns can be observed in bats, the expression of all three SARS-CoV-2 receptors was monitored upon stimulation with uIFN for 4 h, and 8 h respectively (**Figure 4.25**). All values were normalized to an unstimulated, undifferentiated control (treated with PBS instead of RA and uIFN) to determine whether expression of SARS-CoV-2 receptors is affected by either differentiation, uIFN treatment or both in a synergistic manner. It could be confirmed that *ACE2* expression is significantly upregulated in EpiTrachea by uIFN in a time-dependent manner, since expression levels were highest 8 h post stimulation (**Figure 4.25**). However, only total *ACE2* expression could be analyzed, a distinction between isoforms and their role for viral entry needs to be addressed in following experiments. This is of particular interest, since the truncated isoform was recently described to alter host cell susceptibility to SARS-CoV-2 infection[211]. Differentiation with RA

had no impact on the expression level of the receptors, since values did not differ between controls or after stimulation RA. Expression of *TMPRSS2* was not affected by differentiation or uIFN treatment. Expression of *NRP1* was seemingly increased upon uIFN treatment with enhanced expression after differentiation (**Figure 4.25**). However, these differences failed to reach statistical significance.

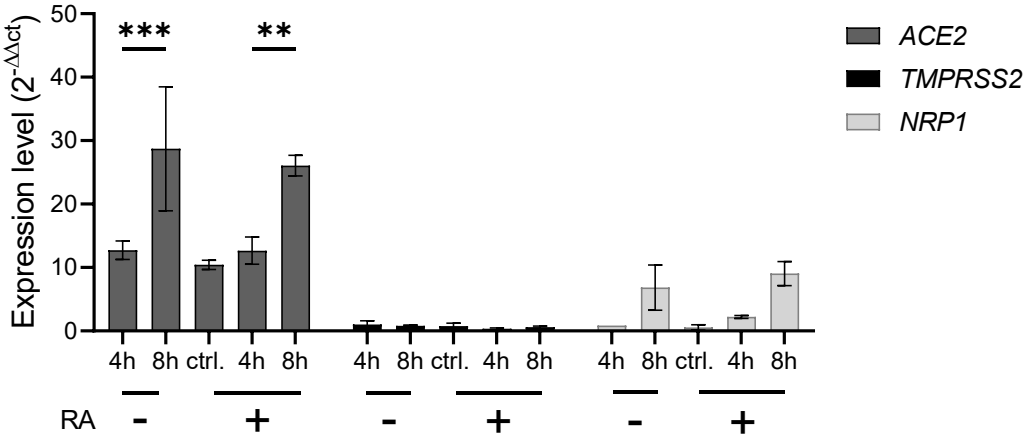

Figure 4.25 | Expression of *ACE2* is increased in EpiTrachea after uIFN treatment, but not differentiation.
EpiTrachea cells were incubated at 37°C ± 1,000 U/ml uIFN and ± RA for 4 h and 8 h, respectively. Expression levels of SARS-CoV-2 receptors *ACE2*, *TMPRSS2*, and *NRP1* was assessed by qRT-PCR and normalized to *EEF1A1* and a PBS-treated control. Graph shows mean±SD of two independent experiments. Statistical significance was calculated with Two-Way ANOVA and Holm-Šidák's post-hoc test. (**) $P \leq 0.01$, (***) $P \leq 0.001$.

4.2.3.3 Expression of pro-inflammatory cytokines upon SARS-CoV-2 infection *in vitro*

After validating that the cells express the receptors essential for SARS-CoV-2 entry, monitoring the expression of pro- and anti-inflammatory cytokines after infection was carried out. In this pilot study, all primary ERB epithelia were infected with SARS-CoV-2 and RNA was isolated after 8, 24, and 48 hpi. The relative expression levels of type-I-IFNs (*IFNA1*, *IFNB1*), type III-IFN (*IFNL*), *IL1B* and *CXCL10* were assessed. In general, the expression level of type-I- and III-IFNs, and *IL1B* were the highest in EpiTrachea after 8 hpi. Levels of *IFNA1* were the highest at 8 hpi in all cell types and declined over time. In cells from the respiratory tract, *IFNA1* levels declined, but did not reach levels of uninfected controls. In gut epithelial cells, *IFNA1* levels were lower at 24 and 48 hpi compared to mock and 8 hpi. Expression of *IFNB1* after SARS-CoV-2 infection showed similar kinetics as *IFNA1* induction. However, except in EpiNose, expression levels declined to reach mock levels at 48 hpi. In contrast to type-I-IFNs, overall *IFNL* expression remained stable between 8 and

24 hpi. Decline in expression over time did not reach levels of uninfected cells in EpiNose and EpiTrachea. Furthermore, no *IFNL* expression could be detected in EpiGut. Expression of pro-inflammatory *IL1B* remained stable over time, even at 48 hpi. Expression of the ISG *CXCL10* was delayed in comparison to expression of type-I- and type-III-IFNs, and *IL1B*. A peak of expression could not be determined, since expression remained increasing even at 48 hpi.

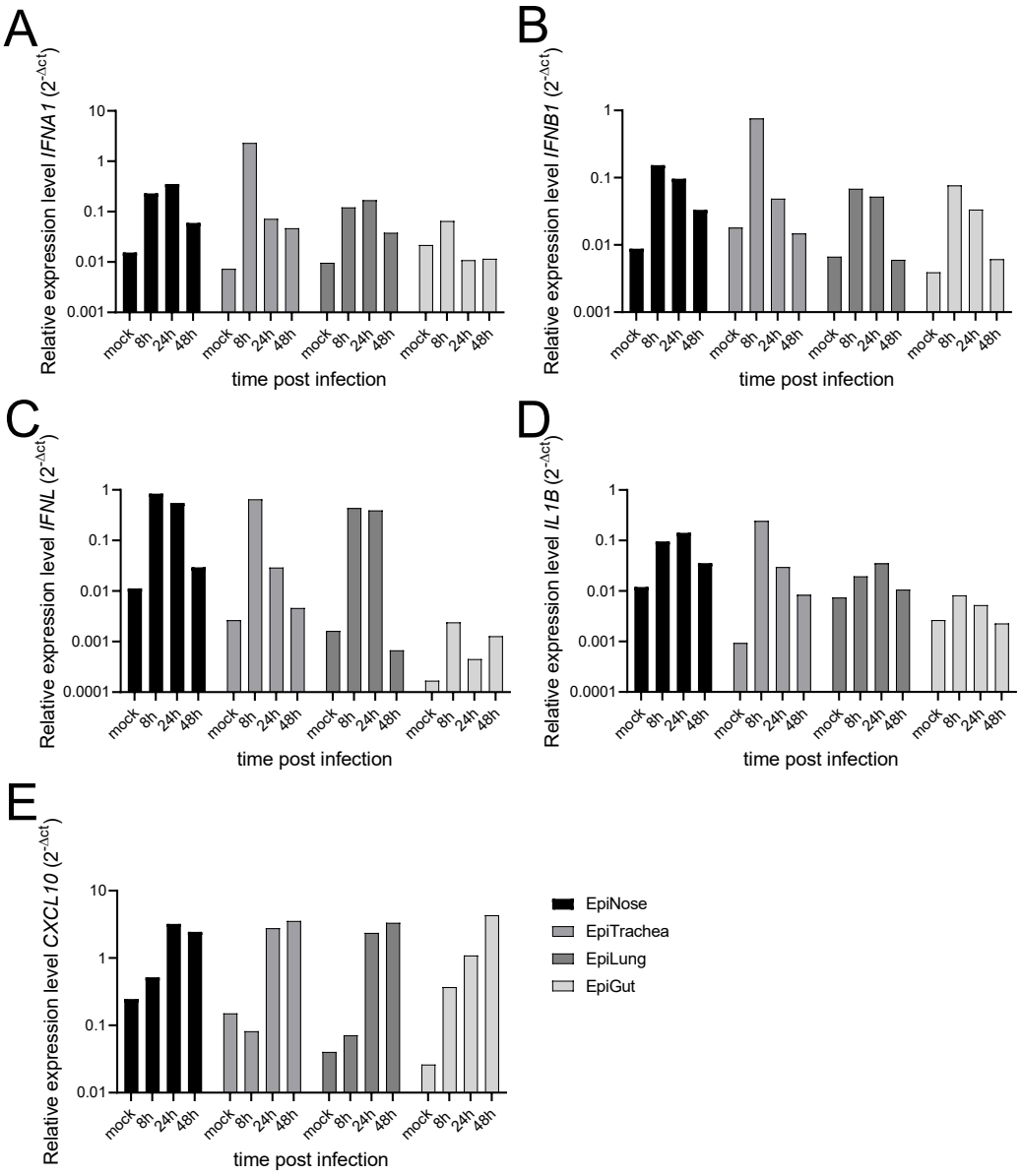

Figure 4.26 | Expression of pro-inflammatory cytokines is induced in primary ERB epithelia after SARS-CoV-2 infection.
Relative expression levels of *IFNA1* (**A**), *IFNB1* (**B**), *IFNL* (**C**), *IL1B* (**D**), and *CXCL10* (**E**) were determined at 8 h, 24 h, and 48 h after SARS-CoV-2 infection by qRT-PCR and normalization to *EEF1A1* expression. Bars represent mean of data derived from one pilot experiment (n = 1) with technical duplicates.

In conclusion, the four different epithelia cell lines showed unique expression kinetics of IFNs upon stimulation and temperature oscillation, especially *IFNL*. Expression of *IFNL* was higher in cells from the upper respiratory tract (EpiNose, EpiTrachea), and undetectable in EpiGut. Furthermore, expression patterns of *ACE2* and *TMPRSS2* varied among the cell lines and *ACE2* was confirmed to be IFN-inducible in EpiTrachea, indicating similar regulation by IFN like human *ACE2*[211]. Infection of all cell lines with SARS-CoV-2 revealed that *IFNL* expression is absent in EpiGut not only upon stimulation, but also subsequent viral infection. This suggests a major role of *IFNL* in susceptibility to SARS-CoV-2 in ERB epithelia cells.

4.3 Cellular immunity in ERB – Immune responses after viral infection and characterization of steady state leukocytes

4.3.1 Expression of pro- and anti-inflammatory cytokines upon infection with SARS-CoV-2 *in vivo*

Since data derived from cell lines, even when primary and heterogenous, is a snapshot of the entirety of immune responses and does not reflect systemic interactions, the expression of pro- and anti-inflammatory cytokines was monitored in various tissue of SARS-CoV-2 infected ERB. However, evaluation of cellular immunity by immunophenotyping ERB leukocytes upon infection was impossible due to a lack of established protocols at that point of the project. Thus, characterization of leukocyte function in periphery and tissues was carried out by monitoring immune-related cytokines typically produced by cells of various origins. Therefore, this transcriptomic data allowed insights into bat-specific immune responses at tissue level in addition to data derived from primary epithelia. To be able to compare the data generated *in vitro* and *in vivo*, the same set of pro-inflammatory cytokines, as well as *IFNG* and *IL10*, was measured in samples from infected animals.

Expression of type-I-IFNs (*IFNA1, IFNB1*) in tissue from the upper respiratory tract (nose, trachea) was significantly higher in animals at 4 dpi compared to all other tissues and time points (**Figure 4.27**). In these tissues, the levels of *IFNA1* and *IFNB1* declined by 12 dpi, but remained stable between 12 and 21 dpi, likely linked to viral clearance. In tissue associated with the lower respiratory compartment (lung, lung LN), the pattern of *IFNA1* induction was comparable to tissue from the upper respiratory tract (**Figure 4.27, A**), while induction of *IFNB1* was less pronounced (**Figure 4.27, B**). Strikingly, *IFNA1* mRNA could be detected in blood and spleen, which indicates a role of *IFNA1* in a systemic antiviral response. While induction of *IFNA1* expression was only undetected in tissues related to the gastrointestinal (GI) tract (duodenum, mLN), *IFNB1* was undetected in spleen, blood, duodenum, and mLN after infection. In conclusion, expression of type-I-IFNs could be detected in several tissues, especially associated to respiratory compartments, of animals sacrificed at 4 dpi. Levels of *IFNA1* and *IFNB1* were lower at 8 dpi, while no significant difference in expression could be observed between 12 and 21 dpi.

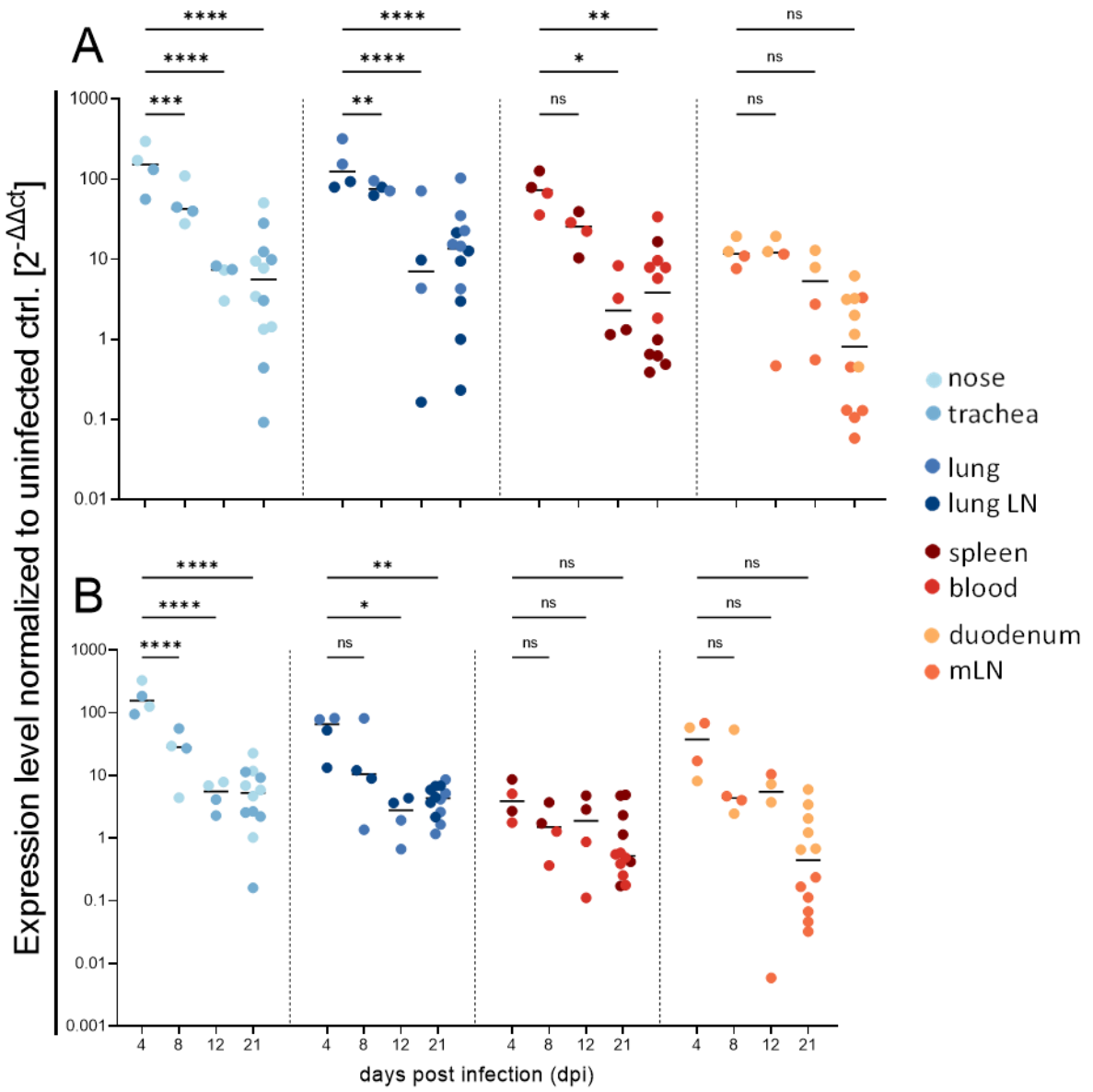

Figure 4.27 | Limited induction of systemic *IFNA1* and *IFNB1* in the GI tract in SARS-CoV-2 infected ERB.
Expression levels of *IFNA1* (**A**) and *IFNB1* (**B**) are depicted as fold change ($2^{-\Delta\Delta ct}$) after normalization to *EEF1A1* and tissue samples from uninfected ERB. Data was generated with qRT-PCR. Each point represents the value of *IFNA1* or *IFNB1* in the tissue of one animal, mean is displayed as horizontal bar respectively. Statistical significance was calculated with One-Way ANOVA and Holm-Šidák's post-hoc test. (*) $P \leq 0.05$, (**) $P \leq 0.01$, (***) $P \leq 0.001$, (****) $P \leq 0.0001$.

Besides type-I-IFNs, the expression of type-II- and III-IFN after infection with SARS-CoV-2 was determined as well (**Figure 4.28**). Strikingly, *IFNG* was significantly higher in the upper respiratory tract (nose, trachea) 4 dpi compared to other timepoints (**Figure 4.28, A**). In the tissue of animals sacrificed at 8 dpi, mRNA levels of *IFNG* were significantly lower compared to 4 dpi, whereas expression was comparable at 12 and 21 dpi. In tissues associated with the lower respiratory and GI tract, a similar pattern like the one observed in the upper respiratory tract could be detected, which however did not

reach statistical significance due to high variance between the individuals. A significant decline in systemic *IFNG* could only be verified between 4 and 21 dpi. Expression of *IFNL* was slightly higher in tissues at 4 dpi, however, no statistical significance could be detected among the tissues of any compartment (**Figure 4.28, B**).

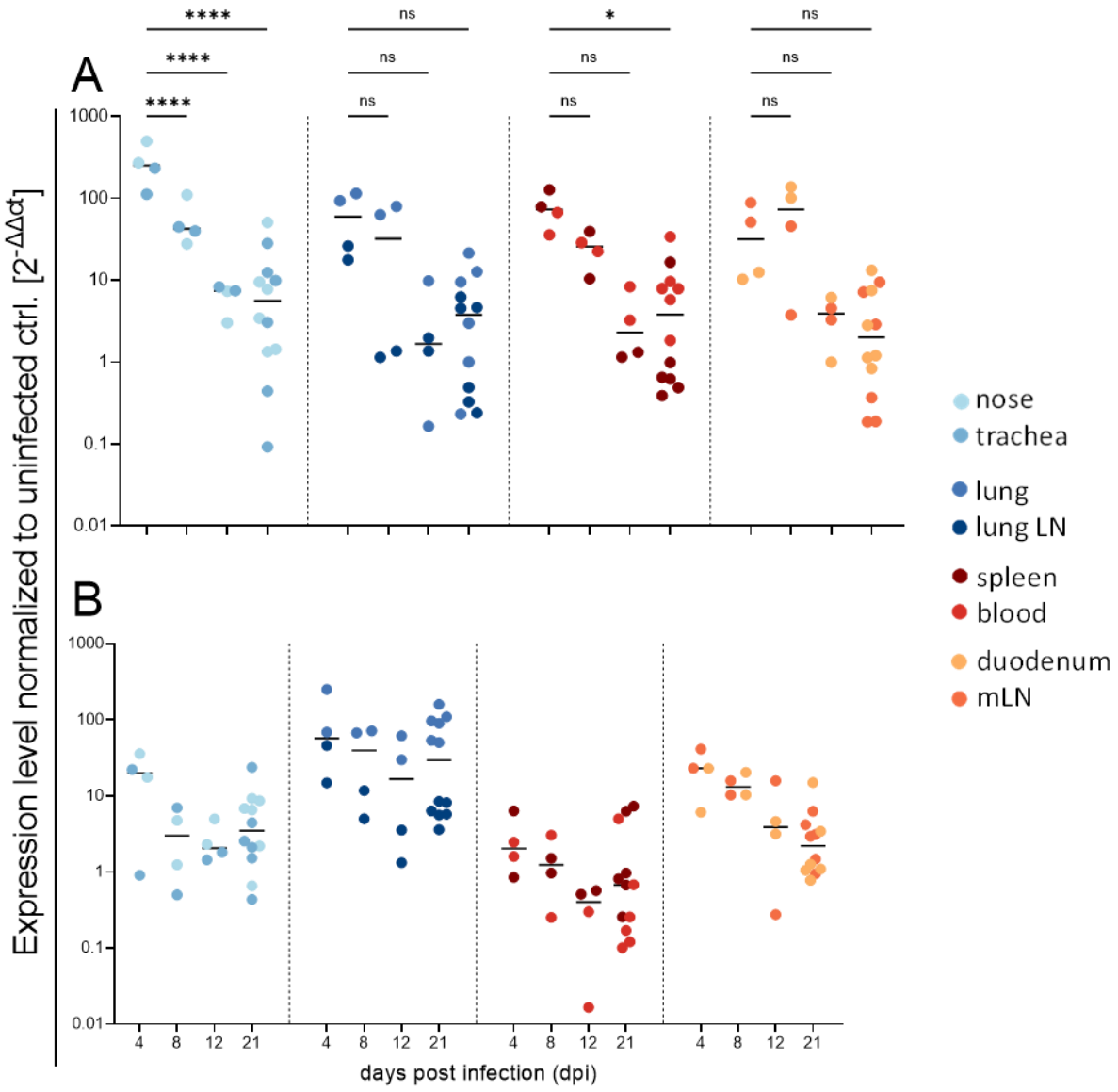

Figure 4.28 | Early *IFNG* expression in the upper respiratory tract of ERB after SARS-CoV-2 infection. Expression levels of *IFNG* (**A**) and *IFNL* (**B**) are depicted as fold change ($2^{-\Delta\Delta ct}$) after normalization to *EEF1A1* and tissue samples from uninfected ERB. Data was generated with qRT-PCR. Each point represents the value of *IFNG* or *IFNL* in the tissue of one animal, mean is displayed as horizontal bar respectively. Statistical significance was calculated with One-Way ANOVA and Holm-Šidák's post-hoc test. (*) $P \leq 0.05$, (****) $P \leq 0.0001$.

Expression of the ISG *CXCL10* and the inflammasome-related pro-inflammatory cytokine *IL1B* was also assessed (**Figure 4.29**). Expression of *CXCL10* was highest in tissue samples at 4 dpi, whereas the levels of mRNA were highest in tissues from the respiratory tract (**Figure 4.29, A**). In tissue of both the upper and lower respiratory tract, the expression of

CXCL10 was significantly lower at 8 dpi compared to 4 dpi. However, the expression levels were comparable at 12 and 21 dpi, in accordance to expression levels of type-I- and II-IFNs. The expression of systemic *CXCL10* remained stable up to 8 dpi, but was significantly lower in tissue collected at 12 and 21 pi. Although the same pattern could be observed in tissue associated with the GI tract, this difference failed to reach statistical significance due to high variance between individuals. Expression levels of *IL1B* were comparable between tissue from the upper respiratory tract and systemic compartments (**Figure 4.29, B**). The levels were highest in nose and trachea from animals sacrificed at 4 dpi and significantly lower in corresponding tissue obtained at 8, 12, and 21 dpi. In blood and spleen, the difference between 4 and 8 dpi was visible, but less pronounced than in the upper respiratory tract. Expression levels of *IL1B* in the lower respiratory and GI tract did not differ significantly among the individuals.

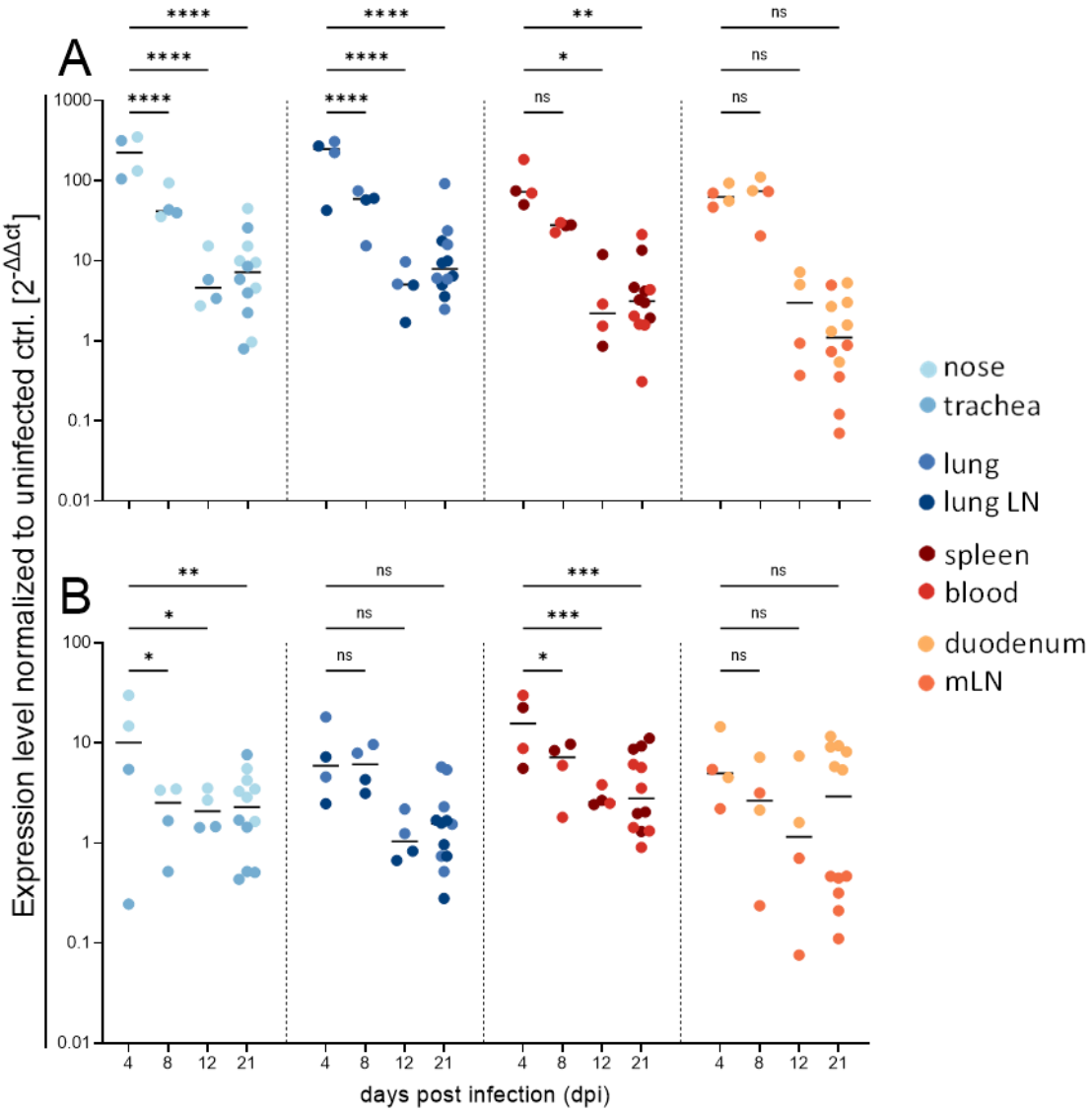

Figure 4.29 | *CXCL10* and *IL1B* are highly expressed in various ERB tissue after SARS-CoV-2 infection. Expression levels of *CXCL10* (**A**) and *IL1B* (**B**) are depicted as fold change ($2^{-\Delta\Delta ct}$) after normalization to *EEF1A1* and tissue samples from uninfected ERB. Data was generated with qRT-PCR. Each point represents the value of *CXCL10* or *IL1B* in the tissue of one animal, mean is displayed as horizontal bar respectively. Statistical significance was calculated with One-Way ANOVA and Holm-Šidák's post-hoc test. (*) $P \leq 0.05$, (**) $P \leq 0.01$, (***) $P \leq 0.001$, (****) $P \leq 0.0001$.

To gain insights into regulatory processes in ERB infected with SARS-CoV-2, the expression of *IL10* was analysed in all tissue samples. In nose, trachea, spleen and blood, the levels of *IL10* were induced at 4 dpi and declined from 8 dpi. As already observed for other cytokines, a significant difference between samples taken at 8 dpi and 12 dpi could be observed, whereas no difference was detected between 12 and 21 dpi. In lung and lung LN, levels of *IL10* between the individuals were slightly lower in proportion to the sampling point and was only significantly lower between samples from 4 and 21 dpi. A similar pattern could be noted in tissue associated with the GI tract as well.

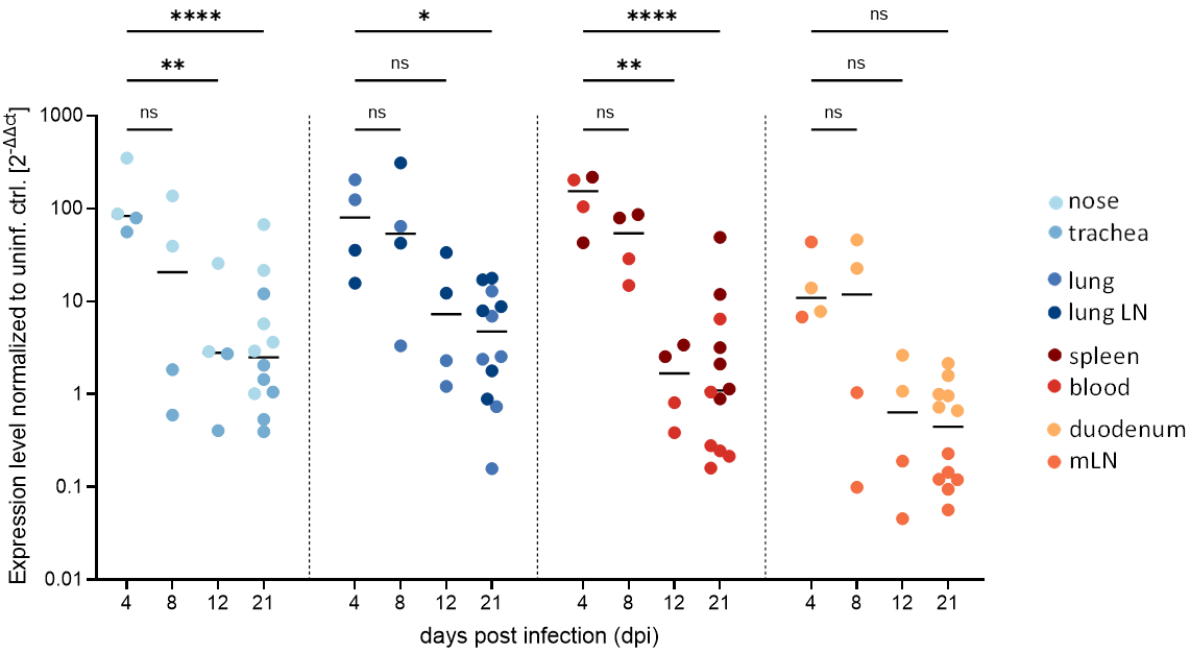

Figure 4.30 | The anti-inflammatory cytokine *IL10* is expressed in ERB after SARS-CoV-2 infection. Expression levels of *IL10* are depicted as fold change ($2^{-\Delta\Delta ct}$) after normalization to *EEF1A1* and tissue samples from uninfected ERB. Data was generated with qRT-PCR. Each point represents the individual value of *IL10* in the tissue of one animal, mean is displayed as horizontal bar respectively. Statistical significance was calculated with One-Way ANOVA and Holm-Šidák's post-hoc test. (*) $P \leq 0.05$, (**) $P \leq 0.01$, (****) $P \leq 0.0001$.

In conclusion, samples taken from ERB after SARS-CoV-2 infection clearly showed an upregulation of pro- and anti-inflammatory cytokines systematically from upper respiratory to GI tract. The expression levels were highest at 4 dpi, whereas the expression levels lowered in later timepoints. For nearly all cytokines evaluated, the expression levels were highest in tissue from the upper respiratory tract. An early upregulation if *IFNG* could be observed, although this cytokine is primarily associated to adaptive immunity[327]. The cellular origin of early *IFNG* expression needs to be determined in consideration of lymphocytes capable of early *IFNG* production, e.g. NKT cells, γδ T cells, and NK cells[328-330].

4.3.2 Phenotypic and functional characterization of leukocytes in adult and juvenile ERB

To enable immunophenotyping in ERB, particularly for future infection studies, immunopanels to define myeloid cells and lymphocytes in ERB were established within this project. Functionality of these cells was assessed by monitoring phagocytosis for professional phagocytes and B cells, as well as proliferative capacity for lymphocytes. Furthermore, distributional and functional differences between leukocytes of adult and juvenile ERB allowed in-depth characterization of leukocytes in this species.

4.3.2.1 Identification and validation of cross-reactive antibodies to define ERB leukocytes in flow cytometry

To characterize ERB leukocytes with flow cytometry, 47 commercially available antibody clones (**Appendix 10.15**) were screened for cross-reactivity with ERB orthologs. In total, eight antibodies exhibited cross reactivity with ERB leukocytes. The antibodies identified target both surface (CD11b, CD172a, MHCII, and CD206) and intracellular molecules (CD3, CD79a, Ki-67). To determine the consensus between ERB proteins and orthologs in humans, mice or cattle, amino acid sequences of molecules targeted by identified antibodies were aligned to human and mouse orthologs. Overall, the homology ranged from 32.7%-86.1%. Particularly, consensus between bat and human proteins was slightly higher than that between bat and mouse (Table 4.3).

Table 4.3 | Consensus of protein sequences between ERB, human, mouse, and bovine.

Target molecule	Distance human [%]	Distance mouse [%]	Distance bovine [%]
CD3ε	63.9	61.4	66
CD11b	78.3	74.3	77.1
CD79a	65.8	62.6	66.5
CD172a	74.3	62.3	75.5
CD206	87	80.6	86.1
Ki-67	40.3	32.7	41.2
MHCII	82	84.5	78.8

To define the entirety of myeloid cells in ERB, an antibody recognizing mouse and human cell adhesion molecule ITGAM (integrin α M, CD11b), previously described as a universal marker for myeloid cells and a subset of activated T cells[331], was used (**Figure 4.31**). Further

identification of subsets within the myeloid compartment was conducted with an antibody against bovine SIRPα (signal regulatory protein α, CD172a) and an antibody recognizing human mannose receptor (CD206). Therefore, monocytes/DCs were defined as $CD11b^{+}CD172a^{+}$, while the CD206+ subset was defined as $CD206^{+}$ mononuclear myeloid cell (MMC) within the fraction of live mononuclear cells (MNCs), (**Figure 4.31**). In addition, an antibody targeting mouse MHCII demonstrated cross-reactivity with the ERB ortholog (**Appendix 10.16**). However, due to presumed haplotype variabilities in the ERB colony, the staining was only successful in about 50% of samples. Therefore, MHCII was not included in the gating strategy to define ERB leukocytes, but promoted precise analysis upon successful staining.

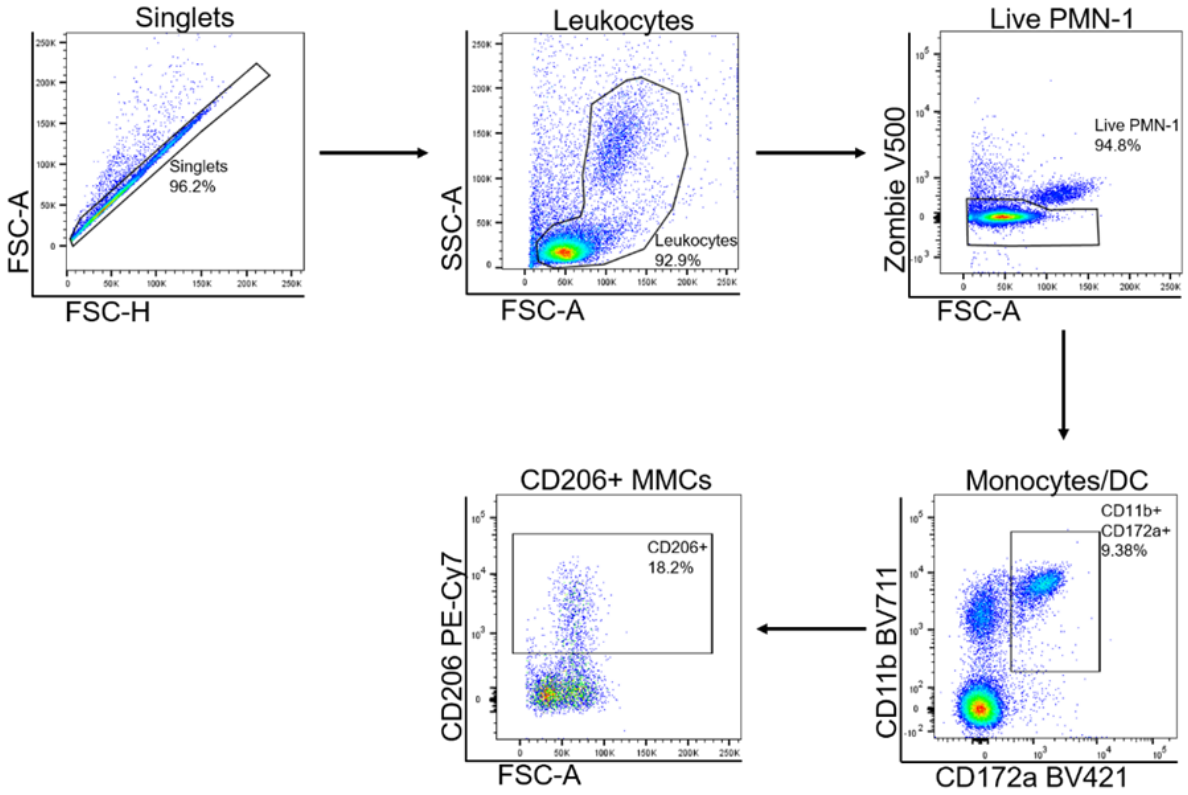

Figure 4.31 | Identification strategy for circulating and tissue-specific myeloid cells in ERB.
Myeloid cells in ERB were defined by flow cytometry, using the following gating strategy: Doublets were excluded by FSC-A/FSC-H properties. Live cells were defined as $Zombie^{-}$ and PMNs were excluded based on size to define live MNCs. Within live MNCs, monocytes/CDs were identified by $CD11b^{+}CD172a^{+}$. Additionally, a $CD206^{+}$ subset could be defined within this population. Representative plots were chosen to generate this figure.

Although no cross-reactive antibodies to define ERB granulocytes by flow cytometry could be identified, definition of these cells was enabled by characteristic morphometric properties of polymorphonuclear cells (PMNs)[332]. Granulocytes were defined as $FSC^{high}SSC^{high}$ and subsequent $CD11b^{+}CD172a^{+}$ population in subsequent analysis. Comparable to granulocytes

in other species, ERB granulocytes also stained positive for the viability stain (Zombie Aqua) despite being viable. This false positive signal originated from autofluorescence[333] and did not lead to an exclusion of these cells (**Figure 4.32**).

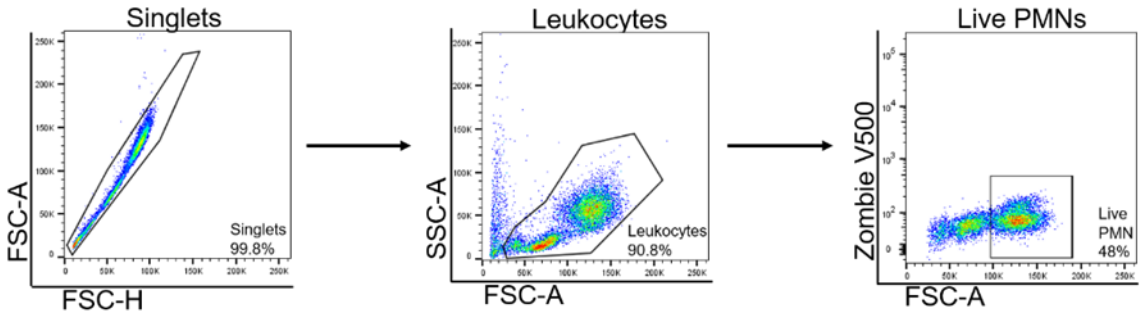

Figure 4.32 | Identification of circulating and tissue-specific granulocytes in ERB.
To define ERB PMNs by flow cytometry, doublets were excluded based on FSC-A/FSC-H properties and live PMNs were identified amongst all single and live leukocytes based on morphometric properties within the Zombie$^-$ population.

To identify ERB lymphocytes, precisely T and B cells, a gating strategy based on an antibody recognizing the cytoplasmic ε-chain of the human T cell co-receptor (CD3ε, pan-T cell) and an antibody recognizing the cytoplasmic α-chain of human B cell receptor (CD79a, pan-B cell) was established (**Figure 4.33**). Although identification of cross-reactive antibodies against the main T cell subsets, namely CD4 and CD8, was unsuccessful, a putative activated T cell subset within the CD8$^+$ compartment[331,334] could be identified by CD11b positivity (**Figure 4.33**).

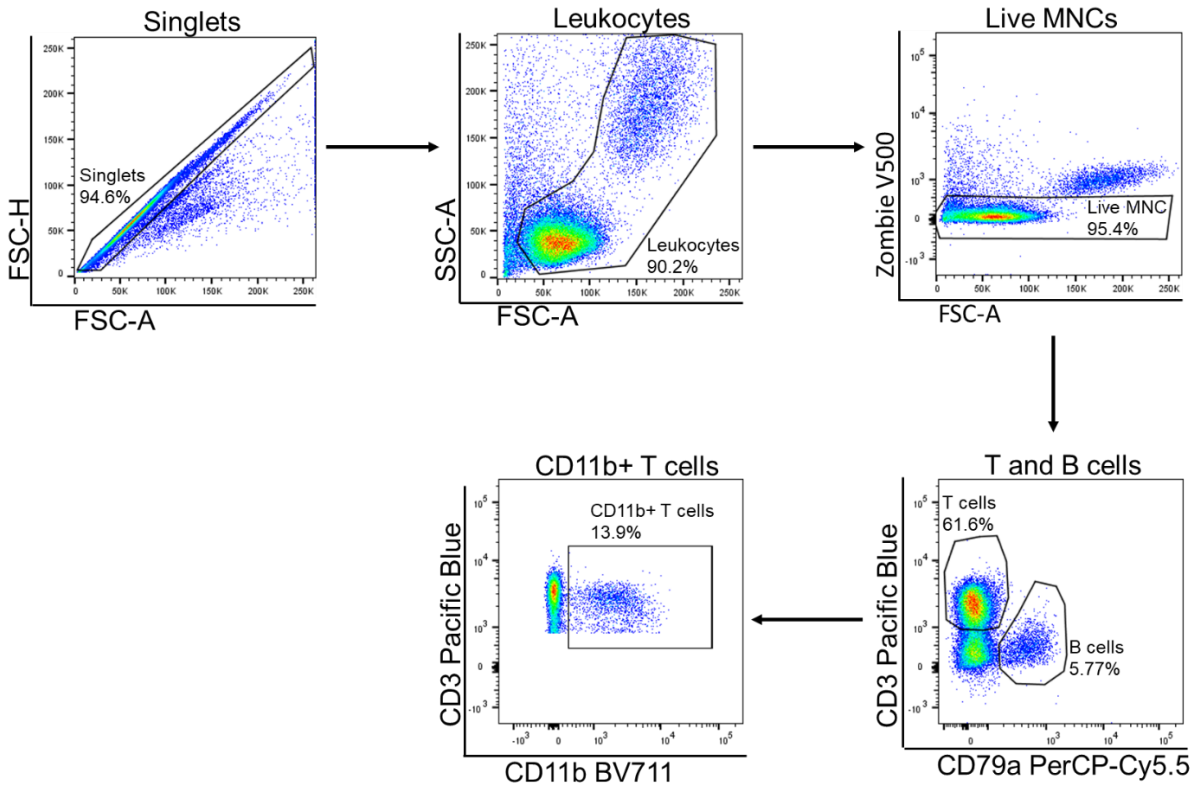

Figure 4.33 | Identification of circulating and tissue-resident lymphocytes in ERB.
To characterise ERB lymphocytes by flow cytometry, the following gating strategy was employed: Doublets were excluded based on FSC-A/FSC-H properties, followed by definition of live MNCs (Zombie$^-$, PMN-1). Lymphocytes within the MNC fraction were divided into T cells (CD3$^+$CD79a$^-$) and B cells (CD3$^-$CD79a$^+$). A putatively activated T cell subset could be further identified as CD3$^+$CD11b$^+$.

To validate the accuracy of the gating strategies and specificity of antibodies employed to identify ERB leukocytes, the following cell subsets were sorted and subsequently analyzed by microscopy and in PCR: CD11b$^+$CD172a$^-$, CD11b$^+$CD172a$^+$, CD172a$^-$ and FSC^{high}SSC^{high} (**Figure 4.34**). CD11b$^+$CD172a$^-$ and CD11b$^+$CD172a$^+$ MNCs were of spherical morphology with an approximate nucleus to cytoplasm ratio (N:C) of 3.1 (**Figure 4.34, A**). Monocytic identity as indicated by morphological analysis was further supported by gene transcript analysis with PCR. The expression pattern of *CD3E* (pan T cell), *CD44*, *ITGAM* (CD11b, pan-myeloid), *CD14* (monocyte), *PTPRC* (CD45, pan leukocyte), *CD68* (macrophage), *CD79a* (pan-B cell), *CD163* (monocyte/macrophage) and *SIRPA* (CD172a, monocyte/DC) suggested accurate definition of myeloid cells utilizing cross-reactive antibodies (**Figure 4.34, A**). The CD206$^+$ monocytic subset could not be sorted due to low abundance in ERB periphery. Sorted FSC^{high}SSC^{high} cells displayed both segmented nuclei and azurophilic granules, indicating neutrophil granulocyte identity (**Figure 4.34, A**). The expression pattern of markers in these cells rendered positive results for *ITGAM*, *SIRPA*, *PTPRC*, *CD14*, and the

neutrophil cytosolic factor *NCF1* (**Figure 4.34, C**). Validation of neutrophil identity based on *NCF1* expression was used after confirming the absence of *CD66b* in the latest annotation of the ERB genome[170] and unsuccessful testing for specific primer pairs to detect *CD56* or *CD15*. Interestingly, analysis of *CD16* expression (*LOC107502476*, mRouAeg1[170], **Figure 4.34, D**) only resulted in positive results for sorted CD11b^{+} and CD11b^{+}CD172a^{+} cells.

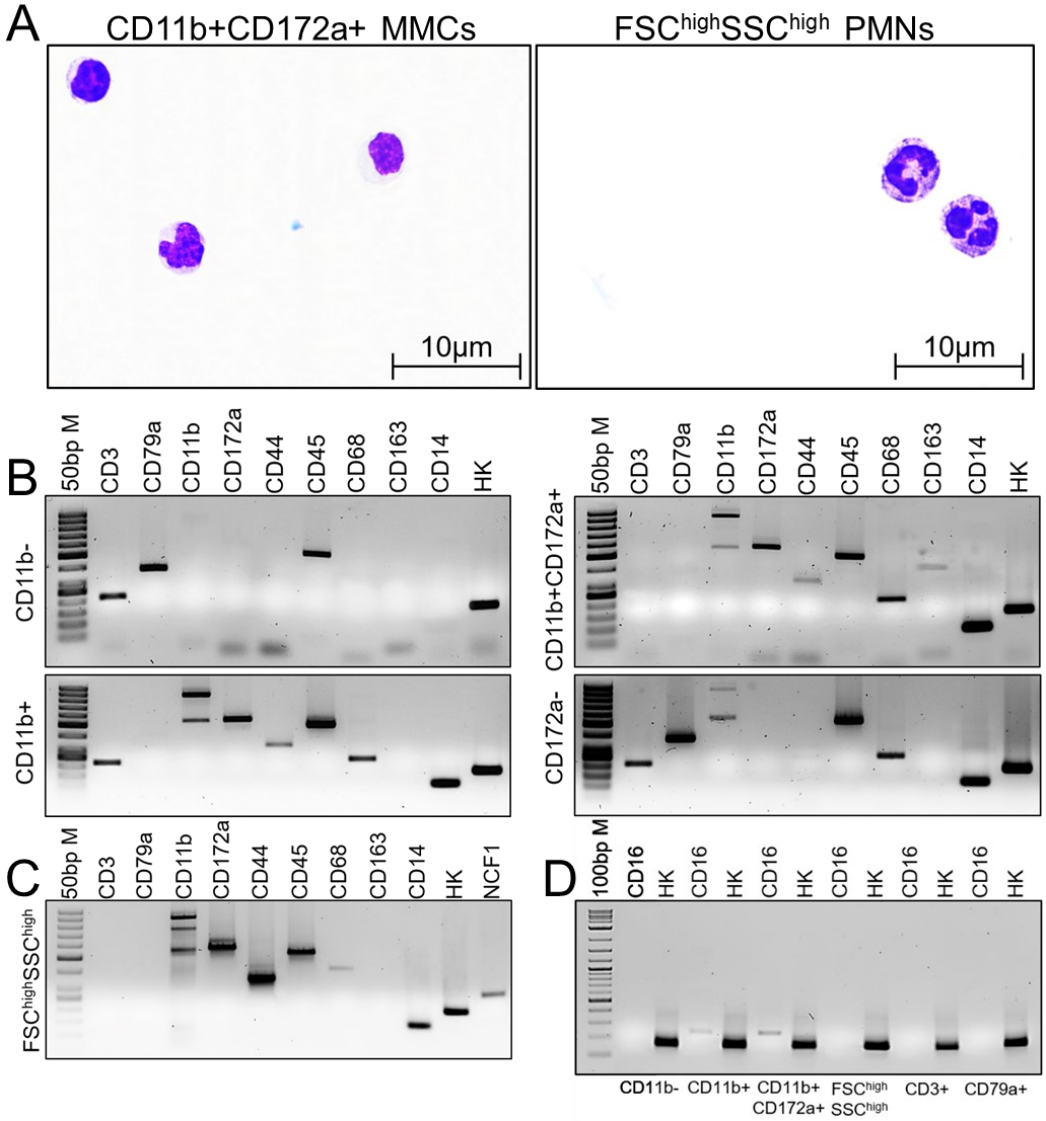

Figure 4.34 | Validation of antibody specificity to ERB MMCs by PCR and morphological analysis confirms identity of myeloid cells.
To verify specificity of cross-reactive antibodies to MMCs CD11b^{+}CD172a^{+} and FSC^{high}SSC^{high} cells were sorted (**A**). Sorted cells were stained with Kwik-Diff Kit and morphological analyses were performed by microscopy (100x magnification). To further investigate antibody specificity to myeloid cells, the following populations were sorted and expression of lineage markers was assessed by PCR: CD11b$^{\pm}$ MNCs, CD11b^{+}CD172a$^{\pm}$ MNCs (**B**). To verify precise identification of PMNs based on morphometric properties, FSC^{high}SSC^{high} cells were sorted and analysed by PCR (**C**). Expression of *CD16* was assessed in all ERB leukocyte populations that can be distinguished by flow cytometry (**D**), except CD206^{+} MMCs due to low abundance. Analysis of *ITGAM* resulted in detection of multiple isoforms. For subsequent verification, bands were cut, purified and sequenced. The obtained sequences were blasted to ensure specificity to ERB transcripts. Reference gene (HK; housekeeping gene) = *EEF1A1*.

To analyze the identity of defined T and B cells, $CD3^+$ and $CD79a^+$ cells were sorted and examined with regard to the expression of cell markers like *CD3E* as pan- T cell and *CD79A* as pan-B cell markers (**Figure 4.35**). Observed expression patterns indicate that utilization of these cross-reactive antibodies successfully defined T and B cells in ERB.

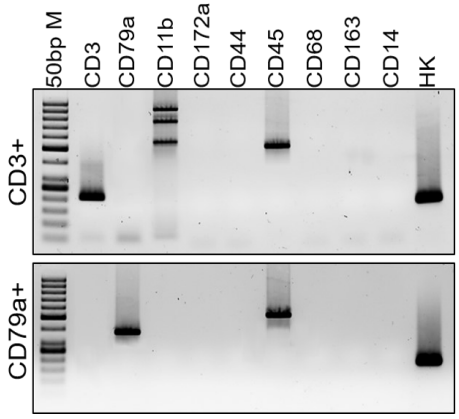

Figure 4.35 | Validation of antibody specificity to ERB lymphocytes by PCR confirms identity of lymphocytes.
To assess specificity of αCD3 and αCD79a antibodies to ERB lymphocytes, $CD3^+$ and $CD79a^+$ cells were sorted and expression of lineage markers was evaluated by PCR. For subsequent verification, bands were cut, purified and sequenced. Analysis of *ITGAM* resulted in detection of multiple isoforms. The obtained sequences were blasted to ensure specificity to ERB transcripts. Reference gene (HK; housekeeping gene) = *EEF1A1*.

4.3.2.2 Abundance of myeloid cells in blood and various tissue of adult and juvenile ERB

After validating specificity of all antibodies exhibiting cross-reactivity to ERB orthologs, the abundance of myeloid cells in both periphery and various tissue was determined (**Figure 4.36**). To gain a deeper insight into age dynamics of this species, adult and juvenile specimens were employed in the analysis. While abundances of $CD11b^+CD172a^+$ monocytes/DCs did not differ in the periphery of adult and juvenile ERB, a significantly higher frequency of $CD206^+$ monocytes were observed in adult bats (**Figure 4.36, A**). In a subsequent step, leukocyte abundances in lymphoid and non-lymphoid compartments were analyzed. Therefore, abundances of myeloid subsets were analyzed in unperfused spleen, mLN and lungs, as well as blood of adult and juvenile ERB. Monocytes/macrophages/DCs, defined as $CD11b^+CD172a^+$, were enriched in the lungs of both age groups (mean adult 14%, juvenile 11%), in comparison to up to 3% in spleen and mLN for both adult and juvenile ERB (**Figure 4.36, B**). The frequencies observed in periphery and tissue of ERB were supported by total cell numbers in corresponding samples. Mean numbers in the lung of adult ERB

were 11.6×10^6, for juveniles 9.8×10^6, in spleen 9.6×10^6 / 3.2×10^6, and 0.04×10^6 / 0.1×10^6 cells in mLN (**Figure 4.36, C**). Putative alveolar macrophages, defined as CD206$^+$ within the CD11b$^+$CD172a$^+$ population, were predominantly identified in the lung of both age groups. In addition, the frequency and total number of CD206$^+$ monocytic cells was high in the spleen of adult and juvenile ERB.

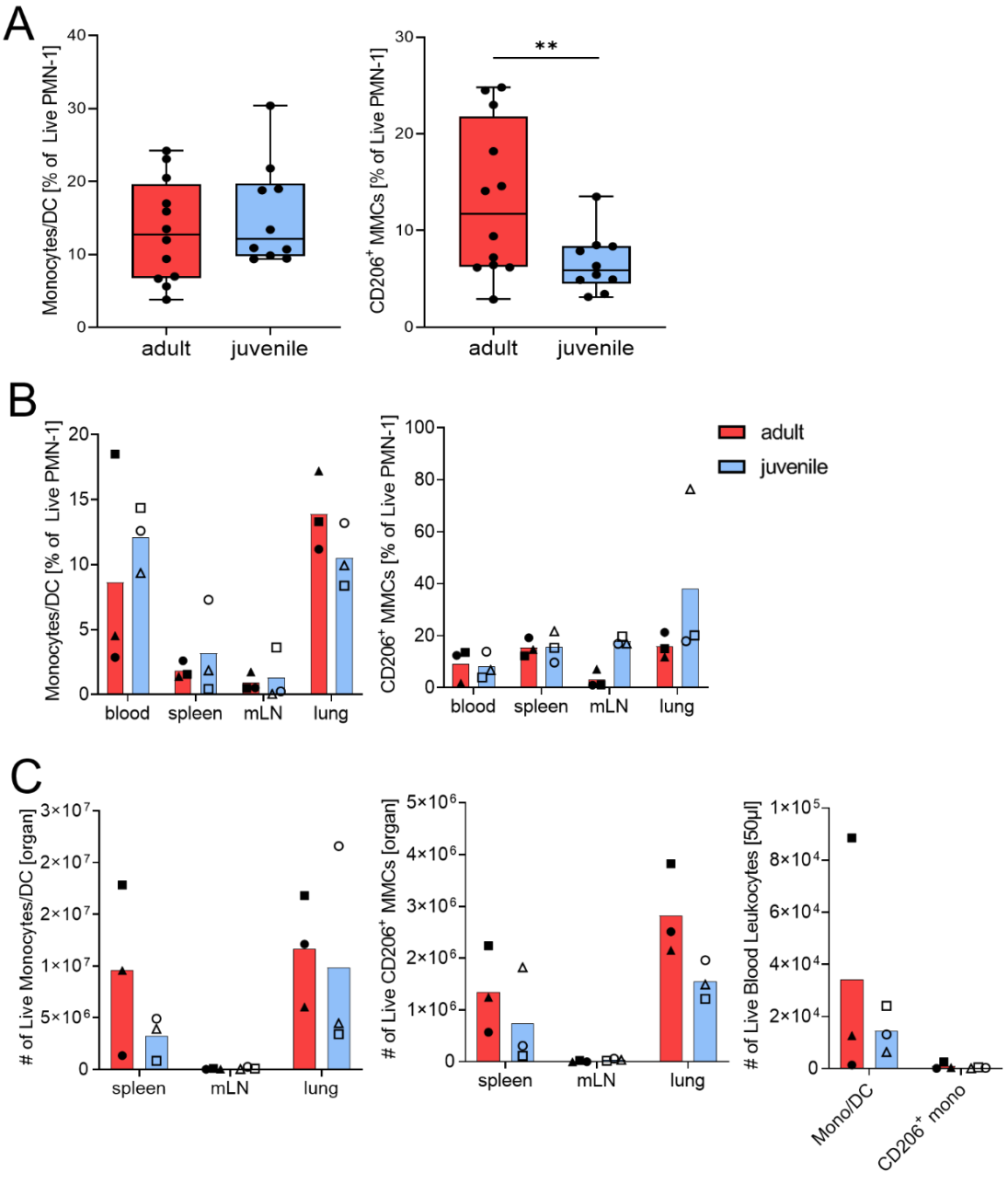

Figure 4.36 | Frequencies of myeloid cells in periphery and tissue of adult and juvenile ERB reveal enrichment of CD206$^+$ MMCs in juveniles.
Frequencies of ERB MMCs in periphery (**A**) and various tissues (**B**), as well as absolute cell counts (**C**) were determined by flow cytometry. Frequencies of peripheral monocytes/DCs (CD11b$^+$CD172a$^+$) and CD206$^+$ MMCs are displayed (*n* adult = 12, *n* juvenile = 10). Frequencies of monocytes/DCs and CD206+ MMCs was assessed in lymphatic and non-lymphatic tissue of adult and juvenile ERB (*n* = 3/group). Absolute cell counts were determined with AccuCheck counting beads. Each individual is represented by a point (**A**) or a symbol (**B**, **C**), bar represents the group mean. Statistical significance was calculated with unpaired *t*-test. (**) $P \leq 0.01$.

Interestingly, the abundance of granulocytes was significantly higher in the periphery of adult bats compared to juveniles (**Figure 4.37, A**). However, this was not reflected in absolute cell counts since the frequency in the specimens selected for necropsy were comparatively low (**Figure 4.37, B**). The overall frequencies and absolute counts of granulocytes in spleen and mLN were low, whereas minimal amounts could be detected in unperfused lung. Frequencies and absolute cell numbers in tissue did not differ between the two age groups (**Figure 4.37, B**).

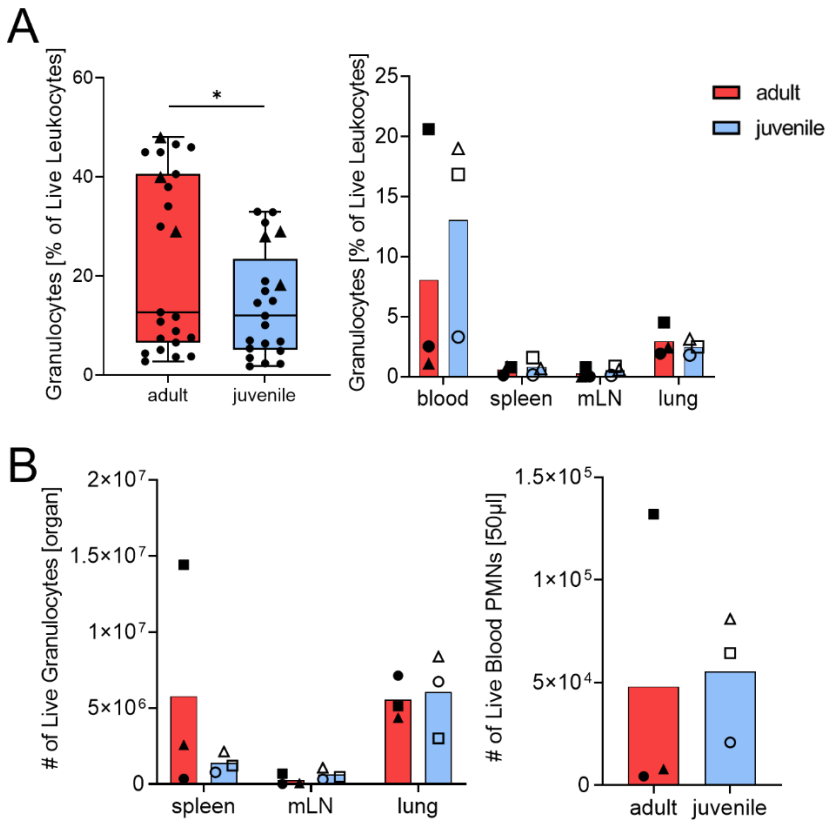

Figure 4.37 | Frequencies of peripheral granulocytes in adult and juvenile ERB reveal enrichment in adults.
Frequencies (**A**) and absolute numbers (**B**) of ERB PMNs were determined by flow cytometry. The frequency of peripheral granulocytes ($FSC^{high}SSC^{high}$) was assessed in adult and juvenile ERB (*n* adult = 23, *n* juvenile = 21). Absolute cell counts were calculated with AccuCheck counting beads. Each individual is represented by a point (**A**) or individual symbol (**A**, **B**), animals marked as triangles in (**A**) were also subjected to scRNA-seq. Each individual is represented by a symbol (**A**, **B**), bar represents the group mean. Statistical significance was calculated with unpaired *t*-test. (*) $P \leq 0.05$.

4.3.2.3 Functional characterization of phagocytic leukocytes in adult and juvenile ERB

To gain insight into functions of characterized cell types, the phagocytic capacity of professional phagocytes and B cells in adult and juvenile ERB was evaluated (**Figure 4.38**). It has already been described for other species like humans that the phagocytic capacity of monocytes, macrophages[335,336] and granulocytes[337-339] declines with age. Therefore, defining phagocytic capacities in adult and juvenile ERB is of particular interest for this reservoir species.

To monitor phagocytosis in periphery and lung of adult and juvenile ERB, the gating strategy for myeloid characterization was utilized. However, few amendments had to be conducted to detect successful phagocytosis of *E. coli* bioparticles by granulocytes ($FSC^{high}SSC^{high}$), monocytes/DCs ($CD11b^+$ MNCs), the $CD206^+$ subset, and B cells ($CD11b^-CD79a^+$). B cells were included based on previous reports on phagocytic activity in B cells of numerous species of high phylogenetic age (e.g. teleost fish[340]) or the B1 B cell subset in mice[341], as well as MHCII positivity in flow cytometry (**Figure 4.38**).

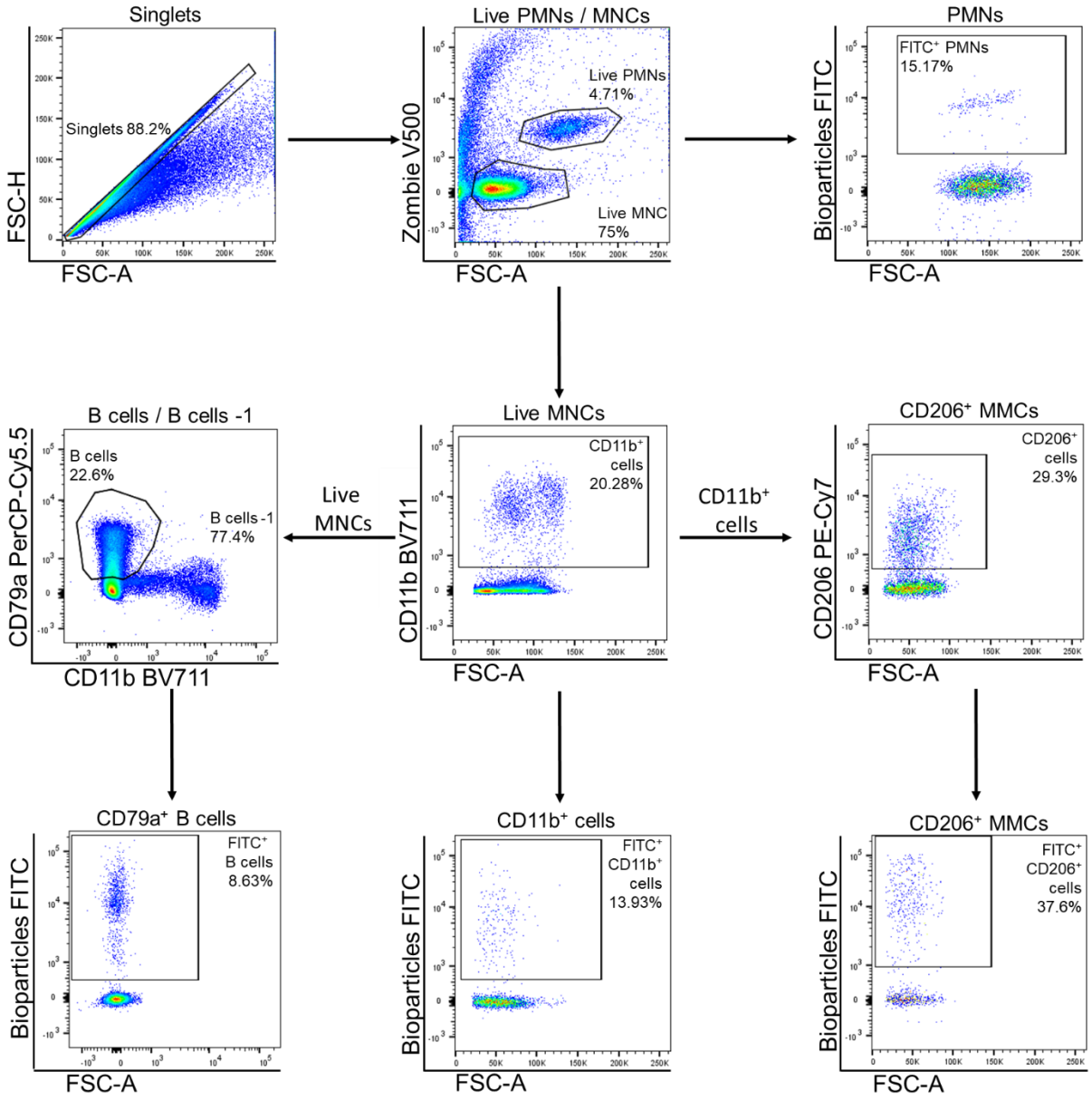

Figure 4.38 | Analysis of phagocytic capacity of ERB leukocytes by flow cytometry.
To identify the phagocytic activity of different immune cell populations of adult and juvenile ERB, doublets were excluded based on FSC-A/FSC-H properties with subsequent exclusion of unphagocytosed bioparticles by selecting live PMNs and MNCs, respectively. To assess phagocytosis of *E. coli* bioparticles by PMNs, FITC signal was evaluated in this population. MNCs (PMN-1) were further divided into $CD11b^+$ MNCs and a $CD206^+$ subsets, and $CD11b^-CD79a^+$ B cells. Phagocytosis was evaluated by analysis of FITC signal in each population. Representative plots were selected to generate this figure.

For both blood and lung, phagocytic activity of all myeloid subsets increased over time, while activity in B cells decreased (**Figure 4.39**). Nevertheless, a general higher phagocytic rate of myeloid cells could be observed in adults for both early and late time points, although failing to reach statistical significance. The phagocytic rate of B cells was higher in juveniles. Up to 52.9% of granulocytes from the periphery of adult bats successfully phagocytosed bioparticles, compared to 39.4% observed for juvenile ERB (**Figure 4.39, A**). The

phagocytosis rate of granulocytes derived from the lung of adult and juvenile bats was comparable (mean 16.4% in adult, 13.1% in juvenile). Consistent with granulocytes, phagocytic rates of monocytes/macrophages were similar between blood and lung samples from adult and juvenile ERB (**Figure 4.39, B**). Up to 44.7% of peripheral monocytes in adult bats phagocytosed bioparticles, while 7,69% of monocytes and macrophages from the lung rendered positive results. In juveniles, 32.1% of peripheral monocytes/macrophages phagocytosed bioparticles, while the phagocytic rate in lung samples ranged around 4,87%. Taken together, the phagocytic capacity of peripheral myeloid cells exceeded those observed in lung samples exempting of putative alveolar macrophages ($CD206^+$) (**Figure 4.39, C**).

Since B cells are known to exhibit phagocytic abilities, and MHCII expression on ERB B cells could be verified (**Appendix 10.16**), the phagocytosis rate of peripheral and lung B cells was assessed (**Figure 4.39, D**). Contrasting the phagocytosis rate of ERB myeloid cells, FITC signal originating from bioparticles peaked after 10' stimulation and declined at 60'. Intriguingly, the amount of $FITC^+$ cells in the myeloid compartment was higher in adults than in juveniles, although failing to reach statistical significance. However, the amount of $FITC^+$ peripheral B cells was higher in juveniles at both 10' (21.5% mean adult and 31.7% mean juvenile) and 60' (7.5% mean adult and 13% mean juvenile). For B cells derived from unperfused lung tissue, FITC signal was comparable between adult and juvenile at 10' (5% mean adult and 4.3% mean juvenile), but higher in adults at 60' (13% mean adult and 5.6% mean juvenile). These findings were ultimately supported by MFI analysis in $FITC^+$ populations (**Appendix 10.17**). The MFI of $FITC^+$ PMNs did not differ significantly between timepoints, age groups or blood and lung (mean adult 45,669, mean juvenile = 52,270). The MFI of $FITC^+$ monocytes/DCs slightly increased in both lung and blood of adult ERB over time (mean 10' = 15,713, mean 60' = 18,454). However, MFI in blood and lung of juveniles remained unchanged (mean 8,360). While only a neglectable amount of $CD206^+$ cells could be detected in the blood of adult ERB and therefore no MFI data could be derived, The MFI of $FITC^+$ $CD206^+$ cells in the lung of adult ERB was higher than in juveniles, but unchanged by time (mean adult = 10,993, mean juvenile =7,334). Strikingly, the MFI of $FITC^+$ B cells was higher in juveniles in both blood and lung, contrasting data derived from other populations (mean adult =6,982, mean juvenile =9,494).

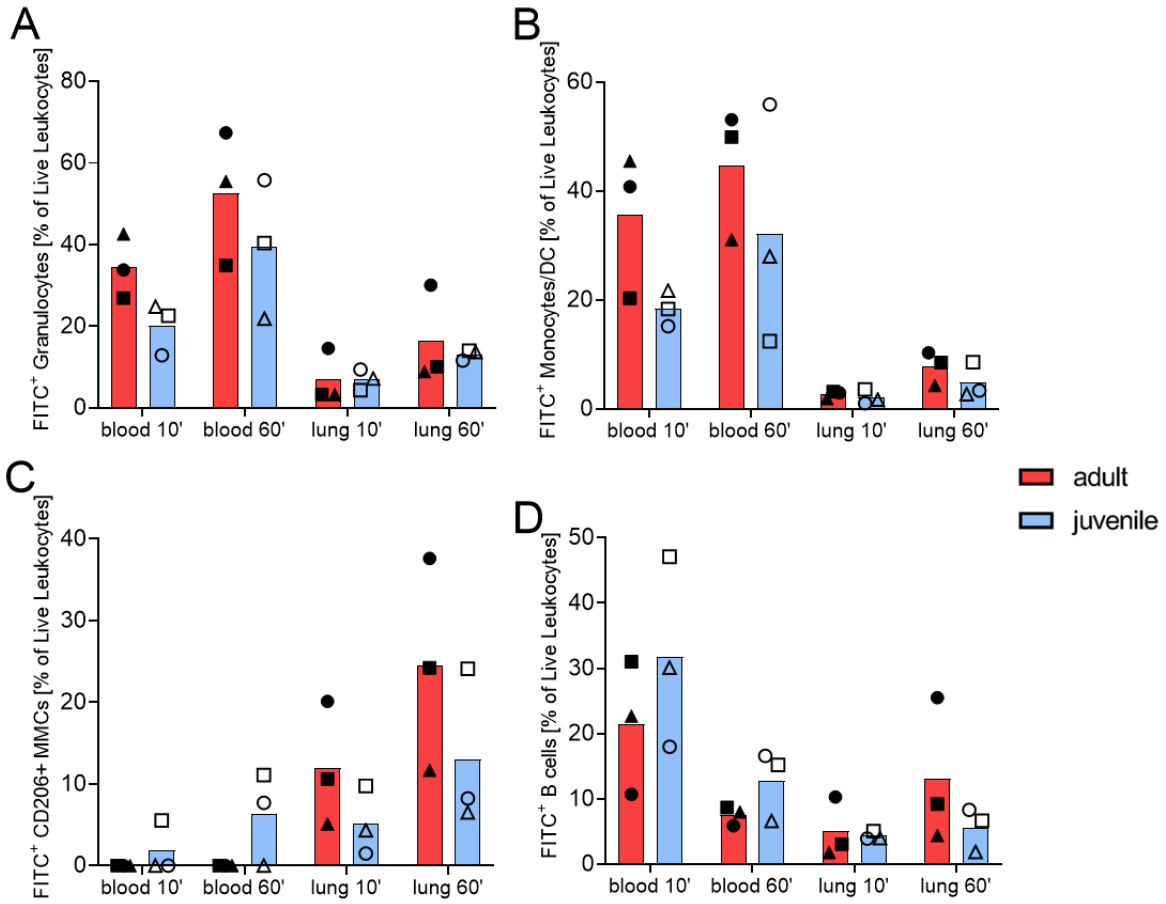

Figure 4.39 | Phagocytic capacity of myeloid cells and B cells in ERB is independent of age.
Phagocytosis of *E. coli* bioparticles (fluorescein-labelled) by PMNs (**A**), monocytes/DCs (**B**), CD206$^+$ MMCs (**C**), and B cells (**D**) was assessed using the gating strategy shown in figure 4.38. The phagocytic rate of myeloid cells (PMNs, monocytes/DCs, and CD206$^+$ MMCs) and B cells by percentage of FITC$^+$ cells within each population. Each individual is represented by a symbol, bar represents the group mean.

4.3.2.4 Abundances of lymphocytes in periphery and tissue of adult and juvenile ERB

Employing the gating strategy to identify ERB T and B cells in flow cytometry rendered significant differences in both T and B cell abundances between adult and juvenile animals. While adult bats displayed significantly higher frequencies and absolute numbers of T cells, B cells were the opposite (**Figure 4.40, A**). Frequencies of an activated T cell subset, defined as CD11b$^+$ within the CD3$^+$ population, were significantly increased in juvenile ERB compared to adults (mean 4.34% for juveniles, 1.32% for adults) (**Figure 4.40, A**). Frequencies of T and B cells in ERB are in line with recent reports from *P. alecto* and *E. spelaea*, in which a T cell enrichment in periphery could be confirmed[225,228]. However, the

exact age of these bats was impossible to determine as these specimens were wild-caught and only housed for a maximum of 6 months prior to experiments[225].

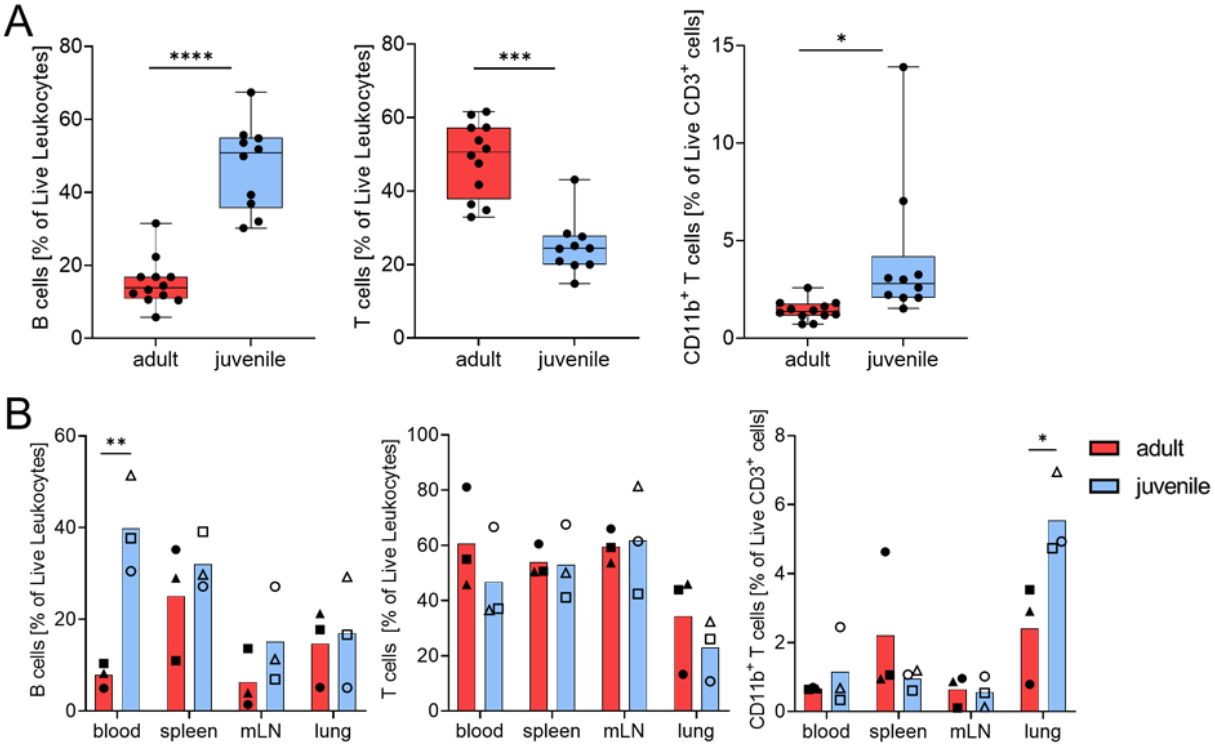

Figure 4.40 | Flow cytometry of ERB lymphocytes reveals striking enrichment of T cells in adults, as well as B cells in juveniles.
Frequencies of T and B cells, as well as a CD11b$^+$ T cell subset were assessed in periphery and lymphatic and non-lymphatic tissue. Frequencies of peripheral lymphocytes were determined with blood sampled from 12 adult and 10 juvenile ERB (**A**, male and female). Frequencies in tissue were determined with samples from adult and juvenile female ERB (n = 3/group). Each individual is represented by points (**A**) or a symbol (**B**). Statistical significance was calculated with unpaired t-test. (*) $P \leq 0.05$, (**) $P \leq 0.01$, (***) $P \leq 0.001$, (****) $P \leq 0.0001$.

To determine the distribution of T and B cells in lymphoid and non-lymphoid tissue of adult and juvenile ERB, frequencies (**Figure 4.40**) and absolute cell counts (**Figure 4.41**) were defined in tissues corresponding to analysis on myeloid cells: periphery, spleen, mLN and lung. Both frequencies and absolute cell numbers concurred for lymphocytes originating from ERB periphery. The frequencies of T and B cells differed significantly between adult and juvenile ERB, as demonstrated by up to 60.65% T cells in the periphery of adult bats compared to 46.67% in juveniles and up to 40% B cells in juveniles compared to 7.87% in adults (**Figure 4.40, B**). These findings were further substantiated by absolute cell counts (**Figure 4.41, B**). Values detected in the spleen of both age groups matches those observed in periphery (**Figure 4.40, B**). However, although similar frequencies for splenic T cells could be defined, absolute cell numbers were higher in adult bats (**Figure 4.41, A**). In line

with the findings for peripheral B cells, splenic B cells were enriched in juvenile bats compared to adults. Abundances for both T and B cells were similar in the lungs of adult and juvenile bats, whereas a tendency of B cell enrichment in mLNs of juvenile ERB could be identified (**Figure 4.40, B**). Frequencies and absolute numbers of putative activated T cells ($CD3^+CD11b^+$) were significantly higher in the lung of juvenile bats, yet only absolute counts reached statistical significance for $CD11b^+$ T cell enrichment in the periphery of juvenile ERB (**Figure 4.41, A**).

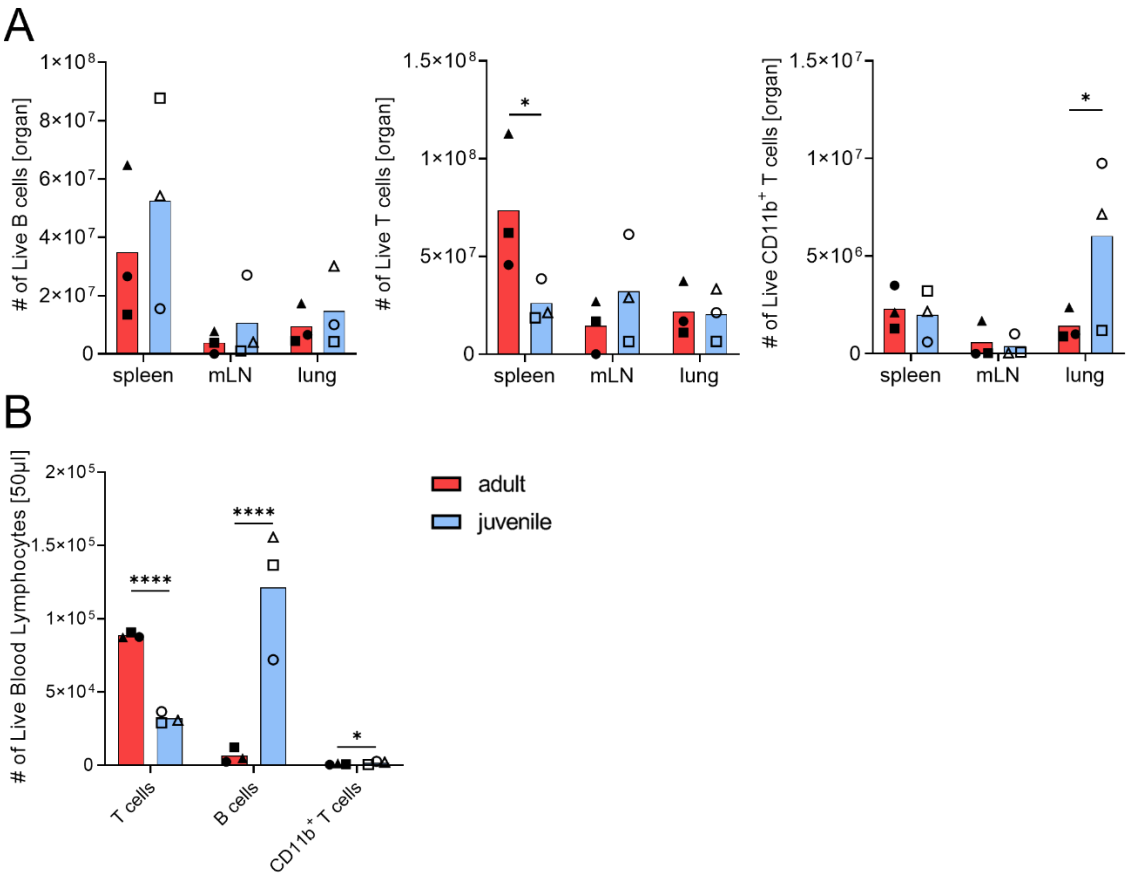

Figure 4.41 | Absolute cell number of peripheral lymphocytes is age-dependent in ERB.
Absolute cell numbers of $CD3^+CD79a^-$ T and $CD3^-CD79a^+$ B lymphocytes, as well as a $CD11b^+$ T cell subset, originating from tissue (**A**) or periphery (**B**) of adult and juvenile female ERB (n = 3/group) were calculated by including AccuCheck counting beads in flow cytometry. Each individual is represented by a symbol, bar represents the group mean. Statistical significance was calculated with unpaired t-test. (*) $P \leq 0.05$, (****) $P \leq 0.0001$.

4.3.2.5 Lymphocyte proliferation capacity is unchanged with age

To evaluate the proliferative capacity of T and B cells of ERB, PBMCs and splenocytes from adult and juvenile specimens were collected. *Ex vivo* stimulation with either ConA, LPS or SEB led to specific induction of T and/or B cell proliferation. To define proliferating cells, the gating strategy for ERB lymphocytes was expanded by including a cross-reactive Ki-67 antibody, a specific marker to detect active proliferation in flow cytometry (**Figure 4.42**).

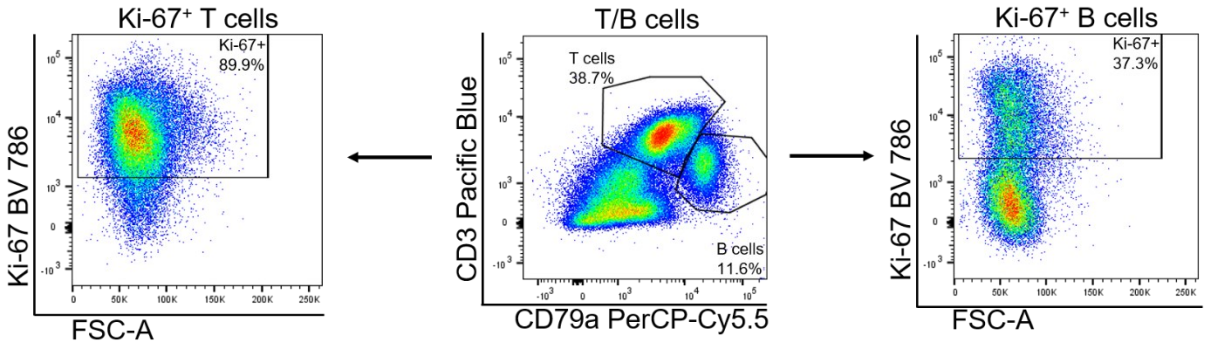

Figure 4.42 | Identification of proliferating lymphocytes in flow cytometry.
Proliferation of T and B cells was evaluated by Ki-67 staining in flow cytometry. Doublets and dead cells were excluded (not shown). T cells were defined as $CD3^{+}CD79a^{-}$, B cells were defined as $CD3^{-}CD79a^{+}$, proliferating cells within each population were defined as Ki-67^{+}. Representative stainings were selected to generate this figure.

Upon stimulation with ConA and SEB, T cells clonally expanded (**Figure 4.43**), while B cells proliferated upon LPS and SEB treatment (**Figure 4.44**), respectively. While B cell proliferation could be observed in adults and juveniles upon LPS treatment, it failed to reach statistical significance in adults (**Figure 4.44**). For T cells, the substantial spread within both age groups impeded on reaching statistical significance (**Figure 4.43**). In addition, overall proliferative capacity of both T and B cells was higher for splenocytes compared to peripheral cells. To obtain more precise results, proliferation was not only assessed by Ki-67 staining, but also CFSE dilution, respectively (**Appendix 10.18**). Proliferating cells were defined as $CFSE^{low}$ and uncovered that peripheral and splenic B cells proliferate upon SEB treatment, although less pronounced than T cells (**Appendix 10.18**).

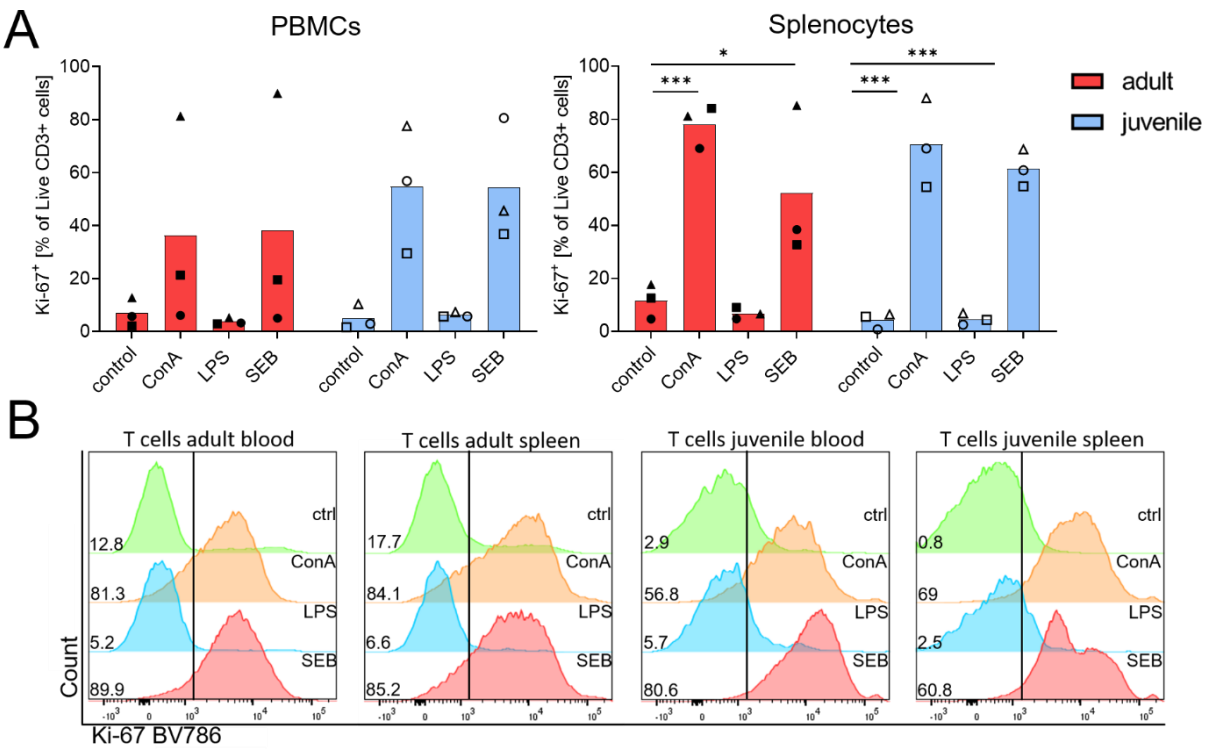

Figure 4.43 | Proliferative activity of peripheral and splenic T cells is independent of age in ERB. Proliferation in peripheral and splenic $CD3^{+}CD79a^{-}$ T cells was assessed after stimulation with ConA, LPS, and SEB for 7 days. Proliferation was measured by Ki-67 staining in each sample. Results are shown as frequencies of Ki-67^{+} T cells (**A**) and representative MFI-plots for both adult and juvenile (**B**). Each individual is represented by a symbol, bar represents the group mean. Statistical significance was calculated with unpaired *t*-test. (*) $P \leq 0.05$, (***) $P \leq 0.001$.

Overall, detection of proliferation by Ki-67 staining rendered more accurate results for splenocytes, while CFSE was more accurate for PBMCs. However, proliferative capacity of neither T nor B cells was significantly different between the age groups, as evaluated by Ki-67 and CFSE. Intriguingly, these findings indicate, although striking differences in cell abundances of T and B cells could be uncovered, that functional capacities of lymphocytes do not differ with age in ERB.

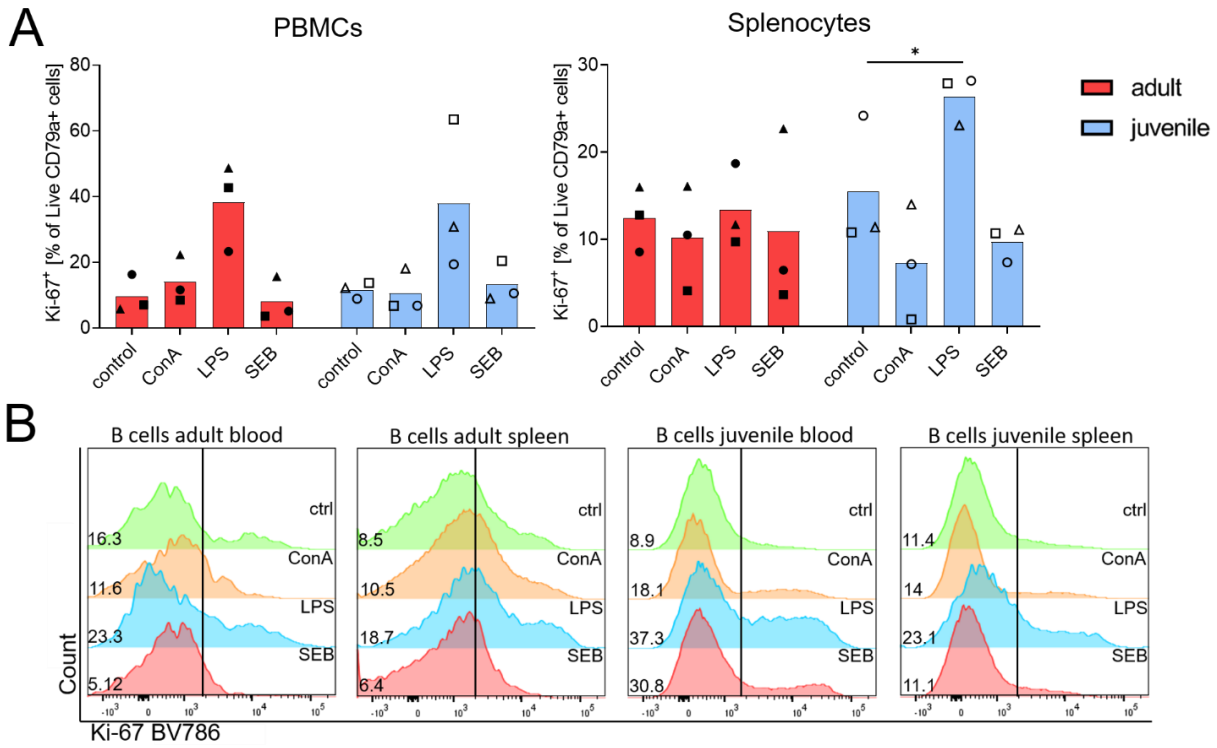

Figure 4.44 | Proliferative activity of peripheral and splenic B cells is independent of age in ERB. Proliferation in peripheral and splenic $CD3^{-}CD79a^{+}$ B cells was assessed after stimulation with ConA, LPS, and SEB for 7 days. Proliferation was measured by Ki-67 staining in each sample. Results are shown as frequencies of $Ki\text{-}67^{+}$ B cells (**A**) and representative MFI-plots for both adult and juvenile (**B**). Each individual is represented by a symbol, bar represents the group mean. Statistical significance was calculated with unpaired *t*-test. (*) $P \leq 0.05$, (***) $P \leq 0.001$.

In conclusion, establishment of immunopanels based on 8 cross-reactive antibodies lead to the successful identification of various myeloid (PMN, monocyte/DC, $CD206^{+}$ MMC) and lymphoid (T and B) cell subsets in ERB. Flow cytometry data revealed a significant enrichment of T cells in adult, and B cells in juvenile ERB. However, a $CD206^{+}$ MMC subset was enriched in adults, while a putatively activated T cell subset ($CD11b^{+}$) was enriched in juveniles. Although the functional characterization of immune cells by phagocytosis and proliferation assay did not result in significant differences between the age groups, the data indicates a shift towards immune tolerance upon immunomaturation in ERB.

4.3.3 Single-cell sequencing of circulating ERB leukocytes enables in-depth definition of leukocyte populations

Since the set of antibodies identified to exhibit cross-reactivity with ERB proteins only allows definition of the major leukocyte populations, single cell sequencing as a high-throughput and high-resolution method was employed to gain an in-depth insight into the different subsets within the major populations. These results were achieved in collaboration with Dr. Emmanuel Saliba and Christophe Toussaint (HZI, HIRI, Würzburg) which performed sequencing, annotation and transcriptomic analysis of libraries generated at the FLI as part of this work.

4.3.3.1 Transcriptomic landscape of peripheral leukocytes in ERB

To get an overview of the immune cell landscape in ERB blood, samples were collected from 3 adult and 3 juvenile individuals. Since ERB have more platelets compared to humans (haematological data, FLI), total leukocytes were sorted after lysis of red blood cells to circumvent excessive platelet contamination. Satisfactory viability (90-95%) of cells post RBC lysis (Zombie staining) and post sorting (PI staining) was achieved to ensure subsequent processing of undamaged cells (**Appendix 10.20 A, B**). Furthermore, recovery rate of cells after sorting was validated to be at least 95% to assure sequencing of all circulating subsets (**Appendix 10.20, C**). Cells of all individuals from the same age were pooled prior to cDNA generation to minimize batch effects. A total of 13,000 cells per age group were loaded onto the Chromium controller and used to generate ERB gene expression libraries. The cDNA of each age group was quantified using a HS chip run in the BioAnalyzer and the result was used to calculate subsequent cycle numbers to determine library construction input masses. The results obtained from quantifying cDNA are shown in **Appendix 10.19 A**, quality control of the generated libraries was also carried out with a HS chip run (**Appendix 10.19, B**). Libraries were sequenced and annotated according to the latest ERB genome[170], individuals were subsequently demultiplexed using Souporcell[280], which assigns each cell to a donor based on genetic variants. Each individual was equally represented in the corresponding libraries (**Appendix 10.20, D**).

In total, 11,678 transcripts were recovered, allowing selection of highly variable genes, dimensional reduction and identification as well as clustering of cell populations upon

unsupervised graph-based clustering (**Figure 4.45, A**). Low quality cells were excluded based on a characteristically high proportion of mitochondrial transcripts; doublets were defined based on factors like droplets which contained two differing genomes. Both low quality cells and doublets grouped in distinct clusters and could therefore be excluded from subsequent analysis. Cells of myeloid and lymphoid lineages were assigned into clusters based on their differentially expressed genes.

Definition of cells of myeloid identity was characterized by *ITGAM* (CD11b) and *SIRPA* (CD172a) expression (**Figure 4.45, B**). Within this compartment, monocytes were identified by exhibiting expression of *CD68* and *CSF1R*. Furthermore, two distinct granulocyte populations could be found in ERB periphery, as defined by *CSF2RB* and *CSF3R* expression. Remaining clusters in the myeloid compartment were specified by *CD68* and *IRF8* expression, therefore annotated and referred to as DCs. The lymphocyte compartment could be divided into the two major subsets: T cells, identified by expression of TCR-related components like *CD3D*, *CD3E* and *CD3G* and B cells defined by *MS4A1* (CD20) and *CD19* expression (**Figure 4.45, B**).

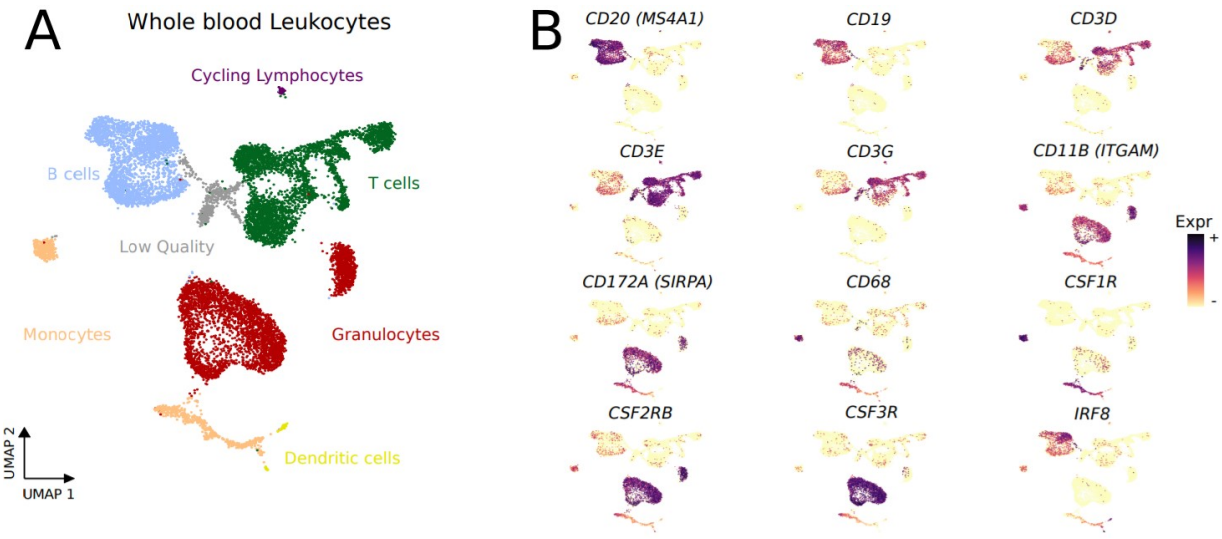

Figure 4.45 | scRNA-seq allows identification of major leukocyte subsets in ERB whole blood.
Total leukocytes from whole blood of three adult and three juvenile ERB were purified and sequenced. UMAP representation contains a total of 11,678 transcripts and cell clusters were defined based on expression of lineage markers in each cell (**A**). Clustering was performed with the Leiden algorithm. (**B**) Granulocytes were defined by expression of *SIRPA*, *CSF2RB*, *CSF3R*, and *ITGAM*, Monocytes/DCs were characterized by *SIRPA*, *CSF1R*, *ITGAM*, and *CD68* expression. T cells were identified by expression of TCR-associated markers like *CD3E*, *CD3G*, and *CD3D*, whereas B cells expressed BCR-associated components like *CD20* and *CD19*, as well as *IRF8*. Sequencing, annotation and clustering was performed by Christophe Toussaint (Helmholtz, HIRI).

To gain deeper insights into the different subsets within each compartment, the analysis was further refined to detect low-abundance subsets. A total of 21 unique cell clusters with different transcriptomic fingerprints could be delineated (**Figure 4.46, Figure 4.47**).

The number of transcripts varied between the different cell types. Granulocytes, known to belong to cells with comparably lower transcript numbers[342], had around 1,000 transcripts to be recovered, while around 5,000 transcripts could be recovered from monocytic and dendritic subsets (**Appendix 10.21**). Further refinement of myeloid clusters revealed *CSF3R* expression in the main granulocyte population, corresponding to neutrophils additionally expressing *CCRL2*, G0/G1 switch gene 2 (*G0S2*), prostaglandin-endoperoxidase (*PTGS2*) and lactotransferrin (*LTF*) (**Figure 4.46**). The main granulocyte population was divided into 3 subclusters upon refinement. However, these subclusters were not defined based on a distinct transcript signature, but the total number of expressed genes per cell. This possibly reflects technical variability or natural ageing processes in circulating neutrophils at steady state. Nevertheless, the second granulocyte population exhibited a specific transcript pattern, including expression of matrix metalloproteinases (*MMP1* and *MMP9*), transmembrane GRB2 binding adaptor protein (*GAPT*) and oligodendrocyte transcription factor 1 (*OLIG1*), as well as absence of *CSF3R* transcripts (**Figure 4.46**). These findings and the presence of leukotriene C4 synthase (*LTC4S*), *CCR3* and GATA binding protein 1 (*GATA1*) transcripts suggested the identity of eosinophil or basophil granulocytes. Further analysis revealed expression of CCAAT enhancer binding protein epsilon (*CEBPE*), *CD24* (*LOC107516222*) and proteoglycan 3 (*PRG3, LOC107518414*), leading to the final conclusion of eosinophil identity of this respective cluster.

Overall, two monocyte subsets could be defined through expression of either *CD14* or *CD16* (*LOC107502476*). Further analysis revealed that *CD14* expressing monocytes co-expressed versican (*VCAN*) and musculoaponeurotic fibrosarcoma oncogene homolog B (*MAFB,* highest expression of all clusters), while *CD16* expressing monocytes were further specified by *CX3CR1* and TNF receptor superfamily member 8 (*TNFRSF8*) expression. The remaining three clusters within the myeloid compartment rendered to be different subsets of DCs. Focusing computed analysis on the myeloid compartment revealed one DC cluster, putative cDCs cDC1, defined by C-Type Lectin Domain Containing 9A (*CLEC9A*) and *XCR1* expression, whereas putative pDCs were defined by transcription factor 4 (*TCF4*), *CD8B* and *IRF7*

expression. The third DC cluster was merged to *CD14* expressing monocytes and could be identified by specific absence of *CD14* and *CD16* expression. Furthermore, cells in this cluster expressed *IL18*, High Mobility Group Nucleosomal Binding Domain 3 (*HMGN3*) and Transcription Elongation Factor A3 (*TCEA3*), which resembles the transcriptomic fingerprint of cDC1s. However, high expression of several MHCII variants indicated cDC2 identity[343] (**Figure 4.46**).

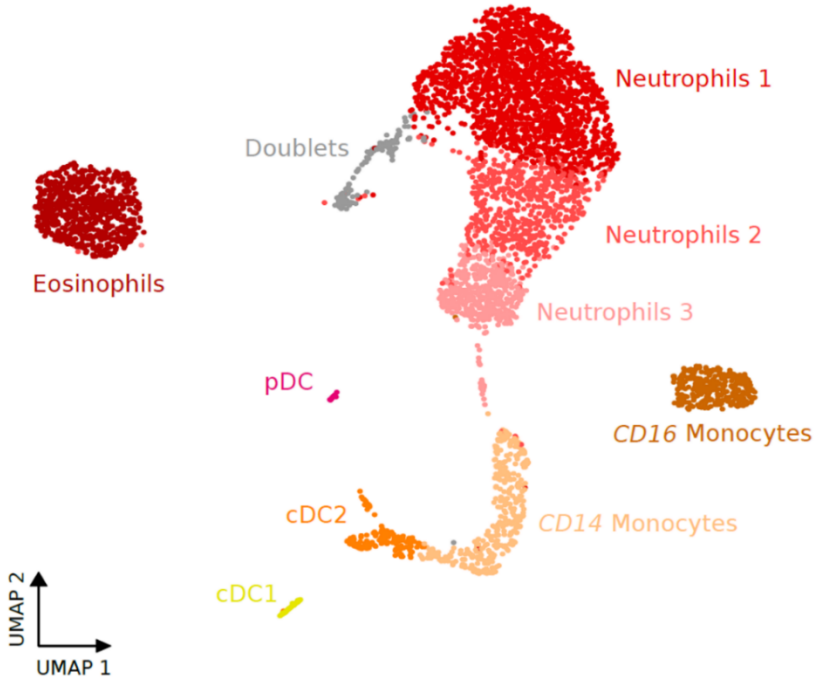

Figure 4.46 | Cluster refinement reveals distinct cell subsets within the myeloid compartment. Additional expression analysis in the myeloid compartment revealed subsets within monocytes, DCs, and granulocytes. A total of 4,540 transcriptomes is displayed as UMAP. Granulocytes could be subdivided into eosinophils (expression of *MMPs*, *LTC4S*, *CCR3*, *GATA1*, *PRG3*) and three neutrophil subsets (*CD24*, *LTF*). The DC cluster turned out to contain a pDC subset (*TCF4*, *CD88*, *IRF7*) and two cDC subsets (*CLEC9A*, *XCR1*). Monocyte subsets were defined by *CD14* (*VCAN*, *MAFB*) and *CD16* (*CXCR1*, *TNFRSF8*) expression. Sequencing, annotation and clustering was performed by Christophe Toussaint (Helmholtz, HIRI).

To gain deeper insight into the vast variety of T cells, analysis was concentrated on the lymphoid compartment. This resulted in the definition of seven specific T cell subsets. Naïve T cells were identified based on markers characteristic for naïve T cells, precisely *FST* and highest expression of *TCF7*, lymphoid enhancer binding factor 1 (*LEF1*), *and CCR7*. On the other hand, Tregs were defined by mainly *FOXP3* expression, specific for Tregs. As already described for other species, double negative (DN) T cells could be defined in ERB and were characterized by the absence of *CD4* and *CD8* expression (**Figure 4.47**). Generally, the transcriptomic profile of DN T cells resembles the one found in Tregs, but could be conclusively distinguished by expression of peptidase inhibitor 3 (*PI3*), inhibitor of DNA

binding 4 (*ID4*), *LIMA1* and *CSF1*. In humans, DN T cells are known to exhibit immunosuppressive functions, however, their exact function in ERB remains to be elucidated[344]. Furthermore, one cluster within the T cells (containing *CD4* and *CD8* expressing cells) was annotated as memory T cells due to a peculiar expression profile of *CXCR3*, *CD40LG* and *CD7*. Additionally, a *CD8* expressing cluster was further specified by the presence of transcripts associated with cytotoxic T cells. These transcripts linked to cytotoxic function were: *CXCR6*, *KLRG1*, zinc finger protein 683 (*ZNF683*) as well as markers for cytolytic activity (Natural killer cell granule protein 7 [*NKG7*] and granzyme B [*GZMB, LOC107513518*, *LOC107513519*]) and activation (*CCL5*, *CCL4* [*LOC107503311*] and *IFNG*). *CXCR6* is associated with maintenance at inflammation sites, while *KLRG1* is distinctively expressed in cytotoxic subsets. Another T cell subset was recognized by an expression pattern, exclusive for NK cells (*NCR1* [*NKp46*], Fc Epsilon Receptor Ig [*FCER1G*], *KLRB1*, *NKG2* [*LOC107516556* and *LOC107505617*] as well as *KLRD1* [*LOC107505366* and *LOC107505367*]). However, these cells also exhibited expression of *CD8*, *CD4* and *CD3* variants, especially *CD3E*, indicating NKT identity[248] with cytotoxic function (perforin [*PRF1*], granzyme M [*GZMM*] and *GZMB*). This main NKT cluster could be further divided into two distinct subsets. The larger cluster contained cells predominantly expressing granulysin (*GNLY*) and increased expression of *TBX21*, *CX3CR1* as well as *GZMB*, similar to the cytotoxic T cell cluster. The smaller subset was characterized by *XCL1* (*LOC107512753*) and *CD160*, an activating receptor on NK cells. Interestingly, they expressed comparable amounts of *CD7* and *TCF7* as memory/naïve T cells. It is of note that NKT-like clusters contained more cells co-expressing *CD4* and *CD8* than any other cluster within the T cell compartment (**Figure 4.47**).

The other major cluster within the lymphocyte compartment, the B cells, could be subdivided into four subpopulations (**Figure 4.47**). The most abundant cluster was identified by specific upregulation of placenta associated 8 (*PLAC8*), family with sequence similarity 149 member A (*FAM149A*) and double PHD fingers 1 (*DPF1*) as well as elevated expression of *S100A4*, *S100A10*, *S100A11*, *CD99* and *CD44*. Cells within this cluster were termed *PLAC8*$^{+}$ B cells and are possibly linked to activation, due to expression of *CD99* and *CD44*[345,346]. One cluster could be defined by a unique and high expression of V-Set Pre-B Cell Surrogate Light Chain 3 (*VPREB3*), A-Kinase Anchoring Protein 12 (*AKAP12*) and *CD72*.

VPREB3 is described to be involved in the assembly of the pre-B cell receptor, indicating the presence of cells at an early stage of maturation. These cells are further referred to as *VPREB3*$^{+}$ B cells. A second cluster differed from the others by exhibiting the highest expression levels of lymphotoxin beta (*LTB*), *IRF8*, *CD69* (*LOC107502080*) and *CR2*, further termed as *LTB*$^{+}$ B cells. The smallest cluster in the B cell compartment consists of cells which resemble the transcriptomic fingerprint of *PLAC8*$^{+}$ B cells, but could be distinguished by specific Zinc Finger And BTB Domain Containing 32 (*ZBTB32*) and Basic Helix-Loop-Helix Family Member E41 (*BHLHE41*) expression. These factors have been associated to activated/memory B cells and are further referred to as *ZBTB32*$^{+}$ B cells[347,348]. The final cluster in the lymphoid compartment could be identified as proliferating/cycling lymphocytes according to their PCNA Clamp Associated Factor (*PCLAF*), claspin (*CLSPN*) and Kinesin Family Member 15 (*KIF15*) expression, markers linked to active replication (**Figure 4.47**).

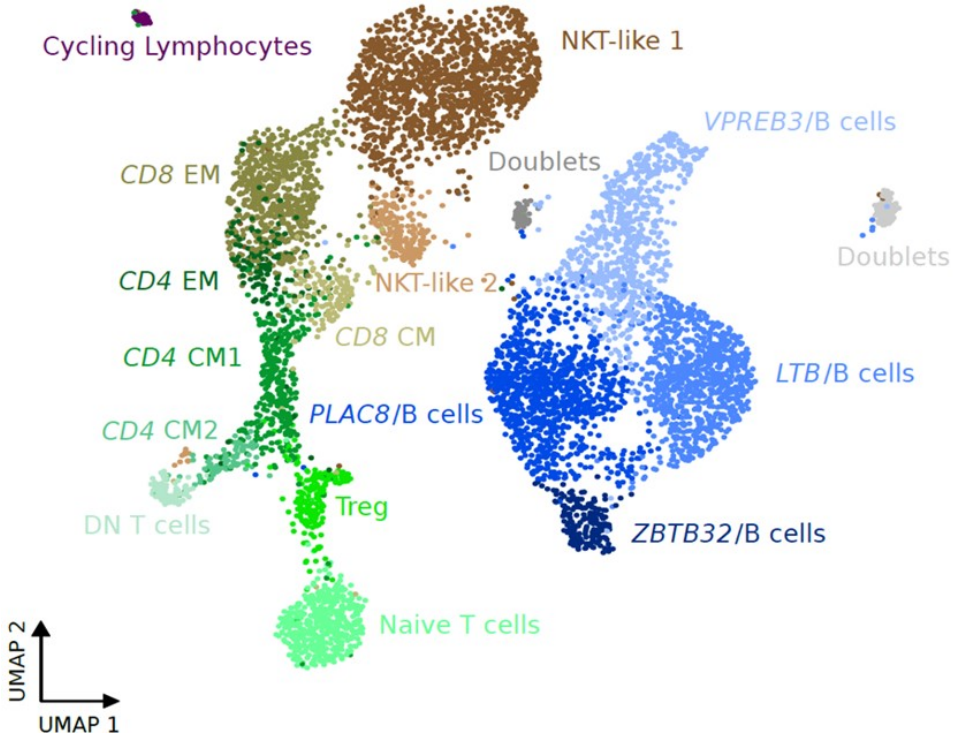

Figure 4.47 | Cluster refinement reveals unique T and B cell subsets in ERB.
Refinement of annotation and clustering of cells belonging to the lymphoid compartment revealed striking richness in T cells as well as unique B cell subsets. T cells, previously defined as *CD3E*, *CD3D*, *CD3G* expressing cells were further subdivided into: naïve T cells (*TCF7*, *LEF1*, *CCR7*), Tregs (*FOXP3*), DN T cells (absence of *CD4* and *CD8*), putative memory T cells (*CXCR3*, *CD4+8*, *CD7*), cytotoxic T cells (*CD8*, *CXCR6*, *KLRG1*, *GZMB*), as well as two distinct NKT-like subsets. These subsets are defined by *CD4*, *CD8*, *CD3*, *KLRB1*, *NCR1*, *GNLY* (subset 1) or *XCL1*, *CD160*, *TCF7* (subset 2) expression. B cells, previously identified by *CD19* and *CD20* expression, could be subdivided into four subsets. These subsets were characterized by expression of *VPREB3* (subset 1), *LTB* (subset 2), *PLAC8* (subset 3), and *ZBTB32* (subset 4). Sequencing, annotation and clustering was performed by Christophe Toussaint (Helmholtz, HIRI).

4.3.3.2 Differences in leukocyte abundances in adult and juvenile ERB could be confirmed with scRNA-seq

After successful annotation of transcripts and clustering of cells derived from ERB periphery, observations obtained with flow cytometry were sought to be verified by scRNA-seq data. Therefore, individuals were demultiplexed and grouped according to their age, resulting in separate dataset for adults and juveniles (**Figure 4.48**). Demultiplexed datasets overall support the findings obtained by flow cytometry, in regard of age-related variations in granulocyte and B cell abundance. Of note, the *VPREB3*$^{+}$ B cell cluster appears to be absent in adult ERB.

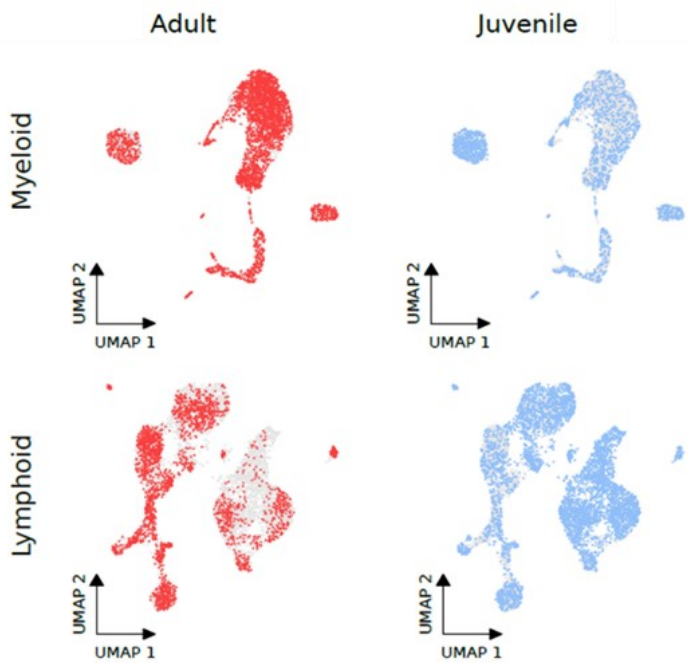

Figure 4.48 | Demultiplexing reveals striking age-dependent variations in the abundance of peripheral leukocytes in ERB.
Myeloid (**top**) and lymphoid (**bottom**) compartments are displayed as UMAPs. Demultiplexing resulted in one dataset for adults (n = 3, red) and juveniles (n = 3, blue). Sequencing, annotation and clustering was performed by Christophe Toussaint (Helmholtz, HIRI).

In conclusion, using scRNA-seq, a total of 22 immune cell subsets could be defined in the periphery of ERB. Demultiplexing of the samples allowed insight into abundances of each subset in adult and juvenile animals. The differences observed in flow cytometry (section 4.3.2) could be verified with scRNA-seq, specifically granulocytes and T cells were enriched in adults, B cells were enriched in juveniles. Separate analysis of cells within the myeloid and lymphoid compartment revealed several subsets which could not be distinguished in flow cytometry. To conclude, the advantage of flow cytometry lies within cost-effectiveness

and the possibility to phenotypically and functionally characterize samples. However, defining immune cell populations by flow cytometry is limited by species-specific antibodies. These limitations could be successfully overcome by scRNA-seq, a high-throughput method independent of species-specific antibodies. By employing both, in-depth characterization of peripheral and tissue-specific leukocytes of adult and juvenile ERB could be accomplished. Demultiplexing revealed striking age-dependent variations in the abundance of peripheral leukocytes in ERB.

5 Discussion

Especially the SARS-CoV-2 pandemic has raised the question of how bats can harbour such a plethora of viruses with shallow or even no manifestation of disease. Spillover events of bat-borne viruses already resulted in epi- and even pandemics in humans and domestic animals, with the latter often being considered as nexus between bats and humans, e.g. during NiV, HeV, MERS-CoV, and lyssavirus outbreaks[24,25,82,83,349-351]. Direct transmission from bats to humans remains also a threat to global health, as demonstrated by EBOV and possibly SARS-CoV-2[68,105].

Although recent advances have uncovered several immune-related distinctions in bats, e.g. constitutive expression of type-I-IFNs[193,203], dampened inflammasome activity[190,191,217,219], and a unique NK cell repertoire[168], the richness of species has led to the generation of isolated datasets. These datasets claim novelties in chiropteran immunity, however, mostly rely on a few selected species only, e.g. *P. alecto*[190,193] or ERB[168,203]. Therefore, coordinated research approaches delivering comprehensive studies on several species, like the Bat1K project[352], aiming to unlock general immune-related particularities in bats, are essential.

This work provides pioneer insights into the unique immunity of ERB, the main reservoir species of MARV and RAVV[74]. Due to good accessibility, this species was already used for multiple virus-associated research in the past[74,168,178,223,353]. As prerequisite for transcriptomic studies in ERB, *EEF1A1* was found to be a superior reference gene, given heterogenous tissue distribution and stability in conditions relevant in chiropteran physiology. Additionally, stability analyses revealed that *GAPDH* is inducible by type-I-IFN in ERB, hinting towards an essential role of this glycolysis-associated enzyme to immunometabolism in ERB. In the frame of this work, five immortalized cell lines as well as four primary epithelia cultures were established to study cell type-dependent innate immunity, with focus on mucosal surfaces and olfactory/neuronal tissue. It has been demonstrated that constitutive and inducable levels of type-I- and III-IFNs are highly cell type-dependent and elevated upon temperature increase. The constitutive expression of IFN and the elevation in higher temperatures suggests a strong link between ERB physiology and immune processes. Furthermore, a distinct susceptibility of ERB cells to lyssavirus

infection was observed. These differences further demonstrate the necessity of comprehensive studies to determine infection progression in infected bats and therefore allow estimations of spillover risks. Furthermore, *in vivo* data suggests variations in leukocyte abundances in adult and juvenile ERB, as well as an extraordinary abundance of circulating NKT-like cells, independent of age. These age-associated variations indicate a differing role of adult and juvenile ERB in the reservoir potential of this species. In addition, IFNγ-producing cells are likely enriched in respiratory tissue of SARS-CoV-2 infected ERB, overall suggesting a unique role of NKT/NK cells in ERB immunity.

5.1 Square one: Selection of a stable reference gene for ERB transcript studies

For accurate analysis, a reliable and thorough stable reference gene is essential to ensure accurate normalization and quantification of the genes of interest. For ERB, *ACTB*, *EEF1A1*, *GAPDH*, and *PGK1* were selected as reference gene candidates based on their previous employment in various species[190,307,354-359]. *ACTB* and *GAPDH* prevail as most widely used reference genes, while *EEF1A1* and *PGK1* were described as more stable and superior reference genes more recently[360,361]. Stability was analyzed under conditions putatively relevant for bat physiology: presence of IFN and temperature oscillations[11,168,193,220,354]. *EEF1A1* and *PGK1* rendered most stable, although values of statistical stability calculations were slightly better for *EEF1A1*, which was therefore chosen as most suitable for ERB transcript studies. Ultimately, although expression of all candidates was homogenous in several tissues, *ACTB* expression turned out to be impaired at high temperatures (40°C), while *GAPDH* rendered inducible by type-I-IFN. These findings are supported by studies with murine and human samples, as *ACTB* and *GAPDH* were described as unstable in numerous tissues, cell types, or under specific conditions[362-365]. By normalization of *GAPDH* to *EEF1A1* expression, a significant induction over time could be observed.

The inconsistency of *ACTB* expression could be explained by a switch in actin bundle dynamics upon exposure to hyperthermia, as reported for several systems[366,367]. Observed induction of *GAPDH* on the other hand, as an essential enzyme in glycolysis, leads to the hypothesis that this enzyme plays a critical role in the immunometabolism of ERB cells. It is known that metabolic reprogramming has immediate effects on cellular immune responses and is therefore applied by several leukocyte subtypes to enable quick responses to invading pathogens[368,369]. For example, aerobic glycolysis in BMDMs facilitates production of IL-1β upon stimulation with LPS or infection with *Bordetella pertussis*[370]. In lymphocytes, such as $CD4^+$ and $CD8^+$ T cells or NK cells, glycolysis is crucial for mounting their effector functions like production of IFNγ and cytotoxicity[371-377]. In human pDCs and monocyte-derived DCs, glycolysis supports production of type-I-IFNs after stimulation of TLR9 or RIG-I[378]. *Vice versa*, glycolysis is induced in an IFN-dependent manner in DCs, as well as fibroblasts, which enhances antiviral activity and antigen presentation[379,380]. As a consequence of this metabolic shift, the end metabolite, lactate, accumulates in the cell and was shown to

suppress production of type-I-IFNs by direct interaction with MAVS[381], thereby limiting overactivation and subsequent tissue damage.

For bats, it has been discussed whether high rates of glycolysis are utilized to rapidly generate ATP during flight, as demonstrated in Pallas's long-tongued bat (*Glossophaga soricina*)[382]. The role of IFN-dependent *GAPDH* expression on ERB cells and tissues remains to be elucidated. It can be speculated, that ERB use this switch in metabolism to efficiently and promptly use dietary sugars and fulfil high metabolic demands during flight[383]. In addition, downstream effects of metabolic shifts on IFN capacity of ERB cells remains to be decoded. Furthermore, *GAPDH*-mediated glycolysis could lead to novel insights into immune tolerance in bats. Besides the key role in glycolysis, *GAPDH* can induce apoptosis upon nutrition deprivation and DNA damage, by direct interaction with voltage-dependent anion channel (VDAC) inside mitochondria[384]. Additionally, inhibition of translation of *TNFA* mRNA was reported in human monocytes and macrophages[385], implying a link to restriction of excessive inflammation.

In conclusion, it could be demonstrated that common reference genes, such as *ACTB* and *GAPDH*, are not suitable for transcriptomic studies in bats. All candidates showed homogenous tissue distribution However, only *EEF1A1* and *PGK1* showed high stability under conditions relevant in chiropteran physiology, while *ACTB* rendered instable upon temperature change and *GAPDH* inducible by type-IFN.

5.2 IFN kinetics in immortalized cell lines and primary ERB epithelia

This work presents five novel and extensively characterized cell lines derived from different tissues of ERB. Given their differences in morphology, expression of various markers and mitotic properties, each cell line represents a specific cell type. As RaNep cells expressed typical markers, proteins and morphology of epithelial cells[285], these cells from the upper respiratory tract of ERB allowed insight into the regulation of immune-related transcripts in cells whose orthologs in other mammals are defined as primary sites of viral entry and shedding, e.g. coronaviruses[386] or rhinoviruses[387]. RaOlf cells on the other hand were isolated from the adjoining olfactory epithelium, a very specialized epithelial tissue within the nasal cavity, protecting the neuronal environment within the olfactory compartment[290]. OECs promote axon renewal by secreting pro-survival neurotrophins and depleting the neuronal environment of contaminations like debris and dead cells by strong phagocytic activity[388-390]. This results in the extraordinary feature of the olfactory epithelium which is unlike other neuronal compartments: due to constant turnover, neurogenesis persists in the adult organism[389,391-393]. Therefore, OECs are a unique cell type with properties of both epithelial cells and glial cells, which keep olfactory neurons permissive to axonal growth. Furthermore, OECs are efficient detectors of and responders to DAMPs and PAMPs[394], which renders them innate immune functions in the nasal cavity and subsequently led to the term 'olfactory innate immunocytes'[395]. The apoptotic rate increased in proportion of the time ERB OECs were kept in culture. This finding is in line with other reports, demonstrating that the naturally anti-apoptotic properties of OECs[396] are influenced by the purification method and failure to reinitiate the resting state after being activated via phagocytosis[395,397]. Behind the olfactory mucosa, the *N. olfactorius* poses a direct connection from the nasal cavity to the brain as shortest cranial nerve. Since this connection can be exploited by several viruses, even respiratory viruses like SARS-CoV-2[398], to invade the brain, it was essential to determine innate immunity in several cell types found along this route. RaNol cells, putative granule cell-like cells from the *N. olfactorius*[288] and RaBulb cells, putative periglomerular cells from the *B. olfactorius*[227] were identified to have inhibitory properties on mitral/tufted cell function in other mammals[227,399]. Furthermore, cells found in the *N. olfactorius* and *B. olfactorius* exhibit specialized IFN capacities in mammals, as the *B. olfactorius* is the part of the brain which is most likely exposed to environmental pathogens. These antiviral

properties were demonstrated by efficient clearance of VSV in this tissue, leading to protection of other areas in the brain from e.g. flavivirus infection[400]. Prompt viral clearance is achieved by IFN expression by cells found along the olfactory route[401], as demonstrated by high mortality of IFNAR$^{-/-}$ mice after intra-nasal inoculation with VSV[402]. In conclusion, the olfactory route, which is the path of least resistance into the brain for neurotropic viruses, enables protection of the central nervous system (CNS) by rapid, IFN-mediated clearance of transnasal virus entry. This work demonstrates that RaCer cells, radial glia cell-like cells from ERB, share immune-related features with brain tissue from mice, humans, and *P. alecto* bats, i.e. induction of type-I- and III-IFN expression after stimulation with viral mimetics[177,403,404].

Epithelial cell morphology and function are heavily influenced by high passage numbers[311]. Indeed, cultivating all ERB cell lines over passage 15 already dampened IFN response. In primary cells, this is linked to the cells converging towards the Hayflick limit (maximum of cell divisions[405]), provoked by progressing telomere shortening[406,407] and subsequent cell cycle arrest[408]. Since cell senescence is typically absent in cancer cells, dampening of IFN induction and signaling pathways is caused by defects introduced by high division numbers (i.e. excessive passaging of immortalized cells): deletions[409], dislocations[410], aberrant splicing[411], hyper-methylation of promotors[412], or dysfunctional activation[413,414]. The impairment in IFN-related responses led to utilization of cancer cells in experimental virus propagation[415]. Only ERB cells under passage 10 were subsequently used to ensure minimal alterations in biological integrity as well as reproducibility of experiments. Furthermore, it is well established that two-dimensional cultivation methods impact genetical and morphological phenotypes on various cells[304,416,417]. Especially cells which are in contact with air *in vivo* and cell lines derived from limited dilution cloning lack essential interactions and factors, e.g. polarization[418], cilia and mucus formation[419], and an apico-lateral complex with high integrity (mediated by e.g. tight junctions[420]). Since Air-Liquid interface or organoid cultures are often impractical, exclusion of significant changes in cellular phenotypes was carried out with RaNep cells, as epithelia cells are most prone to cultivation-induced alterations[416]. It could be shown that RA-induced differentiation had no effect on expression of lineage markers, as well as on expression of PRRs in RaNep cells.

Since evidence regarding extensive impairing effects of immortalization procedures[312] and excessive passaging on IFN capacity on account of cell senescence[421] could be gathered, exclusion of these effects prior to subsequent IFN-related experiments was essential. The advantage of selecting and immortalizing one single cell type is accompanied by the drawbacks related to severe changes upon artificial immortalization[304,422]. Immortalization of cells by transfecting a SV40 large T antigen-carrying plasmid is associated with alterations of immune-related processes. Most viral oncogenes used for immortalization originate from DNA viruses which evolved mechanisms to interfere with DNA sensing pathways[423-425]. These alterations include inhibition of cGAS/STING-induced activity of Interferon-sensitive response elements (ISREs) and NF-κB. Therefore, IFN induction[426,427] and cell type-dependent regulation of proliferation- and IFN stimulation-associated genes is affected[428]. For example, among the viral mimetics used to define IFN expression kinetics and magnitudes in ERB cells, ISD did not result in IFN expression. However, absence of cGAS-mediated IFN expression upon stimulation with ISD cannot undoubtedly be identified as ERB-specific trait. However, these potential limitations were ultimately overcome by obtaining similar results regarding IFN kinetics in immortalized and primary ERB cells.

Monitoring of IFN expression kinetics revealed comparable expression of *IFNA1* and *IFNB1* in all ERB cell lines. However, expression of other type-I-IFNs (*IFNA4, IFNE, IFNK,* and *IFNW*) differed in a cell type-dependent manner. Thorough studies on expression kinetics of all type-I-IFNs upon stimulation with different viral mimetics are largely missing for bats, but could be provided for ERB as part of this work. Elucidating variations in expression kinetics of type-I-IFNs in bats is of particular interest, since corresponding gene loci have evolved differently amongst bat species. As already introduced, the *IFNA* locus is contracted in *P. alecto* while being expanded in ERB, *M. lucifugus*, and *P. vampyrus*, whereas *IFNW* loci are expanded in *P. alecto* and ERB[168,187,193]. It can therefore be postulated that the entirety of genes within such an expanded locus plays a crucial role for antiviral immunity in a species-specific manner. Furthermore, these expanded loci contain a multitude of similar genes, which however vary in antiviral activity, as demonstrated for *IFNW* in ERB[167]. Type-I-IFNs are mainly produced by fibroblasts, epithelial cells, and immune cells, like monocytes, pDCs,

and lymphocytes[429]. Autocrine, paracrine or even systemic functions become effective and lead to activation of IFNγ-producing CTLs and Th1 cells[430,431]. However, viral clearance by inflammation has to be accompanied by quick initiation of resolution phase to avoid hyperinflammation and excessive tissue damage [432]. That bats hardly ever develop cytokine storms, fever, and leucocytosis has been discussed previously[433]. It was eventually shown in velvety free-tailed bats (*Molossus molossus*), as they did not develop fever or leucocytosis after being injected with 50 µg LPS, which is a high amount, considering that the animals weigh only 10-30 g[433]. Although LPS is a PAMP only found in bacteria, similar regulatory processes in bats might be in effect after detection of a viral pathogen, considering high viral loads in bat tissue in absence of excessive inflammation[269,308,434].

Some bat species were shown to exhibit constitutive expression of type-I-IFNs, as verified for *P. alecto*[435]. However, data for ERB is contradictory, since constitutive IFN expression could not be detected in primary kidney cells[168], but in PBMCs[203]. It can be assumed that absence of constitutive IFN in primary ERB kidney cells was either a result of the cells reaching the Hayflick limit or due to cell type-dependent differences in constitutive expression of IFN. In this study, not only constitutive type-I-IFN expression in various cell types derived from ERB tissue was confirmed, but also constitutive type-III-IFN expression in bat cells was reported for the first time. The observed early constitutive expression of IFN in ERB could possibly be linked to bat flight. For ERB, it could be crucial to establish an antiviral state, especially at mucosal sites, before leaving protected roosting caves. This hypothesis is supported by the differences in constitutive IFN expression observed in ERB cell lines, where constitutive expression was mainly found in cells derived from the nasal cavity (RaNep, RaOlf). These cell-dependent differences in IFN expression kinetics support variations in constitutive expression already described for ERB[168,203]. It has been postulated that constitutive expression of type-I-IFNs in bats does not result in excess cytokine production or hyperinflammation as it potentially would in other organisms, but contributes to their unique role as reservoirs for viruses[193]. In mice and humans, high IFN levels are employed on demand, e.g. after viral infection was detected[436], although low levels of constitutive *IFNB* expression have been found in various human cell types[437]. Physiological release of IFNs leads to viral clearance or impairment of replication, but excessive secretion can lead to severe side effects like tissue damage[438] and autoimmune diseases as

demonstrated for humans, e.g. systemic lupus erythematosus[439]. When first described in the 1980s, constitutive mucosal expression of *IFNB* was hypothesized to originate from constant exposure of this tissue to pathogens and damage[440]. However, low levels of *IFNB* could also be detected in mouse embryo fibroblasts without priming, which contributes to a key function of *IFNB*. These functions were defined to contribute in not only immune cell homeostasis, but also autoimmunity[437,441,442]. Later on, functional discrepancies in initiation of virus-induced and constitutive IFN expression were identified. NF-κB, AP-1 (ATF-2 and c-Jun heterodimer), and IRF3/IRF7 each bind to one of four positive regulatory domains (PRD) within the *IFNB* promotor[437]. While virus-induced *IFNB* expression is mainly regulated over activation of PRDI and III (IRF3/7)[443], it was shown that constitutive *IFNB* expression is dependent on activation of PRDII (NF-κB) and PRDIV (AP-1)[444,445]. Given the fact that bats harbour a plethora of viruses without clinical signs of disease, likely a delicate balance between efficient and constant IFN signaling devoid of the ability to mount a systemic inflammatory response syndrome (SIRS) is operative in these species[193,436,446]. It may be assumed that viruses originating from bats developed immune evasion strategies ensuring replication despite continuous release of HSPs and IFNs. As these findings emerged from immortalized cell lines, a thorough validation of the exact origin of PAMP-induced and constitutive IFN remains to be conducted. Of note, expression of several ISGs like *OAS*s, *Mx1* and *IFIT*s[435], as well as *RNASEL*[163] could already be observed in *P. alecto* cells at steady state. Whether the copies of constitutive expression in ERB are subsequently also transcribed and lead to ISG expression remains to be elucidated.

To consider the daily body core oscillations of bats, IFN expression at steady state and upon stimulation at different temperatures was monitored. It was shown that both constitutive expression and stimulus-induced responses were elevated at higher temperatures. Since cellular viability has known effects on IFN capacity[447], viability of all ERB cell lines and negligible temperature-related cell death was validated. The remarkable viability of all ERB cell lines is supposedly the result of temperature oscillations being typical for bat physiology, i.e. constitutive activation of the HSR[20], body core temperature of up to 42°C[220,448], and flight being a demanding way of locomotion[449-451]. In this context, it was shown that cells from *E. spelaea* and *P. alecto* cells survive and proliferate for days at 40°C, while pigeon cells (*Treron vernans* and *Chalcophaps indica*) underwent apoptosis after 24 h[20]. This

extraordinary survival is attributed to basal expression of the genes *HSPA1A*, *HSPA8*, and *HSPA5*, which encode for members of the HSP70 like GRP78, and whose expression levels are 200 to 400 times higher in bat than in human cells[20]. In addition, *HSP70* expression induced by high temperatures is more pronounced in bat cells compared to human, murine or even avian cells[20]. This implies a balance between adequate HSR and mounting IFN expression in a constitutive manner in bats. The advantages of this putative IFN-HSP strategy unique to bats are versatile. Thus, it becomes evident that HSP and IFN expression function in a synergistic manner in bats: HSP70 potentiates *IFNG* expression[452] while type-I- and II-IFNs enhance synthesis and stability of HSP70 mRNA[453,454]. Therefore, exposure of ERB cells to temperatures, e.g. 40°C , which would be defined as fever in most other mammals[455], did not lead to impaired viability in newly established cell lines. This implies bat-specific adaptations to the demanding conditions induces by self-powered flight, even distinct to avian adaptations.

Primary epithelial cell lines from different mucosal tissue of ERB were established to investigate immunobiology of ERB in a system more closely mimicking mucosal barriers. Data from primary ERB cells overall matched findings in immortalized cells. However, these primary cells were neither subjected to limited dilution cloning, nor artificially immortalized to minimize dampening effects on IFN capacity. It could be observed that the temperature-related difference in constitutive type-I- and III-IFN expression was more pronounced in cells from the upper respiratory tract (EpiNose, EpiTrachea), compared to those from the lower respiratory tract (EpiLung). Studies in other mammalian species, e.g. humans focused on IFN efficacy, rather than alteration of expression. It has been shown that IFNα/β[456] and IFNγ[457,458] expression and activity is slightly elevated during hyperthermia, whereas low temperatures reduce the activity of IFN[459]. Therefore, elevated expression and activity of IFN during fever is most likely true for other species. Although differential expression of type-I-IFNs in various tissue was observed in other mammals[460], temperature-associated differences in constitutive expression have not yet been defined. However, this coherence was observed in both primary and immortalized ERB cell lines. Constitutive *IFNL* expression was elevated upon temperature increased in RaNep and RaOlf cells, both derived from the nasal cavity. This leads to the hypothesis that elevation of constitutive IFNs upon

temperature rise plays a key role in the upper respiratory tract of bats. Especially the expression of *IFNL* in upper respiratory regions is critical for protection of lower respiratory regions from viral infection, as demonstrated for SARS-CoV-2[461] in humans and IAV in humans[462] and mice[463]. Unlike type-I-IFNs, type-III-IFNs exhibit both antiviral activity and tissue protective properties[464]. Therefore, initiating an antiviral state at primary sites of viral entry by type-I-IFNs benefits from tissue-protective properties of *IFNL* in addition to shared antiviral activity[465]. Since the pronounced difference in constitutive IFN expression between 37°C and 40°C was diminished after 8 h in all cell lines evaluated, an early elevation of IFN expression at primary sites of viral infection prior to foraging may be essential for chiropteran immunity. Reports on *IFNL* expression in neuronal tissue is scarce and mostly linked to TLR3 stimulation[466]. It can be speculated that constitutive expression and efficient induction of *IFNL* in the bat brain elicit protection from heat shock and invasion of neurotropic viruses into an immune-privileged tissue. The role of *IFNL* in restricting progression of viral infection into neuronal tissue by, among others, tightening the blood brain barrier was already demonstrated in West Nile virus (WNV) infection in mice[148]. Intriguingly, expression of *IFNL* was absent in EpiGut cells in all conditions tested. This is of particular interest since gut epithelial cells of mice were shown to respond solely to IFNλ[467] and human IFNλ plays a critical role in protecting gut epithelial cells from SARS-CoV-2 infection[468]. This either implicates a malfunction in type-III-IFN induction pathways in these cells or natural absence of *IFNL* induction in the upper GI tract of ERB. In *P. alecto*, type-III-IFNs are upregulated as early as 0.5 h after pI:C treatment in primary cells from lung, liver, heart, kidney, salivary gland and brain[177]. However, studies on expression of type-III-IFNs in cells or tissue derived from the bat GI tract are scarce, with only one dataset derived from *P. alecto* primary intestine existing, where *IFNL* expression was induced upon pI:C stimulation[177]. The *P. alecto* datasets were generated using immortalized cells from the lung (PaLu2) and primary cells, where only minor *IFNL* expression could be observed[177]. Overall, the findings of this work in context with previous studies indicate species- and tissue-specific differences in *IFNL* expression. Of note, not only production of, but also responsiveness of cells to IFNλ differs between mammalian species, as demonstrated by human and murine hepatocytes, where only the latter shows responsiveness to IFNλ[469]. However, whether distinctions between chiropteran species exist

cannot be concluded at this stage, since ERB data in this work is derived from cultures gut epithelial cells, while *P. alecto* data was derived from a mix of cells from the small intestine.

In conclusion, the established ERB cells and the generated results complement already existing platforms to study chiropteran immunity *in vitro*, e.g. cell lines from *M. myotis*[470], *E. serotinus*[173], *E. helvum*[471] and *P. alecto*[171]. ERB-specific constitutive and cell type-dependent expression of type-I- and III-IFNs was demonstrated. Expression of *IFNA1*, *IFNB1*, and *IFNL* were elevated upon temperature increase at steady state or stimulus-driven, especially at mucosal sites (nasal cavity). Similar findings were generated with immortalized and primary ERB cells, hinting towards ERB-specific regulation processes rather than immortalization-induced effects. The biological activity of expressed IFNs remains to be elucidated, especially in the context of antiviral activity.

5.3 Arms race: Innate cellular immunity during viral infection in ERB cells and tissue

Despite bat-borne viruses having refined immune-evasion strategies, bat cells and tissue infected with lyssaviruses did not exhibit excessive cell death even upon infection with high viral loads, as shown for *P. alecto*[66]. Dampened viral replication of ABLV in *P. alecto* cells was linked to elevated basal levels of autophagy and a further increase upon infection[66]. In this work, the susceptibility of several ERB cell lines with differing identities to lyssavirus infection was analyzed. Although lyssaviruses are adapted to neuronal tissue, moderate replication could be observed in other cell types, e.g. human/murine muscle or glandular cells[472]. This is of particular importance for viral spread, to ensure infection of neurons in immediate vicinity to the primary site of infection and transmission by saliva from rabid animals. By infecting neurons, lyssavirus infection spreads to the brain of the infected individual via the peripheral CNS. Lethality is linked to lyssavirus-induced encephalitis, however bats as reservoirs supposedly evolved mechanisms to support viral replication while possibly delaying, but not completely restraining disease manifestation. This hypothesis is supported by reports of rabies-related death in bats, as well as seroprevalence and lyssavirus mRNA detection in healthy specimens[473-475]. Additionally, previous studies confirmed host cell tolerance to ABLV using a cell line derived from *P. alecto* brain tissue[66]. Another study showed similar findings in microglia-like cells from *M. myotis* brain[470]. Given the fact that details about lyssavirus maintenance in bat colonies are largely unknown, various cell types (namely from the olfactory route to the brain) were considered in the current study. This facilitated the understanding of lyssavirus infection progression in bats, taking the knowledge about neurotropism of lyssaviruses and possibility to infect cells at mucosal sites into account. This is supported by comprehensive studies about lyssavirus distribution in infected individuals of various bat species, where non- neuronal tissues, namely nasal mucosa, were shown to be affected[476,477].

Infection of various ERB cell lines with lyssaviruses resulted in intriguing differences in regard of susceptibility. First, the virulent dog-Azerbaijan RABV isolate did not replicate efficiently in any of the cell lines. This supports previous observations of poor infectivity of field strains in cell culture, which is hypothesized to be the result of low amounts of infectious virions being released from infected cells[478-480]. SAD B19 infection resulted in

moderate replication in all cell lines except RaNep and RaBulb, while EBLV-1 replicated more efficiently in all cell lines except RaNep. Strikingly, only LBV replicate efficiently in RaNep cells. This finding has several possible explanations: (I) RaNep does not express typical receptors for lyssaviruses, namely *NGFR*, *CHRNA2*, and *GRM2,* and LBV utilizes another, unknown receptor for entry, (II) LBV is more efficient in suppressing antiviral components in ERB cells, or/and (III) RaNep cells are able to mount an antiviral state, which is superior to all other cells included in this study. The first explanation is disproved by the fact that RaNep cells expressed moderate levels of *CHRNA1* and *GRM2*, while *NCAM* expression was even highest in these cells. NCAM, another receptor utilized by lyssaviruses to infect cells, was initially identified as essential molecule for development[481] and function[482] of neuronal synapses. However, further analyses revealed non-neuronal *NCAM* expression, e.g. on cells of the hematopoietic system[483]. Given the broad and differing distribution of NCAM in other species, a unique expression in ERB can be assumed. To determine whether the innate immune responses are heterogenous among the five ERB cell lines upon infection with lyssaviruses, IFN responses were monitored in the least (RaNep) and most susceptible cell line (RaOlf). Interestingly, expression of *IFNA1*, *IFNB1*, and *IFNL* were lower in SAD B19 and EBLV-1 infected cells compared to pI:C treated control cells. However, the overall expression of IFNs was higher in RaNep cells than in RaOlf, rather supporting hypothesis (III), and assuming that lyssaviruses in this study are IFN-sensitive. Furthermore, although both LBV and EBLV-1 are bat-borne viruses with only few reported spillover events[47-49,53,54,56], susceptibility of ERB cell lines to bat-associated lyssaviruses differs considerably. While EBLV-1 infection resulted in moderate (RaOlf, RaNol, RaBulb, and RaCer) or no replication (RaNep), LBV was able to replicate very efficiently. Neither type-I- nor III-IFNs were induced by LBV after infection in any cell line, which supports hypothesis (II). Whether poor infectivity of RaNep is due to high levels of constitutive IFN expression or impaired viral entry, remains to be addressed. Abortive lyssavirus infection has been reported in green monkey (*Chlorocebus sabaeus*) kidney cells, hinting towards hampered entry in ERB RaNep. Suppression of antiviral pathways in infected cells is mainly mediated by interaction of residues 173 to 297 of the C-terminal domain of the lyssaviral P-protein with cellular STAT1/2[484,485]. It has been demonstrated that the phenotype of ABLV P protein (bat-specific virus) is functionally distinct compared to other lyssaviruses[486]. Whether this holds true for

LBV, another virus solely found in bats, and if LBV P protein interacts differently with ERB STAT1/2 or exhibits unique immune evasion strategies, remains to be elucidated. In conclusion, heterogenous susceptibility of ERB cell lines to lyssaviruses may be due to an interplay of efficient immune evasion strategies of LBV and antiviral states of varying efficiency. Since airborne transmission of lyssaviruses within reservoir species remains a matter of discussion[487-489], understanding the role of nasal epithelial cells upon challenge with lyssaviruses is critical. Data obtained herein indicates that epithelial cells derived from the nasal cavity of ERB have lower susceptibility to lyssaviruses than all other cell types tested. Furthermore, it can be assumed that LBV, as a lyssavirus with African bats as reservoir, can infect ERB cells more efficiently than EBLV-1, a lyssavirus circulating in European bats. Also, as differences in IFN kinetics amongst several bat species were already described[168,193], differing susceptibility could possibly be linked to differences in contractions and expansions in IFN loci. This is further highlighted by variations in the potency of different IFNs, as ERB *IFNW1* genes show distinct antiviral properties[167].

The mechanisms underlying cell-dependent differences in susceptibility to lyssaviruses of ERB cells remains to be elucidated. Experimental infection of *E. serotinus* with EBLV-1 resulted in extensive spread of infection, since viral mRNA was found in several organs[67]. However, these animals were infected experimentally and viral distribution differed considerably compared to naturally infected individuals[67,490]. A surveillance study demonstrated that EBLV-1 is primarily found in oro-pharyngeal areas of healthy (symptom-free) individuals[490]. In naturally infected moribund or already succumbed *E. serotinus* bats, EBLV-1 was mainly detected in brain, tongue, and lung[491]. This strongly suggests that natural lyssavirus transmission differs significantly from experimental infection routes. Similar observations regarding persistence in pulmonary tissue is currently discussed for EBOV in bats[492]. In this thesis, solely immortalized ERB cells were used and findings need to verified in unmodified cells or complexes, e.g. primary ERB cells (EpiNose), tissue derived from nasal biopsy or imaging following an animal trial.

In conclusion, the different immortalized ERB cell lines are well-suited to study bat antiviral immunity *in vitro*. The cells showed distinct susceptibility to various lyssaviruses and IFN expression patterns, induced upon infection. The role of the nasal cavity and nasal/olfactory

surfaces therein should be addressed in future studies, especially in the context of LBV infection.

As lyssaviruses are not the only bat-borne family of viruses with high zoonotic impact, expression of immune-related cytokines in primary ERB epithelia was monitored upon SARS-CoV-2 infection. This is of particular importance, since the majority of all 13,778 sequences listed in the chiropteran virome (as of January 2022[35]) belongs to the family of *Coronaviridae*[35]. Furthermore, to gain insights into expression patterns in complex tissue and not only cell culture, cytokine expression patterns were evaluated in tissue lysates derived from SARS-CoV-2 challenged ERB. All primary epithelial cells established in this work expressed the receptors necessary for SARS-CoV-2 entry. While *ACE2* expression was not affected by RA-induced differentiation, it was induced upon uIFN treatment. IFN-related induction of *ACE2* expression has been described for humans as well[326]. However, the previously observed induction of *ACE2* expression is due to an upregulated expression of a truncated isoform, which acts as an ISG[493]. To comprehensively address susceptibility to SARS-CoV-2 and specific antiviral immune responses in ERB nasal epithelia, the role of ERB proteoglycans needs to be examined. Several proteoglycans were recently described to enhance permissiveness of nasal epithelia (as attachment receptors) to SARS-CoV-2 infection in humans[494-496]. Additionally, essential pathways for SARS-CoV-2 sensing downstream to viral entry need to be evaluated in ERB cells, e.g. TLR2 distribution and signalling[497,498]. Although assessment of pro-inflammatory cytokine expression was carried out as a pilot study, first observations indicate a more pronounced cytokine production in cells from the upper respiratory tract, compared to lung and gut.

Infection of primary epithelial cells with SARS-CoV-2 resulted in observations similar to those obtained with viral mimetics, namely EpiGut being devoid of *IFNL* expression. This supports the assumption that unique IFN kinetics in cells from the ERB intestine could lead to elevated susceptibility of cells in the respective tissue to viruses, e.g. NiV, HeV, and possibly coronaviruses. Considering the rather alkaline pH pattern in the digestive tract of fructivorous bats[499], this organ system might play a crucial role for viral transmission processes and overall reservoir function. A possible interplay between alkaline pH and

absence of *IFNL* expression in GI tissue could lead to efficient, but not excessive viral replication, presumably facilitating viral spread via infectious faeces. This route of transmission is considered for NiV and HeV spread, as livestock, e.g. horses and pigs, get infected after being in close proximity to a fruit bat roosting site[500]. Furthermore, NiV and HeV infection was shown to antagonize IFN production in various *P. alecto* cell lines (immortalized and primary)[501]. The probability of henipavirus transmission by infectious faeces contaminating grass and feed of livestock could be considered in the context of IFN kinetics and alkalinity in the bat GI tract. However, the limitations of this study and the concluded hypothesis lie within EpiGut cultures being derived from a small fraction of the ERB GI tract. For comprehensibility, the pH should be evaluated for all major GI tract sections for comparison to data from insectivorous bats (stomach, duodenum, jejunum/ileum, ileum/colon, and colon/rectum[502,503]). Furthermore, different epithelial cells should be derived from the major sections and effects of pH values relevant for ERB physiology on the infectivity of different viruses (e.g. EBOV, NiV, HeV, and nCoV) should be examined.

To address the need for understanding bat immune mechanisms and their role as viral reservoirs, comprehensive *in vivo* data is essential. Since SARS-CoV-2 presumably originated from a member of the *Yangochiroptera*[106], assessment of tissue-specific cytokine profiles upon SARS-CoV-2 infection in ERB was of particular interest to evaluate ERB as possible model organism.

Interestingly, although viral mRNA was detected in various tissues and virus was transmitted to contact animals, none of the individual animals developed clinical signs of disease[504]. Being amongst the first cytokines produced upon viral infection[505], type-I-IFN is essential for induction and orchestration subsequent immune responses in multiple ways. Expression of *IFNB1* was low in the lower respiratory tract but high in the intestine, whereas *IFNA1* showed a converse expression profiles. This strongly suggests that members of the type-I-IFN family exhibit tissue-specific dynamics and exert particular functions in different tissues of infected ERB. These findings are supported by data derived from other species, e.g. mice[318,460]. It was shown that different leukocyte subtypes exhibit differences in expression of *IFNA1* and *IFNB1*. For instance, pDCs produce higher levels of IFNα than

monocytes or monocyte-derived dendritic cells upon viral infection[506]. These differences are thought to also depend on the invading pathogen and distinct expression patterns of *IFNA* subtypes. Monocytes are known to produce IFNα after infection with non-enveloped viruses, while pDCs respond more efficiently to enveloped viruses[506,507]. Additionally, type-I-IFNs were defined as key regulators of NK cell function. However, the exact origin of differentially expressed *IFNA1* and *IFNB1* and their effects remain to be elucidated in SARS-CoV-2 challenged ERB.

IFNG expression was mainly detected 4 dpi in respiratory tissue of SARS-CoV-2 infected ERB. This early expression dynamic indicates that *IFNG* was not expressed by virus-specific T cells (Th1)[327], because adaptive immunity has a delay of several days. Since production of IFNγ is exclusive to immune cells, *IFNG* expression at 4 dpi most likely originated from either NK cells[328], innate lymphoid cells (ILCs)[508], NKT cells[329], γδ T cells[330], MAIT cells[509]. The exact origin of early IFNG expression after SARS-CoV-2 infection remains to be addressed in future studies and could possibly be determined by e.g. scRNA-seq. Similarly to type-I-IFNs, IFNγ promotes maturation of DCs[510], upregulation of MHCII[511], modulation of adaptive immunity, and the generation of effector memory cells[512]. Secreted IFNγ induces NO production and release of reactive oxygen species by macrophages[513], which results in efficient antimicrobial activity. In this context, early expression of *IFNG* seemingly plays a critical role in tissue-specific antiviral immunity in ERB. However, upregulation of pro-inflammatory IFNs not only boosts inflammation, but also actively suppresses differentiation of immune cells into anti-inflammatory phenotypes (e.g. macrophages exhibit the pro-inflammatory M1 rather than the anti-inflammatory M2 phenotype[514]). The fact that bats do not develop excessive tissue damage or clinical signs of disease, strongly suggests that immunopathological effects of IFNs are rapidly antagonized without impairing clearance of infection. This is in line with recent reports demonstrating that IFNγ counteracts local hyperinflammation and tissue damage by suppressing proliferation and cytokine production of tissue-resident leukocytes[515,516].

Interestingly, in ERB expression of *IFNL* was most pronounced in the lower respiratory tract, despite the upper respiratory tract being the tissue with highest viral burden. These findings suggest *IFNL* as possible essential mediator of protection against infection with respiratory viruses. Furthermore, *IFNL* transcripts were low abundant systemically in infected ERB.

This indicates a highly tissue-specific role of *IFNL*, likely both in clearance of infection and tissue regeneration, as previously described for other species[517,518]. However, since *IFNL* expression was detected in the small intestine of infected individuals, it contradicts the findings generated with primary gut epithelial cells. It can be postulated, that *IFNL* expression plays a key role in antiviral immune processes at various mucosal sites in ERB after infection with SARS-CoV-2[518], but shows strict cell type-specificities.

IL1B[519] transcripts were detected in infected tissue, contrasting the recently described absence of *IL1B* expression and IL-1β precursor cleavage, due to impaired inflammasome activity in cells from *P. alecto* and *E. spelaea*[190]. However, *P. alecto* and *E. spelaea* data was derived from cells only, which does not allow concluding on whether these are tissue-specific or species-specific differences. A putative difference between species could result in distinct reservoir function of respective bat species. Furthermore, biological activity of the upregulated cytokines needs to be evaluated in future studies, since counter-regulating pathways are mutually expressed at early timepoints (e.g. *IL1B* and *IFNB1*[520]). Expression of *CXCL10* was most pronounced in affected tissue 4 and 8 dpi, while *IL10* expression was slightly delayed, which supports the general observation of bat ISGs having comparable function and dynamics as ISGs in other mammalian species[169,216]. However, quantification and functional characterization of ERB CXCL10 and IL-10 molecules and other ISGs remain to be executed and have to take species-specific properties of ISGs into consideration[214].

In conclusion, a pilot infection study revealed an intriguing difference in IFN expression kinetics of primary bat epithelia upon SARS-CoV-2 infection. EpiGut was shown to be devoid of *IFNL* expression, which could imply a distinct role of the bat GI tract in viral transmission processes. Furthermore, tissue-specific expression of pro- and anti-inflammatory cytokines upon SARS-CoV-2 infection has been described in this thesis. The data delivers pioneer insight into *IFNG* expression upon viral infection in ERB, e.g. primarily early expression. These analyses are limited, however, by their inability to define exact origins of cytokine mRNA. Definition of cellular origin would considerably advance the understanding of distinct features of chiropteran immunity. These emerging questions could be answered by scRNA-seq, which allows characterization of immune-related transcripts at single cell

resolution. However, experiments with highly pathogenic viruses require special containments, which is often accompanied by impracticabilities for high-throughput methods based on prompt analysis of viable cells. Another limitation of this study is the lack of protein quantification, which would allow correlation calculations between mRNA levels and protein level. This step would be crucial for understanding the biological impacts of transcribed mRNA, since it is known that mRNA:protein ratios can differ significantly, with transcript levels being considerably higher than actual protein levels[521]. Comprehensive studies on post-translational modifications and post-cleavage maturations would also yield essential insights for ERB and chiropteran immunity. Furthermore, analysis of immune-related transcripts (and proteins) at timepoints prior to 4 dpi is essential, especially since many pro-inflammatory cytokines are produced very early after infection.

5.4 Age-dependent immune cell landscape at steady state

Pioneer studies on chiropteran leukocytes date back to the 1980s, providing first morphological and functional analyses of Ig-bearing lymphocytes in *P. giganteus*[230,231]. In this thesis, ERB leukocytes from blood, mLN, spleen and lung were characterized by flow cytometry. This phenotyping revealed notable distinctions in frequencies and numbers of circulating granulocytes and lymphocytes in adult and juvenile ERB. Furthermore, phagocytic cells as well as proliferative lymphocytes were functionally characterized in several tissues, which did not appear to be age-dependent. To overcome the limitations resulting from the paucity of species-specific tools, scRNA-seq was employed and revealed 22 unique leukocyte subsets in the periphery of ERB, contributing identification of leukocyte subsets which could not be defined by flow cytometry, e.g. T ($CD4^+$, $CD8^+$, memory cells) and B cell (*LTB*, *PLAC8*, and *ZBTB32* expressing cells) subsets, NKT cells and DC subsets (pDC/cDC).

Abundances of T and B cells differed significantly between adult and juvenile ERB. While T cells were found to be enriched in adults, B cell abundances were significantly elevated in the periphery of juvenile ERB. These findings are in line with reports on lymphocyte abundances in adolescents and elderly[522,523], however, the difference between the age groups was even more pronounced in ERB. Furthermore, a putative activated T cell subset, defined as $CD3^+CD11b^+$, indicates the presence of highly reactive $CD8^+$ T cells[334] in juvenile ERB. This difference between the age groups suggests features either associated to disease tolerance in the lymphoid compartment of ERB, or maturation of the juvenile immune system. The functional analyses yielded first insights into delayed immune responses in pteropid bats compared to mice and humans. Functional characterization of lymphocytes from other bat species, *P. alecto* and *E. spelaea*, led to comparable results by demonstrating a delayed response of peripheral and splenic lymphocytes to mitogenic stimulation[224,225]. These data have provided detailed insight into proliferative capacity and cytokines produced in the course of stimulation, by identifying and employing bat-specific and cross-reactive reagents[224,225]. The functional properties of *P. alecto* lymphocytes support hypotheses related to delayed and dampened immune responses in bats compared to other mammals. By assessing the proliferative capacity of peripheral and splenic ERB lymphocytes, it could be demonstrated that lymphocyte responses to mitogenic stimulation is largely comparable

between pteropid bat species., e.g. *P. alecto*[224,225] and *E. spelaea*[225]. However, comparative studies between adult and juvenile bats in this work allowed definition of age-dependent differences in functionality of different leukocytes, e.g. only splenic B cells from juveniles proliferate significantly after stimulation with LPS. This indicates that B cells of juvenile ERB execute functions that are largely dominated by regulatory features in adult individuals[522]. These age-dependent differences in B cell reactivity are not exclusive to bats, since similar findings were reported for human B cells. The observations are related to vaccination and effectivity of various adjuvants[524]. Furthermore, characterization of ERB leukocytes was carried out with samples derived from the FLI ERB breeding colony. This did not only enable exact determination of the age of the individuals, but also ensured largely homogenous microbiomes, since quarantine conditions minimize introduction of environmental pathogens. Known age and unchanged microbiome facilitated data interpretation and reproducibility by lower variance, compared to wild-caught bats with unknown age or microbial exposure[224,225,228]. The importance in considering these factors is especially highlighted by significant differences in leukocyte frequencies and numbers between adult and juvenile bats, as demonstrated for ERB.

Considerable differences were found especially in granulocyte and lymphocyte frequencies between the age groups. Strikingly, granulocyte frequencies reported in captive ERB (23% adult, 14% juvenile) varied significantly from abundances reported for other species like *P. alecto* (45% in wild-caught individuals of unknown age[525]). These differences could be explained by either species-specific differences, habitat-associated factors, or differing precision of assays. The high variation within granulocyte frequencies of one age group, especially adults, strongly suggests that different frequencies are due to varying stress exposure, physiological stages or involvement in mating seasons. Free-ranging bats are continually confronted with microorganisms and environmental stress factors, e.g. extreme climatic changes or predators, hampering the definition of steady state under field conditions. It is long known that numerous stress factors result in an increase of circulating granulocytes within 1-2 h[526-531]. Hygiene, steady temperatures and access to food and water will reduce the stress levels of the individuals, resulting in a decrease of circulating granulocytes and differences between wild and captive individuals, as demonstrated for mice[532]. The variation within one ERB age group might be explained by the fact that samples

were taken over a course of 1.5 years and a change in stress within this year due to mating and nursing seasons. Differences between adult and juvenile ERB could be explained by changing abundances during immune maturation, as reported for humans[523]. This highlights the importance of long-term surveillance of leukocyte frequencies in both wild and captive ERB, ideally in respect of age.

The phagocytic activity of myeloid cells and B cells was comparable between the age groups. However, phagocytosis by myeloid cells was slightly elevated in adults, whereas the phagocytic activity of B cells was more pronounced in juveniles. Overall phagocytic activity of PMNs was slightly inferior to human or murine counterparts[533]. An impairing effect by sedation with volatile gases should be considered, since consequences of restraint and anaesthesia on physiology are well-studied[534,535], especially in winged animals[536-538]. However, restraining effects on leukocyte functionalities are diminished quickly upon completion of sample collection as isoflurane mainly affects neurons. Therefore, species-specific differences are likely, as already mentioned in the context of delayed responses of lymphocytes. Phagocytosis rates of ERB B cells were comparable to rates reported for B1 B cells, the human Raji B cell line[539] or primary human follicular B cells[540]. High phagocytic rates of peripheral B cells in ERB indicate bat-specific functionalities or differing distribution of phagocytic B cell subsets in ERB[541]. Of note, the presence of highly phagocytic B cells with potent microbicidal abilities in blood was already described for several species of teleost fish[340]. This could imply unique B cell features, potentially linked to antigen presentation by B cells, exclusive to phylogenetically old species. Additionally, a decline of the phagocytic activity of myeloid cells and possibly B cells is related to age, as previously described for mice and humans[542,543]. However, the actual role of each leukocyte subsets for microbial killing dynamics in ERB remains to be elucidated.

WGS and transcriptomic data, provided by e.g. the Bat1K project[352], already allowed valuable insights into immune-related transcripts in bats by describing the immune-genetic fingerprint in various bat species[168,170,178,179,190,191]. However, by combining flow cytometry and scRNA-seq, leukocytes of adult and juvenile ERB could be characterized on transcriptomic, protein, and functional levels. Flow cytometry data was supported by scRNA-seq, e.g. by validating age-dependent differences in abundance of granulocytes and lymphocytes, while the differences in T cell abundances observed in flow cytometry were

less pronounced. Ultimately, employment of high-throughput methods allowed in-depth characterization of bat leukocytes and therefore detailed insights in chiropteran cellular immunity.

Identification of bat immune cells at single cell resolution was already carried out with tissue samples from *R. sinicus*, the putative origin of SARS-CoV-2[102]. Comparing ERB and *R. sinicus* leukocyte clusters greatly facilitates definition of transcriptomic characteristics of leukocytes of *Yinpterochiroptera*. Comparative analyses unveiled striking differences in the abundance in the lymphocyte compartment. In the periphery of *R. sinicus*, *CD4* expressing T cells are largely missing[544], while no significant difference in abundance of *CD4* or *CD8* expressing T cells could be observed in ERB periphery. An explanation for these variations might be species-specific differences in $CD4^+$ T cells frequencies, aforementioned variations between free-ranging and captive animals or considerable variances in *CD4* sequences. Both NKT-like subsets (NKT-like 1 = *KLRB1*, *NCR1*, *GNLY*, NKT-like 2 = *XCL1*, *CD160*, *TCF7*) in ERB resemble transcriptomic fingerprints of NKT cells and are found in *R. sinicus* in similar abundance[544]. Although NKT cells and activated NK cells share the majority of receptors, these clusters could finally be identified as NKT cells by verifying presence of *CD4*, *CD8*, and *CD3* transcripts, classical markers for cells of the T cell lineage[545]. The intriguingly high abundance of these cells in the periphery of ERB implies a major role of NKT-like cells in chiropteran immunity. Considering the humongous expression of *IFNG* in respiratory tissue of SARS-CoV-2 infected ERB, tissue-resident NKT-like cells could be major contributors of early *IFNG* and putative key actors in efficient viral clearance.

Regarding B cells, *LTB* and *PLAC8/ZBTB32* expressing B cells exhibit transcriptional similarities with putative naïve and activated subsets defined in *R. sinicus*[544]. Absence of *VPREB3* expressing B cells in *R. sinicus* could imply differences between these two species or substantial differences in sample preparation and/or data analysis. However, since this B cell cluster is absent in *R. sinicus* and data was presumably derived from adult specimens and not adult and juvenile, these two species likely share age-dependent dynamics of *VPREB3* expressing B cells. It can be assumed that *PLAC8* expressing B cells play a key role in B cell phagocytosis and microbial killing, since *PLAC8* (≙ *Onzin*) expression is essential for effective microbial killing, e.g. in neutrophils[546]. *PLAC8* deficient cells are not impaired in their ability to phagocytose, but killing properties are significantly hampered[546]. It has

been shown that *PLAC8* is primarily found in lysosomes, co-localising with lysosome-associated membrane protein 2 (LAMP2), which indicates high lysosomal activity in *PLAC8* expressing B cells in ERB[547]. The putative microbicidal properties of this cluster is further underlined by the fact that *Onzin* mRNA could be detected in B cells of other species[546] and only a fraction of all ERB B cells was MHCII^{high}, and effectively phagocytosing bacteria. Putative plasma cells in ERB periphery could be defined by expression of *TNFRSF17*[548], *TXNDC5*[549], and *XBP1*[550], which was found to be exclusive to B cells which simultaneously express *ZBTB32*. However, the annotation of B cells presented in this work remains fragmentary, since precise annotation was impaired by unique transcriptomic fingerprints of ERB B cells, e.g. absence of Ig heavy chain (*IgH*) transcripts or annotations. Nevertheless, expression of *LTB*, *PLAC8*, and *VPREB3* in human B cells corresponds to naïve, activated and transitional B cells, respectively[551]. Based on the annotation of human B cells, especially transitional B cells are essential for ERB immunity. Whether the differences observed between ERB and *R. sinicus* are age- or annotation-related or valid species-specific peculiarities remains to be elucidated.

The fundamental differences in immune cell abundances in adult and juvenile ERB strongly suggest age-related variations in susceptibility to infections. Thus, individuals of various ages most likely have different roles in the reservoir function of ERB. This hypothesis is supported by seasonal pulses of MARV circulation in bats and human infection[272]. The periodic increase in the risk and documentations of MARV spillover events from bats to humans correlate with birthing seasons of ERB, although a small offset was defined. This offset is possibly due to the afore mentioned unique reservoir function of juvenile ERB[272]. Once the nursing period ends, weaned ERB pups are forced to the edges of the colony Since ERB are cave-roosting bats, individuals which are not allowed in the colony center are in close proximity to cave entrances. These individuals, 4-6 months of age, exhibit higher susceptibility to MARV infection than adult specimens. This is demonstrated by 2-3% of active infection in newborn pups and adults, compared to 15% of active MARV infection in juveniles[73,74,272]. The documented MARV cases in humans all correlate with the presence of ERB juveniles at cave entrances. A total of five MARV spillover events is documented[73,74,552-554], amongst which are tourists and miners, infected upon entering caves populated by ERB in Uganda[553] and the Democratic Republic of Congo[552], respectively.

Overall, single cell profiling revealed substantial differences in leukocyte frequencies between adult and juvenile ERB. Enrichment of putative regulatory cells (e.g. $CD206^+$ MMCs) strengthen the hypothesis that ERB prioritizes a fast initiation of tolerance to disease after infection, minimizing downstream reactions e.g. humoral responses. Supporting data could be generated during experiments in other bat species, naturally and experimentally infected with NiV, MERS-CoV, SARS-CoV-2, Bat CoV, Bat IAV, and EBOV. Upon infection, the bats did not develop clinical signs of disease, only minor inflammation at infection sites and moderate humoral responses, although partly exhibiting high viral loads in affected tissue[267-269,308,504,555]. In conclusion, observed leukocyte frequencies in adult and juvenile ERB indicate a state of prioritizing immune tolerance in ERB, which is reached upon immune maturation.

6 Outlook

This work provides detailed insights primarily into the innate immune response of ERB. A suitable reference gene has been identified[556] and immune-related transcripts were monitored upon both stimulation with viral mimetics and experimental infection with zoonotic viruses originating from bats. Furthermore, abundances and function of circulating and tissue-resident immune cells was successfully assessed by flow cytometry, while scRNA-seq analyses of ERB leukocytes allowed identification of elusive leukocyte subsets at a single cell resolution.

Comprehensive stability analyses of different reference gene candidates presented in this work now enable precise quantification of ERB transcripts in conditions relevant in chiropteran physiology[11,22,203,220]. Recent reports already described *ACTB* and *GAPDH* as instable in various tissues, cell types, or under specific conditions in other mammals[362-365]. Whether these commonly used reference genes are temperature-sensitive or IFN-inducible in other bat species, remains to be elucidated. *EEF1A1* is a superior reference gene for transcriptional studies in ERB, but its suitability needs to be verified in other bats.

By providing thorough insights into expression regulation of ERB IFNs at steady state or upon stimulation and viral infection, this work further facilitates the understanding of chiropteran IFN biology. Quantification of IFN transcripts in newly established ERB cell lines not only revealed constitutive expression of type-I- and III-IFNs with cell type-dependent magnitudes, but also elevated expression in higher temperatures. The findings of this work confirm the hypothesis of constitutive IFN expression in bats for ERB on a transcript level[193,203]. Several questions emerge based on the results in this thesis, which remain to be answered in future studies. First, the downstream effects of constitutive and temperature-dependent IFN expression should be evaluated. Expression of IFN at steady state should result in expression of ISGs, which can be quantified by utilizing newly established primers and normalization to *EEF1A1*. Furthermore, it is of utmost importance to determine whether constitutively expressed IFNs hamper viral replication or even viral entry. It was previously postulated that constitutive expression of IFNs, especially at primary sites of viral infection, results in lower susceptibility to viral infection in bats[30,193,557]. This can be achieved by

employing the newly established cell lines and compare viral entry in these cells, and their IFNAR1/2$^{-/-}$ and IFNLR/IL-10R$^{-/-}$ counterparts. Since KO of respective IFN receptors would render the cells unresponsive to the constitutively expressed IFNs, differences in viral entry dynamics could be associated with the loss of constitutive IFN expression. In addition, the elevated IFN expression kinetics at higher temperatures need to be considered in future studies. It remains to be elucidated whether constitutively expressed IFNs inhibit viral entry and replication in ERB cells, as assumed for lyssaviruses. This question could be addressed by executing comparative infection studies, with ERB cell lines experimentally infected at 37°C and 40°C. However, execution of such experiments remains challenging due to limited capacities in high-containment facilities. Furthermore, validation of especially constitutive IFN expression needs to be validated in vivo, e.g. using biopsies from certain tissues.

The findings presented in this work serve as foundation for following studies focusing on interactions between bat cells and bat-borne viruses. In this context, the striking differences of ERB cells in susceptibility to lyssa- or coronavirus infection needs to be studied in detail. Whether the inability of EpiGut cells to express *IFNL* post SARS-CoV-2 infection needs to be analyzed and verified by infection with other bat-borne viruses. In addition, immune evasion strategies exhibited by bat lyssaviruses should be characterized in detail to be able to determine possible spillover risks of newly isolated and sequenced variants. A possible approach would be an in-depth characterization of the interactions between components of bat-specific lyssaviruses with bat cells. Whether the P protein of bat-specific lyssaviruses exhibits distinct interactive features, such as differing nuclear trafficking and STAT1 antagonism in two circulating ABLV lineages (ABLVi, ABLVf)[486], can be elucidated by utilizing the ERB cell lines established in this work. It is especially evident that LBV possesses a unique mechanism to inhibit expression of type-I- and III-IFNs in infected ERB cells. This feature could be key to the enhanced susceptibility of ERB cells towards LBV virus. Since *E. helvum* has been identified as reservoir for LBV, future studies should consider executing comparative studies with ERB and *E. helvum* cells. The pipeline of establishment and characterization of cells from pteropid bats can be utilized to generate a corresponding set of cells from *E. helvum*. The FLI possesses an unparalleled infrastructure for such studies, as ERB and *E. helvum* breeding colonies are maintained under standardized conditions.

This work also provides protocols to monitor immune cell frequencies and absolute numbers in blood, as well as lymphatic and non-lymphatic tissue of ERB. Establishment of immunostaining panels allow definition of circulating and tissue-resident myeloid and lymphoid cell subsets. Furthermore, precise strategies to purify leukocytes from ERB blood resulted in the definition of leukocyte subsets, which remained elusive until now, at a single-cell resolution.

The flow cytometry and scRNA-seq pipelines presented in this work provided pioneer insights into the immune cell landscape of adult and juvenile ERB at steady state. These protocols could be employed in future infection studies to monitor leukocyte dynamics in ERB after viral infection. This work not only delivers reliable tools to analyse ERB leukocytes, but also detailed insights into steady state dynamics, which can subsequently be used as reference for future infection studies. Using scRNA-seq, a striking abundance of NKT-like cells in adult and juvenile ERB was unveiled. Considering abundance and presence in both age groups, these cells possibly play an essential role in chiropteran immunity. It was demonstrated recently, that ERB NK cells exhibit more inhibitory than activating motifs in their receptors[168], which is significantly different to human or murine counterparts[558]. However, since ERB-specific tools are still scarce, functional characterization of these cells specifically remains challenging. One possible approach could utilize more targeted scRNA-seq analyses by identifying transcripts, which are unique or even exclusive to this cluster. By *in silico* translation of these transcripts, immunogenic peptides could be defined and artificially generated to allow production of monoclonals specific to NKT-like cells in ERB. Monoclonals distinctly targeting surface molecules would enable sorting of these populations and functional assays *in vitro*, adding value to the already existing α-CD19 and α-CD14[223]. Furthermore, regulatory features, putatively obtained during immunomaturation in ERB, should be analyzed in detail. Evidence supporting this hypothesis are presented in this work by demonstrating enrichment of $CD206^+$ MMCs (M2 phenotype) in adults and reactogenic $CD11b^+$ T cells in juveniles. Future experiments should consider the possible development of an innate memory and regulatory features upon maturation (as reviewed for other species[559]), which could account for the unique reservoir function of bats.

Altogether, the findings in this thesis provide comprehensive insights into ERB immunity *in vitro* and *in vivo*. These findings include a cell type-dependent constitutive expression of type-I- and III-IFNs in immortalized and primary ERB cells. Together with elevated IFN magnitudes in higher temperatures, these results support the hypothesis that the unique physiology of bats amplifies IFN expression, at steady state and upon stimulation. Of note, the immortalized ERB cells exhibit differential susceptibility to various lyssaviruses, verifying them as suitable model to study ERB- specific antiviral immunity *in vitro*. Furthermore, monitoring of immune cell frequencies and function in adult and juvenile bats as well as definition of all subsets found in the periphery indicates the development of regulatory features, obtained upon immune maturation. For future infection studies, analysis of leukocyte dynamics and tissue-specific expression of immune-related transcripts in challenged ERB would generate comprehensive immune-related datasets. These datasets would immensely facilitate the general understanding of chiropteran immunity, especially in the context of viral infections.

7 References

1 Simmons, N. B. & Cirranello, A. L. Bat Species of the World: A taxonomic and geographic database. *American Museum of Natural History* (2021).

2 Teeling, E. C. *et al.* A molecular phylogeny for bats illuminates biogeography and the fossil record. *Science* **307**, 580-584, doi:10.1126/science.1105113 (2005).

3 Fenton, M. B. & Simmons, N. B. *Bats - A World of Science and Mystery*. (The University of Chicago Press, 2015).

4 Benda, P., Vallo, P., Hulva, P. & Horáček, I. The Egyptian fruit bat *Rousettus aegyptiacus* (*Chiroptera: Pteropodidae*) in the Palaearctic: Geographical variation and taxonomic status. *Biologia* **67**, 1230-1244, doi:10.2478/s11756-012-0105-y (2012).

5 Simmons, N. B. & Conway, T. M. Evolution of ecological diversity in bats. *University of Chicago Press* (2003).

6 Fleming, T. H., Geiselman, C. & Kress, W. J. The evolution of bat pollination: a phylogenetic perspective. *Ann Bot* **104**, 1017-1043, doi:10.1093/aob/mcp197 (2009).

7 Dumont, E. R. & O'Neal, R. Food Hardness and Feeding Behavior in Old World Fruit Bats (*Pteropodidae*). *Journal of Mammalogy* **85**, 8-14, doi:10.1644/bos-107 (2004).

8 Greenhall, A. M. S., U. Natural history of vampire bats. *CRC Press* (2018).

9 Start, A. N., McKenzie, N. L. & Bullen, R. D. Notes on bats in the diets of Ghost Bats (Macroderma gigas: Megadermatidae) in the Pilbara region of Western Australia. *Records of the Western Australian Museum* **34**, doi:10.18195/issn.0312-3162.34(1).2019.051-053 (2019).

10 Kunz, T. H., Braun de Torrez, E., Bauer, D., Lobova, T. & Fleming, T. H. Ecosystem services provided by bats. *Ann N Y Acad Sci* **1223**, 1-38, doi:10.1111/j.1749-6632.2011.06004.x (2011).

11 Thomas, S. P. & Suthers, R. A. The Physiology and Energetics of Bat Flight. *Journal of Experimental Biology* **57**, 317-335, doi:10.1242/jeb.57.2.317 (1972).

12 Tucker, V. A. The energetics of bird flight. *Sci Am* **220**, 70-78, doi:10.1038/scientificamerican0569-70 (1969).

13 Speakman, J. R. Body size, energy metabolism and lifespan. *J Exp Biol* **208**, 1717-1730, doi:10.1242/jeb.01556 (2005).

14 Wilkinson, G. S. & South, J. M. Life history, ecology and longevity in bats. *Aging Cell* **1**, 124-131, doi:10.1046/j.1474-9728.2002.00020.x (2002).

15 Seim, I. *et al.* Genome analysis reveals insights into physiology and longevity of the Brandt's bat *Myotis brandtii*. *Nat Commun* **4**, 2212, doi:10.1038/ncomms3212 (2013).

16 Guevara-Aguirre, J. *et al.* Growth hormone receptor deficiency is associated with a major reduction in pro-aging signaling, cancer, and diabetes in humans. *Sci Transl Med* **3**, 70ra13, doi:10.1126/scitranslmed.3001845 (2011).

17 Koh, J. *et al.* ABCB1 protects bat cells from DNA damage induced by genotoxic compounds. **10**, 2820, doi:10.1038/s41467-019-10495-4 (2019).

18 Foley, N. M. *et al.* Growing old, yet staying young: The role of telomeres in bats' exceptional longevity. *Sci Adv* **4**, eaao0926, doi:10.1126/sciadv.aao0926 (2018).

19 MacRae, S. L. *et al.* DNA repair in species with extreme lifespan differences. *Aging (Albany NY)* **7**, 1171-1184, doi:10.18632/aging.100866 (2015).

20 Chionh, Y. T. *et al.* High basal heat-shock protein expression in bats confers resistance to cellular heat/oxidative stress. *Cell Stress Chaperones* **24**, 835-849, doi:10.1007/s12192-019-01013-y (2019).

21 Ahn, M. *et al.* Dampened NLRP3-mediated inflammation in bats and implications for a special viral reservoir host. *Nat Microbiol* **4**, 789-799, doi:10.1038/s41564-019-0371-3 (2019).

22 Fumagalli, M. R., Zapperi, S. & La Porta, C. A. M. Role of body temperature variations in bat immune response to viral infections. *J R Soc Interface* **18**, 20210211, doi:10.1098/rsif.2021.0211 (2021).

23 Richter, H. V. & Cumming, G. S. First application of satellite telemetry to track African straw-coloured fruit bat migration. *Journal of Zoology* **275**, 172-176, doi:10.1111/j.1469-7998.2008.00425.x (2008).

24 Tarantola, A. Four Thousand Years of Concepts Relating to Rabies in Animals and Humans, Its Prevention and Its Cure. *Trop Med Infect Dis* **2**, doi:10.3390/tropicalmed2020005 (2017).

25 Yuhong, W. Rabies and Rabid Dogs in Sumerian and Akkadian Literature. *Journal of the American Oriental Society* **121**, doi:10.2307/606727 (2001).

26 Olival, K. J. *et al.* Host and viral traits predict zoonotic spillover from mammals. *Nature* **546**, 646-650, doi:10.1038/nature22975 (2017).

27 Brook, C. E. & Dobson, A. P. Bats as 'special' reservoirs for emerging zoonotic pathogens. *Trends Microbiol* **23**, 172-180, doi:10.1016/j.tim.2014.12.004 (2015).

28 Luis, A. D. *et al.* A comparison of bats and rodents as reservoirs of zoonotic viruses: are bats special? *Proc Biol Sci* **280**, 20122753, doi:10.1098/rspb.2012.2753 (2013).

29 Dutheil, F., Clinchamps, M. & Bouillon-Minois, J. B. Bats, Pathogens, and Species Richness. *Pathogens* **10**, doi:10.3390/pathogens10020098 (2021).

30 Irving, A. T., Ahn, M., Goh, G., Anderson, D. E. & Wang, L.-F. Lessons from the host defences of bats, a unique viral reservoir. **589**, 363–370, doi:10.1038/s41586-020-03128-0 (2021).

31 Ripperger, S. P., Stockmaier, S., Carter, G. G. & Pinter-Wollman, N. Tracking sickness effects on social encounters via continuous proximity sensing in wild vampire bats. *Behavioral Ecology* **31**, 1296-1302, doi:10.1093/beheco/araa111 (2020).

32 Moreno, K. R. *et al.* Sick bats stay home alone: fruit bats practice social distancing when faced with an immunological challenge. *Ann N Y Acad Sci* **1505**, 178-190, doi:10.1111/nyas.14600 (2021).

33 Hayman, D. T. Bats as Viral Reservoirs. *Annu Rev Virol* **3**, 77-99, doi:10.1146/annurev-virology-110615-042203 (2016).

34 Bourhy, H., Cowley, J. A., Larrous, F., Holmes, E. C. & Walker, P. J. Phylogenetic relationships among rhabdoviruses inferred using the L polymerase gene. *J Gen Virol* **86**, 2849-2858, doi:10.1099/vir.0.81128-0 (2005).

35 Chen, L., Liu, B., Yang, J. & Jin, Q. DBatVir: the database of bat-associated viruses. *Database (Oxford)* **2014**, bau021, doi:10.1093/database/bau021 (2014).

36 Fooks, A. R. *et al.* Rabies. *Nat Rev Dis Primers* **3**, 17091, doi:10.1038/nrdp.2017.91 (2017).

37 Badrane, H. & Tordo, N. Host switching in Lyssavirus history from the Chiroptera to the Carnivora orders. *J Virol* **75**, 8096-8104, doi:10.1128/jvi.75.17.8096-8104.2001 (2001).

38 Kuzmin, I. V., Hughes, G. J., Botvinkin, A. D., Orciari, L. A. & Rupprecht, C. E. Phylogenetic relationships of Irkut and West Caucasian bat viruses within the Lyssavirus genus and suggested quantitative criteria based on the N gene sequence for lyssavirus genotype definition. *Virus Res* **111**, 28-43, doi:10.1016/j.virusres.2005.03.008 (2005).

39 Kuzmin, I. V. *et al.* Bat lyssaviruses (Aravan and Khujand) from Central Asia: phylogenetic relationships according to N, P and G gene sequences. *Virus Research* **97**, 65-79, doi:10.1016/s0168-1702(03)00217-x (2003).

40 Banyard, A. C., Hayman, D., Johnson, N., McElhinney, L. & Fooks, A. R. Bats and lyssaviruses. *Adv Virus Res* **79**, 239-289, doi:10.1016/B978-0-12-387040-7.00012-3 (2011).

41 Kuzmin, I. V. *et al.* Shimoni bat virus, a new representative of the Lyssavirus genus. *Virus Res* **149**, 197-210, doi:10.1016/j.virusres.2010.01.018 (2010).

42 Botvinkin, A. D. *et al.* Novel lyssaviruses isolated from bats in Russia. *Emerg Infect Dis* **9**, 1623-1625, doi:10.3201/eid0912.030374 (2003).

43 Familusi, J. B. & Moore, D. L. Isolation of a rabies related virus from the cerebrospinal fluid of a child with 'aseptic meningitis'. *Afr J Med Sci* **3**, 93-96 (1972).

44 Familusi, J. B., Osunkoya, B. O., Moore, D. L., Kemp, G. E. & Fabiyi, A. A fatal human infection with Mokola virus. *Am J Trop Med Hyg* **21**, 959-963, doi:10.4269/ajtmh.1972.21.959 (1972).

45 Marston, D. A. *et al.* Ikoma lyssavirus, highly divergent novel lyssavirus in an African civet. *Emerg Infect Dis* **18**, 664-667, doi:10.3201/eid1804.111553 (2012).

46 Shipley, R. *et al.* Bats and Viruses: Emergence of Novel Lyssaviruses and Association of Bats with Viral Zoonoses in the EU. *Trop Med Infect Dis* **4**, doi:10.3390/tropicalmed4010031 (2019).

47 Muller, T. *et al.* Spill-over of European bat lyssavirus type 1 into a stone marten (Martes foina) in Germany. *J Vet Med B Infect Dis Vet Public Health* **51**, 49-54, doi:10.1111/j.1439-0450.2003.00725.x (2004).

48 Tjornehoj, K., Fooks, A. R., Agerholm, J. S. & Ronsholt, L. Natural and experimental infection of sheep with European bat lyssavirus type-1 of Danish bat origin. *J Comp Pathol* **134**, 190-201, doi:10.1016/j.jcpa.2005.10.005 (2006).

49 Dacheux, L. *et al.* European bat Lyssavirus transmission among cats, Europe. *Emerg Infect Dis* **15**, 280-284, doi:10.3201/eid1502.080637 (2009).

50 Muller, T. *et al.* Epidemiology of bat rabies in Germany. *Arch Virol* **152**, 273-288, doi:10.1007/s00705-006-0853-5 (2007).

51 Serra-Cobo, J., Amengual, B., Abellan, C. & Bourhy, H. European bat lyssavirus infection in Spanish bat populations. *Emerg Infect Dis* **8**, 413-420, doi:10.3201/eid0804.010263 (2002).

52 Lumio, J. *et al.* Human Rabies Of Bat Origin in Europe. *The Lancet* **327**, 378, doi:10.1016/S0140-6736(86)92336-6 (1986).

53 Fooks, A. R. *et al.* Case report: isolation of a European bat lyssavirus type 2a from a fatal human case of rabies encephalitis. *J Med Virol* **71**, 281-289, doi:10.1002/jmv.10481 (2003).

54 Annand, E. J. & Reid, P. A. Clinical review of two fatal equine cases of infection with the insectivorous bat strain of Australian bat lyssavirus. *Aust Vet J* **92**, 324-332, doi:10.1111/avj.12227 (2014).

55 Samaratunga, H., Searle, J. W. & Hudson, N. Non-rabies Lyssavirus human encephalitis from fruit bats: Australian bat Lyssavirus (pteropid Lyssavirus) infection. *Neuropathol Appl Neurobiol* **24**, 331-335, doi:10.1046/j.1365-2990.1998.00129.x (1998).

56 Hanna, J. N. *et al.* Australian bat lyssavirus infection: a second human case, with a long incubation period. *Med J Aust* **172**, 597-599, doi:10.5694/j.1326-5377.2000.tb124126.x (2000).

57 Iizuka, K. Australian bat lyssavirus - Australia (02) (QL) human fatality. *International Society for Infectious Diseases* (2013).

58 Sabeta, C. T. *et al.* Mokola virus in domestic mammals, South Africa. *Emerg Infect Dis* **13**, 1371-1373, doi:10.3201/eid1309.070466 (2007).
59 Mebatsion, T., Cox, J. H. & Frost, J. W. Isolation and characterization of 115 street rabies virus isolates from Ethiopia by using monoclonal antibodies: identification of 2 isolates as Mokola and Lagos bat viruses. *J Infect Dis* **166**, 972-977, doi:10.1093/infdis/166.5.972 (1992).
60 von Teichman, B. F. *et al.* Mokola virus infection: description of recent South African cases and a review of the virus epidemiology. *J S Afr Vet Assoc* **69**, 169-171, doi:10.4102/jsava.v69i4.847 (1998).
61 Bingham, J., Javangwe, S., Sabeta, C. T., Wandeler, A. I. & Nel, L. H. Report of isolations of unusual lyssaviruses (rabies and Mokola virus) identified retrospectively from Zimbabwe. *J S Afr Vet Assoc* **72**, 92-94, doi:10.4102/jsava.v72i2.624 (2001).
62 van Thiel, P. P. *et al.* Fatal human rabies due to Duvenhage virus from a bat in Kenya: failure of treatment with coma-induction, ketamine, and antiviral drugs. *PLoS Negl Trop Dis* **3**, e428, doi:10.1371/journal.pntd.0000428 (2009).
63 Paweska, J. T. *et al.* Fatal human infection with rabies-related Duvenhage virus, South Africa. *Emerg Infect Dis* **12**, 1965-1967, doi:10.3201/eid1212.060764 (2006).
64 Crick, J., Tignor, G. H. & Moreno, K. A new isolate of Lagos bat virus from the Republic of South Africa. *Transactions of the Royal Society of Tropical Medicine and Hygiene* **76**, 211-213, doi:10.1016/0035-9203(82)90277-2 (1982).
65 Markotter, W., Kuzmin, I., Rupprecht, C. E. & Nel, L. H. Phylogeny of Lagos bat virus: challenges for lyssavirus taxonomy. *Virus Res* **135**, 10-21, doi:10.1016/j.virusres.2008.02.001 (2008).
66 Laing, E. D. *et al.* Enhanced Autophagy Contributes to Reduced Viral Infection in Black Flying Fox Cells. *Viruses* **11**, doi:10.3390/v11030260 (2019).
67 Freuling, C. *et al.* Experimental infection of serotine bats (*Eptesicus serotinus*) with European bat lyssavirus type 1a. *J Gen Virol* **90**, 2493-2502, doi:10.1099/vir.0.011510-0 (2009).
68 W. H. O. Ebola Response Team, f. *et al.* Ebola virus disease in West Africa--the first 9 months of the epidemic and forward projections. *N Engl J Med* **371**, 1481-1495, doi:10.1056/NEJMoa1411100 (2014).
69 Edenborough, K. M. *et al.* Dendritic Cells Generated From Mops condylurus, a Likely Filovirus Reservoir Host, Are Susceptible to and Activated by Zaire Ebolavirus Infection. *Front Immunol* **10**, 2414, doi:10.3389/fimmu.2019.02414 (2019).
70 Bokelmann, M. *Experimentelle Untersuchungen an Fledermäusen als potenzielles Reservoir von Ebolaviren* Dr. rer. nat. thesis, Humboldt-University Berlin, (2021).
71 Koch, L. K., Cunze, S., Kochmann, J. & Klimpel, S. Bats as putative Zaire ebolavirus reservoir hosts and their habitat suitability in Africa. *Sci Rep* **10**, 14268, doi:10.1038/s41598-020-71226-0 (2020).
72 Leendertz, S. A., Gogarten, J. F., Dux, A., Calvignac-Spencer, S. & Leendertz, F. H. Assessing the Evidence Supporting Fruit Bats as the Primary Reservoirs for Ebola Viruses. *Ecohealth* **13**, 18-25, doi:10.1007/s10393-015-1053-0 (2016).
73 Towner, J. S. *et al.* Marburg virus infection detected in a common African bat. *PLoS One* **2**, e764, doi:10.1371/journal.pone.0000764 (2007).
74 Towner, J. S. *et al.* Isolation of genetically diverse Marburg viruses from Egyptian fruit bats. *PLoS Pathog* **5**, e1000536, doi:10.1371/journal.ppat.1000536 (2009).
75 Guito, J. C. *et al.* Asymptomatic Infection of Marburg Virus Reservoir Bats Is Explained by a Strategy of Immunoprotective Disease Tolerance. **31**, 257-270.e255, doi:10.1016/j.cub.2020.10.015 (2021).

76 Young, P. L. *et al.* Serologic evidence for the presence in *Pteropus* bats of a paramyxovirus related to equine morbillivirus. *Emerg Infect Dis* **2**, 239-240, doi:10.3201/eid0203.960315 (1996).

77 Halpin, K. *et al.* Pteropid bats are confirmed as the reservoir hosts of henipaviruses: a comprehensive experimental study of virus transmission. *Am J Trop Med Hyg* **85**, 946-951, doi:10.4269/ajtmh.2011.10-0567 (2011).

78 Halpin, K., Young, P. L., Field, H. E. & Mackenzie, J. S. Isolation of Hendra virus from pteropid bats: a natural reservoir of Hendra virus. *J Gen Virol* **81**, 1927-1932, doi:10.1099/0022-1317-81-8-1927 (2000).

79 Yob, J. M. *et al.* Nipah virus infection in bats (order Chiroptera) in peninsular Malaysia. *Emerg Infect Dis* **7**, 439-441, doi:10.3201/eid0703.010312 (2001).

80 Epstein, J. H. *et al.* Nipah virus dynamics in bats and implications for spillover to humans. *Proc Natl Acad Sci U S A* **117**, 29190-29201, doi:10.1073/pnas.2000429117 (2020).

81 Wacharapluesadee, S. & Hemachudha, T. Duplex nested RT-PCR for detection of Nipah virus RNA from urine specimens of bats. *J Virol Methods* **141**, 97-101, doi:10.1016/j.jviromet.2006.11.023 (2007).

82 Marsh, G. A. & Wang, L. F. Hendra and Nipah viruses: why are they so deadly? *Curr Opin Virol* **2**, 242-247, doi:10.1016/j.coviro.2012.03.006 (2012).

83 Field, H. *et al.* The natural history of Hendra and Nipah viruses. *Microbes Infect* **3**, 307-314, doi:10.1016/s1286-4579(01)01384-3 (2001).

84 Marsh, G. A. *et al.* Cedar virus: a novel Henipavirus isolated from Australian bats. *PLoS Pathog* **8**, e1002836, doi:10.1371/journal.ppat.1002836 (2012).

85 Williamson, M. M., Hooper, P. T., Selleck, P. W., Westbury, H. A. & Slocombe, R. F. Experimental hendra virus infectionin pregnant guinea-pigs and fruit Bats (*Pteropus poliocephalus*). *J Comp Pathol* **122**, 201-207, doi:10.1053/jcpa.1999.0364 (2000).

86 Williamson, M. M. *et al.* Transmission studies of Hendra virus (equine morbillivirus) in fruit bats, horses and cats. *Aust Vet J* **76**, 813-818, doi:10.1111/j.1751-0813.1998.tb12335.x (1998).

87 Woon, A. P. *et al.* Acute experimental infection of bats and ferrets with Hendra virus: Insights into the early host response of the reservoir host and susceptible model species. *PLoS Pathog* **16**, e1008412, doi:10.1371/journal.ppat.1008412 (2020).

88 Seifert, S. N. *et al. Rousettus aegyptiacus* Bats Do Not Support Productive Nipah Virus Replication. *J Infect Dis* **221**, S407-S413, doi:10.1093/infdis/jiz429 (2020).

89 Drexler, J. F. *et al.* Bats host major mammalian paramyxoviruses. *Nat Commun* **3**, 796, doi:10.1038/ncomms1796 (2012).

90 Baker, K. S. *et al.* Co-circulation of diverse paramyxoviruses in an urban African fruit bat population. *J Gen Virol* **93**, 850-856, doi:10.1099/vir.0.039339-0 (2012).

91 Baker, K. S. *et al.* Novel, potentially zoonotic paramyxoviruses from the African straw-colored fruit bat *Eidolon helvum*. *J Virol* **87**, 1348-1358, doi:10.1128/JVI.01202-12 (2013).

92 Muleya, W. *et al.* Molecular epidemiology of paramyxoviruses in frugivorous *Eidolon helvum* bats in Zambia. *J Vet Med Sci* **76**, 611-614, doi:10.1292/jvms.13-0518 (2014).

93 Dietrich, M. *et al.* Leptospira and paramyxovirus infection dynamics in a bat maternity enlightens pathogen maintenance in wildlife. *Environ Microbiol* **17**, 4280-4289, doi:10.1111/1462-2920.12766 (2015).

94 Chua, K. B. *et al.* Tioman virus, a novel paramyxovirus isolated from fruit bats in Malaysia. *Virology* **283**, 215-229, doi:10.1006/viro.2000.0882 (2001).

95 Amman, B. R. *et al.* A Recently Discovered Pathogenic Paramyxovirus, Sosuga Virus, is Present in *Rousettus aegyptiacus* Fruit Bats at Multiple Locations in Uganda. *J Wildl Dis* **51**, 774-779, doi:10.7589/2015-02-044 (2015).

96 Wilkinson, D. A. *et al.* Identification of novel paramyxoviruses in insectivorous bats of the Southwest Indian Ocean. *Virus Res* **170**, 159-163, doi:10.1016/j.virusres.2012.08.022 (2012).

97 Yuan, L. *et al.* Evidence for retrovirus and paramyxovirus infection of multiple bat species in china. *Viruses* **6**, 2138-2154, doi:10.3390/v6052138 (2014).

98 Boiro, I., Konstaninov, O. K. & Numerov, A. D. [Isolation of Rift Valley fever virus from bats in the Republic of Guinea]. *Bull Soc Pathol Exot Filiales* **80**, 62-67 (1987).

99 Mourya, D. T. *et al.* Malsoor virus, a novel bat phlebovirus, is closely related to severe fever with thrombocytopenia syndrome virus and heartland virus. *J Virol* **88**, 3605-3609, doi:10.1128/JVI.02617-13 (2014).

100 Soldan, S. S. & Gonzalez-Scarano, F. Emerging infectious diseases: the Bunyaviridae. *J Neurovirol* **11**, 412-423, doi:10.1080/13550280591002496 (2005).

101 King, A. M. Q., Adams, M. J., Carstens, E. B. & Lefkowitz, E. J. in *Virus Taxonomy* 784-794 (Elsevier, 2012).

102 Cherry, J. D. The chronology of the 2002-2003 SARS mini pandemic. *Paediatr Respir Rev* **5**, 262-269, doi:10.1016/j.prrv.2004.07.009 (2004).

103 van Boheemen, S. *et al.* Genomic characterization of a newly discovered coronavirus associated with acute respiratory distress syndrome in humans. *mBio* **3**, doi:10.1128/mBio.00473-12 (2012).

104 de Groot, R. J. *et al.* Middle East respiratory syndrome coronavirus (MERS-CoV): announcement of the Coronavirus Study Group. *J Virol* **87**, 7790-7792, doi:10.1128/JVI.01244-13 (2013).

105 Mackenzie, J. S. & Smith, D. W. COVID-19: a novel zoonotic disease caused by a coronavirus from China: what we know and what we don't. *Microbiol Aust*, MA20013, doi:10.1071/MA20013 (2020).

106 Zhou, P. *et al.* A pneumonia outbreak associated with a new coronavirus of probable bat origin. *Nature* **579**, 270-273, doi:10.1038/s41586-020-2012-7 (2020).

107 Zhao, J., Cui, W. & Tian, B. P. The Potential Intermediate Hosts for SARS-CoV-2. *Front Microbiol* **11**, 580137, doi:10.3389/fmicb.2020.580137 (2020).

108 Geneva: World HEalth Organization. WHO COVID-19 Emergency Dashboard. *WHO* (2021).

109 Banerjee, A., Kulcsar, K., Misra, V., Frieman, M. & Mossman, K. Bats and Coronaviruses. *Viruses* **11**, doi:10.3390/v11010041 (2019).

110 Li, R. *et al.* Substantial undocumented infection facilitates the rapid dissemination of novel coronavirus (SARS-CoV-2). *Science* **368**, 489-493, doi:10.1126/science.abb3221 (2020).

111 Larsen, J. R., Martin, M. R., Martin, J. D., Kuhn, P. & Hicks, J. B. Modeling the Onset of Symptoms of COVID-19. *Front Public Health* **8**, 473, doi:10.3389/fpubh.2020.00473 (2020).

112 Latinne, A. *et al.* Origin and cross-species transmission of bat coronaviruses in China. *bioRxiv*, doi:10.1101/2020.05.31.116061 (2020).

113 Cui, J., Li, F. & Shi, Z. L. Origin and evolution of pathogenic coronaviruses. *Nat Rev Microbiol* **17**, 181-192, doi:10.1038/s41579-018-0118-9 (2019).

114 Yang, Y. L., Yu, J. Q. & Huang, Y. W. Swine enteric alphacoronavirus (swine acute diarrhea syndrome coronavirus): An update three years after its discovery. *Virus Res* **285**, 198024, doi:10.1016/j.virusres.2020.198024 (2020).

115 Lau, S. K. *et al.* Recent transmission of a novel alphacoronavirus, bat coronavirus HKU10, from Leschenault's rousettes to pomona leaf-nosed bats: first evidence of interspecies transmission of coronavirus between bats of different suborders. *J Virol* **86**, 11906-11918, doi:10.1128/JVI.01305-12 (2012).

116 Tong, S. *et al.* New world bats harbor diverse influenza A viruses. *PLoS Pathog* **9**, e1003657, doi:10.1371/journal.ppat.1003657 (2013).

117 Karakus, U. *et al.* MHC class II proteins mediate cross-species entry of bat influenza viruses. *Nature* **567**, 109-112, doi:10.1038/s41586-019-0955-3 (2019).

118 Anthony, S. J. *et al.* A strategy to estimate unknown viral diversity in mammals. *mBio* **4**, e00598-00513, doi:10.1128/mBio.00598-13 (2013).

119 Baker, K. S. *et al.* Metagenomic study of the viruses of African straw-coloured fruit bats: detection of a chiropteran poxvirus and isolation of a novel adenovirus. *Virology* **441**, 95-106, doi:10.1016/j.virol.2013.03.014 (2013).

120 He, B. *et al.* Virome profiling of bats from Myanmar by metagenomic analysis of tissue samples reveals more novel Mammalian viruses. *PLoS One* **8**, e61950, doi:10.1371/journal.pone.0061950 (2013).

121 Drexler, J. F. *et al.* Amplification of emerging viruses in a bat colony. *Emerg Infect Dis* **17**, 449-456, doi:10.3201/eid1703.100526 (2011).

122 Li, Y. *et al.* Prevalence and genetic diversity of adeno-associated viruses in bats from China. *J Gen Virol* **91**, 2601-2609, doi:10.1099/vir.0.020032-0 (2010).

123 Lima, F. E. *et al.* First detection of adenovirus in the vampire bat (*Desmodus rotundus*) in Brazil. *Virus Genes* **47**, 378-381, doi:10.1007/s11262-013-0947-6 (2013).

124 Janoska, M. *et al.* Novel adenoviruses and herpesviruses detected in bats. *Vet J* **189**, 118-121, doi:10.1016/j.tvjl.2010.06.020 (2011).

125 Razafindratsimandresy, R. *et al.* Partial molecular characterization of alphaherpesviruses isolated from tropical bats. *J Gen Virol* **90**, 44-47, doi:10.1099/vir.0.006825-0 (2009).

126 Zhang, H. *et al.* A novel bat herpesvirus encodes homologues of major histocompatibility complex classes I and II, C-type lectin, and a unique family of immune-related genes. *J Virol* **86**, 8014-8030, doi:10.1128/JVI.00723-12 (2012).

127 Watanabe, S. *et al.* Novel betaherpesvirus in bats. *Emerg Infect Dis* **16**, 986-988, doi:10.3201/eid1606.091567 (2010).

128 Sasaki, M. *et al.* Isolation and characterization of a novel alphaherpesvirus in fruit bats. *J Virol* **88**, 9819-9829, doi:10.1128/JVI.01277-14 (2014).

129 Wibbelt, G. *et al.* Discovery of herpesviruses in bats. *J Gen Virol* **88**, 2651-2655, doi:10.1099/vir.0.83045-0 (2007).

130 Ge, X. *et al.* Metagenomic analysis of viruses from bat fecal samples reveals many novel viruses in insectivorous bats in China. *J Virol* **86**, 4620-4630, doi:10.1128/JVI.06671-11 (2012).

131 Cibulski, S. P. *et al.* A Novel Anelloviridae Species Detected in *Tadarida brasiliensis* Bats: First Sequence of a Chiropteran Anellovirus. *Genome Announc* **2**, doi:10.1128/genomeA.01028-14 (2014).

132 Rabinovitch, M. Professional and non-professional phagocytes: an introduction. *Trends in Cell Biology* **5**, 85-87, doi:10.1016/s0962-8924(00)88955-2 (1995).

133 Koyama, S., Ishii, K. J., Coban, C. & Akira, S. Innate immune response to viral infection. *Cytokine* **43**, 336-341, doi:10.1016/j.cyto.2008.07.009 (2008).

134 Medzhitov, R. & Janeway, C., Jr. Innate immune recognition: mechanisms and pathways. *Immunol Rev* **173**, 89-97, doi:10.1034/j.1600-065x.2000.917309.x (2000).

135 Romani, L. Immunity to fungal infections. *Nat Rev Immunol* **4**, 1-23, doi:10.1038/nri1255 (2004).
136 Tang, D., Kang, R., Coyne, C. B., Zeh, H. J. & Lotze, M. T. PAMPs and DAMPs: signal os that spur autophagy and immunity. *Immunol Rev* **249**, 158-175, doi:10.1111/j.1600-065X.2012.01146.x (2012).
137 Matzinger, P. Tolerance, danger, and the extended family. *Annu Rev Immunol* **12**, 991-1045, doi:10.1146/annurev.iy.12.040194.005015 (1994).
138 Walsh, D., McCarthy, J., O'Driscoll, C. & Melgar, S. Pattern recognition receptors--molecular orchestrators of inflammation in inflammatory bowel disease. *Cytokine Growth Factor Rev* **24**, 91-104, doi:10.1016/j.cytogfr.2012.09.003 (2013).
139 Zhang, Z. *et al.* The helicase DDX41 senses intracellular DNA mediated by the adaptor STING in dendritic cells. *Nat Immunol* **12**, 959-965, doi:10.1038/ni.2091 (2011).
140 Yang, P. *et al.* The cytosolic nucleic acid sensor LRRFIP1 mediates the production of type I interferon via a beta-catenin-dependent pathway. *Nat Immunol* **11**, 487-494, doi:10.1038/ni.1876 (2010).
141 Unterholzner, L. *et al.* IFI16 is an innate immune sensor for intracellular DNA. *Nat Immunol* **11**, 997-1004, doi:10.1038/ni.1932 (2010).
142 Salt, I. P. & Palmer, T. M. Exploiting the anti-inflammatory effects of AMP-activated protein kinase activation. *Expert Opin Investig Drugs* **21**, 1155-1167, doi:10.1517/13543784.2012.696609 (2012).
143 Collins, S. E. & Mossman, K. L. Danger, diversity and priming in innate antiviral immunity. *Cytokine Growth Factor Rev* **25**, 525-531, doi:10.1016/j.cytogfr.2014.07.002 (2014).
144 Honda, K. *et al.* IRF-7 is the master regulator of type-I interferon-dependent immune responses. *Nature* **434**, 772-777, doi:10.1038/nature03464 (2005).
145 Song, J., Guan, M., Zhao, Z. & Zhang, J. Type I Interferons Function as Autocrine and Paracrine Factors to Induce Autotaxin in Response to TLR Activation. *PLoS One* **10**, e0136629, doi:10.1371/journal.pone.0136629 (2015).
146 Kotenko, S. V. *et al.* IFN-lambdas mediate antiviral protection through a distinct class II cytokine receptor complex. *Nat Immunol* **4**, 69-77, doi:10.1038/ni875 (2003).
147 Sheppard, P. *et al.* IL-28, IL-29 and their class II cytokine receptor IL-28R. *Nat Immunol* **4**, 63-68, doi:10.1038/ni873 (2003).
148 Lazear, H. M. *et al.* Interferon-lambda restricts West Nile virus neuroinvasion by tightening the blood-brain barrier. *Sci Transl Med* **7**, 284ra259, doi:10.1126/scitranslmed.aaa4304 (2015).
149 Yu, J. *et al.* Pro- and antiinflammatory cytokine signaling: reciprocal antagonism regulates interferon-gamma production by human natural killer cells. *Immunity* **24**, 575-590, doi:10.1016/j.immuni.2006.03.016 (2006).
150 Yoshimoto, T. *et al.* IL-12 up-regulates IL-18 receptor expression on T cells, Th1 cells, and B cells: synergism with IL-18 for IFN-gamma production. *J Immunol* **161**, 3400-3407 (1998).
151 Schroder, K., Hertzog, P. J., Ravasi, T. & Hume, D. A. Interferon-gamma: an overview of signals, mechanisms and functions. *J Leukoc Biol* **75**, 163-189, doi:10.1189/jlb.0603252 (2004).
152 Kasahara, T., Hooks, J. J., Dougherty, S. F. & Oppenheim, J. J. Interleukin 2-mediated immune interferon (IFN-gamma) production by human T cells and T cell subsets. *J Immunol* **130**, 1784-1789 (1983).
153 Gao, Y. *et al.* Gamma delta T cells provide an early source of interferon gamma in tumor immunity. *J Exp Med* **198**, 433-442, doi:10.1084/jem.20030584 (2003).

154 Kawai, T. & Akira, S. The roles of TLRs, RLRs and NLRs in pathogen recognition. *Int Immunol* **21**, 317-337, doi:10.1093/intimm/dxp017 (2009).
155 Stark, G. R. & Darnell, J. E., Jr. The JAK-STAT pathway at twenty. *Immunity* **36**, 503-514, doi:10.1016/j.immuni.2012.03.013 (2012).
156 de Weerd, N. A., Samarajiwa, S. A. & Hertzog, P. J. Type I interferon receptors: biochemistry and biological functions. *J Biol Chem* **282**, 20053-20057, doi:10.1074/jbc.R700006200 (2007).
157 Bach, E. A., Aguet, M. & Schreiber, R. D. The IFN gamma receptor: a paradigm for cytokine receptor signaling. *Annu Rev Immunol* **15**, 563-591, doi:10.1146/annurev.immunol.15.1.563 (1997).
158 Meyer, O. Interferons and autoimmune disorders. *Joint Bone Spine* **76**, 464-473, doi:10.1016/j.jbspin.2009.03.012 (2009).
159 Murira, A. & Lamarre, A. Type-I Interferon Responses: From Friend to Foe in the Battle against Chronic Viral Infection. *Front Immunol* **7**, 609, doi:10.3389/fimmu.2016.00609 (2016).
160 Zampieri, C. A., Sullivan, N. J. & Nabel, G. J. Immunopathology of highly virulent pathogens: insights from Ebola virus. *Nat Immunol* **8**, 1159-1164, doi:10.1038/ni1519 (2007).
161 Cameron, M. J., Bermejo-Martin, J. F., Danesh, A., Muller, M. P. & Kelvin, D. J. Human immunopathogenesis of severe acute respiratory syndrome (SARS). *Virus Res* **133**, 13-19, doi:10.1016/j.virusres.2007.02.014 (2008).
162 Totura, A. L. & Baric, R. S. SARS coronavirus pathogenesis: host innate immune responses and viral antagonism of interferon. *Curr Opin Virol* **2**, 264-275, doi:10.1016/j.coviro.2012.04.004 (2012).
163 De La Cruz-Rivera, P. C. *et al.* The IFN Response in Bats Displays Distinctive IFN-Stimulated Gene Expression Kinetics with Atypical RNASEL Induction. *J Immunol* **200**, 209-217, doi:10.4049/jimmunol.1701214 (2018).
164 Zhang, Q. *et al.* IFNAR2-dependent gene expression profile induced by IFN-alpha in *Pteropus alecto* bat cells and impact of IFNAR2 knockout on virus infection. *PLoS One* **12**, e0182866, doi:10.1371/journal.pone.0182866 (2017).
165 Zhou, P. *et al.* Type III IFN receptor expression and functional characterisation in the pteropid bat, *Pteropus alecto*. **6**, e25385, doi:10.1371/journal.pone.0025385 (2011).
166 Shaw, T. I. *et al.* Transcriptome sequencing and annotation for the Jamaican fruit bat (*Artibeus jamaicensis*). *PLoS One* **7**, e48472, doi:10.1371/journal.pone.0048472 (2012).
167 Pavlovich, S. S. *et al.* Egyptian Rousette IFN-omega Subtypes Elicit Distinct Antiviral Effects and Transcriptional Responses in Conspecific Cells. *Front Immunol* **11**, 435, doi:10.3389/fimmu.2020.00435 (2020).
168 Pavlovich, S. S. *et al.* The Egyptian Rousette Genome Reveals Unexpected Features of Bat Antiviral Immunity. *Cell* **173**, 1098-1110 e1018, doi:10.1016/j.cell.2018.03.070 (2018).
169 Glennon, N. B., Jabado, O., Lo, M. K. & Shaw, M. L. Transcriptome Profiling of the Virus-Induced Innate Immune Response in Pteropus vampyrus and Its Attenuation by Nipah Virus Interferon Antagonist Functions. *J Virol* **89**, 7550-7566, doi:10.1128/JVI.00302-15 (2015).
170 Jebb, D. *et al.* Six reference-quality genomes reveal evolution of bat adaptations. *Nature* **583**, 578-584, doi:10.1038/s41586-020-2486-3 (2020).
171 Crameri, G. *et al.* Establishment, immortalisation and characterisation of pteropid bat cell lines. *PLoS One* **4**, e8266, doi:10.1371/journal.pone.0008266 (2009).

172 Banerjee, A., Falzarano, D., Rapin, N., Lew, J. & Misra, V. Interferon Regulatory Factor 3-Mediated Signaling Limits Middle-East Respiratory Syndrome (MERS) Coronavirus Propagation in Cells from an Insectivorous Bat. *Viruses* **11**, doi:10.3390/v11020152 (2019).

173 He, X. *et al.* Anti-lyssaviral activity of interferons kappa and omega from the serotine bat, *Eptesicus serotinus*. *J Virol* **88**, 5444-5454, doi:10.1128/JVI.03403-13 (2014).

174 Janardhana, V. *et al.* Cloning, expression and antiviral activity of IFNgamma from the Australian fruit bat, *Pteropus alecto*. *Dev Comp Immunol* **36**, 610-618, doi:10.1016/j.dci.2011.11.001 (2012).

175 Stewart, W. E., Allen, R. & Sulkin, S. E. Persistant infection in bats and bat cell cultures with Japanese encephalitis virus. *Bacterial Proc* (1969).

176 Tarigan, R. *et al.* Role of pattern recognition receptors and interferon-beta in protecting bat cell lines from encephalomyocarditis virus and Japanese encephalitis virus infection. *Biochem Biophys Res Commun* **527**, 1-7, doi:10.1016/j.bbrc.2020.04.060 (2020).

177 Zhou, P. *et al.* Type III IFNs in pteropid bats: differential expression patterns provide evidence for distinct roles in antiviral immunity. *J Immunol* **186**, 3138-3147, doi:10.4049/jimmunol.1003115 (2011).

178 Lee, A. K. *et al. De novo* transcriptome reconstruction and annotation of the Egyptian rousette bat. *BMC Genomics* **16**, 1033, doi:10.1186/s12864-015-2124-x (2015).

179 Papenfuss, A. T. *et al.* The immune gene repertoire of an important viral reservoir, the Australian black flying fox. *BMC Genomics* **13**, 261, doi:10.1186/1471-2164-13-261 (2012).

180 Kelley, J., de Bono, B. & Trowsdale, J. IRIS: a database surveying known human immune system genes. *Genomics* **85**, 503-511, doi:10.1016/j.ygeno.2005.01.009 (2005).

181 Lin, H. H., Horie, M. & Tomonaga, K. A comprehensive profiling of innate immune responses in *Eptesicus* bat cells. *Microbiol Immunol*, doi:10.1111/1348-0421.12952 (2021).

182 Zhang, G. *et al.* Comparative analysis of bat genomes provides insight into the evolution of flight and immunity. *Science* **339**, 456-460, doi:10.1126/science.1230835 (2013).

183 Fox, B. A., Sheppard, P. O. & O'Hara, P. J. The role of genomic data in the discovery, annotation and evolutionary interpretation of the interferon-lambda family. *PLoS One* **4**, e4933, doi:10.1371/journal.pone.0004933 (2009).

184 Iha, K. *et al.* Molecular cloning and expression analysis of bat toll-like receptors 3, 7 and 9. *J Vet Med Sci* **72**, 217-220, doi:10.1292/jvms.09-0050 (2010).

185 Cowled, C. *et al.* Molecular characterisation of Toll-like receptors in the black flying fox *Pteropus alecto*. *Dev Comp Immunol* **35**, 7-18, doi:10.1016/j.dci.2010.07.006 (2011).

186 Cowled, C., Baker, M. L., Zhou, P., Tachedjian, M. & Wang, L. F. Molecular characterisation of RIG-I-like helicases in the black flying fox, *Pteropus alecto*. *Dev Comp Immunol* **36**, 657-664, doi:10.1016/j.dci.2011.11.008 (2012).

187 Kepler, T. B. *et al.* Chiropteran types I and II interferon genes inferred from genome sequencing traces by a statistical gene-family assembler. *BMC Genomics* **11**, 444, doi:10.1186/1471-2164-11-444 (2010).

188 Omatsu, T. *et al.* Induction and sequencing of Rousette bat interferon alpha and beta genes. *Vet Immunol Immunopathol* **124**, 169-176, doi:10.1016/j.vetimm.2008.03.004 (2008).

189 He, G., He, B., Racey, P. A. & Cui, J. Positive selection of the bat interferon alpha gene family. *Biochem Genet* **48**, 840-846, doi:10.1007/s10528-010-9365-9 (2010).

190 Ahn, M. *et al.* Dampened NLRP3-mediated inflammation in bats and implications for a special viral reservoir host. **4**, 789–799, doi:10.1038/s41564-019-0371-3 (2019).

191 Ahn, M., Cui, J., Irving, A. T. & Wang, L. F. Unique Loss of the PYHIN Gene Family in Bats Amongst Mammals: Implications for Inflammasome Sensing. *Sci Rep* **6**, 21722, doi:10.1038/srep21722 (2016).

192 Wynne, J. W. *et al.* Proteomics informed by transcriptomics reveals Hendra virus sensitizes bat cells to TRAIL-mediated apoptosis. *Genome Biol* **15**, 532, doi:10.1186/PREACCEPT-1718798964145132 (2014).

193 Zhou, P. *et al.* Contraction of the type I IFN locus and unusual constitutive expression of IFN-α in bats. **113**, 2696–2701, doi:10.1073/pnas.1518240113 (2016).

194 Banerjee, A., Rapin, N., Bollinger, T. & Misra, V. Lack of inflammatory gene expression in bats: a unique role for a transcription repressor. **7**, 2232, doi:10.1038/s41598-017-01513-w (2017).

195 Schad, J. & Voigt, C. C. Adaptive evolution of virus-sensing toll-like receptor 8 in bats. *Immunogenetics* **68**, 783-795, doi:10.1007/s00251-016-0940-z (2016).

196 Heil, F. *et al.* Species-specific recognition of single-stranded RNA via toll-like receptor 7 and 8. *Science* **303**, 1526-1529, doi:10.1126/science.1093620 (2004).

197 Demaria, O. *et al.* TLR8 deficiency leads to autoimmunity in mice. *J Clin Invest* **120**, 3651-3662, doi:10.1172/JCI42081 (2010).

198 Zhang, Y. *et al.* HCV RNA Activates APCs via TLR7/TLR8 While Virus Selectively Stimulates Macrophages Without Inducing Antiviral Responses. *Sci Rep* **6**, 29447, doi:10.1038/srep29447 (2016).

199 Banerjee, A. *et al.* Positive Selection of a Serine Residue in Bat IRF3 Confers Enhanced Antiviral Protection. *iScience* **23**, 100958, doi:10.1016/j.isci.2020.100958 (2020).

200 Zhou, P. *et al.* IRF7 in the Australian black flying fox, *Pteropus alecto*: evidence for a unique expression pattern and functional conservation. *PLoS One* **9**, e103875, doi:10.1371/journal.pone.0103875 (2014).

201 Feng, H. *et al.* Hepatovirus 3ABC proteases and evolution of mitochondrial antiviral signaling protein (MAVS). *J Hepatol* **71**, 25-34, doi:10.1016/j.jhep.2019.02.020 (2019).

202 Sang, Y., Bergkamp, J. & Blecha, F. Molecular evolution of the porcine type I interferon family: subtype-specific expression and antiviral activity. *PLoS One* **9**, e112378, doi:10.1371/journal.pone.0112378 (2014).

203 Bondet, V. *et al.* Constitutive IFNα protein production in bats. *front Immunol*, doi:10.1101/2021.06.21.449208 (2021).

204 Pavlovich, S. S. *et al.* The Egyptian Rousette Genome Reveals Unexpected Features of Bat Antiviral Immunity. **173**, 1098-1110.e1018, doi:10.1016/j.cell.2018.03.070 (2018).

205 McFadden, G., Mohamed, M. R., Rahman, M. M. & Bartee, E. Cytokine determinants of viral tropism. *Nat Rev Immunol* **9**, 645-655, doi:10.1038/nri2623 (2009).

206 Lauterbach, H. *et al.* Mouse CD8alpha+ DCs and human BDCA3+ DCs are major producers of IFN-lambda in response to poly IC. *J Exp Med* **207**, 2703-2717, doi:10.1084/jem.20092720 (2010).

207 Yin, Z. *et al.* Type III IFNs are produced by and stimulate human plasmacytoid dendritic cells. *J Immunol* **189**, 2735-2745, doi:10.4049/jimmunol.1102038 (2012).

208 Lohoff, M. & Mak, T. W. Roles of interferon-regulatory factors in T-helper-cell differentiation. *Nat Rev Immunol* **5**, 125-135, doi:10.1038/nri1552 (2005).

209 Jordan, W. J. *et al.* Human interferon lambda-1 (IFN-lambda1/IL-29) modulates the Th1/Th2 response. *Genes Immun* **8**, 254-261, doi:10.1038/sj.gene.6364382 (2007).

210 La Cruz-Rivera, P. C. d. *et al.* The IFN Response in Bats Displays Distinctive IFN-Stimulated Gene Expression Kinetics with Atypical RNASEL Induction. **200**, 209–217, doi:10.4049/jimmunol.1701214 (2018).

211 Acharya, D., Liu, G. & Gack, M. U. Dysregulation of type I interferon responses in COVID-19. *Nat Rev Immunol* **20**, 397-398, doi:10.1038/s41577-020-0346-x (2020).

212 Davidson, S., Maini, M. K. & Wack, A. Disease-promoting effects of type I interferons in viral, bacterial, and coinfections. *J Interferon Cytokine Res* **35**, 252-264, doi:10.1089/jir.2014.0227 (2015).

213 Piehler, J., Thomas, C., Garcia, K. C. & Schreiber, G. Structural and dynamic determinants of type I interferon receptor assembly and their functional interpretation. *Immunol Rev* **250**, 317-334, doi:10.1111/imr.12001 (2012).

214 Shaw, A. E. *et al.* Fundamental properties of the mammalian innate immune system revealed by multispecies comparison of type I interferon responses. *PLoS Biol* **15**, e2004086, doi:10.1371/journal.pbio.2004086 (2017).

215 Zhou, P., Cowled, C., Wang, L. F. & Baker, M. L. Bat Mx1 and Oas1, but not Pkr are highly induced by bat interferon and viral infection. *Dev Comp Immunol* **40**, 240-247, doi:10.1016/j.dci.2013.03.006 (2013).

216 Fuchs, J. *et al.* Evolution and Antiviral Specificities of Interferon-Induced Mx Proteins of Bats against Ebola, Influenza, and Other RNA Viruses. *J Virol* **91**, doi:10.1128/JVI.00361-17 (2017).

217 Xie, J. *et al.* Dampened STING-Dependent Interferon Activation in Bats. **23**, 297-301.e294, doi:10.1016/j.chom.2018.01.006 (2018).

218 Xie, J. *et al.* Dampened STING-Dependent Interferon Activation in Bats. *Cell Host Microbe* **23**, 297-301 e294, doi:10.1016/j.chom.2018.01.006 (2018).

219 Goh, G. *et al.* Complementary regulation of caspase-1 and IL-1β reveals additional mechanisms of dampened inflammation in bats. **117**, 28939–28949, doi:10.1073/pnas.2003352117 (2020).

220 O'Shea, T. J. *et al.* Bat flight and zoonotic viruses. *Emerg Infect Dis* **20**, 741-745, doi:10.3201/eid2005.130539 (2014).

221 Kingston, T. *et al.* in *Bats in the Anthropocene: Conservation of Bats in a Changing World* (eds Christian C. Voigt & Tigga Kingston) Ch. Chapter 17, 539-569 (Springer International Publishing, 2016).

222 Van Der Westhuyzen, J. Haematology and iron status of the egyptian fruit bat, *rousettus aegyptiacus*. *Comparative Biochemistry and Physiology Part A: Physiology* **90**, 117-120, doi:10.1016/0300-9629(88)91015-8 (1988).

223 Prescott, J. *et al.* Rousette Bat Dendritic Cells Overcome Marburg Virus-Mediated Antiviral Responses by Upregulation of Interferon-Related Genes While Downregulating Proinflammatory Disease Mediators. *mSphere* **4**, doi:10.1128/mSphere.00728-19 (2019).

224 Martínez Gómez, J. M. *et al.* Phenotypic and functional characterization of the major lymphocyte populations in the fruit-eating bat *Pteropus alecto*. **6**, 37796, doi:10.1038/srep37796 (2016).

225 Periasamy, P. *et al.* Studies on B Cells in the Fruit-Eating Black Flying Fox (*Pteropus alecto*). **10**, 489, doi:10.3389/fimmu.2019.00489 (2019).

226 Zhou, P. *et al.* Unlocking bat immunology: establishment of *Pteropus alecto* bone marrow-derived dendritic cells and macrophages. *Sci Rep* **6**, 38597, doi:10.1038/srep38597 (2016).

227 Gutierrez-Mecinas, M. *et al.* Characterization of somatostatin- and cholecystokinin-immunoreactive periglomerular cells in the rat olfactory bulb. *J Comp Neurol* **489**, 467-479, doi:10.1002/cne.20649 (2005).

228 Gamage, A. M. *et al.* Immunophenotyping monocytes, macrophages and granulocytes in the Pteropodid bat *Eonycteris spelaea*. **10**, 309, doi:10.1038/s41598-019-57212-1. (2020).

229 Sarkar, S. K. & Chakravarty, A. K. Analysis of immunocompetent cells in the bat, *Pteropus giganteus*: isolation and scanning electron microscopic characterization. *Dev Comp Immunol* **15**, 423-430, doi:10.1016/0145-305x(91)90034-v (1991).

230 Chakravarty, A. K. & Paul, B. N. Analysis of suppressor factor in delayed immune responses of a bat, *Pteropus giganteus*. *Developmental & Comparative Immunology* **11**, 649-660, doi:10.1016/0145-305x(87)90053-x (1987).

231 Chakravarty, A. K. & Sarkar, S. K. Immunofluorescence analysis of immunoglobulin bearing lymphocytes in the Indian fruit bat: *Pteropus giganteus*. *Lymphology* **27**, 97-104 (1994).

232 Paul, B. N. & Chakravarty, A. K. In vitro analysis of delayed immune response in a bat, *Pteropus giganteus*: process of con-A mediated activation. *Dev Comp Immunol* **10**, 55-67, doi:10.1016/0145-305x(86)90044-3 (1986).

233 Paksuz, S., Paksuz, E. & Özkan, B. White Blood Cell (WBC) Count of Different Bat (Chiroptera) Species. *Trakya University Journal of Natural Sciences* (2021).

234 Becker, D. J. *et al.* Leukocyte Profiles Reflect Geographic Range Limits in a Widespread Neotropical Bat. *Integr Comp Biol* **59**, 1176-1189, doi:10.1093/icb/icz007 (2019).

235 Kizhina, A. *et al.* Hematological Parameters in Hibernating Eptesicus nilssonii (Mammalia: Chiroptera) Collected in Northern European Russia. *Acta Chiropterologica* **20**, 273-283, doi:10.3161/15081109acc2018.20.1.021 (2018).

236 Lin, A. & Lore, K. Granulocytes: New Members of the Antigen-Presenting Cell Family. *Front Immunol* **8**, 1781, doi:10.3389/fimmu.2017.01781 (2017).

237 Jakubzick, C. V., Randolph, G. J. & Henson, P. M. Monocyte differentiation and antigen-presenting functions. *Nat Rev Immunol* **17**, 349-362, doi:10.1038/nri.2017.28 (2017).

238 Unanue, E. R. & Allen, P. M. The basis for the immunoregulatory role of macrophages and other accessory cells. *Science* **236**, 551-557, doi:10.1126/science.2437650 (1987).

239 den Haan, J. M., Arens, R. & van Zelm, M. C. The activation of the adaptive immune system: cross-talk between antigen-presenting cells, T cells and B cells. *Immunol Lett* **162**, 103-112, doi:10.1016/j.imlet.2014.10.011 (2014).

240 Turmelle, A. S., Ellison, J. A., Mendonca, M. T. & McCracken, G. F. Histological assessment of cellular immune response to the phytohemagglutinin skin test in Brazilian free-tailed bats (*Tadarida brasiliensis*). *J Comp Physiol B* **180**, 1155-1164, doi:10.1007/s00360-010-0486-6 (2010).

241 Wynne, J. W. *et al.* Characterization of the Antigen Processing Machinery and Endogenous Peptide Presentation of a Bat MHC Class I Molecule. *J Immunol* **196**, 4468-4476, doi:10.4049/jimmunol.1502062 (2016).

242 Ng, J. H. J., Tachedjian, M., Wang, L. F. & Baker, M. L. Insights into the ancestral organisation of the mammalian MHC class II region from the genome of the pteropid bat, *Pteropus alecto*. *BMC Genomics* **18**, 388, doi:10.1186/s12864-017-3760-0 (2017).

243 Qu, Z. *et al.* Structure and Peptidome of the Bat MHC Class I Molecule Reveal a Novel Mechanism Leading to High-Affinity Peptide Binding. *J Immunol* **202**, 3493-3506, doi:10.4049/jimmunol.1900001 (2019).

244 Paul, S. & Lal, G. The Molecular Mechanism of Natural Killer Cells Function and Its Importance in Cancer Immunotherapy. *Front Immunol* **8**, 1124, doi:10.3389/fimmu.2017.01124 (2017).

245 Borrego, F., Masilamani, M., Marusina, A. I., Tang, X. & Coligan, J. E. The CD94/NKG2 Family of Receptors: From Molecules and Cells to Clinical Relevance. *Immunologic Research* **35**, 263-278, doi:10.1385/ir:35:3:263 (2006).

246 Godfrey, D. I., MacDonald, H. R., Kronenberg, M., Smyth, M. J. & Van Kaer, L. NKT cells: what's in a name? *Nat Rev Immunol* **4**, 231-237, doi:10.1038/nri1309 (2004).

247 Van Der Vliet, H. J. *et al.* Effects of alpha-galactosylceramide (KRN7000), interleukin-12 and interleukin-7 on phenotype and cytokine profile of human Valpha24+ Vbeta11+ T cells. *Immunology* **98**, 557-563, doi:10.1046/j.1365-2567.1999.00920.x (1999).

248 Vivier, E. & Anfossi, N. Inhibitory NK-cell receptors on T cells: witness of the past, actors of the future. *Nat Rev Immunol* **4**, 190-198, doi:10.1038/nri1306 (2004).

249 Vivier, E. & Malissen, B. Innate and adaptive immunity: specificities and signaling hierarchies revisited. *Nat Immunol* **6**, 17-21, doi:10.1038/ni1153 (2005).

250 Netea, M. G., Schlitzer, A., Placek, K., Joosten, L. A. B. & Schultze, J. L. Innate and Adaptive Immune Memory: an Evolutionary Continuum in the Host's Response to Pathogens. *Cell Host Microbe* **25**, 13-26, doi:10.1016/j.chom.2018.12.006 (2019).

251 Santarlasci, V., Cosmi, L., Maggi, L., Liotta, F. & Annunziato, F. IL-1 and T Helper Immune Responses. *Front Immunol* **4**, 182, doi:10.3389/fimmu.2013.00182 (2013).

252 Raphael, I., Nalawade, S., Eagar, T. N. & Forsthuber, T. G. T cell subsets and their signature cytokines in autoimmune and inflammatory diseases. *Cytokine* **74**, 5-17, doi:10.1016/j.cyto.2014.09.011 (2015).

253 Leeansyah, E. *et al.* MR1-Restricted T Cells with MAIT-like Characteristics Are Functionally Conserved in the Pteropid Bat *Pteropus alecto*. *iScience* **23**, 101876, doi:10.1016/j.isci.2020.101876 (2020).

254 Dorner, T. & Radbruch, A. Antibodies and B cell memory in viral immunity. *Immunity* **27**, 384-392, doi:10.1016/j.immuni.2007.09.002 (2007).

255 Hong, S. *et al.* B Cells Are the Dominant Antigen-Presenting Cells that Activate Naive CD4(+) T Cells upon Immunization with a Virus-Derived Nanoparticle Antigen. *Immunity* **49**, 695-708 e694, doi:10.1016/j.immuni.2018.08.012 (2018).

256 Cui, J. *et al.* Evolutionary relationships between bat coronaviruses and their hosts. *Emerg Infect Dis* **13**, 1526-1532, doi:10.3201/eid1310.070448 (2007).

257 Bouma, H. R., Carey, H. V. & Kroese, F. G. Hibernation: the immune system at rest? *J Leukoc Biol* **88**, 619-624, doi:10.1189/jlb.0310174 (2010).

258 Subudhi, S., Rapin, N. & Misra, V. Immune System Modulation and Viral Persistence in Bats: Understanding Viral Spillover. **11**, doi:10.3390/v11020192 (2019).

259 Shen, Y. Y. *et al.* Adaptive evolution of energy metabolism genes and the origin of flight in bats. *Proc Natl Acad Sci U S A* **107**, 8666-8671, doi:10.1073/pnas.0912613107 (2010).

260 Phillips, A. M. *et al.* Host proteostasis modulates influenza evolution. *Elife* **6**, doi:10.7554/eLife.28652 (2017).

261 Miller, M. R. *et al.* Broad and Temperature Independent Replication Potential of Filoviruses on Cells Derived From Old and New World Bat Species. *J Infect Dis* **214**, S297-S302, doi:10.1093/infdis/jiw199 (2016).

262 Furman, D. *et al.* Chronic inflammation in the etiology of disease across the life span. *Nat Med* **25**, 1822-1832, doi:10.1038/s41591-019-0675-0 (2019).

263 McNab, F., Mayer-Barber, K., Sher, A., Wack, A. & O'Garra, A. Type I interferons in infectious disease. *Nat Rev Immunol* **15**, 87-103, doi:10.1038/nri3787 (2015).

264 Secombes, C. J. & Zou, J. Evolution of Interferons and Interferon Receptors. *Front Immunol* **8**, 209, doi:10.3389/fimmu.2017.00209 (2017).

265 Holzer, M. *et al.* Virus- and Interferon Alpha-Induced Transcriptomes of Cells from the Microbat Myotis daubentonii. *iScience* **19**, 647-661, doi:10.1016/j.isci.2019.08.016 (2019).

266 Paweska, J. T. *et al.* Experimental Inoculation of Egyptian Fruit Bats (*Rousettus aegyptiacus*) with Ebola Virus. **8**, doi:10.3390/v8020029 (2016).

267 Munster, V. J. *et al.* Replication and shedding of MERS-CoV in Jamaican fruit bats (*Artibeus jamaicensis*). *Sci Rep* **6**, 21878, doi:10.1038/srep21878 (2016).

268 Watanabe, S. *et al.* Bat coronaviruses and experimental infection of bats, the Philippines. *Emerg Infect Dis* **16**, 1217-1223, doi:10.3201/eid1608.100208 (2010).

269 Middleton, D. J. *et al.* Experimental Nipah virus infection in pteropid bats (*Pteropus poliocephalus*). *J Comp Pathol* **136**, 266-272, doi:10.1016/j.jcpa.2007.03.002 (2007).

270 Khan, I. U., Brooks, G., Guo, N. N., Chen, J. & Guo, F. Fever-range hyperthermia promotes cGAS-STING pathway and synergizes DMXAA-induced antiviral immunity. *Int J Hyperthermia* **38**, 30-37, doi:10.1080/02656736.2020.1868582 (2021).

271 Diner, B. A. *et al.* The functional interactome of PYHIN immune regulators reveals IFIX is a sensor of viral DNA. *Mol Syst Biol* **11**, 787, doi:10.15252/msb.20145808 (2015).

272 Amman, B. R. *et al.* Seasonal pulses of Marburg virus circulation in juvenile *Rousettus aegyptiacus* bats coincide with periods of increased risk of human infection. *PLoS Pathog* **8**, e1002877, doi:10.1371/journal.ppat.1002877 (2012).

273 Orbanz, J. & Finke, S. Generation of recombinant European bat lyssavirus type 1 and inter-genotypic compatibility of lyssavirus genotype 1 and 5 antigenome promoters. *Arch Virol* **155**, 1631-1641, doi:10.1007/s00705-010-0743-8 (2010).

274 Schafer, A. *et al.* Porcine Invariant Natural Killer T Cells: Functional Profiling and Dynamics in Steady State and Viral Infections. *Front Immunol* **10**, 1380, doi:10.3389/fimmu.2019.01380 (2019).

275 Tichy, A. *et al.* The first *in vivo* multiparametric comparison of different radiation exposure biomarkers in human blood. *PLoS One* **13**, e0193412, doi:10.1371/journal.pone.0193412 (2018).

276 Cheng, R. *et al.* Influence of Fixation and Permeabilization on the Mass Density of Single Cells: A Surface Plasmon Resonance Imaging Study. *Front Chem* **7**, 588, doi:10.3389/fchem.2019.00588 (2019).

277 MacRae, E. Extraction of plant RNA. *Methods Mol Biol* **353**, 15-24, doi:10.1385/1-59745-229-7:15 (2007).

278 Channathodiyil, P. & Houseley, J. Glyoxal fixation facilitates transcriptome analysis after antigen staining and cell sorting by flow cytometry. *PLoS One* **16**, e0240769, doi:10.1371/journal.pone.0240769 (2021).

279 Lee, C., Kim, J., Shin, S. G. & Hwang, S. Absolute and relative QPCR quantification of plasmid copy number in *Escherichia coli*. *J Biotechnol* **123**, 273-280, doi:10.1016/j.jbiotec.2005.11.014 (2006).

280 Heaton, H. *et al.* Souporcell: robust clustering of single-cell RNA-seq data by genotype without reference genotypes. *Nat Methods* **17**, 615-620, doi:10.1038/s41592-020-0820-1 (2020).

281 Becht, E. *et al.* Dimensionality reduction for visualizing single-cell data using UMAP. *Nat Biotechnol*, doi:10.1038/nbt.4314 (2018).

282 Traag, V. A., Waltman, L. & van Eck, N. J. From Louvain to Leiden: guaranteeing well-connected communities. *Sci Rep* **9**, 5233, doi:10.1038/s41598-019-41695-z (2019).

283 Setien, A. A. *et al.* Experimental rabies infection and oral vaccination in vampire bats (*Desmodus rotundus*). *Vaccine* **16**, 1122-1126, doi:10.1016/s0264-410x(98)80108-4 (1998).
284 Almeida, M. F. *et al.* Experimental rabies infection in haematophagous bats *Desmodus rotundus*. *Epidemiol Infect* **133**, 523-527, doi:10.1017/s0950268804003656 (2005).
285 Charles, D. D. *et al.* Development of a Novel *ex vivo* Nasal Epithelial Cell Model Supporting Colonization With Human Nasal Microbiota. *Front Cell Infect Microbiol* **9**, 165, doi:10.3389/fcimb.2019.00165 (2019).
286 Franzen, O., Gan, L. M. & Bjorkegren, J. L. M. PanglaoDB: a web server for exploration of mouse and human single-cell RNA sequencing data. *Database (Oxford)* **2019**, doi:10.1093/database/baz046 (2019).
287 Takahashi, H., Yoshihara, S. & Tsuboi, A. The Functional Role of Olfactory Bulb Granule Cell Subtypes Derived From Embryonic and Postnatal Neurogenesis. *Front Mol Neurosci* **11**, 229, doi:10.3389/fnmol.2018.00229 (2018).
288 Nunes, D. & Kuner, T. Disinhibition of olfactory bulb granule cells accelerates odour discrimination in mice. *Nat Commun* **6**, 8950, doi:10.1038/ncomms9950 (2015).
289 Tepe, B. *et al.* Single-Cell RNA-Seq of Mouse Olfactory Bulb Reveals Cellular Heterogeneity and Activity-Dependent Molecular Census of Adult-Born Neurons. *Cell Rep* **25**, 2689-2703 e2683, doi:10.1016/j.celrep.2018.11.034 (2018).
290 Ramón-Cueto, A. & Avila, J. Olfactory ensheathing glia: properties and function. *Brain Research Bulletin* **46**, 175-187, doi:10.1016/s0361-9230(97)00463-2 (1998).
291 Ho, H. *et al.* A Guide to Single-Cell Transcriptomics in Adult Rodent Brain: The Medium Spiny Neuron Transcriptome Revisited. *Front Cell Neurosci* **12**, 159, doi:10.3389/fncel.2018.00159 (2018).
292 Furuse, M. *et al.* Claudin-based tight junctions are crucial for the mammalian epidermal barrier: a lesson from claudin-1-deficient mice. *J Cell Biol* **156**, 1099-1111, doi:10.1083/jcb.200110122 (2002).
293 Furuse, M. *et al.* Occludin: a novel integral membrane protein localizing at tight junctions. *J Cell Biol* **123**, 1777-1788, doi:10.1083/jcb.123.6.1777 (1993).
294 van Roy, F. & Berx, G. The cell-cell adhesion molecule E-cadherin. *Cell Mol Life Sci* **65**, 3756-3788, doi:10.1007/s00018-008-8281-1 (2008).
295 Groulx, J. F. *et al.* Collagen VI is a basement membrane component that regulates epithelial cell-fibronectin interactions. *Matrix Biol* **30**, 195-206, doi:10.1016/j.matbio.2011.03.002 (2011).
296 Kozyraki, R. Cubilin, a multifunctional epithelial receptor: an overview. *J Mol Med (Berl)* **79**, 161-167, doi:10.1007/s001090100193 (2001).
297 Adler, K. B., Tuvim, M. J. & Dickey, B. F. Regulated mucin secretion from airway epithelial cells. *Front Endocrinol (Lausanne)* **4**, 129, doi:10.3389/fendo.2013.00129 (2013).
298 Pellitteri, R., Spatuzza, M., Stanzani, S. & Zaccheo, D. Biomarkers expression in rat olfactory ensheathing cells. *Front Biosci (Schol Ed)* **2**, 289-298, doi:10.2741/s64 (2010).
299 Mosmann, T. Rapid colorimetric assay for cellular growth and survival: Application to proliferation and cytotoxicity assays. *Journal of Immunological Methods* **65**, 55-63, doi:10.1016/0022-1759(83)90303-4 (1983).
300 Chan, F. K., Moriwaki, K. & De Rosa, M. J. Detection of necrosis by release of lactate dehydrogenase activity. *Methods Mol Biol* **979**, 65-70, doi:10.1007/978-1-62703-290-2_7 (2013).

301 Kerr, J. F., Wyllie, A. H. & Currie, A. R. Apoptosis: a basic biological phenomenon with wide-ranging implications in tissue kinetics. *Br J Cancer* **26**, 239-257, doi:10.1038/bjc.1972.33 (1972).

302 Fadok, V. A., Bratton, D. L., Frasch, S. C., Warner, M. L. & Henson, P. M. The role of phosphatidylserine in recognition of apoptotic cells by phagocytes. *Cell Death Differ* **5**, 551-562, doi:10.1038/sj.cdd.4400404 (1998).

303 Rieger, A. M., Nelson, K. L., Konowalchuk, J. D. & Barreda, D. R. Modified annexin V/propidium iodide apoptosis assay for accurate assessment of cell death. *J Vis Exp*, doi:10.3791/2597 (2011).

304 Fang, Y. & Eglen, R. M. Three-Dimensional Cell Cultures in Drug Discovery and Development. *SLAS Discov* **22**, 456-472, doi:10.1177/1087057117696795 (2017).

305 Brook, C. E. *et al.* Accelerated viral dynamics in bat cell lines, with implications for zoonotic emergence. **9**, doi:10.7554/eLife.48401 (2020).

306 Sarwar, M. B. *et al.* Identification and validation of superior housekeeping gene(s) for qRT-PCR data normalization in *Agave sisalana* (a CAM-plant) under abiotic stresses. **26**, 567–584, doi:10.1007/s12298-020-00760-y (2020).

307 Klie, M. & Debener, T. Identification of superior reference genes for data normalisation of expression studies via quantitative PCR in hybrid roses (*Rosa hybrida*). **4**, 518, doi:10.1186/1756-0500-4-518 (2011).

308 Halwe, N. J. *et al.* Egyptian Fruit Bats (*Rousettus aegyptiacus*) Were Resistant to Experimental Inoculation with Avian-Origin Influenza A Virus of Subtype H9N2, But Are Susceptible to Experimental Infection with Bat-Borne H9N2 Virus. *Viruses* **13**, doi:10.3390/v13040672 (2021).

309 Vos, A. *et al.* Raccoons (*Procyon lotor*) in Germany as potential reservoir species for Lyssaviruses. *European Journal of Wildlife Research* **59**, 637-643, doi:10.1007/s10344-013-0714-y (2013).

310 Kim, S. W., Seo, K. Y., Rhim, T. & Kim, E. K. Effect of retinoic acid on epithelial differentiation and mucin expression in primary human corneal limbal epithelial cells. *Curr Eye Res* **37**, 33-42, doi:10.3109/02713683.2011.620728 (2012).

311 Briske-Anderson, M. J., Finley, J. W. & Newman, S. M. The influence of culture time and passage number on the morphological and physiological development of Caco-2 cells. *Proc Soc Exp Biol Med* **214**, 248-257, doi:10.3181/00379727-214-44093 (1997).

312 Hare, D., Collins, S., Cuddington, B. & Mossman, K. The Importance of Physiologically Relevant Cell Lines for Studying Virus-Host Interactions. *Viruses* **8**, doi:10.3390/v8110297 (2016).

313 Bustin, S. A. *et al.* The MIQE guidelines: minimum information for publication of quantitative real-time PCR experiments. **55**, 611–622, doi:10.1373/clinchem.2008.112797 (2009).

314 Sommereyns, C., Paul, S., Staeheli, P. & Michiels, T. IFN-lambda (IFN-lambda) is expressed in a tissue-dependent fashion and primarily acts on epithelial cells *in vivo*. *PLoS Pathog* **4**, e1000017, doi:10.1371/journal.ppat.1000017 (2008).

315 Klein, K., Habiger, C., Iftner, T. & Stubenrauch, F. A TGF-beta- and p63-Responsive Enhancer Regulates IFN-kappa Expression in Human Keratinocytes. *J Immunol* **204**, 1825-1835, doi:10.4049/jimmunol.1901178 (2020).

316 Uhlen, M. *et al.* Proteomics. Tissue-based map of the human proteome. *Science* **347**, 1260419, doi:10.1126/science.1260419 (2015).

317 Karlsson, M. *et al.* A single-cell type transcriptomics map of human tissues. *Sci Adv* **7**, doi:10.1126/sciadv.abh2169 (2021).

318 Ivashkiv, L. B. & Donlin, L. T. Regulation of type I interferon responses. *Nat Rev Immunol* **14**, 36-49, doi:10.1038/nri3581 (2014).
319 Wang, J. *et al.* Metabotropic glutamate receptor subtype 2 is a cellular receptor for rabies virus. *PLoS Pathog* **14**, e1007189, doi:10.1371/journal.ppat.1007189 (2018).
320 Vazquez, S., Ibanez, C., Juste, J. & Echevarria, J. E. EBLV1 circulation in natural bat colonies of *Eptesicus serotinus*: a six year survey. *Dev Biol (Basel)* **125**, 257-261 (2006).
321 Meredith, C. D. & Standing, E. Lagos Bat Virus in South Africa. *The Lancet* **317**, 832-833, doi:10.1016/s0140-6736(81)92698-2 (1981).
322 Swanepoel, R. *et al.* Rabies in southern Africa. *Onderstepoort J Vet Res* **60**, 325-346 (1993).
323 Li, W. *et al.* Angiotensin-converting enzyme 2 is a functional receptor for the SARS coronavirus. *Nature* **426**, 450-454, doi:10.1038/nature02145 (2003).
324 Hoffmann, M. *et al.* SARS-CoV-2 Cell Entry Depends on ACE2 and TMPRSS2 and Is Blocked by a Clinically Proven Protease Inhibitor. *Cell* **181**, 271-280 e278, doi:10.1016/j.cell.2020.02.052 (2020).
325 Cantuti-Castelvetri, L. *et al.* Neuropilin-1 facilitates SARS-CoV-2 cell entry and infectivity. *Science* **370**, 856-860, doi:10.1126/science.abd2985 (2020).
326 Ziegler, C. G. K. *et al.* SARS-CoV-2 Receptor ACE2 Is an Interferon-Stimulated Gene in Human Airway Epithelial Cells and Is Detected in Specific Cell Subsets across Tissues. *Cell* **181**, 1016-1035 e1019, doi:10.1016/j.cell.2020.04.035 (2020).
327 Swanson, M. A., Lee, W. T. & Sanders, V. M. IFN-gamma production by Th1 cells generated from naive CD4+ T cells exposed to norepinephrine. *J Immunol* **166**, 232-240, doi:10.4049/jimmunol.166.1.232 (2001).
328 Arase, H., Arase, N. & Saito, T. Interferon gamma production by natural killer (NK) cells and NK1.1+ T cells upon NKR-P1 cross-linking. *J Exp Med* **183**, 2391-2396, doi:10.1084/jem.183.5.2391 (1996).
329 Kling, J. C. *et al.* Temporal Regulation of Natural Killer T Cell Interferon Gamma Responses by beta-Catenin-Dependent and -Independent Wnt Signaling. *Front Immunol* **9**, 483, doi:10.3389/fimmu.2018.00483 (2018).
330 Vermijlen, D. *et al.* Distinct cytokine-driven responses of activated blood gammadelta T cells: insights into unconventional T cell pleiotropy. *J Immunol* **178**, 4304-4314, doi:10.4049/jimmunol.178.7.4304 (2007).
331 Christensen, J. E., Andreasen, S. O., Christensen, J. P. & Thomsen, A. R. CD11b expression as a marker to distinguish between recently activated effector CD8(+) T cells and memory cells. *Int Immunol* **13**, 593-600, doi:10.1093/intimm/13.4.593 (2001).
332 Ruban, G. I., Kosmacheva, S. M., Goncharova, N. V., Van Bockstaele, D. & Loiko, V. A. Investigation of morphometric parameters for granulocytes and lymphocytes as applied to a solution of direct and inverse light-scattering problems. *J Biomed Opt* **12**, 044017, doi:10.1117/1.2753466 (2007).
333 Watt, S. M., Burgess, A. W., Metcalf, D. & Battye, F. L. Isolation of mouse bone marrow neutrophils by light scatter and autofluorescence. *J Histochem Cytochem* **28**, 934-946, doi:10.1177/28.9.7410816 (1980).
334 McFarland, H. I., Nahill, S. R., Maciaszek, J. W. & Welsh, R. M. CD11b (Mac-1): a marker for CD8+ cytotoxic T cell activation and memory in virus infection. *J Immunol* **149**, 1326-1333 (1992).
335 Hearps, A. C. *et al.* Aging is associated with chronic innate immune activation and dysregulation of monocyte phenotype and function. *Aging Cell* **11**, 867-875, doi:10.1111/j.1474-9726.2012.00851.x (2012).

336 Plowden, J., Renshaw-Hoelscher, M., Engleman, C., Katz, J. & Sambhara, S. Innate immunity in aging: impact on macrophage function. *Aging Cell* **3**, 161-167, doi:10.1111/j.1474-9728.2004.00102.x (2004).

337 Butcher, S. K. *et al.* Senescence in innate immune responses: reduced neutrophil phagocytic capacity and CD16 expression in elderly humans. *J Leukoc Biol* **70**, 881-886 (2001).

338 Simell, B. *et al.* Aging reduces the functionality of anti-pneumococcal antibodies and the killing of *Streptococcus pneumoniae* by neutrophil phagocytosis. *Vaccine* **29**, 1929-1934, doi:10.1016/j.vaccine.2010.12.121 (2011).

339 Wenisch, C., Patruta, S., Daxbock, F., Krause, R. & Horl, W. Effect of age on human neutrophil function. *J Leukoc Biol* **67**, 40-45, doi:10.1002/jlb.67.1.40 (2000).

340 Li, J. *et al.* B lymphocytes from early vertebrates have potent phagocytic and microbicidal abilities. *Nat Immunol* **7**, 1116-1124, doi:10.1038/ni1389 (2006).

341 Gao, J. *et al.* Novel functions of murine B1 cells: active phagocytic and microbicidal abilities. *Eur J Immunol* **42**, 982-992, doi:10.1002/eji.201141519 (2012).

342 Pan, Y. *et al.* Discovery and Validation of a Novel Neutrophil Activation Marker Associated with Obesity. *Sci Rep* **9**, 3433, doi:10.1038/s41598-019-39764-4 (2019).

343 Dutertre, C. A. *et al.* Single-Cell Analysis of Human Mononuclear Phagocytes Reveals Subset-Defining Markers and Identifies Circulating Inflammatory Dendritic Cells. *Immunity* **51**, 573-589 e578, doi:10.1016/j.immuni.2019.08.008 (2019).

344 Haug, T. *et al.* Human Double-Negative Regulatory T-Cells Induce a Metabolic and Functional Switch in Effector T-Cells by Suppressing mTOR Activity. *Front Immunol* **10**, 883, doi:10.3389/fimmu.2019.00883 (2019).

345 Park, C. K., Shin, Y. K., Kim, T. J., Park, S. H. & Ahn, G. H. High CD99 expression in memory T and B cells in reactive lymph nodes. *J Korean Med Sci* **14**, 600-606, doi:10.3346/jkms.1999.14.6.600 (1999).

346 Hathcock, K. S., Hirano, H., Murakami, S. & Hodes, R. J. CD44 expression on activated B cells. Differential capacity for CD44-dependent binding to hyaluronic acid. *J Immunol* **151**, 6712-6722 (1993).

347 Jash, A. *et al.* ZBTB32 Restricts the Duration of Memory B Cell Recall Responses. *J Immunol* **197**, 1159-1168, doi:10.4049/jimmunol.1600882 (2016).

348 Kreslavsky, T. *et al.* Essential role for the transcription factor Bhlhe41 in regulating the development, self-renewal and BCR repertoire of B-1a cells. *Nat Immunol* **18**, 442-455, doi:10.1038/ni.3694 (2017).

349 Murray, K. *et al.* A novel morbillivirus pneumonia of horses and its transmission to humans. *Emerg Infect Dis* **1**, 31-33, doi:10.3201/eid0101.950107 (1995).

350 Selvey, L. A. *et al.* Infection of humans and horses by a newly described morbillivirus. *Med J Aust* **162**, 642-645, doi:10.5694/j.1326-5377.1995.tb126050.x (1995).

351 Reusken, C. B. E. M. *et al.* Middle East respiratory syndrome coronavirus neutralising serum antibodies in dromedary camels: a comparative serological study. *The Lancet Infectious Diseases* **13**, 859-866, doi:10.1016/s1473-3099(13)70164-6 (2013).

352 Teeling, E. C. *et al.* Bat Biology, Genomes, and the Bat1K Project: To Generate Chromosome-Level Genomes for All Living Bat Species. *Annu Rev Anim Biosci* **6**, 23-46, doi:10.1146/annurev-animal-022516-022811 (2018).

353 Schuh, A. J. *et al.* Egyptian rousette bats maintain long-term protective immunity against Marburg virus infection despite diminished antibody levels. *Sci Rep* **7**, 8763, doi:10.1038/s41598-017-07824-2 (2017).

354 Dheda, K. *et al.* Validation of housekeeping genes for normalizing RNA expression in real-time PCR. *Biotechniques* **37**, 112-114, 116, 118-119, doi:10.2144/04371RR03 (2004).

355 Aminfar, Z., Rabiei, B., Tohidfar, M. & Mirjalili, M. H. Selection and validation of reference genes for quantitative real-time PCR in *Rosmarinus officinalis L.* in various tissues and under elicitation. *Biocatalysis and Agricultural Biotechnology* **20**, doi:10.1016/j.bcab.2019.101246 (2019).

356 Bai, B., Ren, J., Bai, F. & Hao, L. Selection and validation of reference genes for gene expression studies in *Pseudomonas brassicacearum* GS20 using real-time quantitative reverse transcription PCR. *PLoS One* **15**, e0227927, doi:10.1371/journal.pone.0227927 (2020).

357 Ham, S., Harrison, C., Southwick, G. & Temple-Smith, P. Selection of internal control genes for analysis of gene expression in normal and diseased human dermal fibroblasts using quantitative real-time PCR. *Exp Dermatol* **25**, 911-914, doi:10.1111/exd.13091 (2016).

358 Huggett, J., Dheda, K., Bustin, S. & Zumla, A. Real-time RT-PCR normalisation; strategies and considerations. *Genes Immun* **6**, 279-284, doi:10.1038/sj.gene.6364190 (2005).

359 Fujii, H. *et al.* Functional analysis of *Rousettus aegyptiacus* "signal transducer and activator of transcription 1" (STAT1). *Dev Comp Immunol* **34**, 598-602, doi:10.1016/j.dci.2010.01.004 (2010).

360 Lu, J., Yang, C., Zhang, Y. & Pan, H. Selection of Reference Genes for the Normalization of RT-qPCR Data in Gene Expression Studies in Insects: A Systematic Review. *Front Physiol* **9**, 1560, doi:10.3389/fphys.2018.01560 (2018).

361 Falkenberg, V. R., Whistler, T., Murray, J. R., Unger, E. R. & Rajeevan, M. S. Identification of Phosphoglycerate Kinase 1 (PGK1) as a reference gene for quantitative gene expression measurements in human blood RNA. *BMC Res Notes* **4**, 324, doi:10.1186/1756-0500-4-324 (2011).

362 Glare, E. M., Divjak, M., Bailey, M. J. & Walters, E. H. beta-Actin and GAPDH housekeeping gene expression in asthmatic airways is variable and not suitable for normalising mRNA levels. *Thorax* **57**, 765-770, doi:10.1136/thorax.57.9.765 (2002).

363 Sabath, D. E., Broome, H. E. & Prystowsky, M. B. Glyceraldehyde-3-phosphate dehydrogenase mRNA is a major interleukin 2-induced transcript in a cloned T-helper lymphocyte. *Gene* **91**, 185-191, doi:10.1016/0378-1119(90)90087-8 (1990).

364 Graven, K. K., McDonald, R. J. & Farber, H. W. Hypoxic regulation of endothelial glyceraldehyde-3-phosphate dehydrogenase. *Am J Physiol* **274**, C347-355, doi:10.1152/ajpcell.1998.274.2.C347 (1998).

365 Hazell, A. S., Desjardins, P. & Butterworth, R. F. Increased expression of glyceraldehyde-3-phosphate dehydrogenase in cultured astrocytes following exposure to manganese. *Neurochemistry International* **35**, 11-17, doi:10.1016/s0197-0186(99)00024-8 (1999).

366 Grzanka, D. *et al.* Hyperthermia-induced reorganization of microtubules and microfilaments and cell killing in CHO AA8 cell line. *Neoplasma* **55**, 409-415 (2008).

367 Rivera, R. M., Kelley, K. L., Erdos, G. W. & Hansen, P. J. Reorganization of microfilaments and microtubules by thermal stress in two-cell bovine embryos. *Biol Reprod* **70**, 1852-1862, doi:10.1095/biolreprod.103.024901 (2004).

368 O'Neill, L. A., Kishton, R. J. & Rathmell, J. A guide to immunometabolism for immunologists. *Nat Rev Immunol* **16**, 553-565, doi:10.1038/nri.2016.70 (2016).

369 O'Neill, L. A. & Pearce, E. J. Immunometabolism governs dendritic cell and macrophage function. *J Exp Med* **213**, 15-23, doi:10.1084/jem.20151570 (2016).

370 Tannahill, G. M. *et al.* Succinate is an inflammatory signal that induces IL-1beta through HIF-1alpha. *Nature* **496**, 238-242, doi:10.1038/nature11986 (2013).

371 Cham, C. M., Driessens, G., O'Keefe, J. P. & Gajewski, T. F. Glucose deprivation inhibits multiple key gene expression events and effector functions in CD8+ T cells. *Eur J Immunol* **38**, 2438-2450, doi:10.1002/eji.200838289 (2008).

372 Cham, C. M. & Gajewski, T. F. Glucose availability regulates IFN-gamma production and p70S6 kinase activation in CD8+ effector T cells. *J Immunol* **174**, 4670-4677, doi:10.4049/jimmunol.174.8.4670 (2005).

373 Chang, C. H. *et al.* Posttranscriptional control of T cell effector function by aerobic glycolysis. *Cell* **153**, 1239-1251, doi:10.1016/j.cell.2013.05.016 (2013).

374 Gerriets, V. A. *et al.* Metabolic programming and PDHK1 control CD4+ T cell subsets and inflammation. *J Clin Invest* **125**, 194-207, doi:10.1172/JCI76012 (2015).

375 Keating, S. E. *et al.* Metabolic Reprogramming Supports IFN-gamma Production by CD56bright NK Cells. *J Immunol* **196**, 2552-2560, doi:10.4049/jimmunol.1501783 (2016).

376 Macintyre, A. N. *et al.* The glucose transporter Glut1 is selectively essential for CD4 T cell activation and effector function. *Cell Metab* **20**, 61-72, doi:10.1016/j.cmet.2014.05.004 (2014).

377 Mah, A. Y. *et al.* Glycolytic requirement for NK cell cytotoxicity and cytomegalovirus control. *JCI Insight* **2**, doi:10.1172/jci.insight.95128 (2017).

378 Fekete, T. *et al.* Human Plasmacytoid and Monocyte-Derived Dendritic Cells Display Distinct Metabolic Profile Upon RIG-I Activation. *Front Immunol* **9**, 3070, doi:10.3389/fimmu.2018.03070 (2018).

379 Burke, J. D., Platanias, L. C. & Fish, E. N. Beta interferon regulation of glucose metabolism is PI3K/Akt dependent and important for antiviral activity against coxsackievirus B3. *J Virol* **88**, 3485-3495, doi:10.1128/JVI.02649-13 (2014).

380 Pantel, A. *et al.* Direct type I IFN but not MDA5/TLR3 activation of dendritic cells is required for maturation and metabolic shift to glycolysis after poly IC stimulation. *PLoS Biol* **12**, e1001759, doi:10.1371/journal.pbio.1001759 (2014).

381 Zhang, W. *et al.* Lactate Is a Natural Suppressor of RLR Signaling by Targeting MAVS. *Cell* **178**, 176-189 e115, doi:10.1016/j.cell.2019.05.003 (2019).

382 Kelm, D. H., Simon, R., Kuhlow, D., Voigt, C. C. & Ristow, M. High activity enables life on a high-sugar diet: blood glucose regulation in nectar-feeding bats. *Proc Biol Sci* **278**, 3490-3496, doi:10.1098/rspb.2011.0465 (2011).

383 Amitai, O. *et al.* Fruit bats (*Pteropodidae*) fuel their metabolism rapidly and directly with exogenous sugars. *J Exp Biol* **213**, 2693-2699, doi:10.1242/jeb.043505 (2010).

384 Tarze, A. *et al.* GAPDH, a novel regulator of the pro-apoptotic mitochondrial membrane permeabilization. *Oncogene* **26**, 2606-2620, doi:10.1038/sj.onc.1210074 (2007).

385 Millet, P., Vachharajani, V., McPhail, L., Yoza, B. & McCall, C. E. GAPDH Binding to TNF-alpha mRNA Contributes to Posttranscriptional Repression in Monocytes: A Novel Mechanism of Communication between Inflammation and Metabolism. *J Immunol* **196**, 2541-2551, doi:10.4049/jimmunol.1501345 (2016).

386 Ahn, J. H. *et al.* Nasal ciliated cells are primary targets for SARS-CoV-2 replication in the early stage of COVID-19. *J Clin Invest* **131**, doi:10.1172/JCI148517 (2021).

387 Hendley, J. O. & Gwaltney, J. M., Jr. Viral titers in nasal lining fluid compared to viral titers in nasal washes during experimental rhinovirus infection. *J Clin Virol* **30**, 326-328, doi:10.1016/j.jcv.2004.02.011 (2004).

388 Doucette, R. Glial cells in the nerve fiber layer of the main olfactory bulb of embryonic and adult mammals. *Microsc Res Tech* **24**, 113-130, doi:10.1002/jemt.1070240204 (1993).

389 Doucette, R. Glial influences on axonal growth in the primary olfactory system. *Glia* **3**, 433-449, doi:10.1002/glia.440030602 (1990).
390 Raisman, G. Specialized neuroglial arrangement may explain the capacity of vomeronasal axons to reinnervate central neurons. *Neuroscience* **14**, 237-254, doi:10.1016/0306-4522(85)90176-9 (1985).
391 Cancalon, P. F. Survival and subsequent regeneration of olfactory neurons after a distal axonal lesion. *J Neurocytol* **16**, 829-841, doi:10.1007/BF01611989 (1987).
392 Oakley, B. & Riddle, D. R. Receptor cell regeneration and connectivity in olfaction and taste. *Experimental Neurology* **115**, 50-54, doi:10.1016/0014-4886(92)90220-k (1992).
393 Monti Graziadei, G. A., Karlan, M. S., Bernstein, J. J. & Graziadei, P. P. C. Reinnervation of the olfactory bulb after section of the olfactory nerve in monkey (Saimiri sciureus). *Brain Research* **189**, 343-354, doi:10.1016/0006-8993(80)90095-5 (1980).
394 Nazareth, L. *et al.* Key differences between olfactory ensheathing cells and Schwann cells regarding phagocytosis of necrotic cells: implications for transplantation therapies. *Sci Rep* **10**, 18936, doi:10.1038/s41598-020-75850-8 (2020).
395 Su, Z. *et al.* Olfactory ensheathing cells: the primary innate immunocytes in the olfactory pathway to engulf apoptotic olfactory nerve debris. *Glia* **61**, 490-503, doi:10.1002/glia.22450 (2013).
396 Wu, S. *et al.* The Cotransplantation of Olfactory Ensheathing Cells with Bone Marrow Mesenchymal Stem Cells Exerts Antiapoptotic Effects in Adult Rats after Spinal Cord Injury. *Stem Cells International* **2015**, 1-13, doi:10.1155/2015/516215 (2015).
397 Novikova, L. N., Lobov, S., Wiberg, M. & Novikov, L. N. Efficacy of olfactory ensheathing cells to support regeneration after spinal cord injury is influenced by method of culture preparation. *Exp Neurol* **229**, 132-142, doi:10.1016/j.expneurol.2010.09.021 (2011).
398 Meinhardt, J. *et al.* Olfactory transmucosal SARS-CoV-2 invasion as a port of central nervous system entry in individuals with COVID-19. *Nat Neurosci* **24**, 168-175, doi:10.1038/s41593-020-00758-5 (2021).
399 Manto, M. & De Zeeuw, C. I. Diversity and complexity of roles of granule cells in the cerebellar cortex. Editorial. *Cerebellum* **11**, 1-4, doi:10.1007/s12311-012-0365-7 (2012).
400 Kurhade, C. *et al.* Type I Interferon response in olfactory bulb, the site of tick-borne flavivirus accumulation, is primarily regulated by IPS-1. *J Neuroinflammation* **13**, 22, doi:10.1186/s12974-016-0487-9 (2016).
401 Kalinke, U., Bechmann, I. & Detje, C. N. Host strategies against virus entry via the olfactory system. *Virulence* **2**, 367-370, doi:10.4161/viru.2.4.16138 (2011).
402 Detje, C. N. *et al.* Local type I IFN receptor signaling protects against virus spread within the central nervous system. *J Immunol* **182**, 2297-2304, doi:10.4049/jimmunol.0800596 (2009).
403 Paul, S., Ricour, C., Sommereyns, C., Sorgeloos, F. & Michiels, T. Type I interferon response in the central nervous system. *Biochimie* **89**, 770-778, doi:10.1016/j.biochi.2007.02.009 (2007).
404 Sorgeloos, F., Kreit, M., Hermant, P., Lardinois, C. & Michiels, T. Antiviral type I and type III interferon responses in the central nervous system. *Viruses* **5**, 834-857, doi:10.3390/v5030834 (2013).
405 Hayflick, L. & Moorhead, P. S. The serial cultivation of human diploid cell strains. *Experimental Cell Research* **25**, 585-621, doi:10.1016/0014-4827(61)90192-6 (1961).
406 Fumagalli, M. *et al.* Telomeric DNA damage is irreparable and causes persistent DNA-damage-response activation. *Nat Cell Biol* **14**, 355-365, doi:10.1038/ncb2466 (2012).

407 Rodier, F. *et al.* DNA-SCARS: distinct nuclear structures that sustain damage-induced senescence growth arrest and inflammatory cytokine secretion. *J Cell Sci* **124**, 68-81, doi:10.1242/jcs.071340 (2011).

408 Bauer, E. A., Kronberger, A., Stricklin, G. P., Smith, L. T. & Holbrook, K. A. Age-related changes in collagenase expression in cultured embryonic and fetal human skin fibroblasts. *Experimental Cell Research* **161**, 484-494, doi:10.1016/0014-4827(85)90103-x (1985).

409 Zhang, S. *et al.* Activation of the PKR/eIF2alpha signaling cascade inhibits replication of Newcastle disease virus. *Virol J* **11**, 62, doi:10.1186/1743-422X-11-62 (2014).

410 Ahtiainen, L. *et al.* Defects in innate immunity render breast cancer initiating cells permissive to oncolytic adenovirus. *PLoS One* **5**, e13859, doi:10.1371/journal.pone.0013859 (2010).

411 Marozin, S. *et al.* Inhibition of the IFN-β Response in Hepatocellular Carcinoma by Alternative Spliced Isoform of IFN Regulatory Factor-3. *Molecular Therapy* **16**, 1789-1797, doi:10.1038/mt.2008.201 (2008).

412 Li, Q. & Tainsky, M. A. Epigenetic silencing of IRF7 and/or IRF5 in lung cancer cells leads to increased sensitivity to oncolytic viruses. *PLoS One* **6**, e28683, doi:10.1371/journal.pone.0028683 (2011).

413 Battcock, S. M., Collier, T. W., Zu, D. & Hirasawa, K. Negative regulation of the alpha interferon-induced antiviral response by the Ras/Raf/MEK pathway. *J Virol* **80**, 4422-4430, doi:10.1128/JVI.80.9.4422-4430.2006 (2006).

414 Wollmann, G., Davis, J. N., Bosenberg, M. W. & van den Pol, A. N. Vesicular stomatitis virus variants selectively infect and kill human melanomas but not normal melanocytes. *J Virol* **87**, 6644-6659, doi:10.1128/JVI.03311-12 (2013).

415 Kaur, G. & Dufour, J. M. Cell lines: Valuable tools or useless artifacts. *Spermatogenesis* **2**, 1-5, doi:10.4161/spmg.19885 (2012).

416 Jensen, C. & Teng, Y. Is It Time to Start Transitioning From 2D to 3D Cell Culture? *Front Mol Biosci* **7**, 33, doi:10.3389/fmolb.2020.00033 (2020).

417 Costa, E. C. *et al.* 3D tumor spheroids: an overview on the tools and techniques used for their analysis. *Biotechnol Adv* **34**, 1427-1441, doi:10.1016/j.biotechadv.2016.11.002 (2016).

418 Knowles, M. R., Buntin, W. H., Bromberg, P. A., Gatzy, J. T. & Boucher, R. C. Measurements of transepithelial electric potential differences in the trachea and bronchi of human subjects in vivo. *Am Rev Respir Dis* **126**, 108-112, doi:10.1164/arrd.1982.126.1.108 (1982).

419 Khelloufi, M. K. *et al.* Spatiotemporal organization of cilia drives multiscale mucus swirls in model human bronchial epithelium. *Sci Rep* **8**, 2447, doi:10.1038/s41598-018-20882-4 (2018).

420 Buckley, A. G. *et al.* Visualisation of Multiple Tight Junctional Complexes in Human Airway Epithelial Cells. *Biol Proced Online* **20**, 3, doi:10.1186/s12575-018-0070-0 (2018).

421 Frisch, S. M. & MacFawn, I. P. Type I interferons and related pathways in cell senescence. *Aging Cell* **19**, e13234, doi:10.1111/acel.13234 (2020).

422 Eckerle, I., Lenk, M. & Ulrich, R. G. More novel hantaviruses and diversifying reservoir hosts--time for development of reservoir-derived cell culture models? *Viruses* **6**, 951-967, doi:10.3390/v6030951 (2014).

423 Goubau, D., Deddouche, S. & Reis e Sousa, C. Cytosolic sensing of viruses. *Immunity* **38**, 855-869, doi:10.1016/j.immuni.2013.05.007 (2013).

424 Sun, L., Wu, J., Du, F., Chen, X. & Chen, Z. J. Cyclic GMP-AMP synthase is a cytosolic DNA sensor that activates the type I interferon pathway. *Science* **339**, 786-791, doi:10.1126/science.1232458 (2013).

425 Ishikawa, H. & Barber, G. N. STING is an endoplasmic reticulum adaptor that facilitates innate immune signalling. *Nature* **455**, 674-678, doi:10.1038/nature07317 (2008).

426 Reus, J. B., Trivino-Soto, G. S., Wu, L. I., Kokott, K. & Lim, E. S. SV40 Large T Antigen Is Not Responsible for the Loss of STING in 293T Cells but Can Inhibit cGAS-STING Interferon Induction. *Viruses* **12**, doi:10.3390/v12020137 (2020).

427 Lau, L., Gray, E. E., Brunette, R. L. & Stetson, D. B. DNA tumor virus oncogenes antagonize the cGAS-STING DNA-sensing pathway. *Science* **350**, 568-571, doi:10.1126/science.aab3291 (2015).

428 An, P., Saenz Robles, M. T., Duray, A. M., Cantalupo, P. G. & Pipas, J. M. Human polyomavirus BKV infection of endothelial cells results in interferon pathway induction and persistence. *PLoS Pathog* **15**, e1007505, doi:10.1371/journal.ppat.1007505 (2019).

429 Ali, S. *et al.* Sources of Type I Interferons in Infectious Immunity: Plasmacytoid Dendritic Cells Not Always in the Driver's Seat. *Front Immunol* **10**, 778, doi:10.3389/fimmu.2019.00778 (2019).

430 Lee, A. J. & Ashkar, A. A. The Dual Nature of Type I and Type II Interferons. *Front Immunol* **9**, 2061, doi:10.3389/fimmu.2018.02061 (2018).

431 Lester, S. N. & Li, K. Toll-like receptors in antiviral innate immunity. *J Mol Biol* **426**, 1246-1264, doi:10.1016/j.jmb.2013.11.024 (2014).

432 Chousterman, B. G., Swirski, F. K. & Weber, G. F. Cytokine storm and sepsis disease pathogenesis. *Semin Immunopathol* **39**, 517-528, doi:10.1007/s00281-017-0639-8 (2017).

433 Stockmaier, S., Dechmann, D. K., Page, R. A. & O'Mara, M. T. No fever and leucocytosis in response to a lipopolysaccharide challenge in an insectivorous bat. *Biol Lett* **11**, 20150576, doi:10.1098/rsbl.2015.0576 (2015).

434 Schlottau, K. *et al.* SARS-CoV-2 in fruit bats, ferrets, pigs, and chickens: an experimental transmission study. *The Lancet Microbe* **1**, e218-e225, doi:10.1016/s2666-5247(20)30089-6 (2020).

435 Zhou, P. *et al.* Contraction of the type I IFN locus and unusual constitutive expression of IFN-alpha in bats. *Proc Natl Acad Sci U S A* **113**, 2696-2701, doi:10.1073/pnas.1518240113 (2016).

436 Pfeffer, L. M. The role of nuclear factor kappaB in the interferon response. *J Interferon Cytokine Res* **31**, 553-559, doi:10.1089/jir.2011.0028 (2011).

437 Gough, D. J., Messina, N. L., Clarke, C. J., Johnstone, R. W. & Levy, D. E. Constitutive type I interferon modulates homeostatic balance through tonic signaling. *Immunity* **36**, 166-174, doi:10.1016/j.immuni.2012.01.011 (2012).

438 Feng, E., Balint, E., Poznanski, S. M., Ashkar, A. A. & Loeb, M. Aging and Interferons: Impacts on Inflammation and Viral Disease Outcomes. *Cells* **10**, doi:10.3390/cells10030708 (2021).

439 Ronnblom, L. & Leonard, D. Interferon pathway in SLE: one key to unlocking the mystery of the disease. *Lupus Sci Med* **6**, e000270, doi:10.1136/lupus-2018-000270 (2019).

440 Bocci, V. Is interferon produced in physiologic conditions? *Medical Hypotheses* **6**, 735-745, doi:10.1016/0306-9877(80)90091-2 (1980).

441 Erlandsson, L. *et al.* Interferon-β is required for interferon-α production in mouse fibroblasts. *Current Biology* **8**, 223-226, doi:10.1016/s0960-9822(98)70086-7 (1998).

442 Takaoka, A. *et al.* Cross talk between interferon-gamma and -alpha/beta signaling components in caveolar membrane domains. *Science* **288**, 2357-2360, doi:10.1126/science.288.5475.2357 (2000).
443 Hata, N. *et al.* Constitutive IFN-alpha/beta signal for efficient IFN-alpha/beta gene induction by virus. *Biochem Biophys Res Commun* **285**, 518-525, doi:10.1006/bbrc.2001.5159 (2001).
444 Gough, D. J. *et al.* Functional crosstalk between type I and II interferon through the regulated expression of STAT1. *PLoS Biol* **8**, e1000361, doi:10.1371/journal.pbio.1000361 (2010).
445 Balachandran, S. & Beg, A. A. Defining emerging roles for NF-kappaB in antivirus responses: revisiting the interferon-beta enhanceosome paradigm. *PLoS Pathog* **7**, e1002165, doi:10.1371/journal.ppat.1002165 (2011).
446 Yang, D. *et al.* ZBP1 mediates interferon-induced necroptosis. *Cell Mol Immunol* **17**, 356-368, doi:10.1038/s41423-019-0237-x (2020).
447 Hertzog, P. J., Hwang, S. Y. & Kola, I. Role of interferons in the regulation of cell proliferation, differentiation, and development. *Mol Reprod Dev* **39**, 226-232, doi:10.1002/mrd.1080390216 (1994).
448 Stones, R. C. & Wiebers, J. E. A Review of Temperature Regulation in Bats (Chiroptera). *American Midland Naturalist* **74**, doi:10.2307/2423129 (1965).
449 Powers, D. R. *et al.* Hovering in the heat: effects of environmental temperature on heat regulation in foraging hummingbirds. *R Soc Open Sci* **4**, 171056, doi:10.1098/rsos.171056 (2017).
450 Powers, D. R., Tobalske, B. W., Wilson, J. K., Woods, H. A. & Corder, K. R. Heat dissipation during hovering and forward flight in hummingbirds. *R Soc Open Sci* **2**, 150598, doi:10.1098/rsos.150598 (2015).
451 Rummel, A. D., Swartz, S. M. & Marsh, R. L. Warm bodies, cool wings: regional heterothermy in flying bats. *Biol Lett* **15**, 20190530, doi:10.1098/rsbl.2019.0530 (2019).
452 Jacquemin, C. *et al.* Heat shock protein 70 potentiates interferon alpha production by plasmacytoid dendritic cells: relevance for cutaneous lupus and vitiligo pathogenesis. *Br J Dermatol* **177**, 1367-1375, doi:10.1111/bjd.15550 (2017).
453 Pica, F. *et al.* Effect of combined αIFN and prostaglandin A1 treatment on vesicular stomatitis virus replication and heat shock protein synthesis in epithelial cells. *Antiviral Research* **29**, 187-198, doi:10.1016/0166-3542(95)00834-9 (1996).
454 Zhao, M. *et al.* Double-stranded RNA-dependent protein kinase (pkr) is essential for thermotolerance, accumulation of HSP70, and stabilization of ARE-containing HSP70 mRNA during stress. *J Biol Chem* **277**, 44539-44547, doi:10.1074/jbc.M208408200 (2002).
455 Ogoina, D. Fever, fever patterns and diseases called 'fever'--a review. *J Infect Public Health* **4**, 108-124, doi:10.1016/j.jiph.2011.05.002 (2011).
456 Lane, W. C. *et al.* The Efficacy of the Interferon Alpha/Beta Response versus Arboviruses Is Temperature Dependent. *mBio* **9**, doi:10.1128/mBio.00535-18 (2018).
457 Downing, J. F., Martinez-Valdez, H., Elizondo, R. S., Walker, E. B. & Taylor, M. W. Hyperthermia in humans enhances interferon-gamma synthesis and alters the peripheral lymphocyte population. *J Interferon Res* **8**, 143-150, doi:10.1089/jir.1988.8.143 (1988).
458 Downing, J. F., Taylor, M. W., Wei, K. M. & Elizondo, R. S. In vivo hyperthermia enhances plasma antiviral activity and stimulates peripheral lymphocytes for increased synthesis of interferon-gamma. *J Interferon Res* **7**, 185-193, doi:10.1089/jir.1987.7.185 (1987).

459 Prow, N. A. *et al.* Lower temperatures reduce type I interferon activity and promote alphaviral arthritis. *PLoS Pathog* **13**, e1006788, doi:10.1371/journal.ppat.1006788 (2017).
460 Lienenklaus, S. *et al.* Novel reporter mouse reveals constitutive and inflammatory expression of IFN-beta in vivo. *J Immunol* **183**, 3229-3236, doi:10.4049/jimmunol.0804277 (2009).
461 Sposito, B. *et al.* The interferon landscape along the respiratory tract impacts the severity of COVID-19. *Cell* **184**, 4953-4968 e4916, doi:10.1016/j.cell.2021.08.016 (2021).
462 Lozhkov, A. A. *et al.* The Key Roles of Interferon Lambda in Human Molecular Defense against Respiratory Viral Infections. *Pathogens* **9**, doi:10.3390/pathogens9120989 (2020).
463 Klinkhammer, J. *et al.* IFN-lambda prevents influenza virus spread from the upper airways to the lungs and limits virus transmission. *Elife* **7**, doi:10.7554/eLife.33354 (2018).
464 Lazear, H. M., Nice, T. J. & Diamond, M. S. Interferon-lambda: Immune Functions at Barrier Surfaces and Beyond. *Immunity* **43**, 15-28, doi:10.1016/j.immuni.2015.07.001 (2015).
465 Wack, A., Terczynska-Dyla, E. & Hartmann, R. Guarding the frontiers: the biology of type III interferons. *Nat Immunol* **16**, 802-809, doi:10.1038/ni.3212 (2015).
466 Zhou, L. *et al.* Activation of toll-like receptor-3 induces interferon-lambda expression in human neuronal cells. *Neuroscience* **159**, 629-637, doi:10.1016/j.neuroscience.2008.12.036 (2009).
467 Pott, J. *et al.* IFN-lambda determines the intestinal epithelial antiviral host defense. *Proc Natl Acad Sci U S A* **108**, 7944-7949, doi:10.1073/pnas.1100552108 (2011).
468 Stanifer, M. L. *et al.* Critical Role of Type III Interferon in Controlling SARS-CoV-2 Infection in Human Intestinal Epithelial Cells. *Cell Rep* **32**, 107863, doi:10.1016/j.celrep.2020.107863 (2020).
469 Hermant, P. *et al.* Human but not mouse hepatocytes respond to interferon-lambda in vivo. *PLoS One* **9**, e87906, doi:10.1371/journal.pone.0087906 (2014).
470 He, X. *et al.* Establishment of Myotis myotis cell lines--model for investigation of host-pathogen interaction in a natural host for emerging viruses. *PLoS One* **9**, e109795, doi:10.1371/journal.pone.0109795 (2014).
471 Biesold, S. E. *et al.* Type I interferon reaction to viral infection in interferon-competent, immortalized cell lines from the African fruit bat *Eidolon helvum*. *PLoS One* **6**, e28131, doi:10.1371/journal.pone.0028131 (2011).
472 Yamaoka, S. *et al.* Involvement of the rabies virus phosphoprotein gene in neuroinvasiveness. *J Virol* **87**, 12327-12338, doi:10.1128/JVI.02132-13 (2013).
473 Abbott, R. C. *et al.* Rabies Outbreak in Captive Big Brown Bats (Eptesicus fuscus) Used in a White-Nose Syndrome Vaccine Trial. *J Wildl Dis* **56**, 197-202 (2020).
474 Kuzmin, I. V. *et al.* Lagos bat virus in Kenya. *J Clin Microbiol* **46**, 1451-1461, doi:10.1128/JCM.00016-08 (2008).
475 Freuling, C. *et al.* First isolation of EBLV-2 in Germany. *Vet Microbiol* **131**, 26-34, doi:10.1016/j.vetmic.2008.02.028 (2008).
476 Allendorf, S. D. *et al.* Rabies virus distribution in tissues and molecular characterization of strains from naturally infected non-hematophagous bats. *Virus Res* **165**, 119-125, doi:10.1016/j.virusres.2012.01.011 (2012).
477 Constantine, D. G., Emmons, R. W. & Woodie, J. D. Rabies virus in nasal mucosa of naturally infected bats. *Science* **175**, 1255-1256, doi:10.1126/science.175.4027.1255 (1972).

478 Nitschel, S. *et al.* Point Mutations in the Glycoprotein Ectodomain of Field Rabies Viruses Mediate Cell Culture Adaptation through Improved Virus Release in a Host Cell Dependent and Independent Manner. *Viruses* **13**, doi:10.3390/v13101989 (2021).

479 Nolden, T. *et al.* Reverse genetics in high throughput: rapid generation of complete negative strand RNA virus cDNA clones and recombinant viruses thereof. *Sci Rep* **6**, 23887, doi:10.1038/srep23887 (2016).

480 Takahashi, T. *et al.* Genetic and Phenotypic Characterization of a Rabies Virus Strain Isolated from a Dog in Tokyo, Japan in the 1940s. *Viruses* **12**, doi:10.3390/v12090914 (2020).

481 Chung, W. W., Lagenaur, C. F., Yan, Y. M. & Lund, J. S. Developmental expression of neural cell adhesion molecules in the mouse neocortex and olfactory bulb. *J Comp Neurol* **314**, 290-305, doi:10.1002/cne.903140207 (1991).

482 Bock, E. & Braestrup, C. Regional distribution of the synaptic membrane proteins: synaptin, D1, D2 and D3. *J Neurochem* **30**, 1603-1607, doi:10.1111/j.1471-4159.1978.tb10502.x (1978).

483 Van Acker, H. H., Capsomidis, A., Smits, E. L. & Van Tendeloo, V. F. CD56 in the Immune System: More Than a Marker for Cytotoxicity? *Front Immunol* **8**, 892, doi:10.3389/fimmu.2017.00892 (2017).

484 Brzozka, K., Finke, S. & Conzelmann, K. K. Inhibition of interferon signaling by rabies virus phosphoprotein P: activation-dependent binding of STAT1 and STAT2. *J Virol* **80**, 2675-2683, doi:10.1128/JVI.80.6.2675-2683.2006 (2006).

485 Vidy, A., Chelbi-Alix, M. & Blondel, D. Rabies virus P protein interacts with STAT1 and inhibits interferon signal transduction pathways. *J Virol* **79**, 14411-14420, doi:10.1128/JVI.79.22.14411-14420.2005 (2005).

486 Deffrasnes, C. *et al.* Phenotypic Divergence of P Proteins of Australian Bat Lyssavirus Lineages Circulating in Microbats and Flying Foxes. *Viruses* **13**, doi:10.3390/v13050831 (2021).

487 Johnson, N., Phillpotts, R. & Fooks, A. R. Airborne transmission of lyssaviruses. *J Med Microbiol* **55**, 785-790, doi:10.1099/jmm.0.46370-0 (2006).

488 Horton, D. L. *et al.* Between roost contact is essential for maintenance of European bat lyssavirus type-2 in Myotis daubentonii bat reservoir: 'The Swarming Hypothesis'. *Sci Rep* **10**, 1740, doi:10.1038/s41598-020-58521-6 (2020).

489 Constantine, D. G. Rabies Transmission by Nonbite Route. *Public Health Reports (1896-1970)* **77**, doi:10.2307/4591470 (1962).

490 Schatz, J. *et al.* Lyssavirus distribution in naturally infected bats from Germany. *Vet Microbiol* **169**, 33-41, doi:10.1016/j.vetmic.2013.12.004 (2014).

491 Bourhy, H., Kissi, B., Lafon, M., Sacramento, D. & Tordo, N. Antigenic and molecular characterization of bat rabies virus in Europe. *J Clin Microbiol* **30**, 2419-2426, doi:10.1128/jcm.30.9.2419-2426.1992 (1992).

492 Bokelmann, M. *et al.* Tolerance and Persistence of Ebola Virus in Primary Cells from *Mops condylurus*, a Potential Ebola Virus Reservoir. *Viruses* **13**, doi:10.3390/v13112186 (2021).

493 Onabajo, O. O. *et al.* Interferons and viruses induce a novel truncated ACE2 isoform and not the full-length SARS-CoV-2 receptor. *Nat Genet* **52**, 1283-1293, doi:10.1038/s41588-020-00731-9 (2020).

494 Bermejo-Jambrina, M. *et al.* Infection and transmission of SARS-CoV-2 depend on heparan sulfate proteoglycans. *EMBO J* **40**, e106765, doi:10.15252/embj.2020106765 (2021).

495 Clausen, T. M. *et al.* SARS-CoV-2 Infection Depends on Cellular Heparan Sulfate and ACE2. *Cell* **183**, 1043-1057 e1015, doi:10.1016/j.cell.2020.09.033 (2020).

496 Lempp, F. A. *et al.* Lectins enhance SARS-CoV-2 infection and influence neutralizing antibodies. *Nature* **598**, 342-347, doi:10.1038/s41586-021-03925-1 (2021).

497 Zheng, M. *et al.* TLR2 senses the SARS-CoV-2 envelope protein to produce inflammatory cytokines. *Nat Immunol* **22**, 829-838, doi:10.1038/s41590-021-00937-x (2021).

498 Khan, S. *et al.* SARS-CoV-2 spike protein induces inflammation via TLR2-dependent activation of the NF-kappaB pathway. *Elife* **10**, doi:10.7554/eLife.68563 (2021).

499 Dumont, E. R. Salivary pH and Buffering Capacity in Frugivorous and Insectivorous Bats. *Journal of Mammalogy* **78**, 1210-1219, doi:10.2307/1383064 (1997).

500 Edson, D. *et al.* Routes of Hendra Virus Excretion in Naturally-Infected Flying-Foxes: Implications for Viral Transmission and Spillover Risk. *PLoS One* **10**, e0140670, doi:10.1371/journal.pone.0140670 (2015).

501 Virtue, E. R., Marsh, G. A., Baker, M. L. & Wang, L. F. Interferon production and signaling pathways are antagonized during henipavirus infection of fruit bat cell lines. *PLoS One* **6**, e22488, doi:10.1371/journal.pone.0022488 (2011).

502 Strobel, S., Roswag, A., Becker, N. I., Trenczek, T. E. & Encarnacao, J. A. Insectivorous bats digest chitin in the stomach using acidic mammalian chitinase. *PLoS One* **8**, e72770, doi:10.1371/journal.pone.0072770 (2013).

503 Ishikawa, K., Matoba, M., Tanaka, H. & Ono, K. Anatomical study of the intestine of the insect-feeder bat, Myotis frater kaguae. *J Anat* **142**, 141-150 (1985).

504 Schlottau, K. *et al.* SARS-CoV-2 in fruit bats, ferrets, pigs, and chickens: an experimental transmission study. **1**, e218-e225, doi:10.1016/s2666-5247(20)30089-6 (2020).

505 Meurs, E. *et al.* Molecular cloning and characterization of the human double-stranded RNA-activated protein kinase induced by interferon. *Cell* **62**, 379-390, doi:10.1016/0092-8674(90)90374-n (1990).

506 Izaguirre, A. *et al.* Comparative analysis of IRF and IFN-alpha expression in human plasmacytoid and monocyte-derived dendritic cells. *J Leukoc Biol* **74**, 1125-1138, doi:10.1189/jlb.0603255 (2003).

507 Feldman, S. B., Milone, M. C., Kloser, P. & Fitzgerald-Bocarsly, P. Functional deficiencies in two distinct interferon alpha-producing cell populations in peripheral blood mononuclear cells from human immunodeficiency virus seropositive patients. *J Leukoc Biol* **57**, 214-220, doi:10.1002/jlb.57.2.214 (1995).

508 Colonna, M. Innate Lymphoid Cells: Diversity, Plasticity, and Unique Functions in Immunity. *Immunity* **48**, 1104-1117, doi:10.1016/j.immuni.2018.05.013 (2018).

509 van Wilgenburg, B. *et al.* MAIT cells are activated during human viral infections. *Nat Commun* **7**, 11653, doi:10.1038/ncomms11653 (2016).

510 Nguyen-Pham, T. N. *et al.* Type I and II interferons enhance dendritic cell maturation and migration capacity by regulating CD38 and CD74 that have synergistic effects with TLR agonists. *Cell Mol Immunol* **8**, 341-347, doi:10.1038/cmi.2011.7 (2011).

511 Steimle, V., Siegrist, C. A., Mottet, A., Lisowska-Grospierre, B. & Mach, B. Regulation of MHC class II expression by interferon-gamma mediated by the transactivator gene CIITA. *Science* **265**, 106-109, doi:10.1126/science.8016643 (1994).

512 Borges da Silva, H., Fonseca, R., Alvarez, J. M. & D'Imperio Lima, M. R. IFN-gamma Priming Effects on the Maintenance of Effector Memory CD4(+) T Cells and on Phagocyte Function: Evidences from Infectious Diseases. *J Immunol Res* **2015**, 202816, doi:10.1155/2015/202816 (2015).

513 Watanabe, Y., Suzuki, O., Haruyama, T. & Akaike, T. Interferon-gamma induces reactive oxygen species and endoplasmic reticulum stress at the hepatic apoptosis. *J Cell Biochem* **89**, 244-253, doi:10.1002/jcb.10501 (2003).

514 Kang, K. *et al.* Interferon-gamma Represses M2 Gene Expression in Human Macrophages by Disassembling Enhancers Bound by the Transcription Factor MAF. *Immunity* **47**, 235-250 e234, doi:10.1016/j.immuni.2017.07.017 (2017).

515 Stier, M. T. *et al.* STAT1 Represses Cytokine-Producing Group 2 and Group 3 Innate Lymphoid Cells during Viral Infection. *J Immunol* **199**, 510-519, doi:10.4049/jimmunol.1601984 (2017).

516 Califano, D. *et al.* IFN-gamma increases susceptibility to influenza A infection through suppression of group II innate lymphoid cells. *Mucosal Immunol* **11**, 209-219, doi:10.1038/mi.2017.41 (2018).

517 Mesev, E. V., LeDesma, R. A. & Ploss, A. Decoding type I and III interferon signalling during viral infection. *Nat Microbiol* **4**, 914-924, doi:10.1038/s41564-019-0421-x (2019).

518 Zanoni, I., Granucci, F. & Broggi, A. Interferon (IFN)-lambda Takes the Helm: Immunomodulatory Roles of Type III IFNs. *Front Immunol* **8**, 1661, doi:10.3389/fimmu.2017.01661 (2017).

519 Ren, K. & Torres, R. Role of interleukin-1beta during pain and inflammation. *Brain Res Rev* **60**, 57-64, doi:10.1016/j.brainresrev.2008.12.020 (2009).

520 Guarda, G. *et al.* Type I interferon inhibits interleukin-1 production and inflammasome activation. *Immunity* **34**, 213-223, doi:10.1016/j.immuni.2011.02.006 (2011).

521 Perl, K. *et al.* Reduced changes in protein compared to mRNA levels across non-proliferating tissues. *BMC Genomics* **18**, 305, doi:10.1186/s12864-017-3683-9 (2017).

522 Piatosa, B. *et al.* B cell subsets in healthy children: reference values for evaluation of B cell maturation process in peripheral blood. *Cytometry B Clin Cytom* **78**, 372-381, doi:10.1002/cyto.b.20536 (2010).

523 Valiathan, R., Ashman, M. & Asthana, D. Effects of Ageing on the Immune System: Infants to Elderly. *Scand J Immunol* **83**, 255-266, doi:10.1111/sji.12413 (2016).

524 Burny, W. *et al.* Different Adjuvants Induce Common Innate Pathways That Are Associated with Enhanced Adaptive Responses against a Model Antigen in Humans. *Front Immunol* **8**, 943, doi:10.3389/fimmu.2017.00943 (2017).

525 McMichael, L. *et al.* Haematology and Plasma Biochemistry of Wild Black Flying-Foxes, (Pteropus alecto) in Queensland, Australia. *PLoS One* **10**, e0125741, doi:10.1371/journal.pone.0125741 (2015).

526 Gordon, A. S. Some aspects of hormonal influences upon the leukocytes. *Ann N Y Acad Sci* **59**, 907-927, doi:10.1111/j.1749-6632.1955.tb45990.x (1955).

527 Dhabhar, F. S., Miller, A. H., McEwen, B. S. & Spencer, R. L. Stress-induced changes in blood leukocyte distribution. Role of adrenal steroid hormones. *J Immunol* **157**, 1638-1644 (1996).

528 Dhabhar, F. S., Miller, A. H., McEwen, B. S. & Spencer, R. L. Effects of stress on immune cell distribution. Dynamics and hormonal mechanisms. *J Immunol* **154**, 5511-5527 (1995).

529 Dougherty, T. F. & White, A. Influence of Hormones on Lymphoid Tissue Structure and Function. The Role of the Pituitary Adrenotrophic Hormone in the Regulation of the Lymphocytes and Other Cellular Elements of the Blood1. *Endocrinology* **35**, 1-14, doi:10.1210/endo-35-1-1 (1944).

530 Davis, A. K., Maney, D. L. & Maerz, J. C. The use of leukocyte profiles to measure stress in vertebrates: a review for ecologists. *Functional Ecology* **22**, 760-772, doi:10.1111/j.1365-2435.2008.01467.x (2008).

531 Keresztes, M., Rudisch, T., Tajti, J., Ocsovszki, I. & Gardi, J. Granulocyte activation in humans is modulated by psychological stress and relaxation. *Stress* **10**, 271-281, doi:10.1080/10253890701248079 (2007).

532 Abolins, S. *et al.* The comparative immunology of wild and laboratory mice, *Mus musculus domesticus*. *Nat Commun* **8**, 14811, doi:10.1038/ncomms14811 (2017).

533 Gupta-Wright, A. *et al.* Functional Analysis of Phagocyte Activity in Whole Blood from HIV/Tuberculosis-Infected Individuals Using a Novel Flow Cytometry-Based Assay. *Front Immunol* **8**, 1222, doi:10.3389/fimmu.2017.01222 (2017).

534 Markovic, S. N., Knight, P. R. & Murasko, D. M. Inhibition of interferon stimulation of natural killer cell activity in mice anesthetized with halothane or isoflurane. *Anesthesiology* **78**, 700-706, doi:10.1097/00000542-199304000-00013 (1993).

535 Berg, K. J. *et al.* Effects of Isoflurane Anesthesia on the Hematologic Values of Rehabilitated Wild Owls. *J Avian Med Surg* **33**, 369-380, doi:10.1647/2017-333 (2019).

536 Ludders, J. W., Rode, J. & Mitchell, G. S. Isoflurane anesthesia in sandhill cranes (*Grus canadensis*): minimal anesthetic concentration and cardiopulmonary dose-response during spontaneous and controlled breathing. *Anesth Analg* **68**, 511-516 (1989).

537 Barnas, G. M., Mather, F. B. & Fedde, M. R. Are avian intrapulmonary CO2 receptors chemically modulated mechanoreceptors or chemoreceptors? *Respiration Physiology* **35**, 237-243, doi:10.1016/0034-5687(78)90024-5 (1978).

538 Granone, T. D. *et al.* Comparison of three different inhalant anesthetic agents (isoflurane, sevoflurane, desflurane) in red-tailed hawks (*Buteo jamaicensis*). *Vet Anaesth Analg* **39**, 29-37, doi:10.1111/j.1467-2995.2011.00668.x (2012).

539 Zhu, Q. *et al.* Human B cells have an active phagocytic capability and undergo immune activation upon phagocytosis of *Mycobacterium tuberculosis*. *Immunobiology* **221**, 558-567, doi:10.1016/j.imbio.2015.12.003 (2016).

540 Martinez-Riano, A. *et al.* Antigen phagocytosis by B cells is required for a potent humoral response. *EMBO Rep* **19**, doi:10.15252/embr.201846016 (2018).

541 Cunningham, A. F. *et al.* B1b cells recognize protective antigens after natural infection and vaccination. *Front Immunol* **5**, 535, doi:10.3389/fimmu.2014.00535 (2014).

542 Li, W. Phagocyte dysfunction, tissue aging and degeneration. *Ageing Res Rev* **12**, 1005-1012, doi:10.1016/j.arr.2013.05.006 (2013).

543 Swift, M. E., Burns, A. L., Gray, K. L. & DiPietro, L. A. Age-related alterations in the inflammatory response to dermal injury. *J Invest Dermatol* **117**, 1027-1035, doi:10.1046/j.0022-202x.2001.01539.x (2001).

544 Ren, L. *et al.* Single-cell transcriptional atlas of the Chinese horseshoe bat (Rhinolophus sinicus) provides insight into the cellular mechanisms which enable bats to be viral reservoirs. *PrePrint*, doi:10.1101/2020.06.30.175778 (2020).

545 Mak, T. W., Saunders, M. E. & Jett, B. D. NK, γδ T and NKT Cells. *Primer to the Immune Response*, doi:10.1016/b978-0-12-385245-8.00011-x (2014).

546 Ledford, J. G., Kovarova, M. & Koller, B. H. Impaired host defense in mice lacking ONZIN. *J Immunol* **178**, 5132-5143, doi:10.4049/jimmunol.178.8.5132 (2007).

547 Kinsey, C. *et al.* Plac8 links oncogenic mutations to regulation of autophagy and is critical to pancreatic cancer progression. *Cell Rep* **7**, 1143-1155, doi:10.1016/j.celrep.2014.03.061 (2014).

548 Cho, S. F., Anderson, K. C. & Tai, Y. T. Targeting B Cell Maturation Antigen (BCMA) in Multiple Myeloma: Potential Uses of BCMA-Based Immunotherapy. *Front Immunol* **9**, 1821, doi:10.3389/fimmu.2018.01821 (2018).

549 Horna-Terron, E., Pradilla-Dieste, A., Sanchez-de-Diego, C. & Osada, J. TXNDC5, a newly discovered disulfide isomerase with a key role in cell physiology and pathology. *Int J Mol Sci* **15**, 23501-23518, doi:10.3390/ijms151223501 (2014).

550 Jourdan, M. *et al.* Characterization of a transitional preplasmablast population in the process of human B cell to plasma cell differentiation. *J Immunol* **187**, 3931-3941, doi:10.4049/jimmunol.1101230 (2011).

551 Stewart, A. *et al.* Single-Cell Transcriptomic Analyses Define Distinct Peripheral B Cell Subsets and Discrete Development Pathways. *Front Immunol* **12**, 602539, doi:10.3389/fimmu.2021.602539 (2021).

552 Bausch, D. G. *et al.* Marburg hemorrhagic fever associated with multiple genetic lineages of virus. *N Engl J Med* **355**, 909-919, doi:10.1056/NEJMoa051465 (2006).

553 Timen, A. Response to Imported Case of Marburg Hemorrhagic Fever, the Netherlands. *Emerging Infectious Diseases* **15**, 1171-1175, doi:10.3201/eid1508.090051 (2009).

554 Towner, J. S. *et al.* Marburgvirus genomics and association with a large hemorrhagic fever outbreak in Angola. *J Virol* **80**, 6497-6516, doi:10.1128/JVI.00069-06 (2006).

555 Swanepoel, R. *et al.* Studies of reservoir hosts for Marburg virus. *Emerg Infect Dis* **13**, 1847-1851, doi:10.3201/eid1312.071115 (2007).

556 Friedrichs, V., Balkema-Buschmann, A., Dorhoi, A. & Pei, G. Selection and stability validation of reference gene candidates for transcriptional analysis in Rousettus aegyptiacus. *Sci Rep* **11**, 21662, doi:10.1038/s41598-021-01260-z (2021).

557 Banerjee, A. *et al.* Novel Insights Into Immune Systems of Bats. *Front Immunol* **11**, 26, doi:10.3389/fimmu.2020.00026 (2020).

558 Kwon, H. J., Kim, N. & Kim, H. S. Molecular checkpoints controlling natural killer cell activation and their modulation for cancer immunotherapy. *Exp Mol Med* **49**, e311, doi:10.1038/emm.2017.42 (2017).

559 Boraschi, D. & Italiani, P. Innate Immune Memory: Time for Adopting a Correct Terminology. *Front Immunol* **9**, 799, doi:10.3389/fimmu.2018.00799 (2018).

8 List of Tables

9 List of Figures

10 Appendix

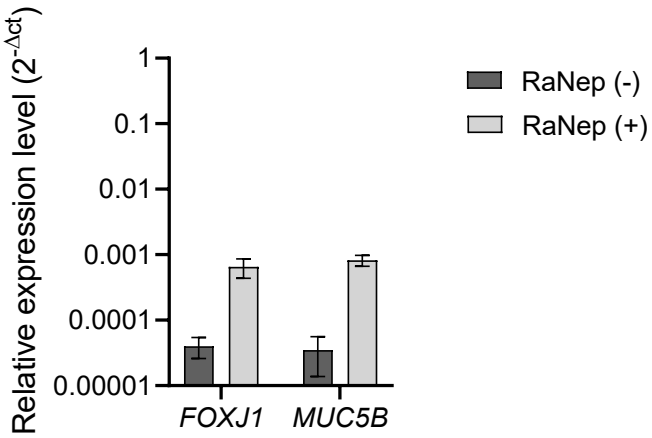

Appendix 10.1 | Differentiation with retinoic acid induces *FOXJ1* and *MUC5B* expression.
Expression levels of *FOXJ1* and *MUC5B* were analyzed in RaNep cells after incubation with or without 50 nm RA for 7 days. Expression levels were determined by qRT-PCR and normalized to *EEF1A1* expression. Bars represent mean±SD of two independent experiments.

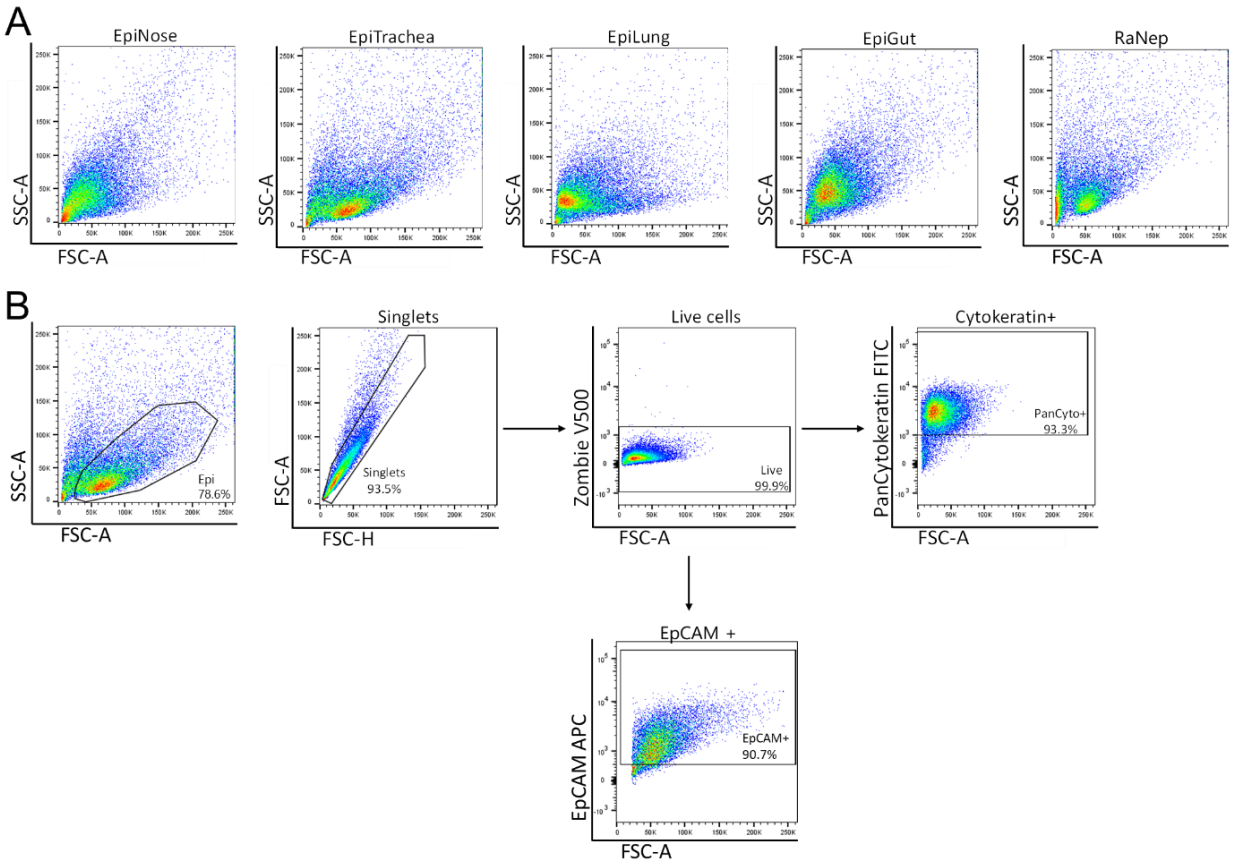

Appendix 10.2 | Identification of Cytokeratin and EpCAM expressing ERB epithelia by flow cytometry. FSC-A/SSC-A properties of all epithelia cells (**A**) and the gating strategy to identify cytokeratin and EpCAM expression (**B**). Cells were separated from debris based on FSC-A/SSC-A properties. Doublets were excluded based on FSC-H/FSC-A properties and dead cells were excluded after previously being defined as Zombie^{+}. Fraction of cytokeratin (FITC signal) or EpCAM (APC signal) expressing cells was evaluated from live single cells. Shown are representative plots.

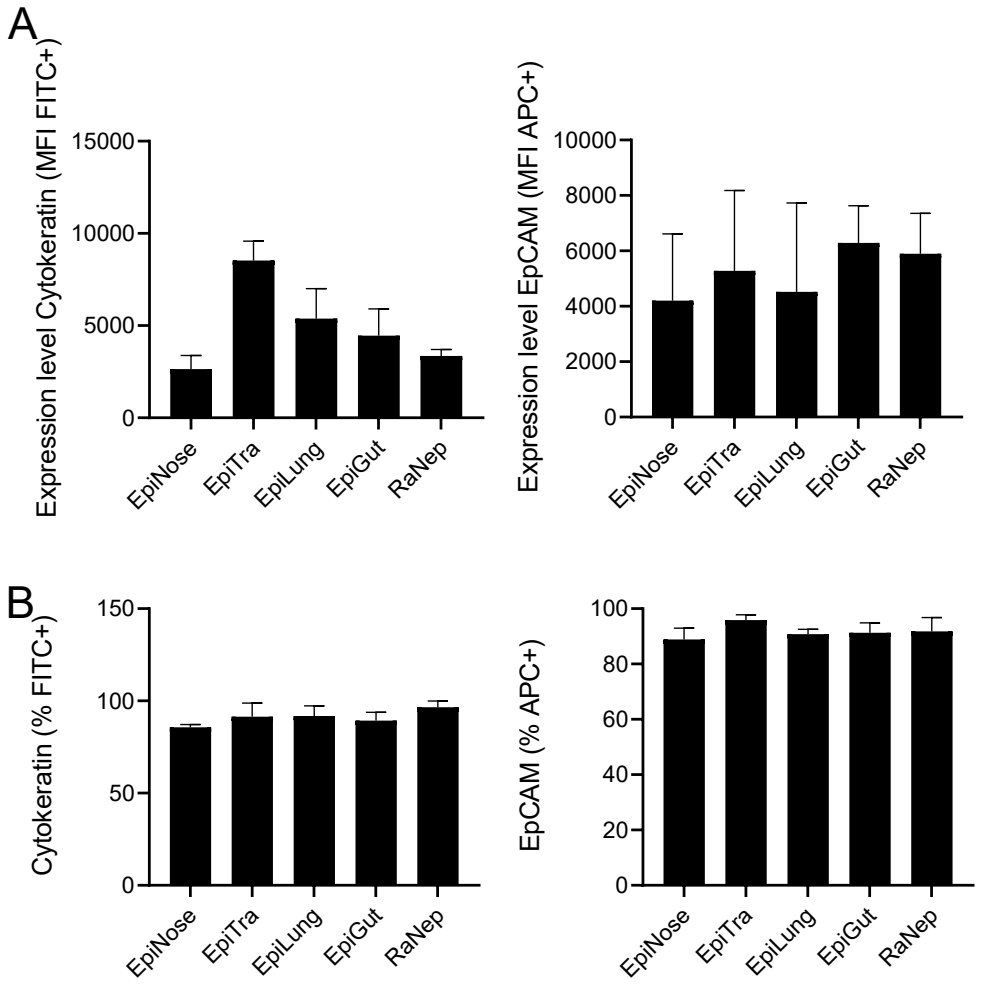

Appendix 10.3 | Analysis of expression of cytokeratins and EpCAM in all epithelial cells used.
Quantification of cytokeratin and EpCAM expression of epithelial cells by MFI of FITC and APC signal (**A**) and percent of expressing cells from live single cells (**B**). All epithelial cells were evaluated via flow cytometry. Graphs show mean of three individual experiments ± SD.

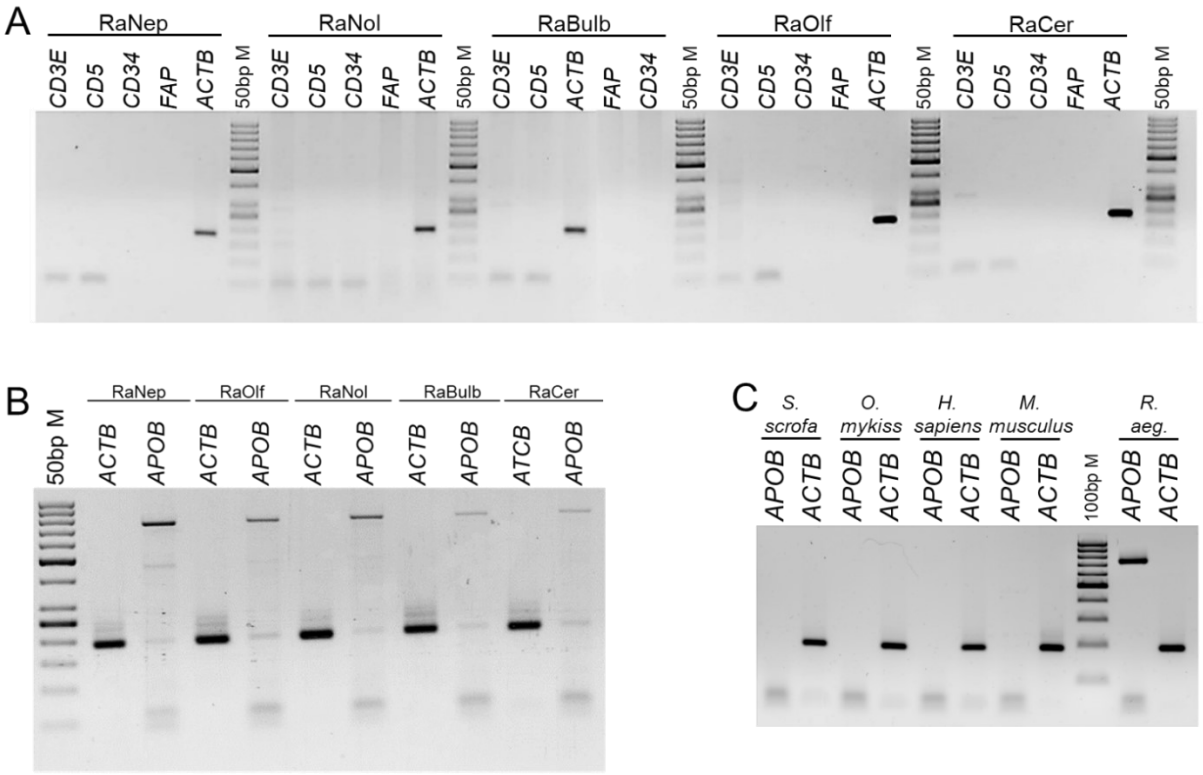

Appendix 10.4 | Exclusion and ERB-specific *APOB* PCR.
Further characterization of all immortalized ERB cell lines by exclusion (**A**) and *APOB* (**B**, **C**) PCR. Exclusion of hematopoietic cells and fibroblasts was carried out with respective lineage markers (**A**). Expression of ERB-specific *APOB* was verified in all cell lines with *ACTB* as reference gene(**B**). Specificity of *APOB*-PCR was verified with genomic DNA of various mammals and trout (**C**). *APOB* = apolipoprotein B, *ACTB* = actin beta, *FAP* = fibroblast activation protein.

Appendix 10.5 | Primer sequences for *APOB* species-PCR with porcine, murine, human, and fish DNA.

Gene symbol	Gene name	Gene ID	Primer sequences [5'-3']	Amplicon size [bp]
***ACTB* human**	actin beta	60	F-AGGCTGTGCTATCCCTGTA R-CGTGGTGGTGAAGCTGTAG	198
***Actb* murine**	actin beta	11461	F-TACCACAGGCATTGTGATGG R-CTTTGATGTCACGCACGATTTC	201
***ACTB* porcine**	actin beta	414396	F-TGGACTTCGAGCAGGAGAT R-TAGAGGTCCTTGCGGATGT	221
***ACTB* trout**	actin beta	100135845	F-TACCCATCTACGAGGGCTAC R-CCCATCTCCTGCTCAAAGTC	194
***APOB* human**	apolipoprotein B	338	F-CCATCTCTTCTGCTGCCTTATC R-CTTCTCAACGGCATCTCTCATC	623
***Apob* murine**	apolipoprotein B	238055	F-GGGACTGTCTGACTTCCATATTC R-CTCTCACAAGACAGGCCATATT	723
***APOB* porcine**	apolipoprotein B	100523371	F-CCAGAGAAAGAGGAGCCTAAAC R-CCAGGTAGGTCACAACATCTATC	811
***apoba* trout**	apolipoprotein Ba	110505694	F-CGACTCCACCTACAGACATAAC R-GAACCTGTGAGAAGGGAGTAAG	363

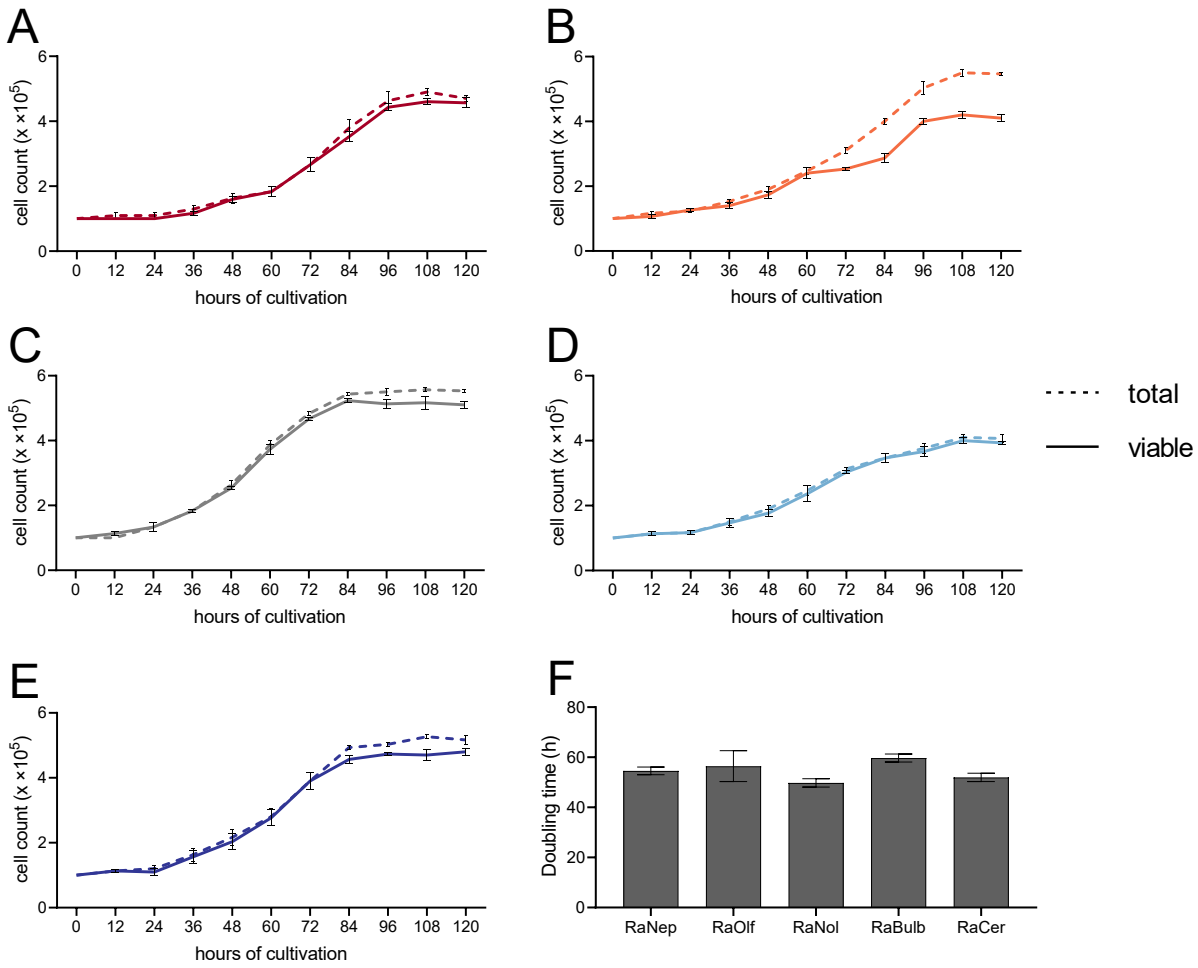

Appendix 10.6 | Growth of ERB cell lines at 40°C.
Growth of all cell lines upon incubation at 40°C was assessed by counting dead and viable cells after each 12 h for 10 days. Viable cells were determined by substracting dead from total cells. Doubling time of all cell lines was calculated based on the formula provided in the method section. Graphs A-E show mean of three individual experiments ± SD, bars represent mean doubling time±SD.

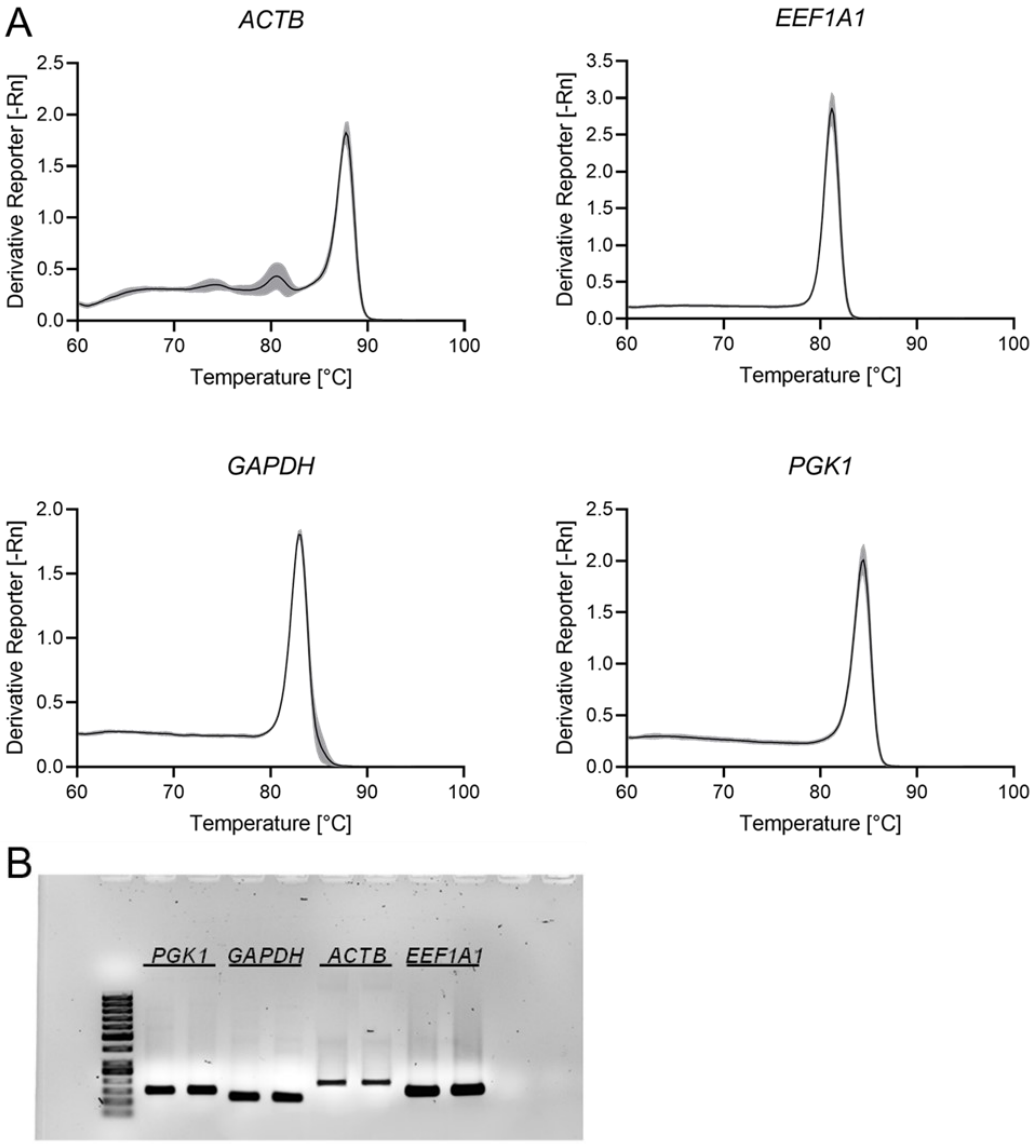

Appendix 10.7 | MST and size analysis of reference gene candidate amplicons.
Accuracy of primer pairs of all reference gene candidates was determined by verifying generation of one amplicon only. Specificity was evaluated by MST analysis (**A**) and agarose gel electrophoresis (**B**). Graphs show mean of three individual experiments ± SD (grey area).

Appendix 10.8 | Performance summary of selected ERB reference genes.

Gene symbol	Gene name	Gene ID	Primer sequence [5'-3']	Amplicon size [bp]
ACTB	actin beta	107515934	F- GCCTTGGTCGTGGATAATG R- GGGATACTTCAGGGTCAGGATA	193
EEF1A1	eukaryotic translation elongation factor 1 alpha 1	107509282	F- GTATGCCTGGGTCTTGGATAAA R- GCCTGTGATGTGCCTGTAA	162
GAPDH	glyceraldehyde-3-phosphate dehydrogenase	107519804	F- CAAGTTCAAAGGCACAGTCAAG R- TATTCAGCACCAGCATCACC	120
PGK1	phosphoglycerate kinase 1	107503843	F- GATTACCTTGCCTGTTGACTTTG R- GACAGCCTCAGCATACTTCTT	148

Appendix 10.9 | Stability calculations based on statistical algorithms.
Stability calculations based on the BestKeeper algorithm.

Parameter [BestKeeper]	**Reference gene**			
	ACTB	*EEF1A1*	*GAPDH*	*PGK1*
geo Mean [CP]	33.19	22.44	27.86	28.78
ar Mean [CP]	33.25	22.44	27.87	28.79
min [CP]	29.74	21.14	26.14	28.17
max [CP]	33.00	23.07	28.96	29.93
std dev [± CP]	**1.40**	**0.34**	**0.76**	**0.36**
CV [% CP]	4.22	1.53	2.73	1.25
min [x-fold]	-10.97	-2.46	-3.29	-1.53
max [x-fold]	55.98	1.55	2.15	2.22
std dev [± x-fold]	2.64	1.27	1.69	1.28
Coeff. of corr. [r]	**0.52**	**0.96**	**0.78**	**0.88**
p-value	0.02	0.00	0.01	0.00

Stability calculations based on the NormFinder algorithm.

NormFinder	**Stability in various conditions**		
	total	uIFN	Temperature
EEF1A1	0.013	0.015	0.014
PGK1	0.015	0.017	0.016
GAPDH	0.050	0.069	0.049
ACTB	0.097	0.085	0.170

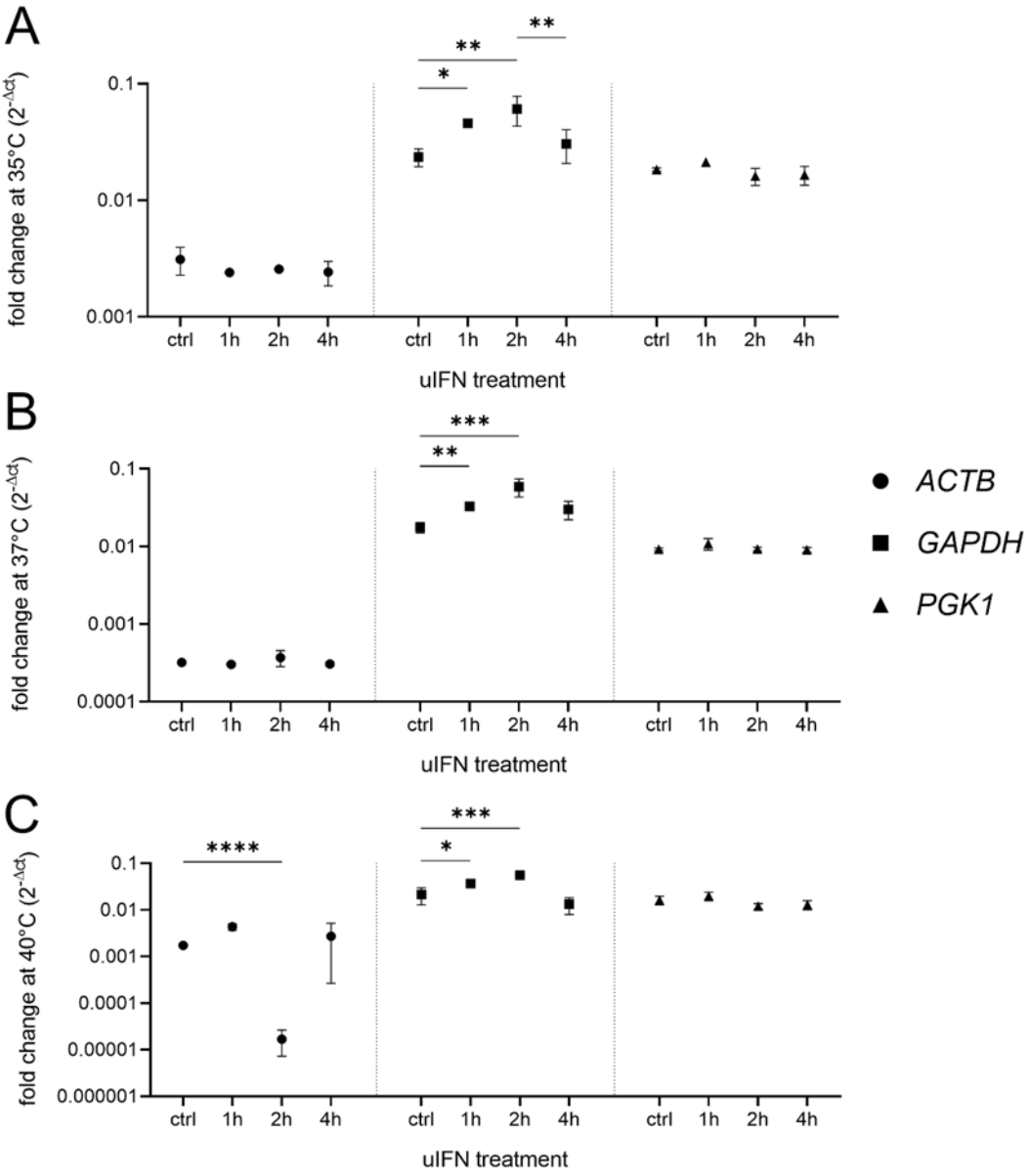

Appendix 10.10 | Expression of *GAPDH* is induced by uIFN in ERB primary fibroblasts.
Expression of *ACTB*, *GAPDH* and *PGK1* was normalized to *EEF1A1*. Relative expression levels at 35°C (**A**), 37°C (**B**) and 40°C (**C**) in absence (PBS control) or presence of 1,000 U/ml uIFN is shown. Individual gene expression levels were determined by qRT-PCR and graphs represent data from three independent experiments, shown as mean±SD. Statistical significance was determined by One-Way-ANOVA with Holm- Šidák's post-hoc test. (*) P≤0.05, (**) P≤0.01, (***) P≤0.001, (****) P≤0.0001.

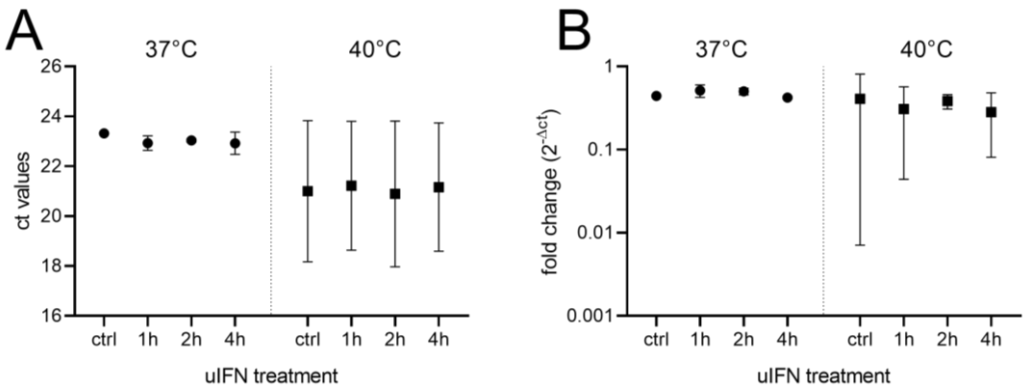

Appendix 10.11 | Expression of *ACTB* and *GAPDH* is impaired in human fibroblasts at 40°C.
Human dermal fibroblasts were incubated at 37°C and 40°C in presence or absence of 1,000 U/ml and expression of *ACTB* and *GAPDH* was assessed (**A**). Fold change of *GAPDH* upon uIFN treatment and temperature variations was calculated by normalization to *ACTB* (**B**). Graph shows mean of three individual experiments ± SD.

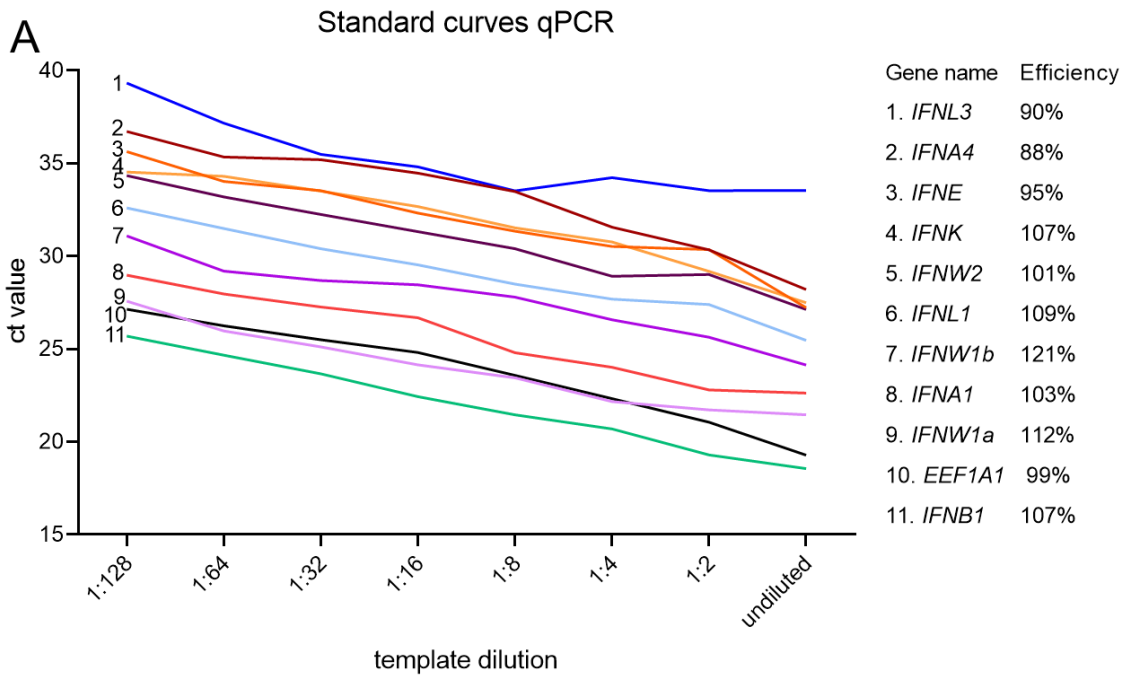

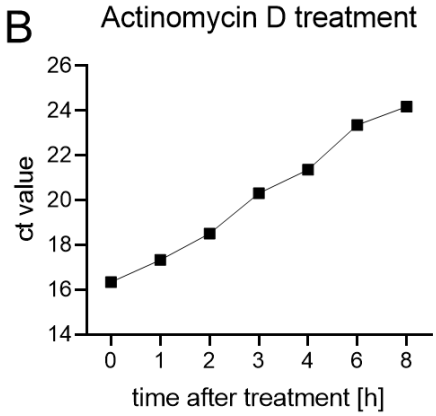

Appendix 10.12 | Standard curves and ActD treatment to assess efficiency of primer pairs for qRT-PCR. Standard curves of all IFNs found in the ERB genome were generated by template dilution in steps of 1:2 (**A**). Accuracy of qRT-PCR assays was exemplarily assessed by ActD treatment of RaNep cells upon pI:C treatment (10 µg/ml) by quantification of *IFNA1* (**B**).

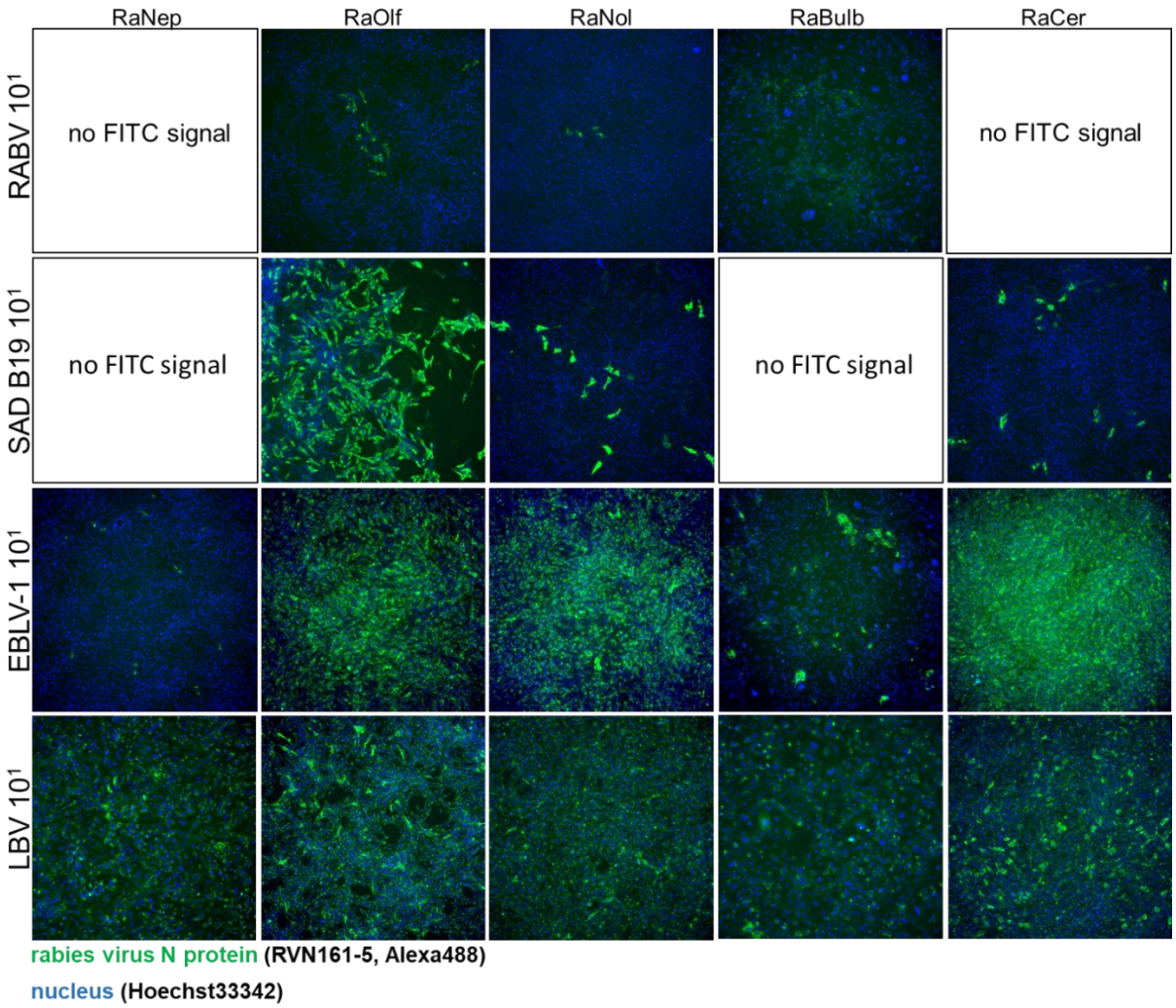

Appendix 10.13 | Distinct susceptibility of ERB cell lines to various lyssaviruses. Lyssaviruses RABV, SAD B19, EBLV-1, and LBV were titrated in 10-fold dilution steps on all immortalized ERB cell lines. The figure shows nuclei (Hoechst 33342, blue) and RVN protein (Alexa488, green) signal at a 10^1 dilution. The infected cells were incubated for 24 h before signal acquisition.

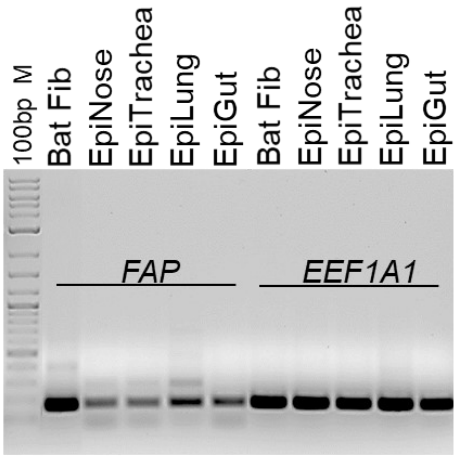

Appendix 10.14 | Expression of *FAP* in heterogenous ERB epithelia cell culture.
Presence of fibroblasts was assessed by *FAP* detection in PCR in indicated primary cells. Homogenous input was verified by *EEF1A1* detection.

Appendix 10.15 | List of cross-reactive antibodies tested for reactivity to ERB peripheral leukocytes.

Target Molecule	Clone	Target Species
CD3	**CD3-12**	**human**
CD4	5B4	human
CD4	RM4-5	human/mouse
CD4	YKIX302.9	canine
CD5	YKIX322.3	canine
CD8	53-6.7	mouse
CD8	UCHT4	human
CD11b	**M1/70**	**human/mouse**
CD11c	N418	mouse
CD11c	Clone3.9	human
CD14	TÜK4	human
CD14	M5E2	human
CD14	CAM36A	bovine
CD15	W6D3	human
CD16	3G8	human
CD25	P4A10	canine
CD33	WM53	human
CD45	HI30	human
CD45.1	A20	human/mouse
CD45.2	104	mouse
CD49d	R1-2	mouse
CD45R	RA3-6B2	mouse

CD62L	*DREG-56*	*human*
CD64	X54-5/7.1	mouse
CD79a	**HM47**	**human**
CD80	16-10A1	mouse
CD90.2	53-2.1	mouse
CD115	AFS98	mouse
CD117	2B8	mouse
CD172a	**DH59B**	**bovine**
CD182	SA044G4	mouse
CD183	CXCR3-173	human/mouse
CD184	12G5	human
CD206	**15-2**	**human**
CD244.1	C9.1	mouse
CD335	29A1.4	mouse
GATA3	TWAJ	human/mouse
Ki-67	**B56**	**human**
Ki-67	Ki-67	human
Ki-67	SolA15	human/mouse
MHCII	M5/114.15.2	mouse
MHCII	YKIX334.2	canine
MHCII	**2G9**	**mouse**
NK1.1	PK136	human
T-bet	**4B10**	**human/mouse**

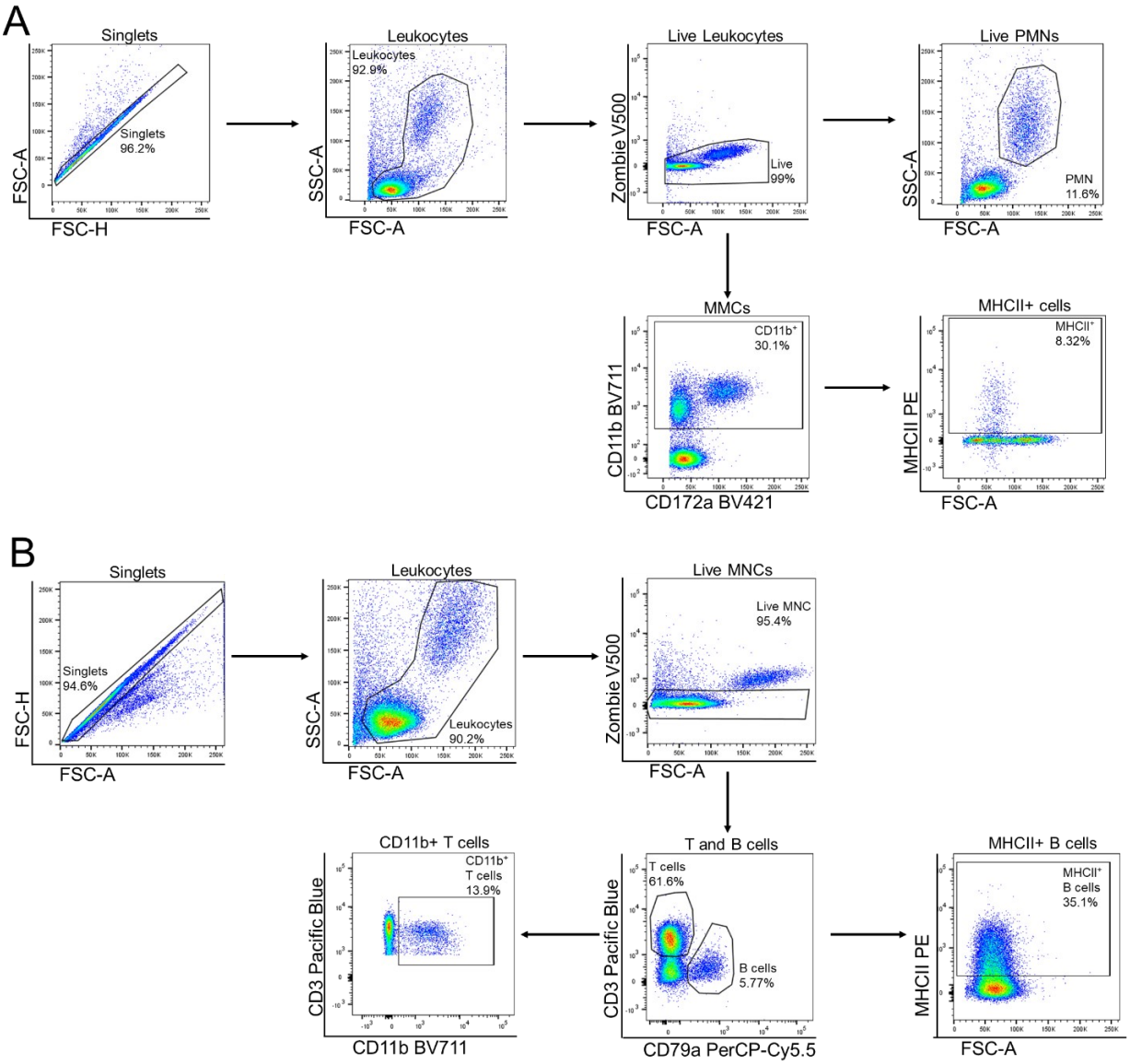

Appendix 10.16 | Successful staining of MHCII facilitated definition of leukocyte subsets.
Identification of MHCII expressing myeloid (**A**) and B cells (**B**) was carried out by utilization of gating strategies to define myeloid and lymphoid cells in ERB. In brief, doublets and dead cells were excluded and MMCs were defined as $CD11b^{+}CD172a^{+}$ expressing cells (PMN-1)(**A**). T and B cells were defined by $CD3^{+}CD79a^{-}$ and $CD3^{-}CD79a^{+}$ cells withing live, single MNCs. A CD11b expressing subset was defined within the $CD3^{+}$ expressing T cell population (**B**). Shown are representative plots.

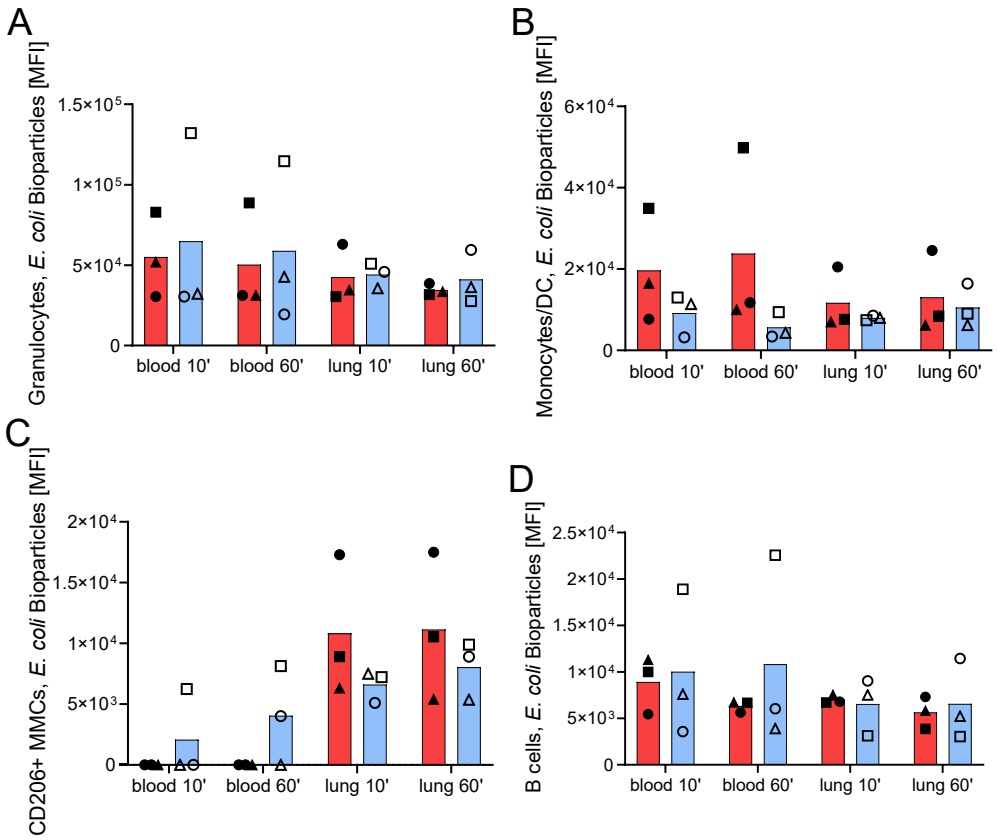

Appendix 10.17 | Analysis of phagocytic activity in ERB leukocytes based on MFI of phagocytosed particles.

Phagocytosis of *E. coli* bioparticles by granulocytes (**A**), monocytes/DCs (**B**), CD206 expressing MMCs (**C**), and B cells (**D**) was quantified by MFI analysis of FITC signal. Each individual is represented by a symbol, bars represent the group mean.

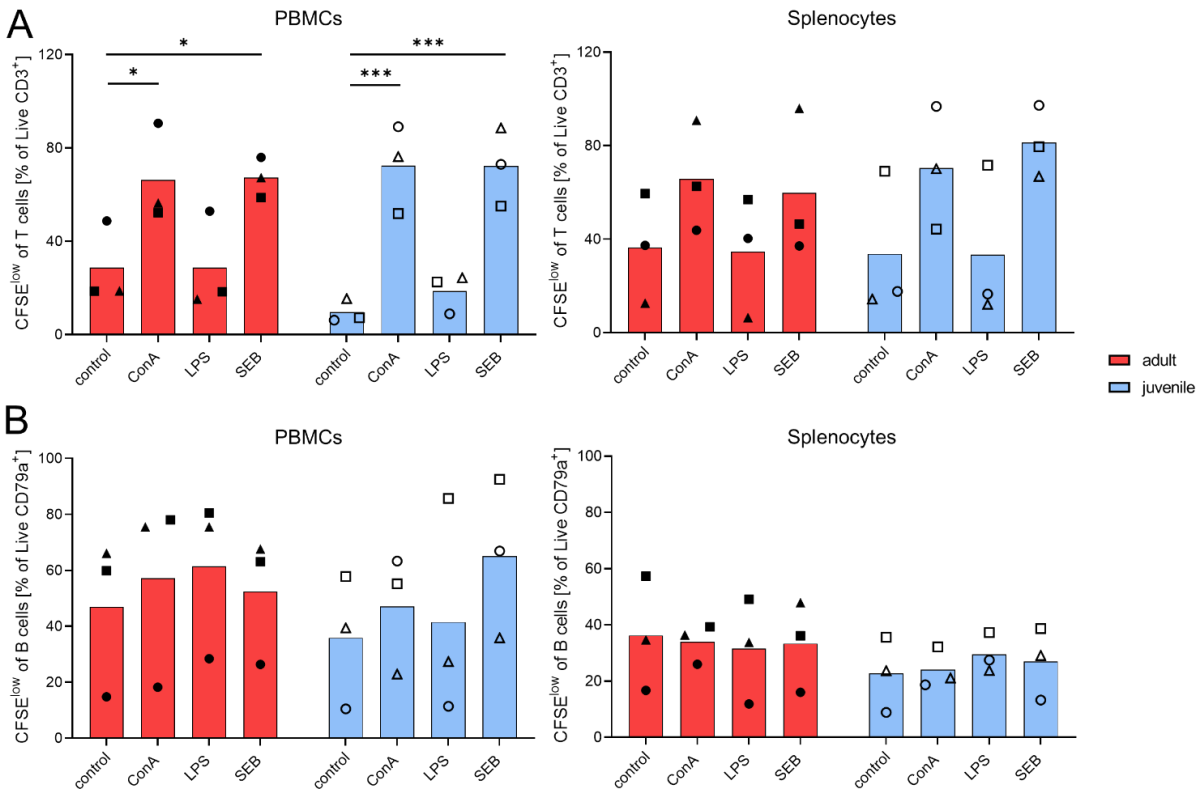

Appendix 10.18 | Assessment of proliferation in ERB lymphocytes upon mitogenic stimulation by CFSE staining.

T (**A**) and B cell (**B**) proliferation of ERB spleen and periphery upon mitogenic stimulation by CFSE detection in flow cytometry. $CFSE^{low}$ cells were defined as proliferating cells. Each individual is represented by a symbol, bars represent the group mean. (*) $P \leq 0.05$, (**) $P \leq 0.01$, (***) $P \leq 0.001$.

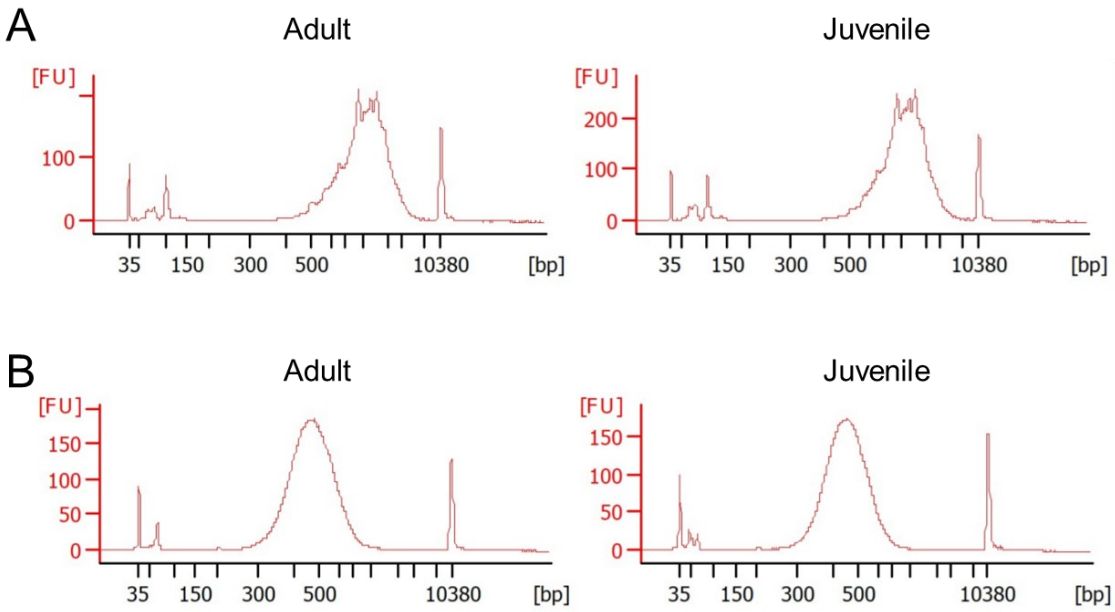

Appendix 10.19 | Quantification and quality control of cDNA and libraries used for scRNA-seq. Quantification of cDNA (**A**) and generated libraries (**B**) was carried out on high sensitivity chips and BioAnalyzer runs. Quantification served as both quality control and calculation of cDNA input in subsequent PCR steps.

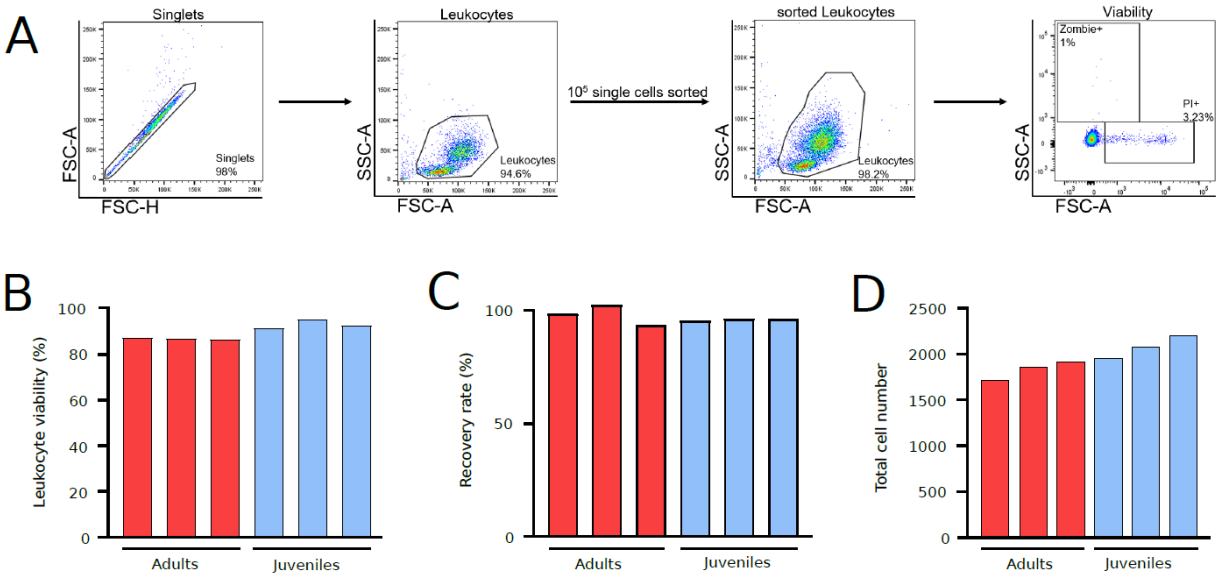

Appendix 10.20 | Satisfactory viability and recovery rate of ERB leukocytes after cell sorting.
Viability of sorted ERB leukocytes was assessed by flow cytometry. In brief, doublets were excluded and cell death prior ($Zombie^+$) and post sorting (PI^+) was determined (**A**). Viability of all samples from adult and juvenile ERB that were subjected to scRNA-seq was determined (**B**). Recovery of sorted leukocytes after centrifugation was calculated (**C**) as well as homogenous representation of all individuals in pooled samples of adult and juvenile ERB (**D**). Bars represent cell numbers from each individual used for scRNA-seq, determined by Christophe Toussaint, (Helmholtz, HIRI).

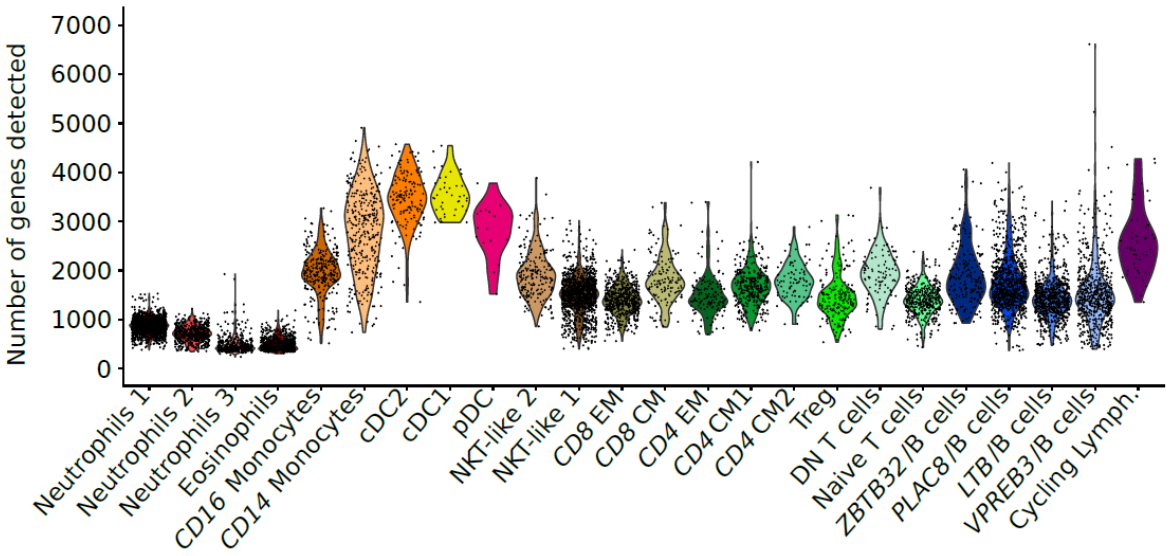

Appendix 10.21 | Total number of genes detected in each leukocyte subset.
Total gene numbers derived from each leukocyte found in each annotated subset. Each point within the violin plot represents a single cell. Sequencing, annotation and clustering was performed by Christophe Toussaint (Helmholtz, HIRI).

11 Academic career path

11.1 Publications

PUBLIKATIONEN

2022

Rissmann, M., Kley, N., Straube, M., Sadeghi, B., **Friedrichs, V.**, Balkema-Buschmann, A. „Baseline of Physiological Body Temperature and Hematological Parameters in Captive *Rousettus aegyptiacus* and *Eidolon helvum* Fruit Bats", submitted to *MDPI Microorganisms*

2021

Friedrichs, V., Toussaint, C.; Schäfer, A.; Rissmann, M.; Mettenleiter, T.C.; Pei, G.; Balkema-Buschmann, A.; Saliba, A.; Dorhoi, A. „Landscape and age dynamics of immune cells in the Egyptian Rousette Bat", submitted to *Cell Reports*

Friedrichs, V.; Balkema-Buschmann, A.; Dorhoi, A.; Pei, G. "Selection and Stability Validation of Reference Gene Candidates for Transcriptional Analysis in *Rousettus aegyptiacus*", *Scientific Reports,* DOI: 10.1038/s41598-021-01260-z

Te Kamp V, **Friedrichs V**, Freuling CM, Vos A, Potratz M, Klein A, Zaeck LM, Eggerbauer E, Schuster P, Kaiser C, Ortmann S, Kretzschmar A, Bobe K, Knittler MR, Dorhoi A, Finke S, Müller T. „Comparable Long-Term Rabies Immunity in Foxes after Intra-Muscular and Oral Application Using a Third-Generation Oral Rabies Virus Vaccine", *Vaccines (Basel)*, DOI: 10.3390/vaccines9010049

2020

Freuling CM, Breithaupt A, Müller T, Sehl J, Balkema-Buschmann A, Rissmann M, Klein A, Wylezich C, Höper D, Wernike K, Aebischer A, Hoffmann D, **Friedrichs V**, Dorhoi A, Groschup MH, Beer M, Mettenleiter TC. „Susceptibility of Raccoon Dogs for Experimental SARS-CoV-2 Infection. "*Emerging Infectious Diseases*, DOI: 10.3201/eid2612.203733

Leelahapongsathon K, Kasemsuwan S, Pinyopummintr T, Boodde O, Phawaphutayanchai P, Aiyara N, Bobe K, Vos A, **Friedrichs V**, Müller T, Freuling CM, Chanachai K. „Humoral Immune Response of Thai Dogs after Oral Vaccination against Rabies with the SPBN GASGAS Vaccine Strain.", *Vaccines (Basel)*, DOI: 10.3390/vaccines8040573

11.2 Contributions to scientific congresses

WISSENSCHAFTLICHE BEITRÄGE ZU KONFERENZEN

07/2021	**Friedrichs V.**, Balkema-Buschmann A., Pei G., Dorhoi A. (Vortrag) „Investigations on innate reactivity of novel *Rousettus aegyptiacus* cell lines to viral mimetics and temperature oscillations" Veterinärimmunologischer Arbeitskreis (VIA, DGfI)
10/2020	**Friedrichs V.**, Balkema-Buschmann A., Pei G., Dorhoi A. (Posterpräsentation) „ Novel *Rousettus aegyptiacus* cell lines enable analysis of Type I and III Interferon responses to European Bat Lyssaviruses and other unique immunological traits in distinct reservoir species" *Spring School of Immunology*, Ettal, Deutschland
03/2020	**Friedrichs V.**, Köllner B., Pei G., Dorhoi A. (Vortrag) „Deciphering regulation of interferons by torpor and antiviral responses in *Rousettus aegyptiacus*" *Symposium "Infektion und Immunabwehr" Burg Rothenfels*, Rothenfels, Deutschland
09/2019	**Friedrichs V.**, Dorhoi A., Köllner B. (Posterpräsentation) "Novel *Rousettus aegyptiacus* cell lines allow insight in Type I and III Interferon responses to European Bat Lyssaviruses in distinct reservoir species" *Nachwuchswissenschaftler-Symposium, Solutions for Future – upcoming challenges in animal and human health*, Jena, Deutschland
08/2019	**Friedrichs V.**, Dorhoi A., Köllner B. (Vortrag) „*Rousettus aegyptiacus* cell lines enable analysis of Type I and III interferon responses to highly pathogenic viruses in reservoir species" *International Veterinary Symposium*, Seatlle, WA, USA

12 Eigenständigkeitserklärung

Hiermit erkläre ich, dass diese Arbeit bisher von mir weder an der Mathematisch-Naturwissenschaftlichen Fakultät der Universität Greifswald noch einer anderen wissenschaftlichen Einrichtung zum Zwecke der Promotion eingereicht wurde.

Ferner erkläre ich, dass ich diese Arbeit selbstständig verfasst und keine anderen als die darin angegebenen Hilfsmittel und Hilfen benutzt und keine Textabschnitte eines Dritten ohne Kennzeichnung übernommen habe.

.....	.....
Ort, Datum	Virginia Friedrichs

13 Acknowledgement

The science of successful group projects – a review, in which this thesis could be used as reference. This section is dedicated to the many people who contributed in one way or another to making this thesis a success.

First of all, I would like to thank Prof. Dr. Anca Dorhoi for the possibility to continue on the path of bat research and to use my full potential by guiding the studies. I know, a student's thoughts can be confusing, but I experienced improvement and encouragement when needed while still being able to learn scientific independence. I am, and always will be, grateful for all your support throughout the years!

Secondly, I thank Dr. Gang Pei, who always had answers to my questions and solutions to problems. I learned new things everyday since becoming a lab member and I wholeheartedly enjoyed countless discussions about science and the great beyond. Thank you! Further, I thank everyone involved in the Lyssavirusverbund: Prof. Dr. Dr. h.c. Thomas C. Mettenleiter, Dr. Conrad Freuling, Dr. Thomas Müller, Dr. Bernd Köllner and thesis committee: Prof. Dr. Ulf Dittmer and especially Prof Dr. Stefan Finke, for always providing support and guidance when needed. I appreciate all the trust that was placed in me and my work, resulting in wonderful collaborations, which I enjoyed a lot!

Not to forget my lab mates, Lisa Loerzer, Silke Rehbein and Sabine Weber. You contributed to this thesis by helping out on stressful days and, more importantly, keeping a wonderful atmosphere in the lab. I was always looking forward to going to the lab because of you! A big thank you also to PD Dr. Anne Balkema-Buschmann for sharing bat knowledge and the excitement for these unique and cute little animals. I enjoyed every minute in the stable!

Another section of appreciation is dedicated to Dr. Alexander Schäfer for always picking me up once I was again defeated by the Fortessa and saving many experiments with your Nordic 'cool head'. And I did not forget to catch up: Thank you, Prof. Dr. Michael U. Martin for nurturing my excitement for immunology and encouraging me to continue on this scientific path. You have laid the foundation of this thesis.

Last, but definitely not least, I would like to thank my parents. I am who I am because of you. I could not have taken even the first step without your help throughout all these years!